

AFRL-RY-HS-TR-2007-0037 Volume I

PROCEEDINGS OF THE 2007 ANTENNA APPLICATIONS SYMPOSIUM
Volume I of II

Daniel Schaubert, Editor

University of Massachusetts at Amherst
Electrical and Computer Engineering
100 Natural Resources Road
Amherst MA 01003

Final Report

20 December 2007

APPROVED FOR PUBLIC RELEASE; DISTRIBUTION UNLIMITED



AIR FORCE RESEARCH LABORATORY
Sensors Directorate
Electromagnetics Technology Division
80 Scott Drive
Hanscom AFB MA 01731-2909

NOTICE AND SIGNATURE PAGE

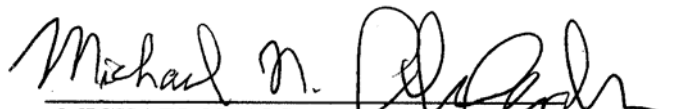
Using Government drawings, specifications, or other data included in this document for any purpose other than Government procurement does not in any way obligate the U.S. Government. The fact that the Government formulated or supplied the drawings, specifications, or other data does not license the holder or any other person or corporation; or convey any rights or permission to manufacture, use, or sell any patented invention that may relate to them.

This report was cleared for public release by the Electronic Systems Center Public Affairs Office for the Air Force Research Laboratory Electromagnetic Technology Division and is available to the general public, including foreign nationals. Copies may be obtained from the Defense Technical Information Center (DTIC) (<http://www.dtic.mil>).

AFRL-RY-HS-TR-2007-0037 HAS BEEN REVIEWED AND IS APPROVED FOR PUBLICATION IN ACCORDANCE WITH ASSIGNED DISTRIBUTION STATEMENT.



DAVID D. CURTIS
Chief, Antenna Technology Branch



MICHAEL N. ALEXANDER
Technical Advisor
Electromagnetic Technology Division

This report is published in the interest of scientific and technical information exchange, and its publication does not constitute the Government's approval or disapproval of its ideas or findings.

REPORT DOCUMENTATION PAGE

*Form Approved
OMB No. 0704-0188*

Public reporting burden for this collection of information is estimated to average 1 hour per response, including the time for reviewing instructions, searching existing data sources, gathering and maintaining the data needed, and completing and reviewing this collection of information. Send comments regarding this burden estimate or any other aspect of this collection of information, including suggestions for reducing this burden to Department of Defense, Washington Headquarters Services, Directorate for Information Operations and Reports (0704-0188), 1215 Jefferson Davis Highway, Suite 1204, Arlington, VA 22202-4302. Respondents should be aware that notwithstanding any other provision of law, no person shall be subject to any penalty for failing to comply with a collection of information if it does not display a currently valid OMB control number. **PLEASE DO NOT RETURN YOUR FORM TO THE ABOVE ADDRESS.**

1. REPORT DATE (DD-MM-YYYY) 20-12-2007		2. REPORT TYPE FINAL REPORT		3. DATES COVERED (From - To) 18 Sep 2007 - 20 Sep 2007	
4. TITLE AND SUBTITLE Proceedings of the 2007 Antenna Applications Symposium, Volume I				5a. CONTRACT NUMBER F33615-02-D-1283	
				5b. GRANT NUMBER	
				5c. PROGRAM ELEMENT NUMBER	
6. AUTHOR(S) Daniel Schaubert, Editor				5d. PROJECT NUMBER	
				5e. TASK NUMBER	
				5f. WORK UNIT NUMBER	
7. PERFORMING ORGANIZATION NAME(S) AND ADDRESS(ES) University of Massachusetts Amherst Electrical and Computer Engineering 100 Natural Resources Road Amherst, MA 01003				8. PERFORMING ORGANIZATION REPORT	
9. SPONSORING / MONITORING AGENCY NAME(S) AND ADDRESS(ES) Electromagnetics Technology Division Sensors Directorate Air Force Research Laboratory 80 Scott Drive Hanscom AFB MA 01731-2909				10. SPONSOR/MONITOR'S ACRONYM(S) AFRL-RY-HS	
				11. SPONSOR/MONITOR'S REPORT NUMBER(S) AFRL-RY-HS-TR-2007-0037	
12. DISTRIBUTION / AVAILABILITY STATEMENT APPROVED FOR PUBLIC RELEASE; DISTRIBUTION UNLIMITED					
13. SUPPLEMENTARY NOTES Volume I contains pages 1 – 271 Public Affairs release Number ESC 07-1445, 18 DEC 2007 Volume II contains pages 272 – 561					
14. ABSTRACT The Proceedings of the 2007 Antenna Applications Symposium is a collection of state-of-the art papers relating to antenna arrays, millimeter wave antennas, simulation and measurement of antennas, integrated antennas, and antenna bandwidth and radiation improvements.					
15. SUBJECT TERMS Antennas, phased arrays, digital beamforming, millimeter waves, antenna measurements, airborne antenna applications, Vivaldi antennas, waveguide antenna arrays, broadband arrays, electrically small antennas					
16. SECURITY CLASSIFICATION OF:			17. LIMITATION OF ABSTRACT UU	18. NUMBER OF PAGES 281	19a. NAME OF RESPONSIBLE PERSON David D. Curtis
a. REPORT Unclassified	b. ABSTRACT Unclassified	c. THIS PAGE Unclassified			19b. TELEPHONE NUMBER (include area code) N/A

Table of Contents

2007 ANTENNA APPLICATIONS SYMPOSIUM (Volumes I & II)
18 - 20 September 2007, Monticello, Illinois

Current Capabilities of Digital Beamforming D.D. Curtis, D. Spendley and D.Q. Luu	1
Flex Based L-Band Phased Array Antenna Demonstration P. Buxa, T. Dalrymple, C. Lesniak and R. Neidhard	34
Parameter Variation for Broadband Arrays of Irregular Polyomino Subarrays R.J. Mailloux, S.C. Santarelli, T.M. Roberts and B.C. Kaanta	46
Sub-Array Mirroring for Mediation of Second-Order Beams in Planar Edge Slot Waveguide Antenna Arrays B.J. Herting, M.W. Elsallal and J.B. West	65
Planar Edge Slot Waveguide Antenna Array Design using COTS EM Tools M.W. Elsallal, B.J. Herting and J.B. West	76
A Cross-Flux Method for Coupling Prediction of Two Installed Antennas C.C. Lu	90
Proposed Coincident Phase Center Orthogonal Dipoles W.R. Pickles and W.M. Dorsey	106
Scan Impedance for an Infinite Dipole Array: Hansen's Formulas vs. Ansoft HFSS Simulations S.N. Makaorv	125
High Performance Phased Arrays of Doubly Mirrored Balanced Antipodal Vivaldi Antenna (DmBAVA): Current Development and Future Considerations M.W. Elsallal and D.H. Schaubert	148
Miniaturization of Cavity-Backed Slot Antennas M. Al-Joumayly and N. Behdad	160

A Compact Ku/Ka Band Feed for Airborne Antenna Applications	169
J.P. Creticos and D.H. Schaubert	
UWB Tapered Slot Antenna Array Using SIW Technology	181
S. Lin, S. Yang and A.E. Fathy	
A Study of the Performance Properties of Small Antennas	193
S.R. Best	
Non-Foster Matching of a Lossy, Electrically-Small Antenna Over an Extended Frequency Range	220
S.E. Sussman-Fort and R.M. Rudish	
Microfluidic Reconfiguration of Antennas	241
G.H. Huff, P. Bahukudumbi, W.N. Everett, A. Beskok, M.A. Bevan, D. Lagoudas and Z. Ounaies	
Novel Reconfigurable Multi-Band Antennas for Wireless Receivers	259
S. Yang, H.K. Pan, A.E. Fathy, S.M. El-Ghazaly and V.K. Nair	
Performance Predictions for Linear Antennas with Offset Loading and Offset Excitation	272
P.E. Mayes, P.W. Klock and S. Barot	
Improvements on MF Ground Wave Antennas for the Global Maritime Distress and Safety System (GMDSS)	284
T.R. Vogler, T.C. Kramer and W.A. Davis	
A Compact, Wide Bandwidth UHF / L-Band Communications System Antenna for Ground-Based Applications	313
T. Goodwin	
Effects of Modulation Ratio on the Performance of 4 Arm MAW Spirals	328
W.N. Kefauver, T.P. Cencich and D.S. Filipovic	
Dual-Substrate Capacitive Loading Technique in Linearly and Circularly Polarized Shorted Annular Ring Antennas	347
W.M. Dorsey, J. Valenzi and A.I. Zaghloul	

A Connector Design for Coplanar Waveguide	366
Y.M. Lee and T.K. Anthony	
A New Radio Direction Finder for Wildlife Research	384
T.A. Borrowman, S.J. Franke and G.W. Swenson, Jr.	
Challenges and Solutions for the Efficiency Measurement of an Electrically Small Antenna for Animal Tracking	395
J.M. Martin, G.W. Swenson, Jr. and J.T. Bernhard	
Transformational Element Level Arrays (TELA) Testbed	406
T. Dalrymple, J. Buck, P. Buxa, J. McCann, R. Neidhard, G. Scalzi, C. Shreffler, D. Spendley and P. Watson	
A Transportable VHF Ground Plane Antenna Range for Azimuthal Pattern Measurement	431
A. Adrian and J.M. Huk	
Exponentially Tapered and Folded Wideband TEM Horn Array for 20 KV of Impulse	447
Y-J Ahn, J-S Lee, S-J Kim, F.J. Harackiewicz and B. Lee	
Multipath Rejection by Virtue of a Choke Ring for a Broadband Droopy Turnstile Antenna	467
S.N. Makarov and F. Scire Scappuzzo	
Leaky Wave Antenna Research at AFRL	508
D. Janning, J. McCann, M. Corwin, T. Dalrymple, L. Kempel, D. Killips, K. Pasala, R. Penno, J. Radcliffe, S. Schneider and K. Zeller	
Scalar and Tensor Artificial Impedance Surface Conformal Antennas	526
J.S. Colburn, D.F. Sievenpiper, B.H. Hong, J.J. Ottusch, J.L. Visher and P.R. Herz	
Three-Dimensional Electronic Band Gap (3-D EBG) Structures for Advanced Conformal Antennas	541
F. Scire Scappuzzo, J.P. Towle and M. Lazzaro	

Identifiers for Proceedings of Symposia

The USAF Antenna Research and Development Program

Year	Symposium No.	Identifier
1951	First	
1952	Second	ADB870006
1953	Third	ADB283180
1954	Fourth	AD63139
1955	Fifth	AD90397
1956	Sixth	AD114702
1957	Seventh	AD138500
1958	Eighth	AD301151
1959	Ninth	AD314721
1960	Tenth	AD244388 (Vol. 1) AD319613 (Vol. 2)
1961	Eleventh	AD669109 (Vol. 1) AD326549 (Vol. 2)
1962	Twelfth	AD287185 (Vol. 1) AD334484 (Vol. 2)
1963	Thirteenth	AD421483
1964	Fourteenth	AD609104
1965	Fifteenth	AD474238L
1966	Sixteenth	AD800524L
1967	Seventeenth	AD822894L
1968	Eighteenth	AD846427L
1969	Nineteenth	AD860812L
1970	Twentieth	AD875973L
1971	Twenty-First	AD888641L
1972	Twenty-Second	AD904360L
1973	Twenty-Third	AD914238L

Antenna Applications Symposium

Year	Symposium No.	Technical Report No.	Identifier
1977	First	_____	ADA955413
1978	Second	_____	ADA955416
1979	Third	_____	ADA077167
1980	Fourth	_____	ADA205907
1981	Fifth	_____	ADA205816
1982	Sixth	_____	ADA129356
1983	Seventh	_____	ADA142003; 142754
1984	Eighth	85-14	ADA153257; 153258
1985	Ninth	85-242	ADA166754; 165535
1986	Tenth	87-10	ADA181537; 181536
1987	Eleventh	88-160	ADA206705; 206704
1988	Twelfth	89-121	ADA213815; 211396
1989	Thirteenth	90-42	ADA226022; 226021
1990	Fourteenth	91-156	ADA237056; 237057
1991	Fifteenth	92-42	ADA253681; 253682
1992	Sixteenth	93-119	ADA268167; 266916
1993	Seventeenth	94-20	ADA277202; 277203
1994	Eighteenth	95-47	ADA293258; 293259
1995	Nineteenth	96-100	ADA309715; 309723
1996	Twentieth	97-189	ADA341737
1997	Twenty First	1998-143	ADA355120
1998	Twenty Second	1999-86	ADA364798
1999	Twenty Third	2000-008 Vol. I & II	ADA386476; 386477
2000	Twenty Fourth	2002-001 Vol. I & II	ADA405537; 405538
2001	Twenty Fifth	2002-002 Vol. I & II	ADA405328; 405327
2002	Twenty Sixth	2005-001 Vol. I & II	ADA427799; 427800
2003	Twenty Seventh	2005-005 Vol. I & II	ADA429122; 472514
2004	Twenty Eighth	2005-016 Vol. I & II	ADA431338; 431339
2005	Twenty Ninth	2005-039 Vol. I & II	ADM001873
2006	Thirtieth	2006-0047 Vol. I & II	ADA464058, 464059
2007	Thirty First	2007-0037 Vol. I & II	

2007 Author Index

Adrian, A.	431	Lazzaro, M.	541
Ahn, Y-J	447	Lee, B.	447
Al-Joumayly, M.	160	Lee, J-S	447
Anthony, T.K.	366	Lee, Y.M.	366
Bahukudumbi, P.	241	Lesniak, C.	34
Barot, S.	272	Lin, S.	181
Behdad, N.	160	Lu, C.C.	90
Bernhard, J.T.	395	Luu, D.Q.	1
Beskok, A.	241	Mailloux, R.J.	46
Best, S.R.	193	Makarov, S.N.	125, 467
Bevan, M.A.	241	Martin, J.M.	395
Borrowman, T.A.	384	Mayes, P.E.	272
Buck, J.	406	McCann, J.	406, 508
Buxa, P.	34, 406	Nair, V.K.	259
Cencich, T.P.	328	Neidhard, R.	34
Colburn, J.S.	526	Neidhard, R.	406
Corwin, M.	508	Ottusch, J.J.	526
Creticos, J.P.	169	Ounaires, Z.	241
Curtis, D.D.	1	Pan, H.K.	259
Dalrymple, T.	34, 406, 508	Pasala, K.	508
Davis, W.A.	284	Penno, R.	508
Dorsey, W.M.	106, 347	Pickles, W.R.	106
El-Ghazaly, S.M.	259	Radcliffe, J.	508
Elsallal, M.W.	65, 76, 148	Roberts, T.M.	46
Everett, W.N.	241	Rudish, R.M.	220
Fathy, A.E.	181, 259	Santarelli, S.G.	46
Filipovic, D.S.	328	Scalzi, G.	406
Franke, S.J.	384	Schaubert, D.H.	148, 169
Goodwin, T.	313	Schneider, S.	508
Harackiewicz, F.J.	447	Scire Scappuzzo, F.	467, 541
Herting, B.J.	65, 76	Shreffler, C.	406
Herz, P.R.	526	Sievenpiper, D.F.	526
Hong, B.H.	526	Spendley, D.	1, 406
Huff, G.H.	241	Sussman-Fort, S.E.	220
Huk, J.M.	431	Swenson, Jr., G.W.	384, 395
Janning, D.	508	Towle, J.P.	541
Kaanta, B.C.	46	Valenzi, J.	347
Kefauver, W.N.	328	Visher, J.L.	526
Kempel, L.	508	Vogler, T.R.	284
Killips, D.	508	Watson, P.	406
Kim, S-J	447	West, J.B.	65, 76
Klock, P.W.	272	Yang, S.	181, 259
Kramer, T.C.	284	Zaghoul, A.I.	347
Lagoudas, D.	241	Zeller, K.	508

CURRENT CAPABILITIES OF DIGITAL BEAMFORMING

David D. Curtis, Daniel N. Spendley, Danh Q. Luu
Air Force Research Laboratory, Sensors Directorate
Electromagnetics Technology Division
Antenna Technology Branch - AFRL/SNHA
Hanscom AFB, MA 01731-2909

Abstract: This paper surveys the current state of the art of digital beamforming (DBF) with an emphasis on current capabilities and practical implementation techniques. Digital control of phased arrays in both receive and transmit modes will be covered, including such key issues as hardware, integration, processing load, and cost. The viability of future trends in DBF will be examined in terms of feasibility and cost of the enabling technologies of adaptive hardware and embedded software.

1. Introduction

Digital beamforming was first introduced in the 1980s [1]. Initial experiments validated the basic concepts of DBF [2, 3] and demonstrated a wide range of adaptive null forming and direction finding algorithms that had been first developed for analog phased array antennas [4, 5, 6]. Following the initial interest in DBF, many specific details were then examined and several experimental test beds followed. Some of these prototyped real-time sampled data processing [6, 7], elimination of element pattern effects [8], various channel calibration approaches [9], the use of DBF for control of exotic conformal arrays, and experimental prototypes at nearly all the common radar frequencies [10, 11, 12]. While much has been demonstrated, most of this work remained in the realm of the laboratory, and very little of it was at a technology readiness level suitable for transition to either the commercial sector or to military applications. That was due to an initially slow evolution in the state of the art in digital array channel hardware.

Over the past four to five years, however, there has been a virtual explosion of high performance commercial-off-the-shelf (COTS) digital array channel hardware and signal processing chips. Leading the way are tremendous advances in field programmable gate array (FPGA) logic chips. FPGAs are now approaching the speeds of application specific integrated circuits (ASIC) and other dedicated digital signal processing (DSP) chips, yet the ease of programming embedded logic in FPGAs permits the array designer to make significantly simpler redesigns in order to scale the array or achieve different functional goals. ASICs also enable great levels of digital signal processing performance, and they may be the best choice for hardware designs which do not change frequently, but usually, ASIC design is not a trivial task. It often involves an iterative process of partial redesign

and re-layout in order to achieve desired functionality and bring signal timing issues within specified criteria. DSPs offer speed and programmability in one package. These forms of processors are all integrated circuits. In some applications where size, weight, and power consumption (SWaP) are not at a premium, high speed computer systems with real-time operating systems are sufficient. For airborne applications where SWaP and processing speed is truly important, the FPGAs, ASICs and DSPs win hands down.

The analog to digital converter (ADC) has long been the single most important component in a digital array. It not only enabled digital beamforming, it also limits array performance to a certain number of bits of digital resolution at a particular maximum sampling rate. As the sampling rate goes up, the effective number of bits comes down, and visa versa. These two parameters are very tightly coupled and the state of the art in ADCs advances at a rate of about 1 bit of added resolution every 4 years or so, for a specific sampling frequency [13]. However, the recent evolution of processing hardware has resulted in companies marketing the latest and very best available A/Ds, FPGAs, and random access memory (RAM) chips on demonstration boards that have standard personal computer interfaces like peripheral component interconnect (PCI) and virtual measurement environment (VME). The available performance has rocketed over the last two to three years, and prices are starting to come down. This has allowed array designers to prototype digital channel hardware fairly easily. In turn, digital array channel hardware is now in demand more than ever in many array antenna applications, and in certain cases, can be fielded as a subsystem in an phased array antenna system with high confidence.

This paper aims to provide an update on the current state of the art of digital beamforming technology. We begin by discussing a generalized digital array architecture which can be morphed to suit commercial radar and satellite communications applications and a wide variety of military missions, including radar, communications, signals intelligence, and satellite ground station telemetry, tracking and commanding, to name just a few. Changes in mission cause changes in key performance parameters such as scan volume, center frequency, instantaneous bandwidth, dynamic range, the number of simultaneous beams, and data processing load. In the next two sections of this paper we describe the functionality and the key components of receive array channel hardware and transmit array channel hardware, respectively, including elementary forms of digital beamforming on receive and transmit, and we discuss how the basic channel hardware changes with changes to the mission key performance parameters. Next, we describe processing for DBF, including algorithms, how channel weights are formed, the hardware that is used, data processing workload, or simply, processing load, and the impact on processing due to changes in dynamic range and bandwidth. Finally, we address future trends in DBF, including modularity, multi-functionality, nonlinear digital filtering, receiver-on-a-chip (ROC) technology, wideband null forming, localized signal generation, and orthogonal waveforms.

2. Digital Array Architectures

Digital beamforming is the term often used to refer to the merger of three interrelated technologies: digital transceivers, digital signal processing, and phased array antennas. Digital array architectures are the desired end results of merging these technologies. A block diagram of a generalized N-channel digital array architecture is shown in Figure 1.

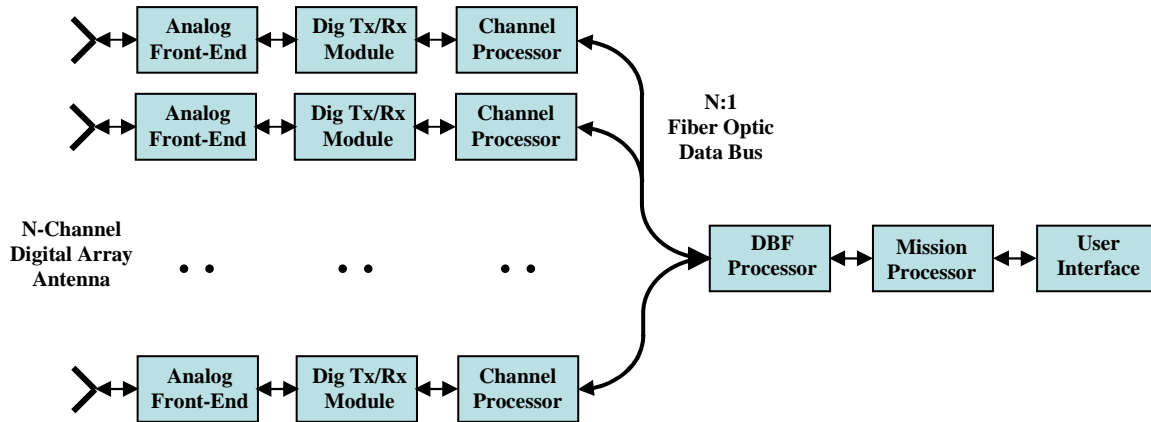


Figure 1: Block diagram of a generalized N-channel digital array architecture.

This generalized architecture is composed of N parallel digital array channels, an $N:1$ data and command signal distribution network, shown here as a fiber optic bus, and dedicated processors that perform digital beamforming computations and mission specific signal processing tasks. A user interface also may be included, but is not required in general. Depending on cost and the suitability of available hardware to meet mission requirements, each digital array channel may be connected to an individual array element, an array column or row, or a subarray. An analog beamformer is required to combine individual array antenna elements into columns, rows, or subarrays before they are connected to the digital array channel.

All the digital signal processing functions may be handled by a centralized processor, as was typically the case in the early experimental DBF prototypes. However, the current approach is to distribute the processing load across the array in N channel processors, as well as perpendicular to the array in a DBF processor and a mission-specific processor. Distributed processors reduce the overall data throughput in the architecture because each time two data streams are added together, the result is a single data stream representing their sum. While fairly generalized, the digital array architecture shown in Figure 1 emphasizes this approach.

2.1 Analog Front-End

Each digital array channel is composed of an analog front-end, a digital transceiver module and a channel processor. The analog front-end is the hardware interface between the array antenna and the digital electronics. It typically contains microwave frequency low noise amplifiers, power amplifiers, mixers, and switches. A block diagram of a typical analog front-end is shown below in Figure 2.

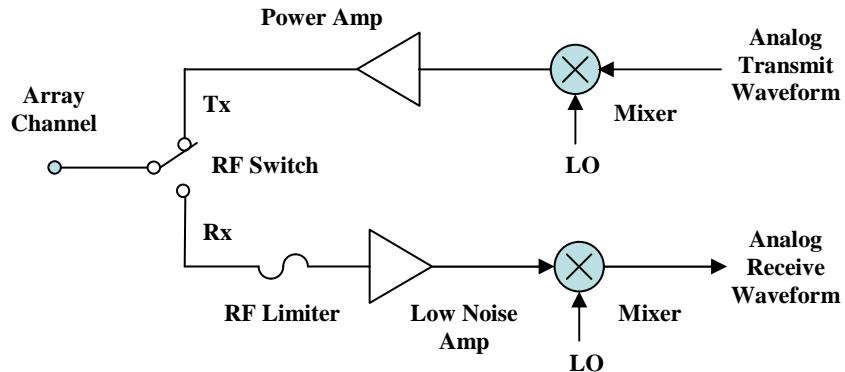


Figure 2: A typical Analog Front-End module for digital arrays.

In this diagram, the array channel is connected to either the transmit path or receive path of the analog front-end by a switch. On the transmit side of the module, the analog transmit waveform is up-converted by a mixer, amplified, and routed to the array channel through the switch. On the receive side, the signal from the array channel is routed by the switch into a limiter that protects the sensitive receiver electronics from high power signals, a low noise amplifier boosts the signal, and a mixer performs down-conversion. The resulting analog receive waveform is passed to the digital transceiver module. For full-duplex transmit and receive operation the switch may be replaced with a circulator. For frequencies around 500 MHz and lower, the mixer hardware and LO signals may be eliminated. Two or three stages of mixers and LO signals may be required for GHz frequencies.

2.2 Digital Transceiver Module

The second element in the digital array channel hardware chain is the digital transceiver module, shown in Figure 3. Detailed block diagrams of the digital transceiver module and the channel processor are shown with data paths represented by dashed lines and control signals represented by solid lines. The digital transceiver module is composed of four functional blocks. Each functional block performs a variety of related functions, as enumerated within the blocks in the figure.

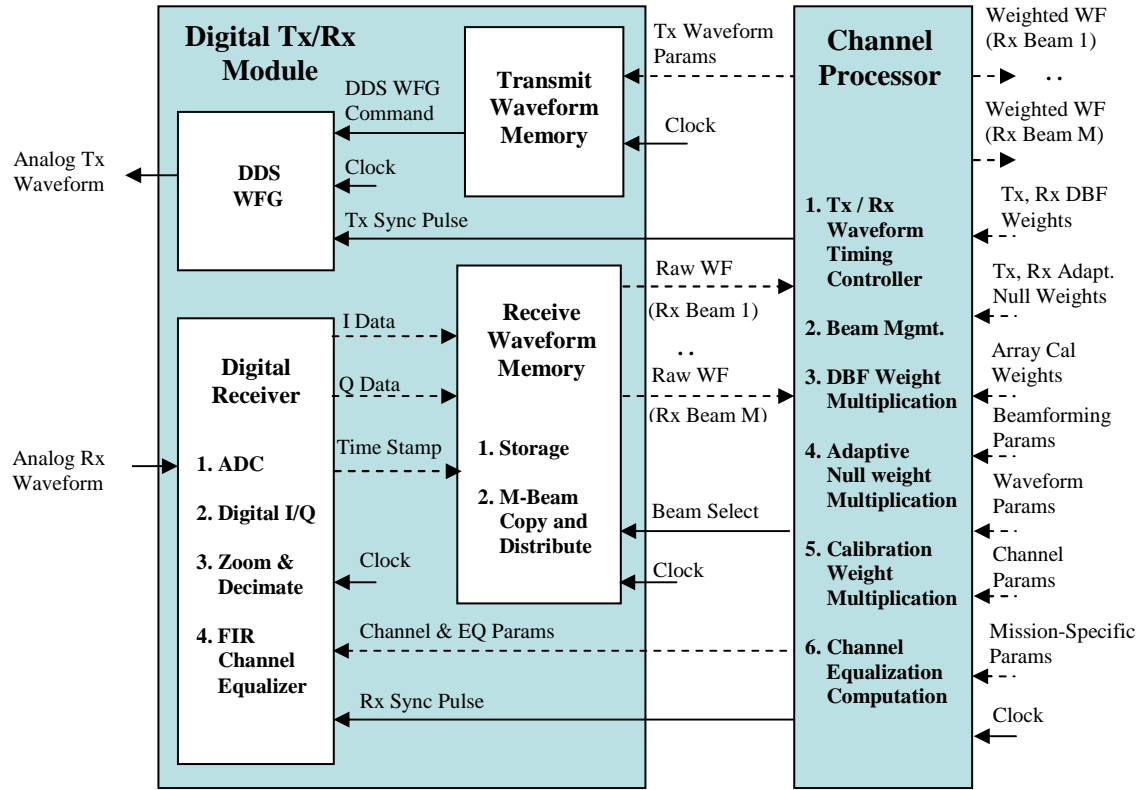


Figure 3: Block diagrams of the digital transceiver and channel processor modules.

The digital transceiver module transmit path is composed of a transmit waveform memory and a direct digital synthesis waveform generator (DDS WFG). In this scheme, a set of transmit waveform parameters are inputs to the transmit waveform memory. These parameters may include instantaneous bandwidth, center frequency, amplitude, digital modulation format, duty cycle, etc. These parameters are translated into command words for the DDS WFG. All modules in the digital array architecture run on the same clock signal. When a transmit synchronization pulse arrives at the DDS WFG, it triggers the DDS WFG to generate and send the desired analog transmit waveform to the analog front-end for up-conversion.

The receive path is composed of a digital receiver and a receive waveform memory. Channel configuration parameters are sent to the digital receiver as control variables. They set the sampling rate, instantaneous bandwidth, and digital resolution. Channel instantaneous bandwidth is controlled by zoom and decimation filtering, and a channel equalization filter is set up by the equalization parameters. The receive synchronization pulse triggers the digital receiver to sample the incident analog received waveform on the next clock pulse. The digital receiver decomposes the raw sampled data into in-phase (I) and quadrature (Q) data streams. This data, along with a time stamp, is briefly stored in

the receive waveform memory. If M multiple beams are desired, the received data is copied and distributed into M identical raw data streams. The receive waveform memory uses the beam select signal to select data corresponding to one or more of the M beams which will be forwarded to the channel processor.

2.3 Channel Processor

The third and final element in the digital array channel is the channel processor, which is also shown in Figure 3. This is the first of the processors. It accepts a wide range of parameters that are generated in the mission-specific processor, as well as a variety of complex-valued data weights generated by the DBF processor. Some of these parameters are passed through to the digital transceiver module, and others are used in the channel processor to perform specific array signal processing functions. This includes application of array calibration weights to the raw I/Q channel data, which correct for differences in amplitude and phase between any and all pairs of array channels. Once the array is calibrated, the beamforming weights can be applied to the calibrated channel data along with the null forming weights. Nulls may be formed deterministically, but most often, this is done adaptively, to counteract strong interfering signals. Alternatively, the array calibration weights, beamforming weights and adaptive null weights may be lumped into a single composite weight for each array channel. The channel processor performs a complex-valued multiplication of the raw I/Q data stream with the weights. A beam management function in the channel processor generates the beam select command that is sent to the digital transceiver module in order to extract the stored raw I/Q waveform data from the receive waveform memory. The selected waveform data streams are weighted in the channel processor and passed to the DBF processor where they are summed to form beams and nulls, and for use in other array processing such as direction finding.

2.4 N:1 Fiber Optic Data and Command Bus

The weighted data streams from all N channels must be added to form beams and nulls. This can be done in a systolic processor, which has several processor nodes distributed across the array backplane. Each node performs a mathematical operation on its input data, and passes its output to the next processor node. One node is the final processor which completes the mathematical operation. These architectures are typical in DBF systems that support a single dedicated application, where a variety of beamforming and nulling algorithms is not required. When flexibility is needed, a centralized processor often is the answer. In Figure 4, we show an $N:1$ fiber optic data bus that performs the collection and distribution function between the N digital array channels and the DBF processor. This bus has electro-optic data transceivers at the end of each optical fiber, and it contains fiber optic power dividers that multiplex the data onto a single fiber that is incident to the DBF processor. Parameters, weights and the clock signal flow from the DBF processor to the channel processors. Array pre-calibration channel data and weighted waveforms from the N receive beams flow back.

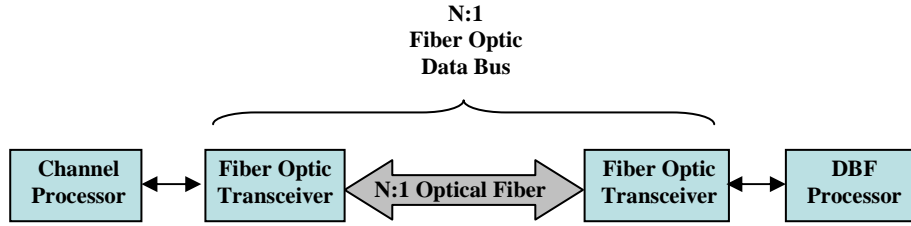


Figure 4: The N:1 Fiber optic data bus manages the transfer of data and command signals between the channel processors and DBF processor.

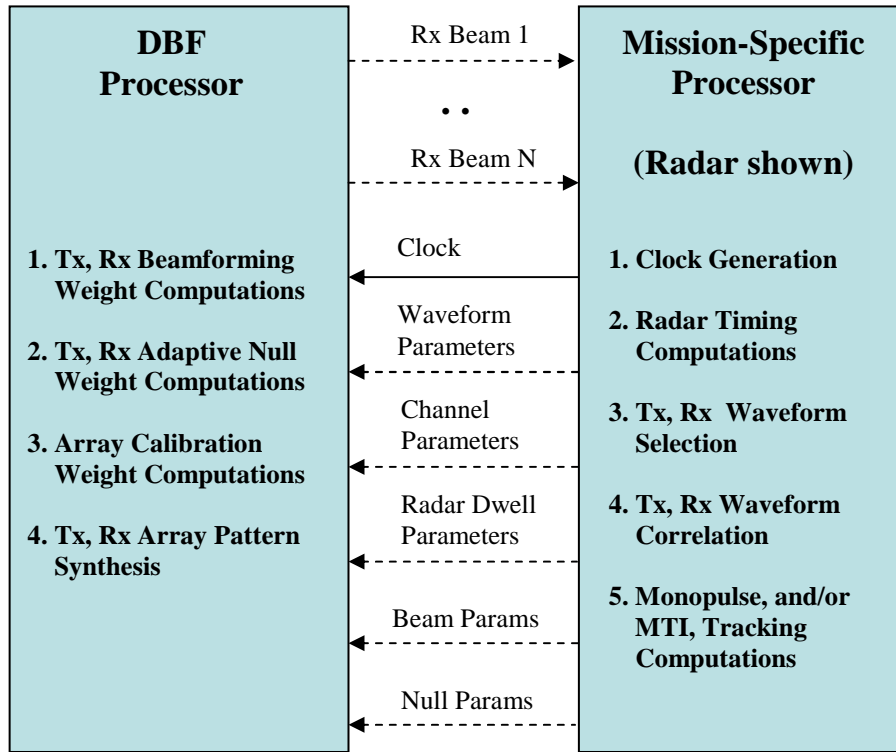


Figure 5: Illustration of the computational roles of the DBF processor and the mission-specific processor, which in this figure, is shown as a generalized radar signal processor.

2.5 DBF Processor

The DBF Processor performs four main functions. First, it is the collection point for the channel data. Channel data is accumulated in a covariance matrix which represents the statistics of the environment in which the array antenna is operating. Second, the DBF

Processor inverts the covariance matrix, and forms the weights according to an adaptive algorithm. Typically, the weights that result from adaptive beamforming algorithms are composite weights that include the beamforming and nulling behavior. The DBF processor sends the computed weights back to the channels where the channel processors apply the weights to the raw data streams, and third, the returning weighted channel data streams are summed in the DBF processor, thus forming the beams. This beam data is then passed on to the mission-specific processor. While adaptive algorithms are designed to converge to a solution to a particular parameter minimization or maximization problem, some of the more advanced digital beamforming algorithms can be classified as array pattern synthesis. The method of alternating projections is one such algorithm. It allows the array designer, or potentially, the mission-specific processor to generate a spatial mask that represents the desired array far field power pattern. The algorithms then adapts until a set of weights are found which closely approximate the mask [14]. Our team has used this algorithm to obtain beamforming weights for an experimental conformal digital array that wrapped completely around an aircraft wing. Such an array would normally have been an impossible application for most adaptive beamforming algorithms due to the complexity of the conformal array curvature [15].

The fourth main function of the DBF processor is calibration. To perform calibration the DBF processor shuts down all normal array operation, and sends unitary-valued weights to the channel processors so that the returning weighted channel data streams contain the only the raw I/Q data from each channel. The DBF processor selects one channel as the reference channel, and data from all the other channels is normalized to the reference channel data. The complex-valued calibration weights are obtained by the normalization process. Once this has been done, the DBF processor allows the array to resume normal beamforming operations and the calibration weights are combined with the beamforming and nulling weights to form the composite weights for each channel.

2.6 Mission-Specific Processor

The mission-specific processor generates the mission-specific parameters, the waveform parameters, the system clock signal, and it controls the timing between transmit and receive beams. In Figure 5, the mission-specific processor is shown as a generic radar processor. Different parameters would be generated if this digital array architecture was to be used in a communication system or an intelligence collection system. Based on these mission parameters, up to N transmit beams are formed, or up to N receive beams are formed and returned from the DBF processor to the mission-specific processor.

3. Key Components of Receive Architectures

In the previous section we described a generalized digital array architecture that emphasized distributed processing as a means of reducing data volume, and ultimately, processing load. In this section we explore variations of the digital receiver hardware, shown in Figure 3, and the overall receive mode digital array architecture.

The main components of a digital beamforming system's receive architecture are shown below in Figure 6. The functionality of each individual block may vary greatly between different DBF systems, and each is heavily influenced by its neighboring components. For instance, the techniques and algorithms used to perform beam weighting are extremely dependent upon the sampled data's format. The overall system functionalities will also help determine the detailed architecture by specifying the operational RF spectrum, instantaneous and system bandwidths, timing constraints, and other factors key to any DBF system's mission. Moving through and considering each operational block in step-by-step fashion will allow a full understanding of the hardware's capabilities and limitations as well as options for implementing efficient and practical DBF systems.

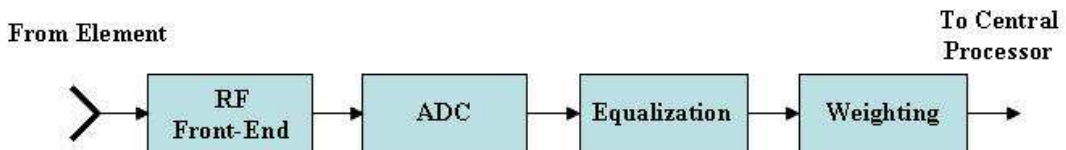


Figure 6: Illustration of the key processes in a typical DBF receive channel. Some architectures may combine one or more blocks, but these processes are still performed.

3.1 Analog Front-End

The radio frequency (RF), or analog front-end demodulates the message signal from the RF carrier to an intermediate frequency (IF), or to baseband, where sampling and signal processing are performed. The input bandwidth and output bandwidth are important design parameters that govern analog front-end design. Designing a wideband tunable front-end used for surveillance is markedly more complex than designing a narrowband front-end for a fixed frequency communications system. The wideband front-end must span the tunable bandwidth, and hold the noise floor down to preserve spur-free dynamic range. This often requires expensive custom components and considerable design expertise. If the tuning range requirements exceed the bandwidth limits of state of the art ADCs, one approach is to parse the tuning range into smaller frequency ranges, or analog sub-bands, that can be handled using available components. Diplexers, triplexers, and active circuit versions of such hardware are typically employed for this purpose. If the instantaneous bandwidth is too wide for the available components, the same approach may be used. By comparison, the design of a narrowband front-end is trivial unless it requires an extremely high spur-free dynamic range that exceeds state of the art ADCs. In this case, custom multi-stage ADCs may be constructed to sample the full dynamic range, but this is not frequently done due to the complexity and cost of the custom integrated circuit design. In addition to a relatively simple design process, COTS narrowband front ends are readily available from a large number of vendors.

Differences between narrowband and wideband front-ends often can be obvious if one examines their implementation. The relative ease of designing and implementing narrowband components and transmission lines enables them to be implemented in compact, power efficient packages such as the 2" x 2" printed circuit board shown in Figure 7. Issues with wideband component manufacturing and impedance matching often makes state of the art wideband front-end specifications harder to achieve.

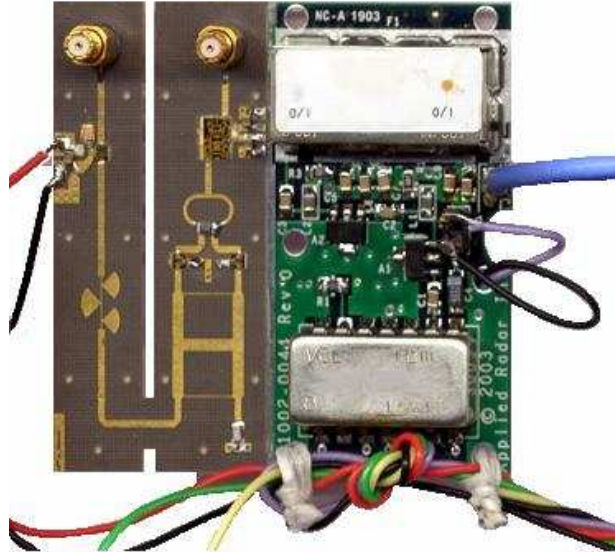


Figure 7: Example of a custom X-band analog front-end with a 15 MHz instantaneous bandwidth, that utilizes a signal stage mixer to down-convert from 10 GHz to 75 MHz.

3.2 Analog to Digital Converter

The next component in the receive channel block diagram in Figure 6 is the analog to digital converter. ADCs with sampling speeds ranging from a few kilohertz to multi-gigahertz are currently available from a limited number of commercial retailers. When combined with a properly designed analog front-end, ADCs can provide more than a gigahertz of instantaneous bandwidth. The maximum sampling rate and the digital word length, or number of bits representing each sample, are two important parameters to consider when selecting an ADC for a particular digital array application. The digital word length governs the sampled signal's potential resolution and helps establish both the dynamic range (DR) and signal-to-noise ratio (SNR) of the receive channel hardware. It can be shown that 1 bit of digital resolution corresponds to 6.02 dB of analog dynamic range [16]. Thus, a 48 dB dynamic range may be sampled using an ADC that has an effective number of bits (ENOB) of at least 8 bits. The DR and SNR of the total system must be calculated by considering the contributions of all the components in the receive channel and processing chain. However, the DR and SNR of the ADC alone provides a

good initial estimate of the system's performance limits. The digital word length and the maximum sampling rate also establishes the data throughput rate which the rest of the signal processing components must accommodate. The data throughput rate of a digital array consisting of a small number of narrowband channels may seem very low, but the data throughput rate becomes a limiting factor in a large scale digital array containing hundreds or thousands of elements. Systems such as these could easily drive the data throughput rate into the terabytes per second range, causing the data throughput rate to be a limiting factor in a practical system realization. Design trades must be performed to determine the most cost effective and high performance design for a given application.

The analog front-end and the ADC have the greatest effect on the digital receiver design compared to any other combination of the components in the receive channel. Consider a narrowband digital receiver operating in the ultra-high-frequency (UHF) band. The low center frequency and narrow instantaneous bandwidth in this case enables the designer to chose how the sampling will be performed. As one option, a low cost ADC having a low maximum sampling rate may be used if a suitable analog front-end is designed to down-convert the UHF signal to baseband. As a second option, down-conversion may be eliminated altogether if a more expensive high speed ADC is used which can sample the UHF signal directly. The design trade space is usually a multi-dimensional problem. In this simple example, it is a matter of the cost, size, weight, and power consumption of the components taken in context with the performance of each approach, including dynamic range, noise figure, and signal-to-noise ratio.

3.3 Channel Equalization and Array Calibration

A simple narrowband normalization approach to array calibration was briefly described in section 2.5 for the generalized digital array architecture. However, a variety of other approaches may be used to ensure that all channels in the array are as highly correlated as possible. An array is said to be calibrated when all its channels have nearly identical insertion losses and path lengths. In a digital array this means the channels are nearly identical mathematically, usually to within the least significant bit of the processor and data distribution hardware. A calibrated array is capable of forming deep nulls in its far field power pattern because of the high degree of correlation between the channels. However, when the array is of moderate to wide bandwidth the analog front-end components typically have frequency responses that are not well correlated from one channel to the next, and all of this precision is lost quite quickly. In order to calibrate arrays of moderate to wide bandwidths, channel equalization must be used in conjunction with array calibration.

The goal of channel equalization is to flatten the magnitude and linearize the phase of the channel frequency response over the entire instantaneous bandwidth of the channel. This is accomplished in a two-step process. First, the channel is fed with a linearly swept sinusoidal signal and the frequency response is measured by taking samples of the output at a finite number of discrete frequencies. That response may be stored in memory, but

ultimately is used to form an inverse filter whose frequency response is the complex conjugate of the measured frequency response of the channel. The second step is the design of a finite impulse response (FIR) filter [17, 18], which is often implemented as a digital tapped delay line with coefficients related to the frequency response of the inverse filter. The convolution of the channel response with the inverse filter produces the desired result. Because the channels in the array may have different frequency responses, it is necessary to equalize each channel independently, but this may be done in parallel if the processor architecture can support it. Once each channel is equalized, the narrowband normalization approach [19] may be used to perform array calibration. This is because the channel frequency responses now have constant magnitudes and linear phases within each channel, but the magnitudes and phases differ from one channel to the next.

Alternatively, one may calibrate the array and achieve a form of channel equalization over the instantaneous bandwidth using a different technique. After measuring and recording the channel frequency responses of all the channels, the frequency response magnitude and phase at the k^{th} discrete frequency may be compared across all N channels in the array. This comparison may be a normalization to the amplitude and phase of one channel chosen to be the reference channel, or it may be the average complex value of all the channels at this one discrete frequency. This is narrowband calibration which is valid only at the k^{th} discrete frequency. If this process is repeated at all K discrete frequencies of the measured channel frequency responses, K discrete frequency array calibrations will be performed and each channel in the array will have K calibration coefficients which span the entire instantaneous bandwidth. The channels will not be equalized in a true sense, meaning that the frequency response magnitudes will not be flat and the phases will not be linear, but the relative differences in magnitude and phase between all the N channels will be nearly zero at each discrete frequency.

Like calibration, the equalization process typically requires the array to cease all normal operations while the channel frequency responses are measured and the coefficients of the inverse filters are calculated. However, in some applications, it may be necessary to perform channel equalization and array calibration more frequently. This may be necessary when the array undergoes some physical change such as the displacement of an element due to mechanical deformation, vibration or thermal expansion and contraction. Situations such as these require a re-evaluation of the relative spatial dimensions between each receive element before further equalization can occur.

3.4 Local Memory Blocks

Physical memory blocks may be inserted in the receive array hardware to support calibration and equalization, but these can also support data transfers, further processing, and data re-evaluation. Due to its wide range of uses, memory can be integrated into or around many of the functional blocks in the receive architecture or included separately as can be seen in Figure 8. A small amount of memory connected to the ADC enables the processor to collect raw data for calculating adaptive beamforming weights or playback

of received incoming waveforms. Large blocks of memory can also be attached to the channel or array processing board, allowing for a vast amount of data to be collected before being sent to a central processor for final calculations and evaluations. These large data depositories are able to collect data at a high rate, allowing the DBF system to run at its maximum speed for a limited time and then transfer the recorded data to the processor at speeds realizable using current data bus technology. In many applications, running in this “quasi-real time” mode is sufficient for operation given that relatively large wait times may be necessary in between processing periods.

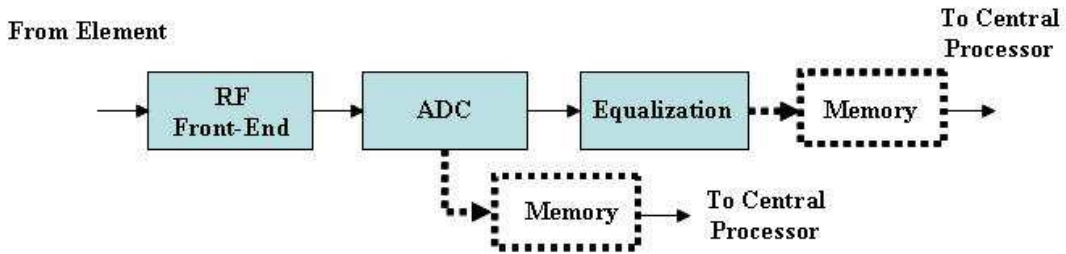


Figure 8: Examples of optional memory locations for DBF receive architectures. On-board memory can be inserted almost anywhere on the receiver board permitting the available real estate exists. The above architecture includes optional memory after the ADC as well as after equalization for weight generation and beamforming offline.

3.5 Weighting

The last block in the general receiver architecture in Figure 6, applies beamforming weights and other signal processing algorithms to the sampled data. Beamforming is often thought to occur in a central processing unit, but application of weights may be performed at the channel level. This allows a designer to apply the beam weights at either the channel or the central processor. In the narrowband case, the beamforming weights can simply be represented as a complex number representing an amplification and phase shift. Most array processing textbooks [20, 21], as well as the current beamforming literature [22], represent the weighting scheme as the inner product between two complex vectors, the input signal, x , and the corresponding weights, w .

$$y = w^* x \quad (1)$$

Equation 1 provides the mathematical relationship for the weight-and-sum beamforming architecture familiar to both the analog and digital array communities. The inner product calculates the power of the received signal in a direction specified by beam weights, w .

In general, three main architectures exist for applying beamforming weights:

1. **Real-time**: All weighting is performed at the same rate data is inputted to the digital processor. The resulting data is continuously streamed out of the processor for further analysis without interruptions.
2. **Quasi-Real-time**: Weighting may be performed in a real-time manner, but a data bottle neck occurs at some point in the architecture resulting in a time lag between available processed data sets. Bottle necks are often caused by a large data throughput which the digital bus hardware is unable to accommodate.
3. **Offline**: Sometimes referred to as “Poor Man’s DBF”. All channel data is placed in a data depository to be processed at a later time in software. This architecture allows digital beamforming to be implemented at a basic, cost efficient level, but not an operational ready level.

Real-time and quasi-real-time architectures are most often implemented using components designed for parallel processing, such as FPGAs and ASICs. These chips provide a DBF designer with an abundance of resources including a flexible application platform, high number of input/output (I/O) pins and specialized processing circuitry. Of these two options, FPGAs provide the most design flexibility because they can be reconfigured easily. This offers the designer a large number of debugging options as well as the ability to add additional processing capabilities for applications defined at some time after the initial design. The ASIC provides a more restrictive processing block because its architecture is hardwired, and it is inherently non-adaptable to future applications. But since the processing components are predefined, ASICs typically require less power and may achieve lower costs when manufactured in high numbers compared to the FPGA.

4. Key Components of Transmit Architectures

A general block diagram highlighting the main components of the DBF transmitting architecture is shown below in Figure 9. Transmit beamforming is often considered the “dual” problem to receive beamforming and thus a simple reversal of the receive chain components is expected to achieve a high performance system. This general philosophy is not without merit, but is still a somewhat naive design process. As with the receive architecture, the operation of every functional block affects the other components in the transmitting chain, but a new, important design issue arises that is not an issue for DBF on receive. That is, the coherence of the channels relative phases. The channel-to-channel signal coherence will be shown to be both the transmitter’s enabling feature as well as its inhibitor. For this reason, each of the transmitter architecture’s components will be discussed from the right to left to provide a greater understanding of the signal coherence’s importance from the steps of signal generation to transmittance.

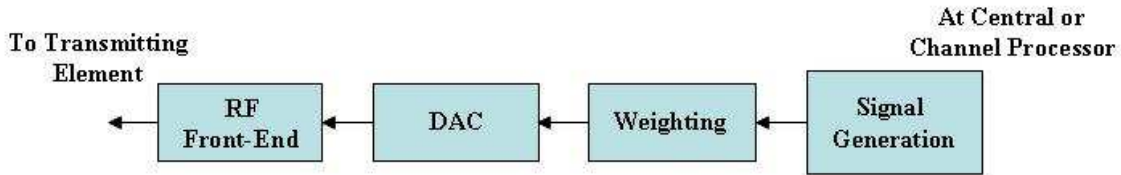


Figure 9: Key components of general DBF transmit architecture. The message signal is first generated at the far right and is processed through the functional blocks for weighting and RF up-conversion by moving left.

As in the receive case, the transmitting beamformer must implement a desired phase progression across the transmitting channels in order to properly cohere the individual signals for beamforming. Similar to a basic, general receive architecture where many designs can be implemented to receive, sample, and apply weights to the incoming signal, multiple options exist for implementing phase progressions across the transmit channels. One such option implements a single desired digital signal at a central processor and distributes it to each channel where weights are applied in parallel, as illustrated in Figure 10, below. Although this approach reduces the quantity of signal generation hardware required, it requires a large volume of data to be transferred from the central processor to the channel processors, which ties up valuable power and data bus resources.

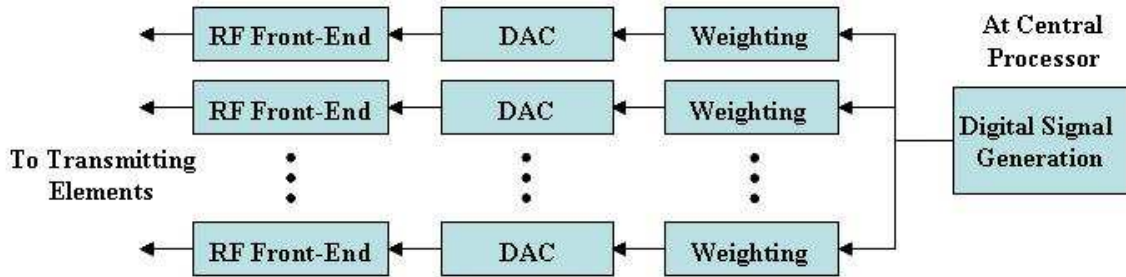


Figure 10: Architecture to implement transmit phase progressions from a single signal generator located at the central processor. Signal is then passed to channels processors which perform both the weighting and up-conversion.

Another architecture option utilizes waveform generation control signals at the channel level as seen in Figure 11. The resulting system takes advantage of current signal generation techniques, but requires the control and waveform timing to be extremely accurate. In both architectures, it is pertinent that the channel responses are taken into account during the initial signal generation. Failure to consider the different responses will result in a corrupted phase progression at the transmitting array.

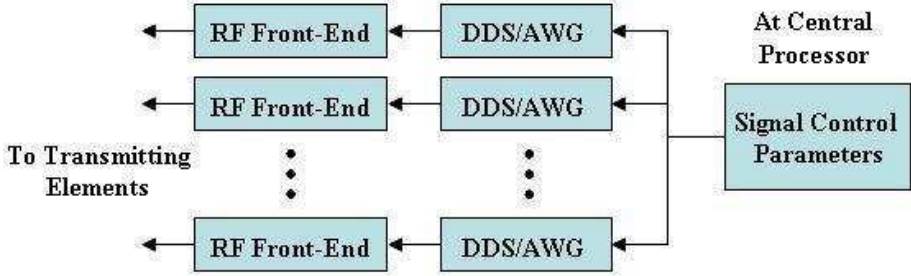


Figure 11: Architecture to implement transmit phase progressions from multiple signal generators located on each channel processor. Control and timing parameters for waveform generation are passed to the channel processor to generate the signal. Signal phasing could be performed using weights or through signal's control parameters.

The memory blocks in a transmit DBF architecture can be used to alleviate some of the strict timing constraints mentioned in the previous paragraph. By utilizing memory to hold actual digital waveforms or their specific generating parameters such as frequency, amplitude and phase, implementation of the resulting waveforms is now focused on the control timing rather than the waveforms themselves. Waveform parameters stored in memory can be transferred easily to signal generators such as Direct-Digital-Synthesis (DDS) chips and actual digital waveforms can be readily applied to an Arbitrary-Waveform-Generator (AWG). These components are key building blocks in transmit DBF systems. These possible enhancements demonstrate that using memory blocks for waveform generation may increase the control signal overhead, but decrease the transmit system's total data throughput, thus simplifying the overall design.

As has been stressed throughout this section, that accurate signal generation is a key component of a transmit DBF system. Two of the most popular techniques for signal generation leverage the abilities of DDS and AWG chips. DDS chips rely on accurate timing circuitry and phase accumulators to produce digital waveforms [23]. Common features on these chips include frequency, phase, or amplitude modulation modes which are specified by input parameters made available either at external I/O ports or within their on-chip memory components. This enables accurate, simple waveform generation, provided that all timing constraints are met. In addition to pre-programmed modes, AWG chips possess the capability to transform previously stored digital waveforms into their analog counterparts. This allows for the user to create and upload waveforms to the channel processors for signal generation. Both the DDS and AWG chips heavily rely on digital-to-analog chip (DAC) technology which is often integrated into the packaging to produce the output analog waveforms. DAC technology currently allows the creation of waveforms exceeding 1 GHz of bandwidth, providing the transmitter with a great deal of flexibility for a variety of applications.

Even though the analog front-end design of a DBF transmitter is similar to a standard RF up-conversion chain, these components often cause the most headaches in designing a transmit channel due to the difficulty of eliminating channel-to-channel inconsistencies. Calibration on receive, as mentioned in Section 3.0, has been found to be a relatively simple processes since channel response measurements are readily available. Due to the nature of transmit DBF, more effort must be placed on accurate measurements of the transmit channel performance. Since channel response of the front end is highly sensitive to frequency, systems operating in different bands may encounter this issue with varying severities. For high frequency, stand-alone applications, the up-conversion process may require multiple RF stages requiring precise coherent local oscillator (LO) generation between channels. Applications at lower RF frequencies are achievable with current DAC technology and can avoid these issues, but nonetheless, the remaining analog components must be carefully characterized to implement an accurate phase progression.

5. Processing Algorithms and Hardware

In an array, a beam can be formed by delaying and summing the signal from each element. One of the key steps in beamforming is to accurately delay the signals at each channel so that they sum in phase. In a narrowband analog array, phase shifters can be used for beamforming instead of the time delay units. The received signal in each of the channels of the array consists of the message signal modulated upon the carrier. Small arrays with moderate bandwidth are classified as "narrow band" arrays because the delay of the message signal from channel to channel is insignificant when compared to the period of the message signal, and thus, can be ignored. The beamforming problem is then reduced to the problem of removing the time delay from the carrier signal, which can be accomplished by applying the appropriate phase shift to each channel. To form a beam in large arrays with moderate to wideband instantaneous bandwidths, a time delay is required to correct for the propagation delay from the wavefront that impinges on an array at various angles to the array aperture.

5.1 Wideband Beamforming via Fractional Sampling Delay

One technique to form a wideband beam is by using fractional sampling delay filtering. After the analog signal is digitized at a sampling period T , the digital signal can be delayed exactly, if and only if the delay value is an integer multiple of T . However, the delay required to form a beam at a specified direction may be only a fraction of T . One can round the delay amount to the nearest multiple of T but in cases where the delay amount is small, rounding adds significant delay error to the total amount of delay, which causes the array pattern sidelobes to rise.

Given a discretized signal $x[n]$, if the desired time delay values D_a is a multiple of the signal sampling period T , then a delayed version of $x[n]$ can be obtained by simply shifting $x[n]$ by D samples. However, it is not immediately clear what $x[n - D]$ should be if D_a is not a multiple of T or if D_a is less than T .

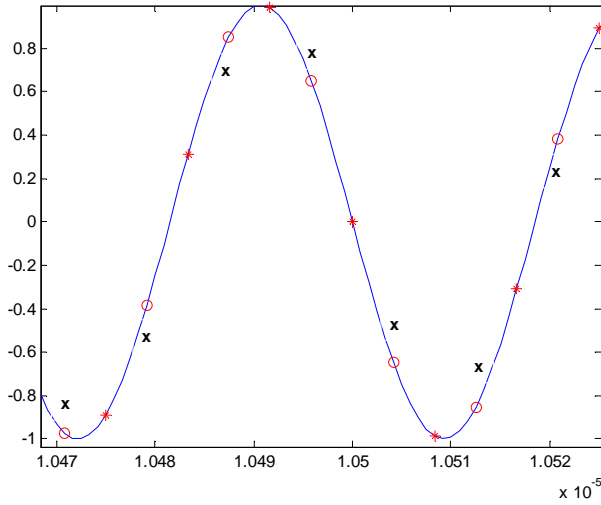


Figure 12: Time plots of a continuous signal $x(t)$ are shown in solid blue and a discretized version of $x(t)$, $x[n]$, is shown in '*' red. Two possible versions for $x[n - 0.5]$ are also shown as 'o' red and 'x' black.

For example, consider Figure 12 above, which shows time plots of a continuous signal $x(t)$, its discretized version $x[n]$ and two possible versions of $x[n - 0.5]$, where 0.5 denotes a delay amount of half of the sampling period T . At first, from looking at the discrete samples $x[n]$ alone there seems to be an infinite number of possibilities for $x[n - 0.5]$ since we don't know the values that $x[n]$ assumes between sample intervals. However if the sampling rate meets or exceeds the Nyquist requirement then there is a unique continuous curve $x(t)$ that passes through $x[n]$. This means that $x(n-D)$ is unique for any D . An obvious strategy to compute $x[n - D]$ is to first reconstruct $x(t)$ from $x[n]$ using the Nyquist theorem [24],

$$x(t) = \sum_{m=-\infty}^{\infty} x[m] p(t - mT), \quad (2)$$

where T is the sampling period and $p(t)$ is the ideal reconstruction filter, and

$$p(t) = \frac{\sin\left(\frac{\pi t}{T}\right)}{\frac{\pi t}{T}},$$

After $x(t)$ is known, $x(t - D_a)$ can be computed by using (2), which gives the following.

$$x(t - D_a) = \sum_{m=-\infty}^{\infty} x[m] p[t - mT - D_a], \quad (3)$$

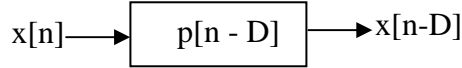
where D_a is a delay amount, in seconds. Finally, the desired delayed signal $x[n - D]$ is simply a sampled version of (3),

$$x[n - D] = \sum_{m=-\infty}^{\infty} x[m] p[n - m - D], \quad (4)$$

where $p[n - D]$ is the ideal fractional delay filter, described as

$$p[n - D] = \frac{\sin((n - D)\pi)}{(n - D)\pi}, \quad \text{for } n = -\infty, \dots, -1, 0, 1, \dots, \infty$$

Another way to express (4) is with the following:



One of the properties of the ideal infinite length fractional delay filter is that it delays the discrete signal $x[n]$ exactly DT seconds for any fractional value D , but it does not distort $x[n]$. In practice, one must truncate the ideal fractional delay filter to some finite length so that the filter can be implemented in hardware. A simple way to truncate the ideal fractional delay filter is to multiply it with a rectangular window, which is defined to have a value of 1 between over time period and zero elsewhere. Because the rectangular window has very high sidelobes, the resulting windowed delay filter will have significant amplitude ripples in the frequency response especially at the edge of the band. One way to reduce the amplitude ripples and delay error of the truncated fractional delay filter is to reduce the sidelobe levels of the window [25]. For example, using a Chebyshev window with low sidelobes in place of the rectangular window causes the amplitude ripples of the truncated delay filter to be reduced significantly.

The group delay plot of a delay filter designed to have a delay value of 0.4 over about half of the normalized Nyquist bandwidth is shown in Figure 13. The integer delay amount can be neglected since one can compensate for it by shifting samples forward or backward in time. Even with only eleven taps and working with Matlab double precision, this delay filter had a maximum delay error of only 0.0004 of the sampling period. In practice when the filter coefficients are quantized to be implemented in DSP hardware, the delay error increases moderately. For a given filter length, there is an

inverse relationship between the usable bandwidth region and the peak error of the delay filter. An effective way to reduce the peak error of the windowed delay filter is to somehow reduce the usable bandwidth region of the filter. When the usable bandwidth region is reduced, the zeros of the filter are concentrated into a smaller frequency region. Each zero corresponds to a degree of freedom and with more degrees of freedom we are able to shape the frequency responses of the filter more precisely and reduce filter errors.

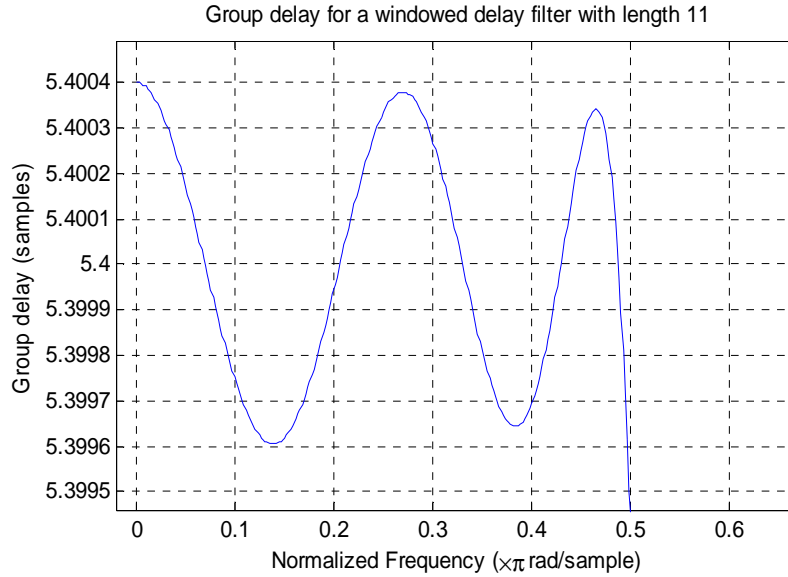


Figure 13: Group delay plot for a delay filter of length 11 that was designed to have a delay of 5.4. The usable bandwidth region for this filter is 0 to 0.5 (normalized frequency) and the peak delay error is 0.0004.

To demonstrate the fractional sampling delay with real hardware we have set up two delay experiments. The first demonstrates the case when the delay is comparable to the sampling period. The second demonstrates fractional sample delays when the delay amount is very small compared to the sampling period. The experimental setup for the first case is similar to the illustration shown in Figure 14. In this experiment we intentionally added a severe phase mismatch to the system providing a delay amount comparable to the sampling period, which can be used to correct for the phase mismatch. A phase difference of 37.28 degrees was added to the two channels by using two SMA cables of different length to connect the outputs of the power divider to the input of the ADCs. The sampling rate of the ADC is 100 MHz at 14 bits and the frequency of the input signals to the ADCs is 34 MHz. Figure 15 shows the time plot of two ADC channels. Because the two waveforms are offset by 37.28 degree, they are completely misaligned.

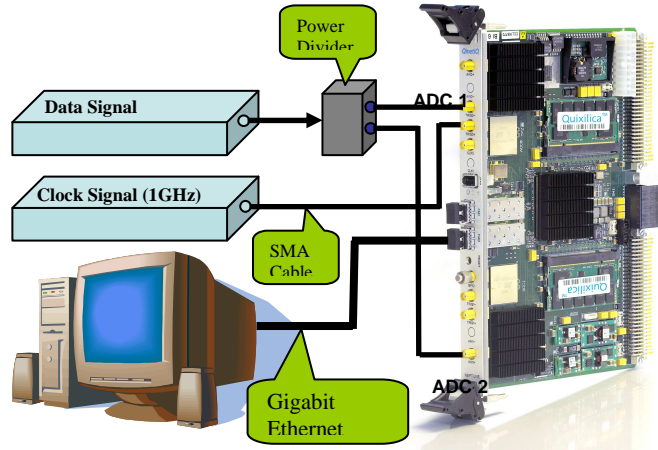


Figure 14: Hardware setup for the delay experiment. The two SMA cables that connect the outputs of the power divider to the input of the ADC have the different lengths.

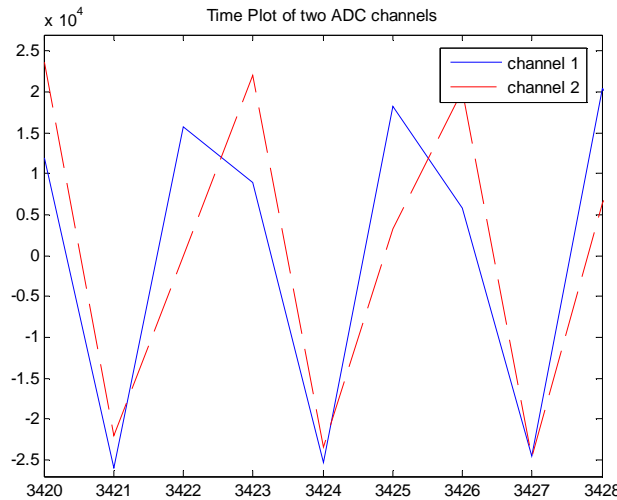


Figure 15: Time waveforms from the two ADCs, sampled synchronously at 100 MHz. The severe misalignment between the two waveforms was caused by the use of cables with different lengths that connect the outputs of the power divider to the inputs of the two ADC channels.

Using a windowed fractional delay filter, a time delay of 3.0459 ns, which is equal to 0.3045 of the sampling period, was applied to the second channel. Figure 16 shows time plots of the data before and after time delay. After implementing the time delay, channel 2, shown in dashed black, is almost identical to channel 1, shown in solid blue. Not

shown here, in the second experiment the delay amount is about 0.0679T and using digital delay filter we were able to compensate for the small mismatches between the two ADC channels.

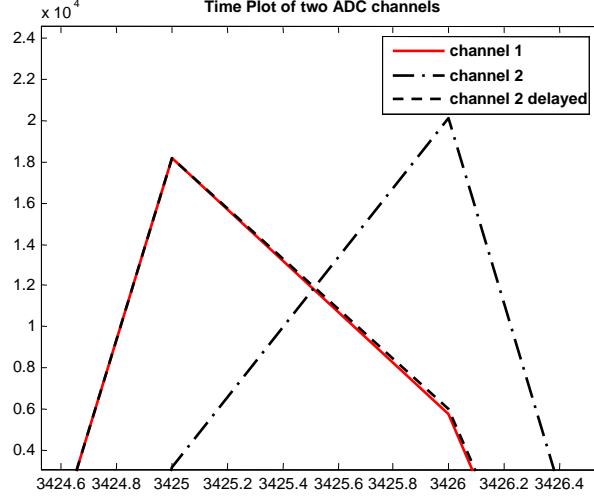


Figure 16: Time waveform of the data from channel 1, channel 2, and channel 2 after calibration (time delay). After digital delay, the time waveform of channel 2 looks almost identical to the time waveform of channel 1.

5.2 Narrowband Adaptive Beamforming

In addition to forming beams, some applications require the steering of the array pattern nulls to mitigate the affects of interference sources. There are numerous adaptive beamforming techniques in the literature that steer nulls toward interferences at the same time while keeping the beam at the desired angle. Most of these adaptive techniques use the narrow band assumption, which greatly simplifies the formulation and solving of the adaptive beamforming problem.

Under the narrow band assumption, the received signals of the array can be modeled as

$$\mathbf{x}(t) = \mathbf{A}\mathbf{s}(t) + \mathbf{n}(t), \quad (5)$$

where,

$\mathbf{A} = [\mathbf{a}(\theta_1), \mathbf{a}(\theta_2), \dots, \mathbf{a}(\theta_K)]$, and $\mathbf{a}(\theta_k)$ is the steering vector for the k^{th} source.

The received power signal for the set of weights \mathbf{w} is

$$\mathbf{w}^H R \mathbf{w}, \quad (6)$$

$$R = E[\mathbf{x}(t)\mathbf{x}^H(t)]$$

One of the earliest adaptive beamforming techniques is based on the idea that the optimum weights can be obtained by solving the following constrained equation for w

$$\text{minimize } \mathbf{w}^H R \mathbf{w} \text{ subject to } \mathbf{w}^H \mathbf{v} = \text{constant}, \quad (7)$$

where \mathbf{v} is the steering vector of the desired direction. The solution of (6) is given as

$$\mathbf{w} = \alpha R^{-1} \mathbf{v}, \quad \text{where } \alpha \text{ is a constant.} \quad (8)$$

Although the weights (8) minimize the output power (6) while pointing the beam to the direction specified by v , it has the effect of steering nulls toward interference sources. The difficulty in solving (8) gives rise to many adaptive beamforming algorithms, which address different practical issues including not having enough samples to accurately estimate R , numerical stability, and algorithm complexity.

Inverting R is a computationally intensive step and requires $O(N^3)$ operations where N is the number of adaptive channels. Other adaptive algorithms may not require the direct inversion of R but their complexity also is directly related to N . Clearly as N increases, the algorithm complexity grows exponentially. In the ideal case, one would want to use all of the channels in the array in the adaptive processing step. To reduce computational requirements in large, wideband practical arrays, many more degrees of freedom are required to suppress interferences. N is chosen to be the minimum value that enables the adaptive processor to achieve a specified performance in a given environment.

5.3 Subarraying

The classic approach to reduce the number of degrees of freedom and system cost in large arrays is subarraying. In the subarray approach, the array elements are partitioned into M groups and non-adaptive beamforming is used within each group. To reduce the number of expensive receivers in the system the non-adaptive beamforming is usually done in the analog domain. The outputs of each subarray are sampled and then sent to an adaptive processing unit for further processing. Using analog subarraying, one can

reduce the degrees of freedom and number of digital receivers of a system by a factor of N/M , where N is the total number of elements in the array and M is the number of subarrays. Subarraying is an integrated part of large practical wideband array and without subarrays the system may not be technologically or financially feasible. Although some subarraying schemes will reduce system cost and computational requirements, the subarray grouping must be carefully chosen in such a way as not to cause the quantization lobe to rise. Some proposed approaches to reduce quantization lobes include overlapped subarrays, use of subarrays of different optimally chosen sizes, and the related polyomino scheme [26].

The other major aspect of DBF affected by subarraying is the generation of multiple independent beams, which is one of the highly desired features of digital beamforming systems. In the fully adaptive process where we have access to data at every element, one can generate an arbitrary number of simultaneous beams pointing to any desired set of independent angles. In almost all of the existing subarray architectures the number of independent beams is bounded by the shape and gain of the subarray pattern. The use of Subarrays not only affects computational complexity and system cost but it also greatly influences the performance of the adaptive processor. In large, wideband arrays, the subarray architecture is tightly integrated with many other aspects of the system and digital beamforming in particular. The digital beamforming architecture tradeoffs among performance, cost, computation complexity and desired features, such as multiple beams, should not be done without taking into account the system subarray architecture.

5.4 Hardware

The feasibility and limitations of a digital beamforming system is determined by the cost, size, power consumption and processing capabilities of digital hardware. The general purpose processing unit such as an FPGA is often bulky and expensive but it is readily available, fully reconfigurable, and can be integrated into a system very quickly. Highly customized solutions, such as ASICs, are inexpensive to mass produce, they are small, and power efficient, but they require a significant initial investment of time and resources to properly design and test.

The computational resources required in a DBF system are directly related to the system bandwidth, dynamic range and algorithm complexity. Increasing the instantaneous bandwidth will increase the volume of data that must be processed. Increasing the dynamic range will require the arithmetic to have greater precision and algorithms with greater complexity to preserve the dynamic range throughout the computation process. In either case we need to increase the processing resources in order to keep the system response time unchanged. In practice, system bandwidth and dynamic range are fixed by the application so a typical way to reduce the resource requirement is by simplifying the algorithm, which unfortunately degrades system performance. One of the challenges in the field of digital beamforming is that currently desired system bandwidth and dynamic range performance exceeds the capability of present COTS hardware, given practical

limits on budget, size, and power. In these cases tradeoffs must be made between lowering system performances and using highly simplified processing algorithms in order to make the system feasible.

Key pieces of hardware in a DBF system are ADC, FPGA or ASIC, embedded processors and high speed buses to transfer data from the ADC to FPGA and then to other embedded processors. Computation tasks in a DBF system are typically assigned to either FPGA or embedded processors depending on whether or not the task is suitable for parallel computations. Tasks that are highly parallelizable such as the FFT and FIR filtering are usually done at the FPGA, which can apply these algorithms to the incoming data at a much higher rate than embedded processor. Complex serial algorithms not suitable for implementation in the FPGA architecture are assigned to fast processors.

In wideband systems, data must be sent between FPGAs, and from an FPGA to a processor. Ideally, we would integrate the ADC, FPGA and processors into one board and transfer massive amount of data among these components using one of the many standard interfaces. However, in practice we need to send data in one FPGA to a different FPGA or to a processor that resides on a different board at a significant distance away. In this case, a high speed bus that is able to carry data over a significant distance is required. Implementing this complex bus adds computation complexity and cost to the system since the sending and receiving protocols need to be installed in both the sending and the receiving boards.

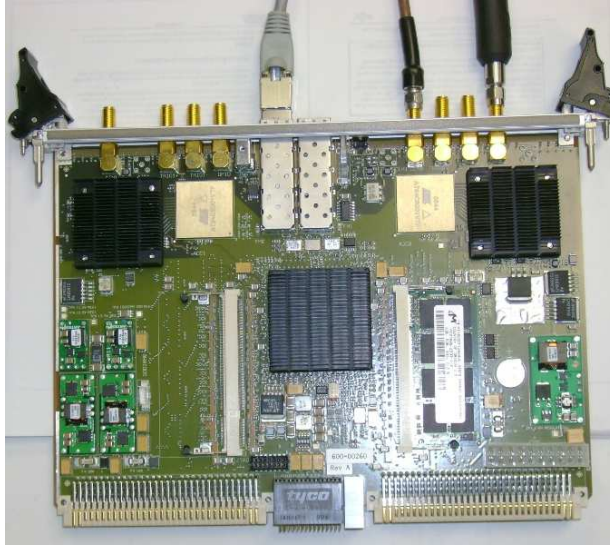


Figure 17: Neptune 2 VSX board from Quixilica with dual 2.2 GSPS ADCs and a Xilinx Virtex II Pro FPGA.

Currently, the highest speed commercial ADC is made by National Semiconductor that can sample up to 3 GSPS at 8 bits and consumes 1.8 watts. The latest FPGA from Xilinx is the Virtex 5. It has twenty four 3.2 Gbps Rocket transceivers for high speed serial communication and a processing capability of 352 GMACS. Figure 17 shows a somewhat obsolete board with high speed ADCs and fairly large FPGA which we have used at AFRL/SNHA for various experiments. Although this board does not have an integrated processor, to apply complex algorithms to the incoming data they must be streamed to a separate processor module via gigabit Ethernet module. The bandwidth limitation in this case is the gigabit Ethernet bus which has a bandwidth of about 90 Mbytes per second.

6. Future Trends

Future trends in DBF that are likely to be realized over the next few years include advances in modularity, multi-functionality, nonlinear digital filtering, receiver-on-a-chip (ROC) technology, wideband nulling, localized signal generation, and use of orthogonal waveforms. These are possible due to the ever advancing state of the art in digital signal processing hardware. Other, longer-term future trends may include the use of switch fabrics as a foundation for adaptive channel hardware that changes configuration in order to cope with changes in mission key performance parameters. Such new hardware may find use in conformal apertures that adhere to nearly every inch of the leading edges and undersides of an aircraft, and be used to adapt the array aperture shape, location, or orientation, in order to optimize array performance or make up for failed portions of the aperture.

6.1 Modularity

Component cost is a key driver in commercial electronics, and it is always an issue in phased array antennas, where RF electronics are notoriously expensive and economy of scale has never yet been achieved, at least not to the degree seen in the automobile industry. However, as DBF technology matures, attention is also being turned to building digital array channel hardware in repeatable blocks that can be concatenated together to form arrays of varying sizes. Scalability of an array architecture is often the intended result of modularity, but with it may come a certain amount of component cost savings.

Our team worked with Applied Radar, Inc., over a four year period to develop a prototype 32-channel, X-band, DBF receive array using COTS components [19, 27]. While cost savings was not a main goal of this project, modularity was, and with it came re-use of components which reduces cost. This hardware contained 2" x 2" x 1" tall custom receiver and transmitter modules, which plugged directly into a custom array processor backplane. The processor backplane facilitated calibration of the array and performed digital beamforming on both transmit and receive. These "plug and play array" modules contained two miniature circuit boards, constituting the Analog Front-End and the Digital Back-End, respectively. As mission needs change, theoretically, one

could swap out the X-band Analog Front-End for one designed at a different center frequency and still utilize the same Digital Back-End, provided the instantaneous bandwidth and the intermediate frequency output from the Analog Front-End was constant. This approach was intended to reduce costs if we chose to demonstrate DBF at a variety of microwave frequencies.

This experimental prototype demonstrated some elementary forms of modularity, but greater degrees of hardware re-use and array scalability will likely be realized as more and more low-cost processor components are pushed into the array aperture. As processor and memory costs drop, less of a premium will be placed on the digital array channel electronics, enabling the channel hardware to be over-designed. This will enable built-in flexibility which will lead to a more generalized channel hardware design, or family of designs, that can be adapted to a variety of mission requirements. This in turn may lead to the use of a common hardware channel module that can be programmed to handle a variety of applications.

6.2 Multi-functionality

A modular common hardware channel also will enable multi-functionality, in which a digital array may be designed to serve more than one mission, sometimes simultaneously. Most aircraft must carry several antennas, and it is common to seek more functionality using fewer antennas. In military aircraft, it is useful to consider an array that could perform both MTI and SAR radar functions. This, however, requires digital array hardware that can be narrowband with high resolution for MTI, but also be wideband with less resolution for SAR. This requires the Analog Front-End electronic circuits to be reconfigurable in order to cope with competing key performance parameters. Again, if low cost processor components are used in the digital array channel, hardware will be at less of a premium and intentional over-designing will result in flexibility and programmability. However, if an array must produce multiple simultaneous beams at different frequencies, or operate in a full duplex communications mode, a greater challenge exists in reducing high levels of interference between the transmit and receive channels, and preventing frequencies that are harmonically related from coupling into the channels from the array apertures. To achieve reasonably good performance, very low loss, high isolation Analog Front-Ends must be designed, coupled with high roll-off bandpass digital filters, and potentially other forms of diversity like orthogonal waveforms.

6.3 Nonlinear Digital Filters

Currently available analog electronics, such as low noise amplifiers and analog filters, and most A/Ds, suffer from inter-modulation products and spurious signals that degrade performance. Recent work in nonlinear digital filters is gaining back some of this lost performance. First, the designer must interrogate the digital array channel hardware with a large set of two and three tone sinusoidal signals spanning the pass band of the

component and measure the resulting spectrum of inter-modulation products. Based on this result, a nonlinear filter is designed that counteracts the nonlinear behavior of the component which was revealed from the measured data set. When the nonlinear digital filter is inserted into the channel hardware path, spur-free dynamic range is increased, and in the case of A/Ds, the effective number of bits is increased, often approaching the actual number of bits in the A/D converter. All of this is done just once per channel, during the initial calibration of the digital array and equalization of its channels, when the array is first built. A dedicated built-in test capability and a dedicated processor would be required to realize dynamic nonlinear filter implementation on the fly, but it is not clear that it would be warranted unless the channel hardware was exposed to great swings in temperature such as on a spacecraft.

6.4 Receiver On a Chip (ROC)

The advent of receiver on a chip (ROC) technology offers great promise for miniaturizing digital channel hardware and pushing digital arrays to higher GHz frequencies. Mixed signal integrated circuit technology, which combines analog and digital circuits on a single chip, is key to the rapid progress in this area. Several companies are engaged in this work and one in-house team in AFRL/SND is developing ROC technology [28]. The designs are generally less complicated than the Digital Tx/Rx Module shown in Figure 3, but the designs realized to date are amazing in their functionality and small size. This technology is an enabler for low cost digital arrays, and may very well be the key to proliferating DBF across many military applications and into the commercial sector.

6.5 Wideband Beamforming and Nulling

Wideband null forming, or nulling, poses a challenge to the very foundation of adaptive beam-forming and direction finding algorithms. Most algorithms were developed based on a narrow band assumption pertaining to the statistics of the array environment [21]. This assumption does not hold when array instantaneous bandwidths go into the hundreds of MHz, and ultimately, the algorithms still produce weights, but the results are often less accurate than desired, if not invalid. One approach to counteract this problem is digital sub-banding, which uses polyphase filters, such as quadrature mirror filters, to split the instantaneous bandwidth into many contiguous narrow sub-bands. Each sub-band is then processed using the traditional algorithms, and the resulting beams and/or nulls can be reassembled, if desired, using polyphase filters.

If the beamforming is deterministic, an alternative method for wideband beamforming is to implement digital time delays using fractional sample delay filters for fine resolution down to fractions of a wavelength, and use shift registers and other approaches for coarse resolution delays of more than one clock pulse. This approach is not effective for adaptively generated beams or nulls because the computed weights are derived from narrowband algorithms.

6.6 Localized Signal Generation

In digital arrays that require mixers and local oscillator signals, a great penalty is incurred from the additional size and weight of microwave transmission lines at each channel. Ideally, it would be better to generate the LO signal right at the channel and merely route bias voltages and digital command words that control the LO generation. The Digital Tx/Rx Module shown in Figure 3, provides the hardware capability to support local signal generation of both the message carrying signal and all LO signals needed in the Analog Front-End for up-conversion to the final transmit waveform. The LOs are not depicted in Figure 3, but they pass from the DDS WFG to the Analog Front-End Module, and are used in both the Tx and Rx sides of the Analog Front-End Module.

The key challenge in localized signal generation is developing and maintaining phase lock on all LOs across the array when there is apparently no feedback mechanism available for phase locking to a single master oscillator. One way to test the waveforms is to couple a small fraction of the signal power into the receive channel but this could only be done in cases where full duplex operation is not required. Else, one could provide an auxiliary receiver, which drives up the cost of the channel hardware. The goal is to synchronize the formation of the waveforms across the array using the Tx Sync Pulse at each channel. The distribution of synchronizing pulses must account for path length through the processor chain and make corrections for errors at each channel. In our plug and play array channel modules, Applied Radar included clock skewing integrated circuits commonly used in digital sampling oscilloscopes to provide coarse time delay adjustment to within one clock pulse [27]. Additional time delay resolution can be achieved by imparting fractional sample delays in the beamforming weights or in the channel calibration weights, to counteract errors in sync pulse distribution.

6.7 Orthogonal Waveforms

An orthogonal waveform is typically a digital signal that is part of a set of related digital signals which are constructed according to a design rule that makes them mutually orthogonal in energy over a period of time. Orthogonal waveforms are used in modern communications systems like code-division multiple access (CDMA) cell phones, because they offer added diversity, enabling multiple users to be in the same cell on the same frequency at the same time. In the Digital Tx/Rx Module depicted in Figure 3, the DDS WFG and the Digital Receiver provide the hardware capability to support orthogonal waveforms. While not explicitly shown in the figure, a matched filter can be implemented in the Digital Receiver to sort out multiple orthogonal waveforms. Sorted orthogonal waveforms are then passed to the Receive Waveform Memory, where they wait to be sent through the Channel Processor to the DBF Processor for beamforming. At the DBF Processor, beamforming may be done separately on each orthogonal waveform, resulting in separate beams which may point in the same direction or in different directions.

While greatly used in digital communications systems, orthogonal waveforms have not been in the main stream of radar system design. Much research is being conducted in orthogonal waveforms for use in a variety of applications [29, 30]. One potential benefit may lie in simultaneously transmitting two or more radar pulse sequences at the same frequency, but at different pulse repetition frequencies and embedded in orthogonal waveforms. The beamforming and radar processing would need to handle the orthogonal waveforms, but a single beam could be used to resolve range ambiguities in a shorter time. Orthogonal waveforms may also be used if an array could support multi-functionality, enabling the MTI and SAR functions to occur simultaneously.

7. Conclusion

Our intent for this paper was to provide an update on the current state of the art of digital beamforming technology. We began with a generalized digital array architecture that emphasized the use of distributed processing to reduce the overall data volume and the associated processing load. In describing the roles of the functional blocks and data parameters used in this architecture, we also described some of the main issues of digital array operation, including signal generation, beamforming and calibration. We then showed variations of the key elements of digital array architectures, including the receive channel hardware, the transmit channel hardware, and the processor hardware. For each of these elements, we described the various hardware components which currently form the building blocks of digital array architectures. We delved into various implementation techniques and illustrated the major design trade issues that one must consider in order to maximize performance while minimizing cost and SWaP.

As it stands today, digital beamforming is now a rapidly emerging technology that can be used in specific kinds of real-world applications. Namely, DBF can be used in systems requiring narrow to moderate bandwidths up to few hundred MHz, at frequencies up to X-band, in arrays up to a few hundred elements. At X-band and higher, the digital array channel hardware is not yet miniature enough fit behind a single element, so some form of sub-banding is required. For bandwidths wider than a few hundred MHz, processing load and component cost will likely be the limiting factors. For arrays larger than a few hundred elements the same will be true. Specific cases exist where DBF is absolutely a viable design option and should be considered over conventional analog beamforming. For example, in an airborne UHF array where SWaP is very important, a DBF system employing direct sampling may be used. Such an array will provide considerable savings in weight due to the elimination of the large UHF feed network and cables common in analog phased arrays at this frequency.

In the future, array design engineers should expect to see a wider range of lower cost COTS components, with highly integrated functionality, including receivers on a chip, at frequencies well beyond X-band. Nonlinear filtering will likely be incorporated directly into ADCs and ROCs. Processor and memory chips are expected to continue to improve, and the conversion between analog and digital domains will be achievable at lower cost

and for wider instantaneous bandwidths. As this happens, one would imagine that the cost of digital arrays may drop to levels significantly less than that of conventional phased array antennas. The array designer can then expect to enjoy significantly more degrees of freedom and significantly higher control precision, and have greater number of design options at one's disposal as component cost is reduced. Digital arrays will likely incorporate many of the future capabilities cited in section 6, of this paper, making digital array antennas extraordinarily useful over a wide range of applications. The use of digital arrays and digital beamforming, will likely see widespread use the military, commercial, and scientific sectors.

8. References

- [1] Barton, P., "Digital Beamforming for Radar", *Proceedings of the IEEE*, vol. 127, Pt-F 4, Aug, 1980.
- [2] Steyskal, H., Rose, J. P., "Digital Beamforming for Radar Systems", *Microwave Journal*, vol. 32, pp. 121-136, Jan, 1989.
- [3] Steyskal, H., "Digital Beamforming", *European Microwave Conference*, pp. 49-57, Oct, 1988.
- [4] Applebaum, S.P., "Adaptive Arrays", *IEEE Transactions on Antennas and Propagation*, vol. 24, pp. 585-598, Sept, 1976.
- [5] Widrow, B., *et al*, "Adaptive Antenna Systems" *Proceedings of the IEEE*, vol. 55, pp. 2143-2159, Dec, 1967.
- [6] Steyskal, H, "Digital Beamforming at Rome Laboratory", *Microwave Journal*, vol. 39, No. 2, 1 Feb, 1996.
- [7] Herd, J., "Experimental Results from a Self-Calibrating Digital Beamforming Array", *IEEE AP Society International Symposium*, Dallas, TX, 7-11 May, 1990.
- [8] Herd, J.S., "Array Element Pattern Correction in a Digitally Beamforming Array: An Experiment Study", *URSI National Radio Science Meeting*, Canada, 1985.
- [9] Mailloux, R.J., "Array Failure Correction with a Digitally Beamformed Array", *IEEE Transactions on Antennas and Propagation*, vol. 44, pp. 1543-1550, Dec, 1996.
- [10] Pettersson, L., *et al*, "An Experimental S-Band Digital Beamforming Antenna", *IEEE International Symposium on Phased Array Systems and Technology*, Boston, MA, 15-18 October, 1996.

- [11] Miyauchi, M., “Development of DBF Radars”, *IEEE International Symposium on Phased Array Systems and Technology*, Boston, MA, 15-18 October, 1996.
- [12] Garrod, A., “Digital Modules for Phased Array Radar”, *IEEE International Symposium on Phased Array Systems and Technology*, Boston, MA, 15-18 October, 1996.
- [13] Walden, R.H., “Analog-to-Digital Converter Survey and Analysis”, *IEEE Journal on Selected Areas in Communications*, vol. 17, April, 1999.
- [14] Bucci, O.M., et al, “Intersection Approach to Array Pattern Synthesis”, *IEE Proceedings-Pt. H*, vol. 137, pp. 349-357, Dec, 1990.
- [15] Curtis, D., et al, “Conformal Array Control Using Digital Beamforming”, *Antenna Application Symposium*, Monticello, IL, Oct 2001.
- [16] Couch, Leon W., “Digital and Analog Communication Systems”, Prentice Hall, Upper Saddle River, NJ, 2001.
- [17] Rabiner, L., and Gold, B., “Theory and Application of Digital Signal Processing”, Prentice Hall, Inc., Englewood Cliffs, NJ 1975.
- [18] Oppenheim, A., Schafer, R., and Buck, J., “Discrete-Time Signal Processing”, Prentice Hall, Inc., Upper Saddle River, NJ, 1999.
- [19] Spendley, *et al*, “Initial Demonstration of an X-Band Digital Beamforming (DBF) Receive Array”, *2006 IEEE Aerospace Conference*, Big Sky, MT, March 4-11, 2006.
- [20] Malliou, Robert J., “Phased Array Antenna Handbook”, Artech House Inc, Norwood, MA, 1994.
- [21] Van Trees, Harry L., “Optimum Array Processing”, John Wiley & Sons, Inc., New York, 2002.
- [22] Gershman, A. B., “Robust Adaptive Beamforming: An Overview of Recent Trends and Advances in the Field”, *International Conference on Antenna Theory and Techniques*, 9-12 September 2003, Sevastopol, Ukraine.
- [23] “A Technical Tutorial on Digital Signal Synthesis”, An Analog Devices Tutorial, Analog Devices, Inc., 1999. www.analog.com
- [24] T. I. Laakso, V. Valimaki, M. Karjalainen, and U. K. Laine, “Splitting the Unit Delay”, *IEEE Signal Processing Magazine*, Vol. 13, Issue 1, pp. 30-60, Jan. 1996.

- [25] T. I. Laakso, T. Saramaki, and G. D. Cain. “Asymmetric Dolph-Chebyshev and Transitional Windows for Fractional Delay FIR Filter Design”, *Midwest Symposium on Circuits and Systems*, Rio de Janeiro, Brazil, 13 August, 1995.
- [26] Mailloux, R.J., Santarelli, S.G., Roberts, T.M., “Polyomino Shaped Subarrays for Limited Field of View and Time Delay Control of Planar Arrays”, *Antenna Application Symposium*, Monticello, IL, 21 Sept 2005.
- [27] Curtis, D., *et al*, “32-Channel X-Band Digital Beamforming Plug-and-Play Receive Array”, *IEEE International Symposium on Phased Array Systems and Technology*, Boston, MA, 14-17 Oct, 2003.
- [28] Quach, T., Wyatt, P., X-Band Receiver Front-End Components in Silicon Technology”, *GOMACTech Conference*, Lake Buena Vista, FL, 19-22 March 2007.
- [29] Robey, F., *et al*, “MIMO Radar Theory and Experimental Results”, *37th Asilomar Conference on Signals, Systems, and Computers*, Pacific Grove, CA, 7-10 Nov, 2004.
- [30] Donnet, B., Longstaff, I. “MIMO Radar, Techniques and Opportunities”, *Proceedings of the 3rd European Radar Conference*, September 2006, Manchester, UK.

Flex Based L-Band Phased Array Antenna Demonstration

Peter Buxa, Thomas Dalrymple, Christopher Lesniak, Robert Neidhard

Air Force Research Laboratory

2241 Avionics Circle, Bldg 620

Wright Patterson AFB, Ohio 45433

Abstract: An L-Band phased array tile using “RF on Flex” technology to minimize array mass and cost has been fabricated and tested. The demonstration tile incorporates many novel technologies, including highly integrated T/R MMICs, low cost plastic packaging, light-weight flex board materials, and aluminum honeycomb support structures. Array tile control is achieved through a low cost commercial Field Programmable Gate Array (FPGA) controller and a Windows graphical user interface (GUI). The tile architecture and technologies demonstrate the potential for an array mass of $< 6 \text{ Kg/m}^2$ and cost less than \$100K / m^2 . Several of these techniques have been transitioned to a new program focused on building a large number of tiles to demonstrate the low cost, highly manufacturable nature of this approach.

1. Introduction

Phased arrays are in great demand for many systems and are actual enablers for several future operational concepts. Even though significant cost reduction has been achieved, many applications still require further major cost reductions. Development of affordable phased array sub-array building blocks (tiles) and low cost modules and components is the specific challenge to be addressed. A more focused problem is having the technical awareness and understanding of industry’s state of the art multi-layer board, module, and component fabrication capabilities that can be used to guide the correct development path for affordable tiles/sub-arrays. This paper details the AFRL/SN in-house proof of concept demonstration of an L-Band receive only array tile.

The purpose of this effort was to demonstrate a low cost, light weight ($<6\text{kg/m}^2$) electronically scanned phased array antenna tile capitalizing on technology developed through various Air Force Research Laboratory (AFRL) contracted efforts. The array tile is based on the laminate panel architecture, sometimes referred to as “RF on Flex.” The RF routing and DC bias and control lines are all routed in a flexible printed circuit containing only 3 metal layers. The highly integrated Monolithic Microwave Integrated Circuits (MMICs) contain a Power Amplifier (PA), Low Noise Amplifier (LNA), phase shifters, attenuators, and a Transmit/Receive (T/R) switch. Each MMIC was packaged in a Quad

Flat No lead (QFN) plastic package that also included a matching circuit. Control of the array tile was accomplished using an off tile Field Programmable Gate Array (FPGA), avoiding the high cost proprietary Application-Specific Integrated Circuits (ASICs) typically seen on phased arrays. Using an FPGA allows flexibility in the field for changing missions and also can support open control architectures that can further drive down costs. This array tile was controlled with a graphical user interface set up to run in Microsoft Windows. The tile was calibrated and phase settings were calculated using a MATLAB script and the tile was scanned by adjusting the phase and attenuation settings in the FPGA control program.

2. Antenna Tile Design

This effort leveraged deliverables and knowledge gained from several contracted efforts. At the heart of the antenna array tile is a custom 5W L-Band T/R MMIC designed for AFRL by REMEC Defense & Space. The highly integrated T/R MMIC contains a PA, a 21 dB LNA, a 5 bit attenuator, and a 6 bit phase shifter. Designed into a 0.15 micron gate length power pHEMT process, the chip area is less than 15 sq. mm (Figure 1)¹⁻².

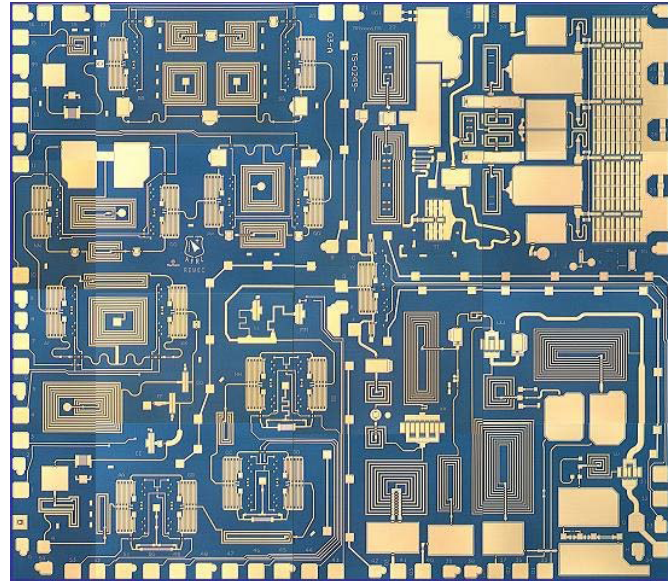


Figure 1. L-Band T/R MMIC

In addition, significant cost and mass reduction was achieved by using low cost, light weight plastic packaging (Figure 2) as an alternative to traditional ceramic packaging². Replacing the multilayer ceramic package with a Micro Lead Frame (MLF) style package is not entirely straightforward and forces a trade between module package and flex board complexity. The ceramic multi-chip module that was replaced contained matching

circuitry, passive components, a T/R switch MMIC, and antenna matching circuitry. By transitioning to a single or dual chip MLF package, these components are separately packaged and mounted directly to the flex board which increases board complexity and possibly necessitates additional dielectric flex layers. This could adversely impact overall array tile cost and mass.

Tyco Electronics' MLF packaging technology utilizes multiple protective layers to keep moisture and contaminants from the chip(s) surface. This approach leads to very good reliability and moisture resistance, even without traditional hermeticity³. For this demonstration, a package was designed to include two chips (Figure 3): the T/R chip and a circuit matching chip. In addition, part of the lead frame was designed to serve as a passive component.



Figure 2. Plastic Micro Lead Frame Module

By combining two die into one package, complexity at the flex level was reduced while still maintaining a very small T/R module package weighing 0.17 grams. Figure 3 shows the MLF module with the over-mold material removed, exposing the die and the lead frame structure.

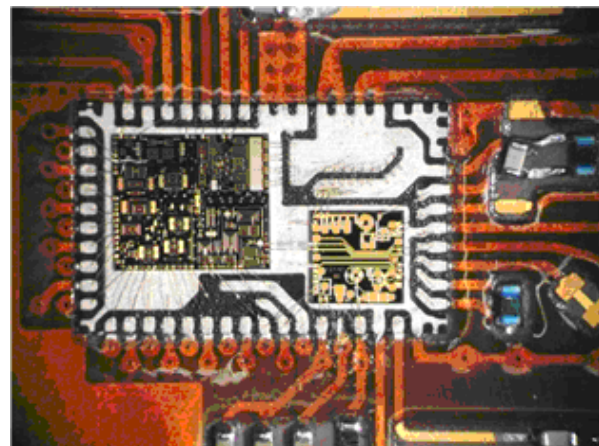


Figure 3. Top View of MLF T/R Module

To reduce project complexity and risk, the antenna tile was designed as receive only. However, the plastic packaged MMICs did have the full T/R functionality and a flex board design could be designed for full capability for future efforts.

The “RF on Flex” tile consisted of three metal layers separated by two layers of polyimide dielectric (Figures 4 and 5). The total flex board thickness is only 13 mils. Current board vendors often struggle to reliably fabricate large multi-layer boards with many layers and large numbers of blind and hidden vias. By reducing the number of flex layers required, the flex board mass and cost is significantly reduced as well as improving yield. Another area of concern for circuit board manufacturers is the large number of plated through vias. The board design contained over 30,000 vias. Many of these vias served as “ground fence” connections to shield RF transmission lines within the board.

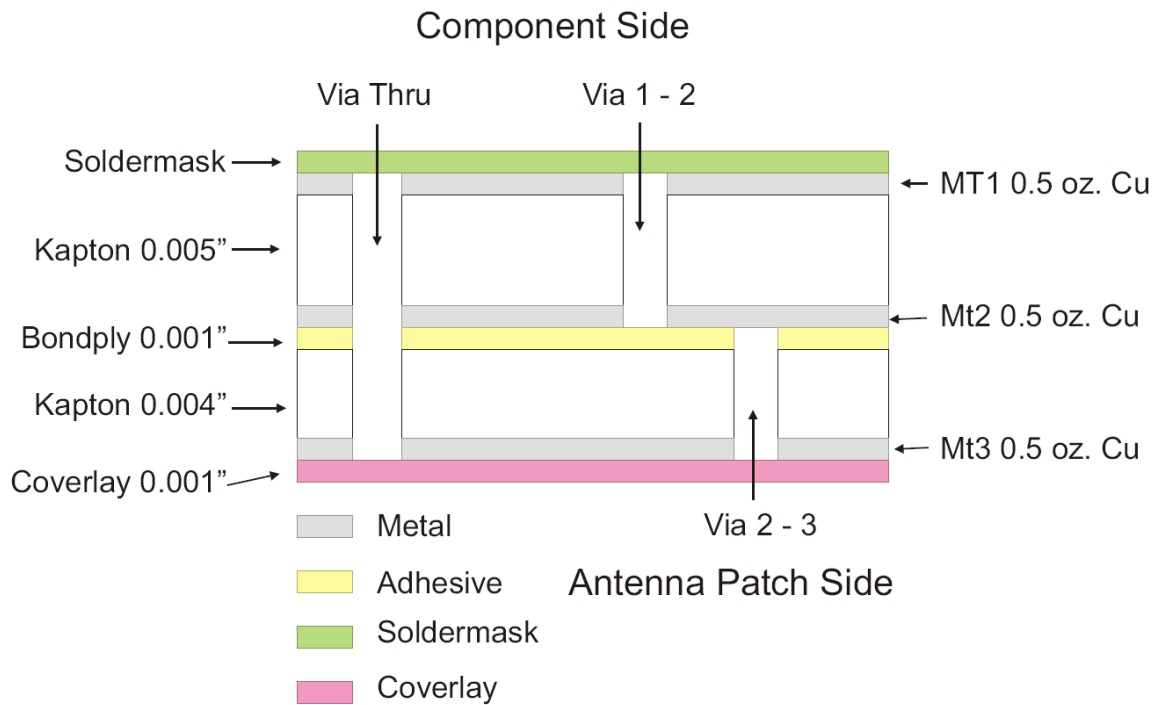


Figure 4. Multi-Layer Flex Board Cross Section

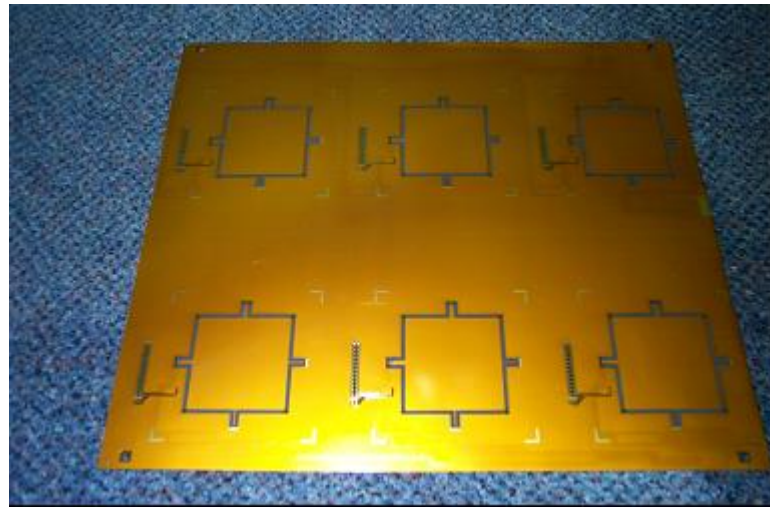


Figure 5. Multi-Layer Flex Board

The 13" x 15" multi-layer flex tile contains all RF, DC, and control interconnects in a stripline configuration and was fabricated using industry standard infrastructure and processes. Using current commercial circuit board materials, manufacturing infrastructure, and processes to fabricate the array tiles is a key feature of our architecture and approach to reducing array cost.

The antenna elements are a stacked patch design with the driver patch integrated into the flex. The parasitic patch is positioned above the driver patch and separated by a 15.7 mm foam spacer. To provide additional bandwidth capability, a 110 mil deep air dielectric cavity sits below the driver patch on the back side of the flex as depicted in Figure 6. The element design is such that it meets performance goals while being highly manufacturable. It also minimizes weight and cost and can be assembled using standard pick and place technology. Each array tile has six 58.6 mm x 58.6 mm driver elements.

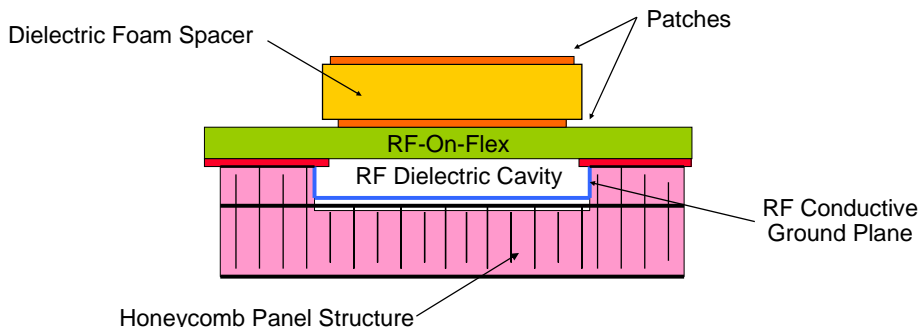


Figure 6. Radiating Element Cross Section

The assembled flex board is attached to an aluminum honeycomb structure which provides planarity, environmental protection for the modules and passive components, and a path for thermal management. The honeycomb core may have either aluminum face sheets (as demonstrated in this effort) or if required, carbon composite face sheets for added lateral heat spreading capability. A thermally conductive adhesive is used to bond the honeycomb to the flex surface. Figure 7 shows the aluminum honeycomb with carbon composite face sheets. It should be noted that the wells are cut to accommodate the features of the modules and passives which are mounted to the flex.

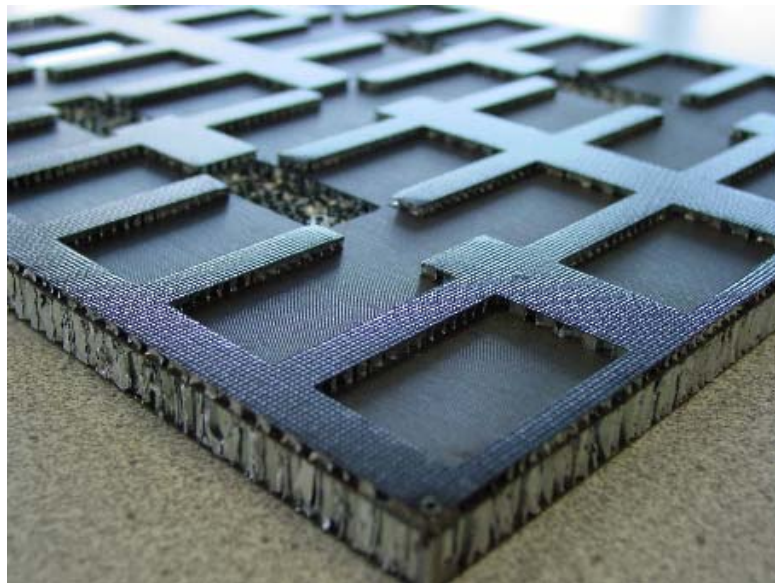


Figure 7. Honeycomb Support Structure

The entire tile assembly was assembled at AFRL using industry standard techniques. The process flow included surface mount attachment of the T/R modules and various passives, screen printed adhesive to attach the foam antenna patches, and dispensed adhesive to attach the honeycomb stiffener/heat spreader. All of these processes could easily be transferred to a large scale manufacturing facility, thereby enabling low cost manufacturing of similar tiles for a variety of Active Electronically Scanned Array (AESAs) applications in the future. Figure 8 shows the panel cross section with the flex layer highlighted in yellow. The red arrows show the thermal paths through the honeycomb face-sheet and through the flex. Figure 9 shows the fully assembled antenna tile.

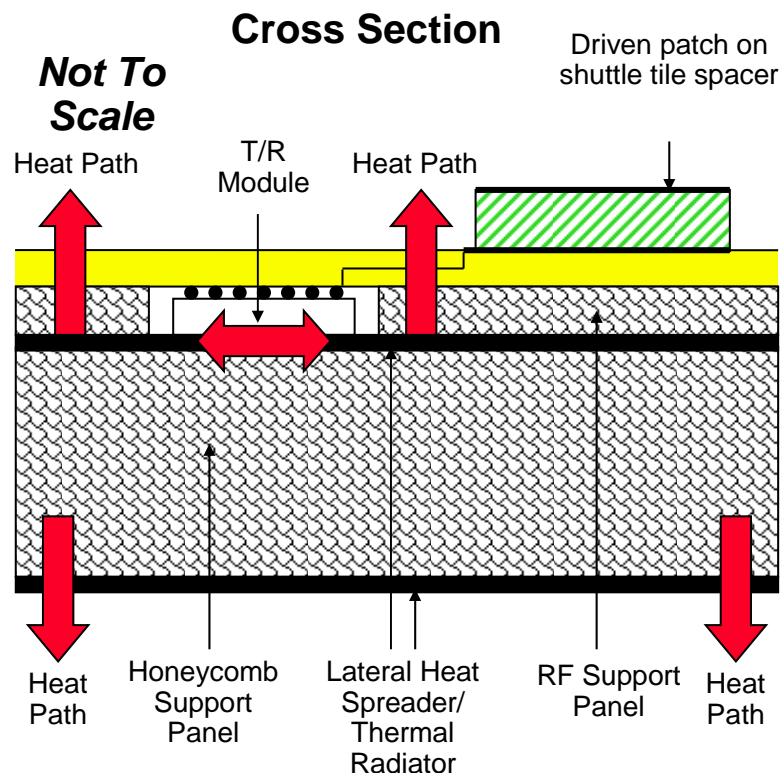


Figure 8. Flexible Tile Cross Section

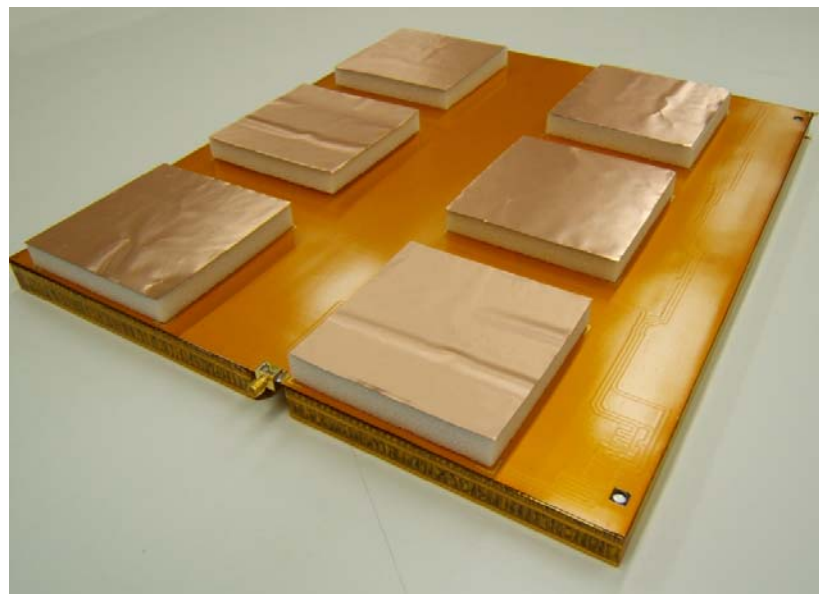


Figure 9. Fully Assembled Antenna Tile

3. Panel Control Architecture

The tile control architecture for the L-Band phased array tile consists of an FPGA controller, FPGA-to-T/R module interface board, and a Windows-based graphical user interface. These components enabled AFRL engineers to easily verify and test operation of the L-Band tile through a straightforward method of control.

Using FPGAs for T/R module control is a novel idea. Currently, T/R modules designed by RF manufacturers need a custom companion ASIC controller to control the power amplifier, T/R switch, phase, and attenuator functions. Designing custom ASICs is costly in terms of design, fabrication, integration and tile real estate. In addition, these controllers are only designed to address specific T/R modules. If the T/R module design is changed or a different manufacturer is used, a specific custom ASIC controller design has little chance of reuse. For this reason, there is a great need for modularity. FPGAs have revolutionized the digital industry in terms of their reprogrammability and short development cycles.

By using an FPGA for T/R module control, the tile designer is not limited by the specific T/R module they can control, and standard interfaces can be developed to address many types of T/R modules. Also, FPGAs have a large number of programmable I/O, which is essential for addressing phased-arrays with a significant number of elements. Consequently, one FPGA could potentially replace many custom ASIC controllers.

For this effort, one Xilinx Virtex II FPGA was programmed to address the phase, attenuation, and PA/LNA bits for the six REMEC L-Band T/R Modules on the tile. This required a total of 72 control line outputs to be allocated from available FPGA I/O. In addition, a Windows-based user interface was designed to send control commands to the FPGA board through a PC or laptop serial port. A picture of the user interface is shown in Figure 10. The user interface enables the control of each module individually or many simultaneously. In order for the FPGA to properly address the T/R Modules, an interface board was designed to convert positive voltage control (0V to 3.3V) to negative voltage control (-5V to 0V) required by the T/R Modules. The interface board mates directly to the FPGA board which connects to the L-Band tile T/R modules via 0.100" vertical headers.

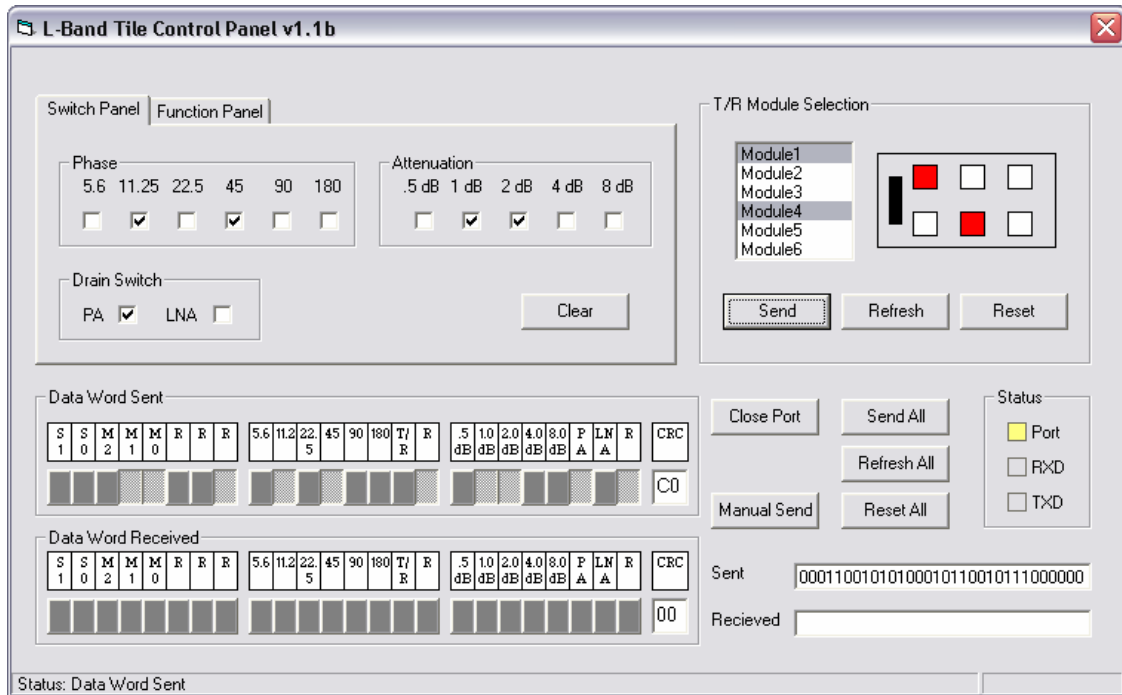


Figure 10. L-Band Tile Control User Interface

4. Antenna Tile Testing

Following assembly and debugging, it was discovered that three of the T/R modules could operate with full control. The three remaining T/R modules were found to operate erratically, which was due to opens at the solder connections. This was caused by insufficient solder paste deposits during assembly.

The three functional elements were tested in the Sensors Directorate Radio Frequency Countermeasures Test Facility as shown in Figure 11. The testing procedure included measurement of phase and gain at each element. This information was used to calculate the phase and attenuation bits that calibrated the antenna for bore sight and scanned operation. Figures 12 and 13 depict the performance of the array through vertical scanned beams and sum and difference patterns. The array performed well and closely matched the predicted performance. The measured 10dB bandwidth is 160MHz.

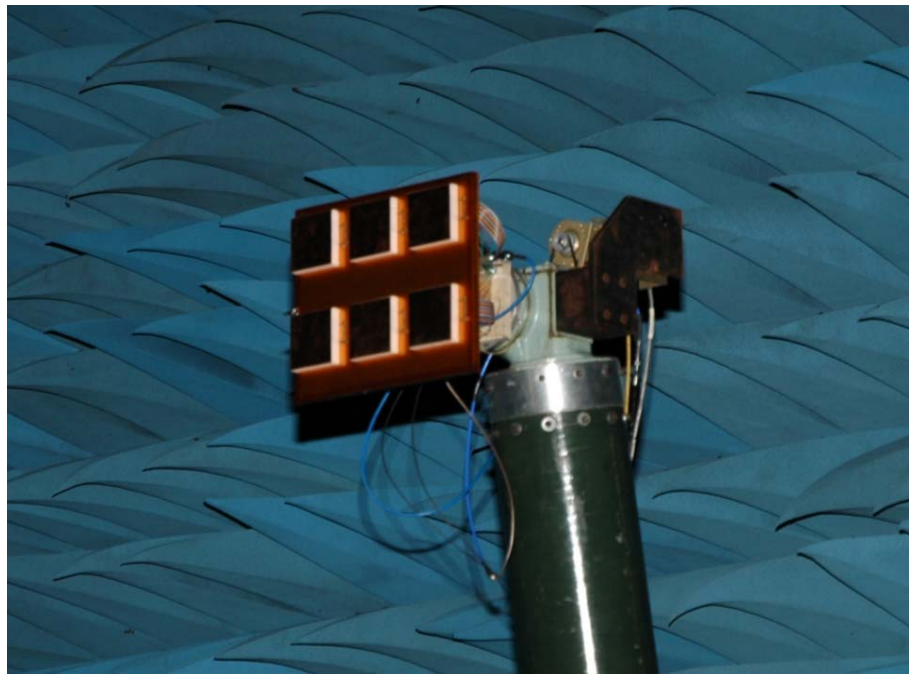


Figure 11. Antenna Tile Mounted in Test Chamber

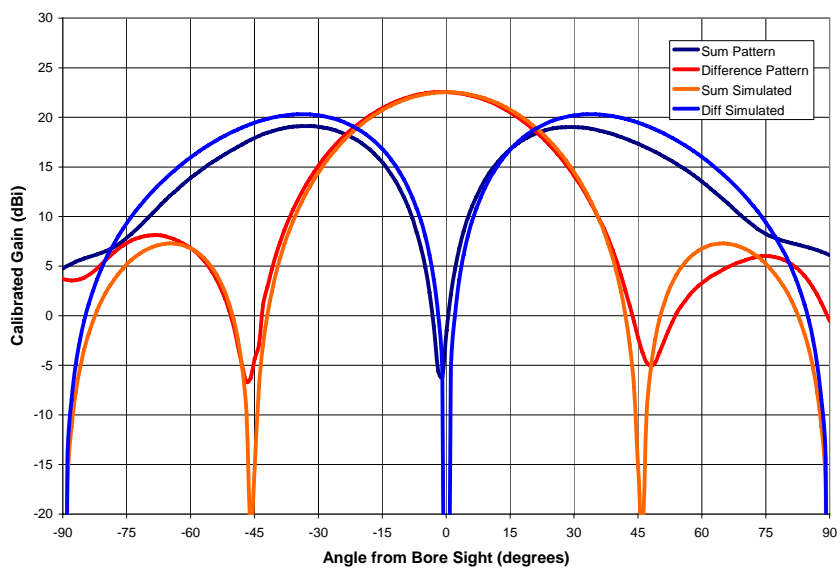


Figure 12. Vertically Scanned Sum & Difference Antenna Patterns

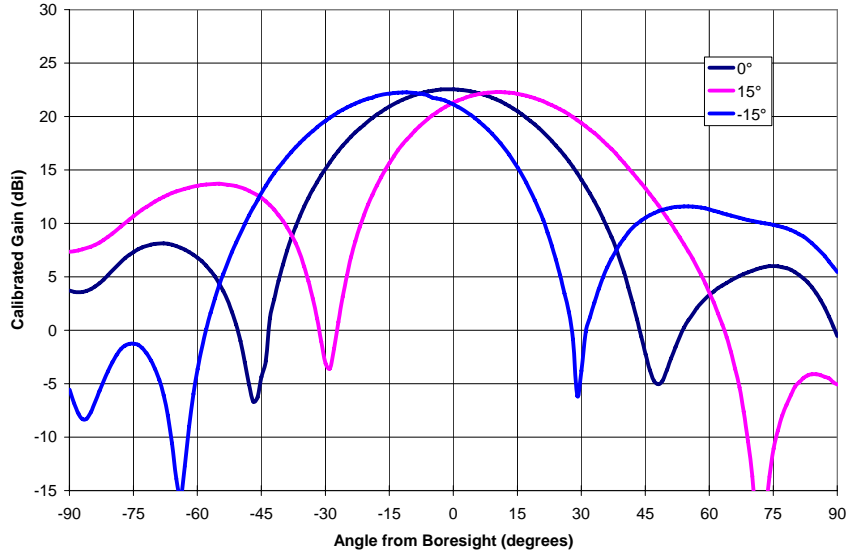


Figure 13. Vertically Scanned Antenna Patterns $\pm 15^\circ$

5. Conclusions

Although several tile elements were non-functional due to a fabrication process error, this effort successfully demonstrated a proof of concept tile architecture and technologies that enable light weight, thin, low cost AESA's for both military and commercial applications. All of the project objectives and tasks were achieved resulting in an in-house proof of concept L-Band receive-only phased array tile.

There were many lessons learned and several technology development areas were a first for AFRL. A significant understanding of costs and issues associated with tile development was gained. This effort demonstrated RF on Flex, plastic packaging, low cost honeycomb structures, array design, assembly, and testing for plastic packages and array testing. The FPGA control methodology developed and demonstrated was successfully transitioned to REMEC Defense & Space. The plastic packaging, aluminum honeycomb, and assembly processing approaches have also been transitioned to a Lockheed Martin program focused on large quantities of panels similar to those described in this paper. It is expected that these technologies will help lead to low cost, large area phased arrays for military applications in the near future.

6. Acknowledgements

The AFRL team gratefully acknowledges the expert assistance and support of REMEC, Tyco Electronics (formerly M/A-COM), and Lockheed Martin.

7. References

- [1] Greg Clark, John Dishong, Steve Nelson, Paul Schurr, Roger Thornton, Mark Walker, Dean White, and Saphan Yok “Small Area L-Band T/R MMIC,” GOMAC 2004.
- [2] Greg Clark, John Dishong, Steve Nelson, Paul Schurr, Roger Thornton, Mark Walker, Dean White, Saphan Yok, “Highly Integrated L-band T/R Module RF Performance,” GOMAC 2005.
- [3] Helms, D., Anderson, R., Lanteri, J.P., “Plastic Package T/R Module Performance for Ground or Space Based Phased Arrays,” GOMAC 2005.
- [4] Jacomb-Hood, A., Melcher, R., Lier, E., Talley, E., Destefano, T., Kraft, P., Fardella, N., Ozuna, V., “RF on Flex Panel for X-Band Phased Arrays,” GOMAC 2005.

Parameter Variation for Broadband Arrays of Irregular Polyomino Subarrays

R.J. Mailloux*, S.C. Santarelli**, T.M. Roberts**, B.C. Kaanta**

*Department of Electrical and Computer Engineering, University of Massachusetts, Amherst Massachusetts

** Electromagnetic Technology Division, Sensors Directorate, Air Force Research Laboratory

Introduction

During the past several years we have investigated the use of polyomino subarrays for wideband and limited field of view (LFOV) arrays. We have shown that this new technology competes favorably against other technologies suited for the same applications. In this paper we will establish guidelines to describe system bandwidth and compare gain and sidelobe levels of subarrayed systems. In addition we will present our latest data showing gain, average and peak sidelobe levels for arrays of up to 16000 elements.

Broadband and LFOV Scan Criteria

Array elements are often grouped together into subarrays for two reasons: to reduce the number of time delay controls in wideband arrays or to reduce the number of phase shifters in LFOV arrays. Both of these array types are indicated in Figure 1. Simple rectangular or linear subarrays produce quantization lobes at the direction cosines

$$u_q = u_0 + q \frac{\lambda}{D_x}, \quad v_p = v_0 + p \frac{\lambda}{D_y} \text{ for } Dx \text{ and } Dy \text{ the subarray spacings in the principal}$$

planes and u_0 and v_0 the scan angle direction cosines in those planes. Figure 2 shows the main beam and quantization lobes for an array with large (32 element) subarrays in an array of 16 subarrays. The array is scanned to $u_0=0.5$ and $f/f_0=1.03$. The figure illustrates that quantization lobes can become the major factor limiting system bandwidth (or LFOV scan).

Figure 3a shows the subarray pattern of a uniformly illuminated rectangular subarray scanned to the angle θ_0 , and plotted against $\frac{D}{\lambda}(u - u_0)$ for $u=\sin\theta$. The quantization lobes occur at the values $\pm(1, 2, 3, \dots)$ of the abscissa, and so are shown to be located at the zeros of the periodic sinc function for the pattern as shown. However, when the frequency is varied (from f_0) for the wideband array, or when the LFOV array is scanned away from broadside ($u_0=0$), then the quantization lobes are moved out of the nulls and the nearest one (at $q=\pm 1$) begins to 'ride-up' the side of the subarray main beam pattern.

Figure 3a also shows the width of an “ideal” pulse subarray pattern (dashed), as having a constant level for $\frac{D}{\lambda}(u - u_0) = -0.5$ to 0.5. This shape is ideal in the sense that the quantization lobe can sample the array factor from -1.0 to $-0.5 - \epsilon$ (ϵ for small), while being totally suppressed, and the main beam can sample the subarray pattern up to 0.5 without significant loss of gain. Beyond that point the main beam is totally suppressed for this case.

If gain were the primary issue, then the subarray 3-dB pattern width would be the relevant constraint, but with a periodic rectangular grid the quantization lobes become larger than the main beam before the gain criterion is reached.

The figure also shows several other horizontal lines indicating the pattern width at the -10 and -20 dB levels. These are the widths at which the quantization lobes would rise to these levels. Since these are much closer to both ± 1 on the horizontal axis, it’s clear that for periodic subarray locations, the quantization lobes are a far more severe restriction on array bandwidth or scan than the loss in gain.

Unlike the array element patterns, the patterns of large subarrays are relatively unaffected by mutual coupling, and one can use the pattern of a single subarray to estimate the subarray pattern in the array. So, for any given subarray pattern shape one can determine the bandwidth or LFOV scan behavior using the simple relations that follow.

The expression below that is based on a general subarray pattern of width Δ at some given quantization lobe level in the pattern at center frequency f_0 , for the pattern centered at θ_0 . The maximum subarray size is:

$$\frac{D}{\lambda_0} = \frac{f_{\min} + f_{\max}}{(f_{\min} + f_{\max})\frac{\Delta}{2} + \sin \theta_0 \Delta f} \quad (1)$$

where $\Delta f = f_{\max} - f_{\min}$.

For modest bandwidth $f_{\max} + f_{\min} \approx 2f_0$, and in this case the equation is conveniently rewritten to solve for the fractional bandwidth times $\sin \theta_0$, which we will call the bandwidth constant:

$$C_{bw} = \frac{\Delta f}{f_0} \sin \theta_0 = 2 \left[\frac{\lambda_0}{D} - \frac{\Delta}{2} \right] \quad (2)$$

This reduces to the equation for the bandwidth of an ideal ‘pulse’ shaped subarray pattern if the subarray pattern width Δ is chosen to be $\Delta = \frac{\lambda_0}{D}$.

Figure (3b) shows a number of curves corresponding to different limits of allowed quantization lobe levels for uniformly illuminated subarrays. These were obtained from

equation 2 using $\Delta/2 = 0.7381\lambda_0/D$ for quantization sidelobe level of -10dB , and $\Delta/2 = 0.908\lambda_0/D$ for -20 dB quantization lobe level. The figure emphasizes the fact that it is the quantization lobe level that dictates the bandwidth. One of the upper curves in the figure is the bandwidth based on half power gain $\Delta/2 = 0.443\lambda_0/D$, and the other upper curve is for the “Ideal” case $\Delta/2 = 0.5\lambda_0/D$. The curves show, for example, that a subarray of 2 wavelengths long in a chosen direction has about 0.17 times the bandwidth or scan than that of the ideal subarray for -20 dB quantization lobes, while for -10dB lobes the bandwidth or scan is about 0.44 of the ideal. Although Figure 3 is based on the uniformly illuminated subarray, the equations are applicable to any subarray pattern.

:

A similar relationship can be obtained for the limited field of view case, for the array with phase shifters only at the subarray input ports, and scanning the array from $-\sin\theta_{\max}$ to $+\sin\theta_{\max}$, over the range $2\sin\theta_{\max}$, then one obtains the solution for a maximum LFOV scan constant C_{LFOV} , again based on the quantization lobe constraints used earlier..

$$C_{LFOV} = 2 \sin \theta_{\max} = 2 \left[\frac{\lambda_0}{D} - \frac{\Delta}{2} \right] \quad (3)$$

so the same curves from Figure 3a relate $2 \sin \theta_{\max}$ to $\frac{\Delta f}{f_0} \sin \theta_0$, and Figure (3) is used for both applications. These equations thus allow one to evaluate bandwidth by inspecting the shape of the subarray pattern.

Subarray Options:

Effect of Displacing Sources in a Periodic Array

It has been suggested that one could achieve quantization lobe suppression by simply displacing the feed locations of a periodic array. Some success has been claimed for very small subarrays [2].

Figure 4 suggests how this is implemented for a one-dimensional LFOV array. The conventional periodic excitation of an array of subarrays would mean that all elements of some p'th subarray being excited with the one signal $\exp\left(-j\frac{2\pi}{\lambda}u_0pD_x\right)$. The black circles in the upper figure indicate that the reference is always taken at the same point in the subarray. The resulting array pattern is:

$$F(u) = f(u) \sum_p A_p [e^{j\frac{2\pi}{\lambda}pD_x(u-u_0)}] \quad (4)$$

Where the element pattern is assumed to be $f(u)$ and u_0 is the scan angle. The array factor part of this pattern repeats whenever the exponential term $\frac{2\pi}{\lambda} D_x (u - u_0) = 2\pi q$ for any integer q , and so leads to quantization lobes at $u = u_0 + q \frac{\lambda}{D_x}$.

The lower figure indicates that the reference point can be moved to be different for each subarray, and so the periodicity of the applied source would be disrupted. The applied source is then $\exp\left[-j \frac{2\pi}{\lambda} u_0 (p D_x + \Delta_p)\right]$. The resulting array pattern is:

$$F(u) = f(u) \sum_p A_p e^{-j \frac{2\pi}{\lambda} u_0 \Delta_p} [e^{j \frac{2\pi}{\lambda} p D_x (u - u_0)}] \quad (5)$$

This equation shows that there will be quantization lobes at the same locations as for the previous case, and their amplitude will be that of the main beam at u_0 reduced by the element pattern.. The pattern gain will be reduced because of the introduced error

(instead of a peak value of $\sum_p A_p$, the peak is reduced to $\sum_p A_p e^{-j \frac{2\pi}{\lambda} u_0 \Delta_p} \leq \sum_p A_p$).

In the general case then this procedure reduces the gain, increases the average sidelobes, and does not suppress quantization lobes except for special cases with very small subarrays where it may distort the pattern in the area of the quantization lobes.

Alternative Polyomino Options:

There is a wide range of polyomino choices, but with 269 possible octominoes, only a small number are ‘rectifiable’ , meaning that they will completely tile a rectangle without leaving any spaces. Figure 5 shows 9 of the rectifiable octominoes, The basic L-octomino that we have used primarily thus far is shown in the center left of Figure 5.Two other L shapes are denoted L1 and L2 on the figure. The names we have given to the other shapes are fairly obvious.

There are several reasons for investigating the L-octomino first. The most obvious is that some shapes, like the Hop-octomino can only be put together one way. In this case rotating one 180 degree and adding it to the original constructs a 16 element square, and so again is subject to quantizaton lobes. Others are shaped in such a way as to result in significant repetition across the array, again resulting in quantization lobes or large residual sidelobes. For example, a glance at L1 reveals only a few ways of arranging them.

Yet another issue is that some of the less compact subarrays have large phase errors. The equation below gives the phase error variance for several subarray shapes.

For an element in a subarray with location index (m,n) , with spacing d in both x and y directions, and scanned to u_0, v_0 , and $\Delta_m = m - m_c$ and $\Delta_n = n - n_c$, where the subscript c means the phase center location, then the variance is given [3] :

$$\bar{\varepsilon}^2 = \frac{1}{N_{nor}} \left(\frac{2\pi d}{\lambda} \right)^2 \left(\sum (\Delta_m^2 + \Delta_n^2) \right) (u_0^2 + v_0^2) \quad (6)$$

The normalization N_{nor} is 2 times the number of elements in the subarray. The term $u_0^2 + v_0^2$ is replaced by $\sin^2 \theta$. In a reduced form :

$$\bar{\varepsilon}^2 = c1 \left(\frac{2\pi d}{\lambda} \right)^2 \sin^2 \theta \quad (7)$$

where $c1$ is given:

$$c1 = \frac{1}{N_{nor}} \left(\sum (\Delta_m^2 + \Delta_n^2) \right).$$

For the time delay case, the phase error variance is given as:

$$\bar{\varepsilon}^2 = c1 \left(\frac{2\pi d}{\lambda} \right)^2 \left(\frac{f}{f_0} - 1 \right)^2 \sin^2 \theta \quad (8)$$

The table below gives the values of the constant $c1$ for the octomino shapes of Figure 5

Shape	c1
Sawtooth	1.0
Point up	0.875
U	1.2
C	1.0
L	0.875
L2	1.125
L1	2.5
L3	1.125
HOP	1.125

Notice that two octominos with smallest error are the chosen L-octomino and the Point up octomino. One of the others, the L1 octomino has over twice the error. These phase variances can lead to significant sidelobes and reduced gain if the array is scanned to larger LFOV angles or wider frequency variations in the wideband case.

A detailed comparison of peak and average sidelobes of these various subarrays will be published at a later time.

Parameter Variation with Array Scan:

The primary goal of this research has been to evaluate the performance of polyomino subarrays in comparison with periodic subarrays and then to develop a set of design rules for selection of subarray types and sizes. Although our data is not yet complete, we can now begin to use our results to make approximate but highly intuitive engineering choices.

Figures 6 and 7 show several curves of array gain (computed by evaluating the pattern integrals). These data describe increasing fractions of each array from 32 to either 64 or 128 elements per side. The arrays are scanned to $u_0=0.5$, $v_0=0.5$ and at $f/f_0=1.3$. Figure 6 shows three curves, the one with highest gain is that of an array with time delay at each element, the lower two are nearly identical and show the gain of the same arrays arranged in rectangular (2×4 element) subarrays or as L-octomino subarrays. The reduction in gain is due to the phase error introduced by the phase-shifted subarrays and appears to be constant with array size.

Figure 7 shows two curves of gain, that for a periodic array of rectangular subarrays and one for an array of L-octominoes. Again these gain curves are nearly identical.

The conclusions drawn from these curves are that:

- Both rectangular and polyomino subarrays have small constant loss due to phase error.
- There is almost no added error due to using L-octomino subarrays in place of rectangular ones.

Later it will be shown that the polyomino subarrays fully suppress the quantization lobes and have peak sidelobes that decrease with array size. Thus, for a large array the main bandwidth constraint is not the quantization level of Figure 3, but the reduction of gain as shown in Figure 3. This makes the polyomino subarrays much wider band than the rectangular subarrays (as indicated in Figure 3b).

Figure 8 shows the average (error) sidelobe level for an array of up to 64 elements on a side. This curve shows the expected result, that the sidelobe level varies from -42 to -48 dB, a change of 6 dB for a quadrupling of array area. Figure 9 shows that the ratio of peak sidelobes to the average sidelobes of Figure 8 is within a dB of constant over the same range.

Figures 10 and 11 describe the peak sidelobes of two arrays one with up to 64 elements per side and one with up to 128 elements per side. The arrays were designed to have nearly random subarray locations and orientations. The two are remarkably similar, both having sidelobes at about -21 dB for 32 elements on a side, and about -26 dB for 64 elements on a side. The larger array had a minimum sidelobe level of -31 dB for 128 elements on a side. Both show about -5 dB for each quadrupling of array area.

Conclusion:

This paper has investigated the issue of bandwidth in an array of subarrays and defined constraints for rectangular subarrays that present a useful bandwidth criterion. Next the paper showed that simply moving source points around in a subarray did not suppress quantization lobes, but merely distorted the array patterns. Third, the paper looked at the average variance parameters of a variety of octomino subarrays. Finally the paper presented data from two arrays to show that the gain for rectangular and polyomino based arrays is nearly identical, but that the sidelobe levels of polyomino subarray based arrays continues to decline at about the -5dB per increase of four in array area.

The overall result is that it is shown that not only do the polyomino arrays have lower sidelobes, no loss in gain, but also they have wider bandwidth than rectangular subarrays because their bandwidth is limited by system gain, not quantizaton lobes.

References:

1. R.J. Mailloux, S.G. Santarelli, T.M. Roberts, "Wideband arrays using irregular (polyomino) shaped subarrays", Electronics Letters, 31Aug.2006, Vol.42, No 18, pp. 1019-1020
2. R.C. Hansen, Gregory G. Charlton, "Subarray Quantization Lobe Decollimation", IEEE Trans. AP-47, No.8, August 1999
3. R. J. Mailloux, S.G. Santarelli, T.M. Roberts, "Polyomino Shaped Subarrays for Limited Field of View and Time Delay Control of Planar Arrays", 2005Antenna Applications Symposium

Acknowledgments:

The authors acknowledge the support of the Air Force Office of Research, administered by Dr. Arje Nachman.

This work was performed at the Air Force Research Laboratory, Electromagnetic Technology Division, Hanscom AFB, MA 01731

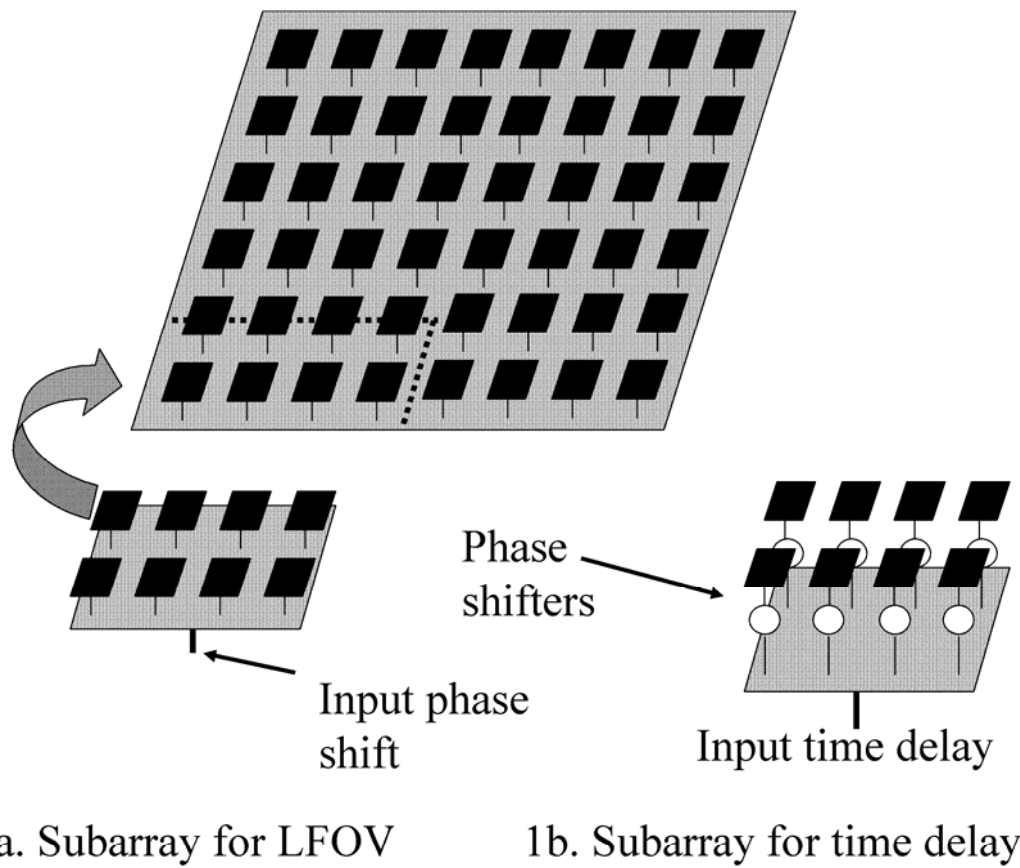


Figure 1: Periodic subarrays for LFOV and Time Delayed Subarrays

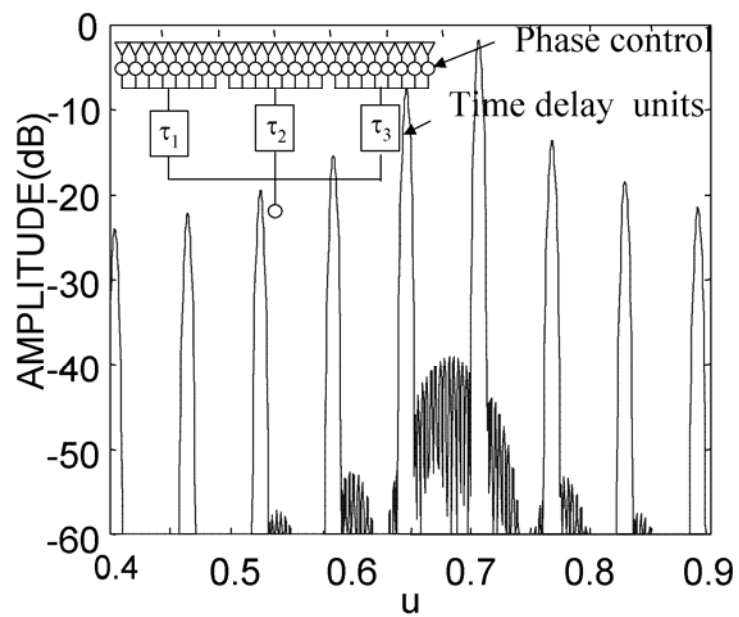


Figure 2: Pattern of array with 32 element periodic subarrays $f/f_0=1.03$

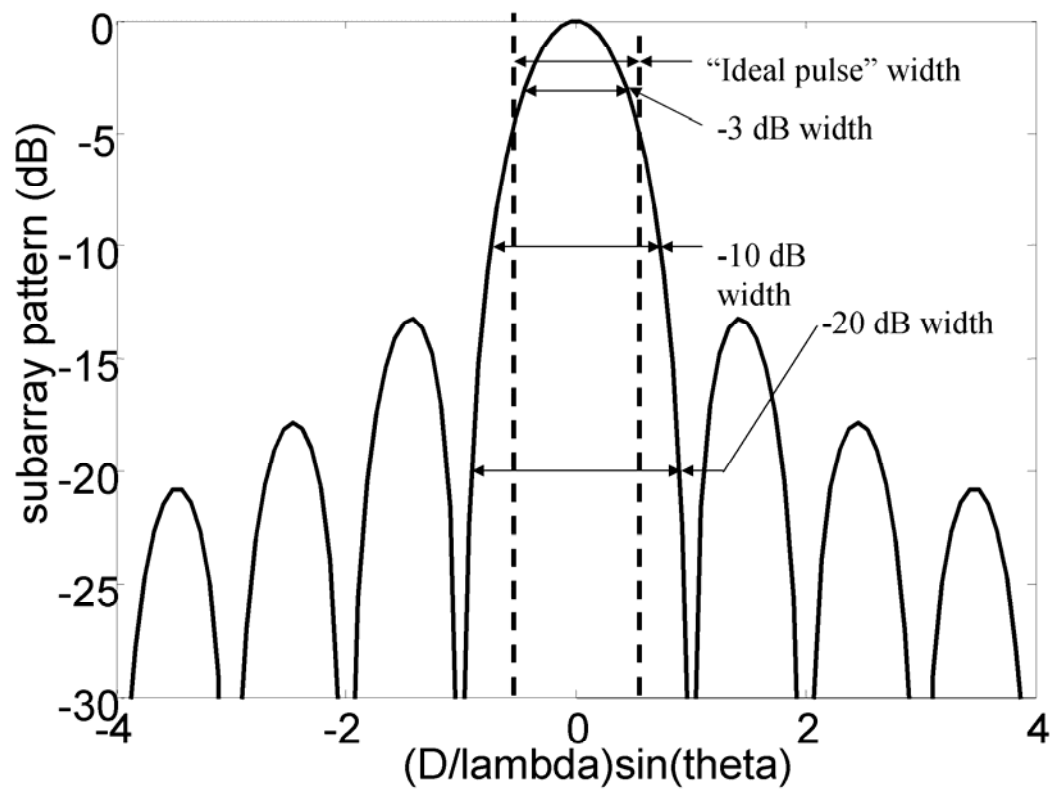


Figure 3a: Pattern of uniform subarray of width D

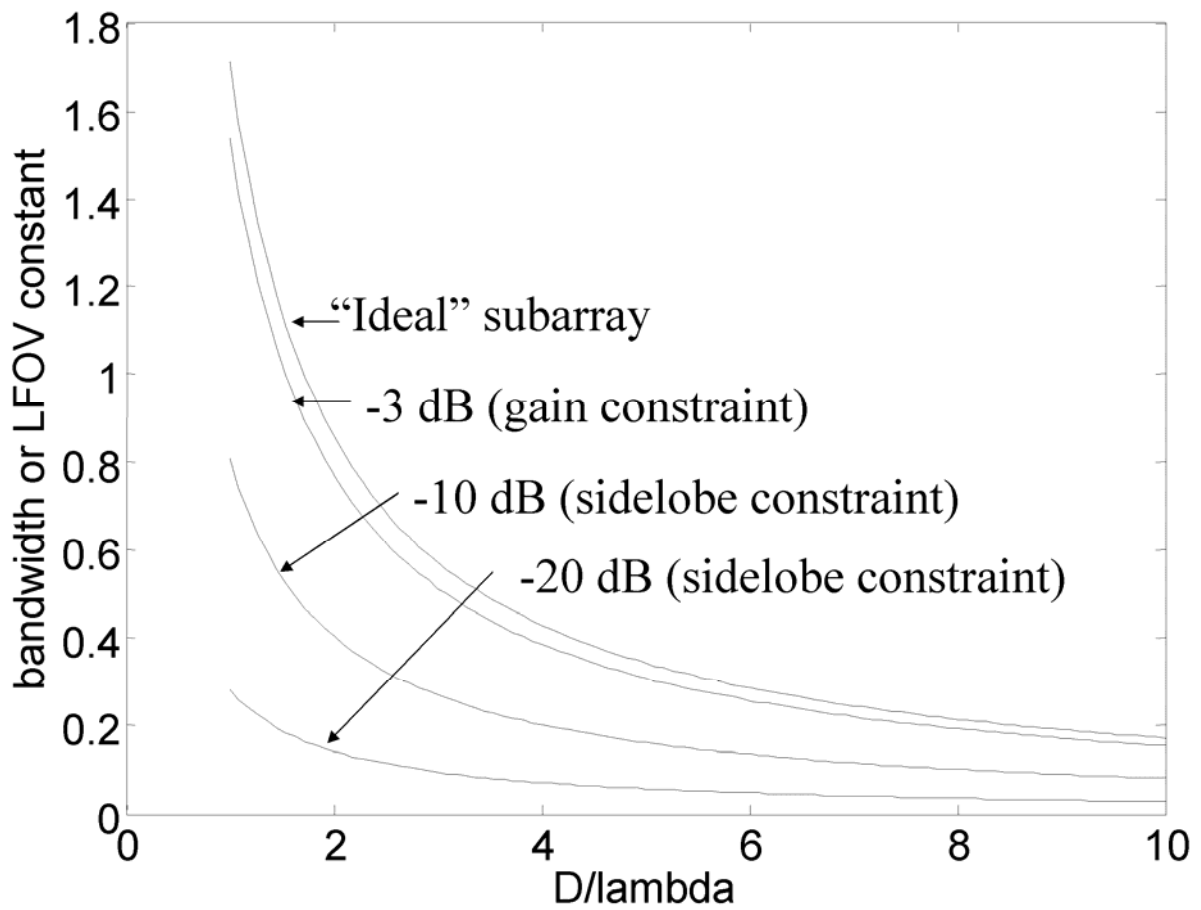


Figure 3b: Bandwidth for subarrays of width D

Subarrays with common
excitation point

Subarrays with ‘random’
excitation points

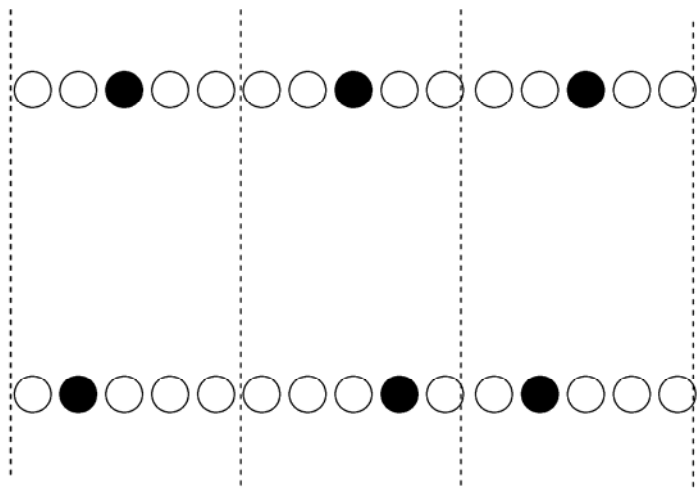


Figure 4: Subarrays with displaced
excitation

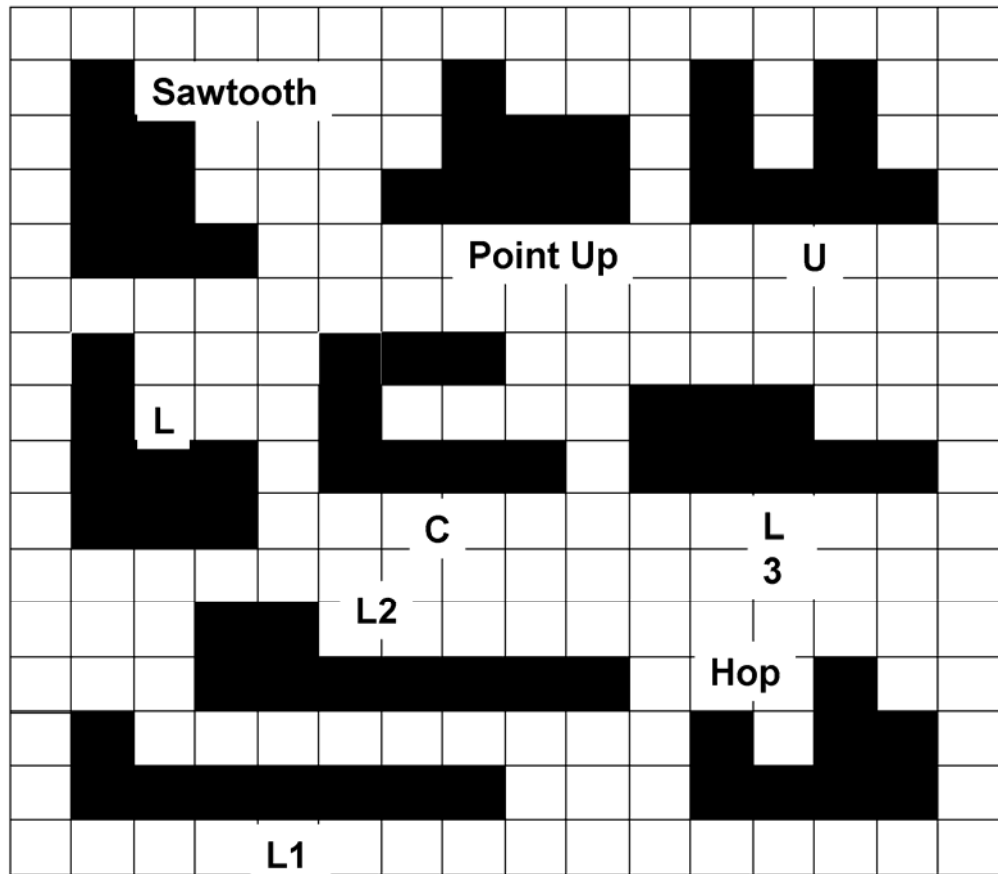


Figure 5: Alternative octomino figures

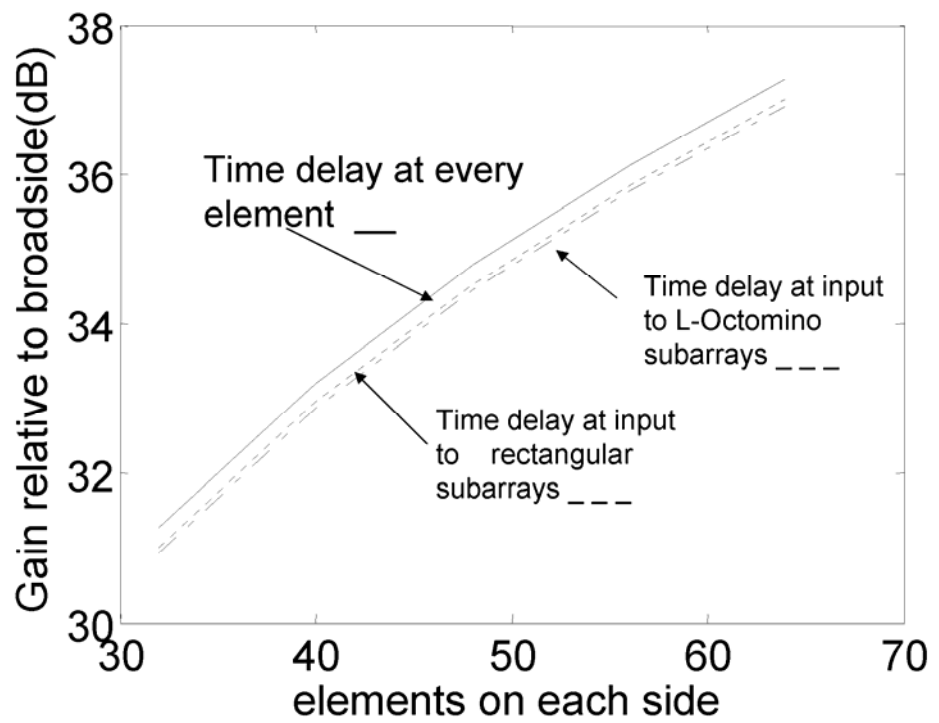


Figure 6: Integrated Gain for Time Delay at Every Element vs. at Input to Rectangular or L-Octomino Subarrays

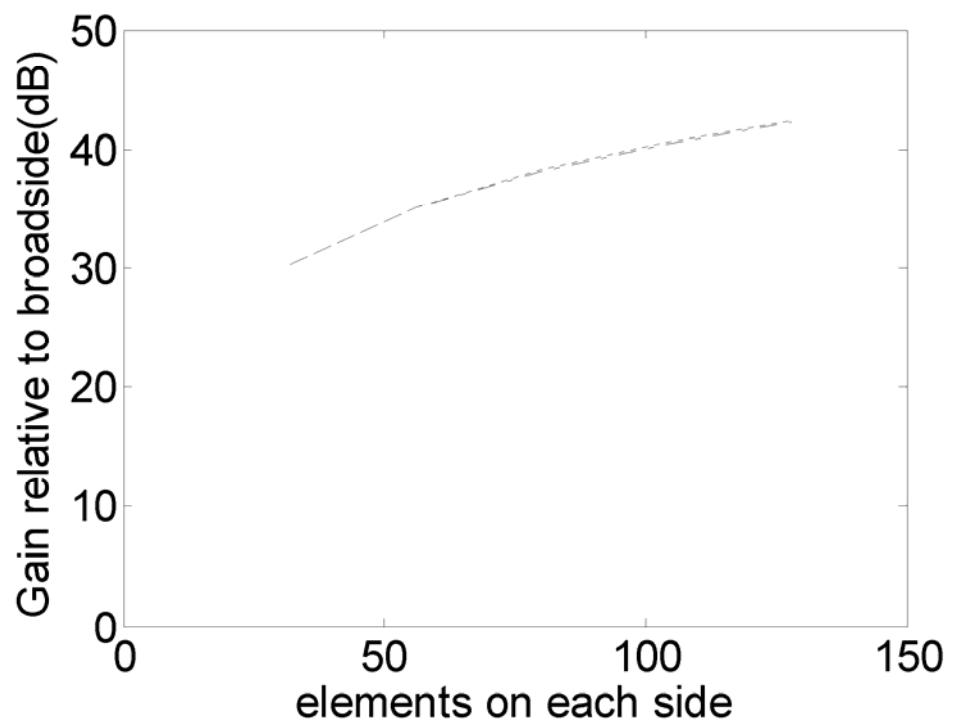


Figure 7: Gain Comparison, Rectangular vs L-octomino Subarrays ($f/f_0=1.3$)

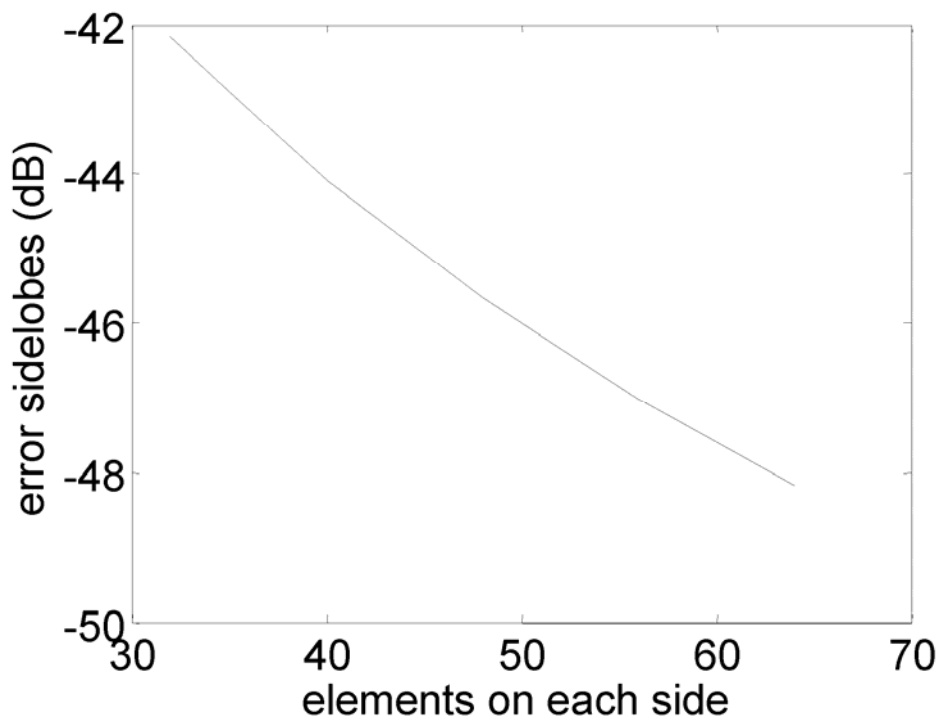
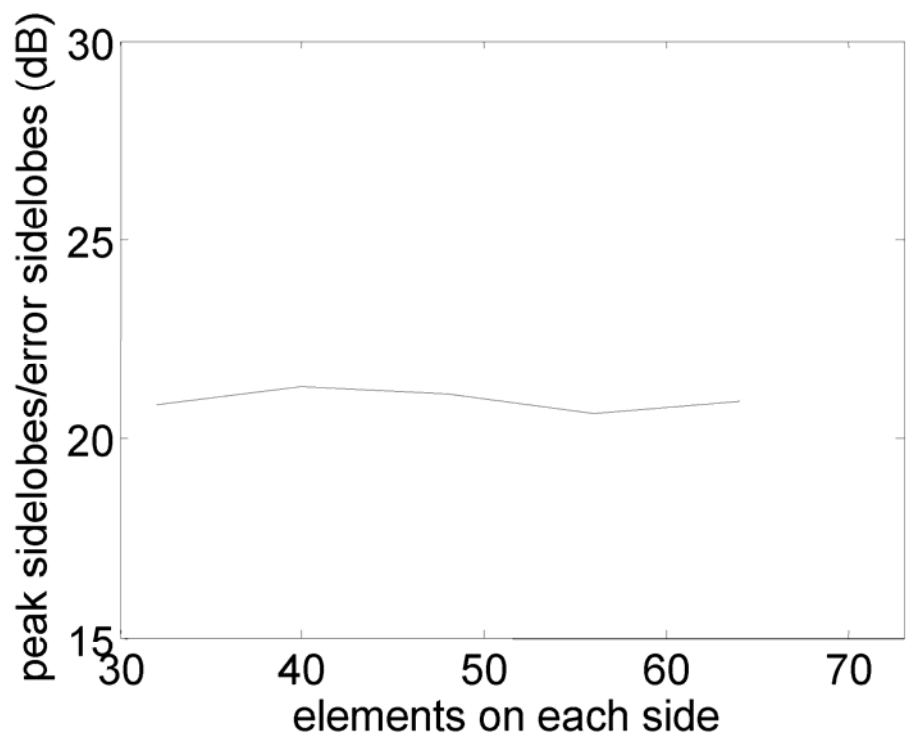


Figure 8: Integrated Average Sidelobe Level vs. Array Size



**Figure 9: Ratio of Peak to Average Sidelobe Levels
($f/f_0=1.3$)**

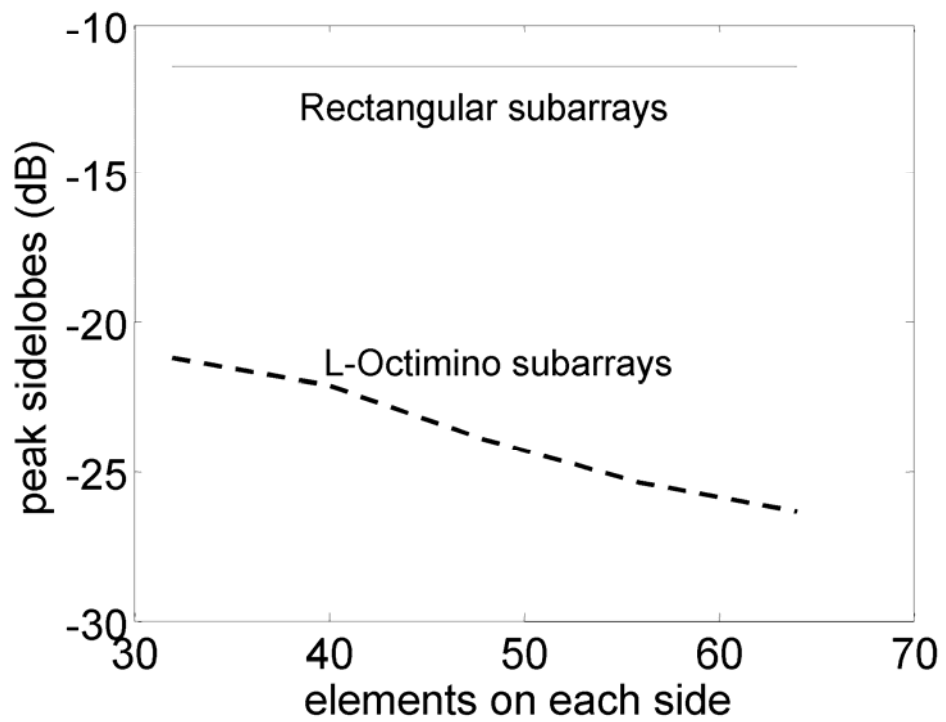


Figure 10: Peak Sodelobe Comparison , Rectangular vs. L-Octomino Subarrays ($f/f_0=1.3$)

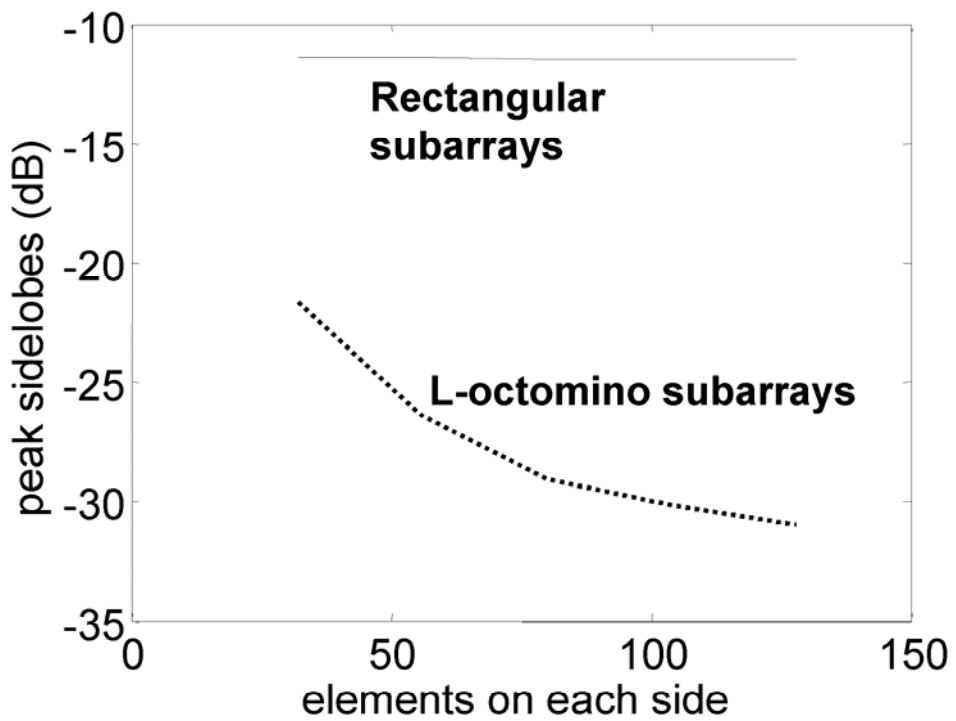


Figure 11: Peak Sidelobe Comparison, Rectangular vs. L-octomino subarrays

Sub-Array Mirroring for the Mediation of Second-Order Beams in Planar Edge Slot Waveguide Antenna Arrays

B. J. Herting, M. W. Elsallal and J. B. West

Advanced Technology Center

Rockwell Collins, Inc. Cedar Rapids, IA 52498 USA

bherting @rockwellcollins.com, waelsall @ rockwellcollins.com, jbwest @rockwellcollins.com

Abstract: Edge slot waveguide antenna arrays have been extensively employed in surveillance radar applications, such as the Airborne Warning and control System (AWACS), where large volume coverage at a relatively low cost can be achieved via phase shifter electronic scanning in elevation and 360° mechanical scanning in azimuth. One of the requirements typically set forth in such applications is an extremely low side lobe level (SLL). In the Co-pol, this is achieved through the use of proper amplitude tapering. In the Cx-pol, however, edge slot waveguide antenna arrays exhibit grating lobe phenomenon, or second-order beams [1], whose relative strength is proportional to the tilt of the waveguide slots and often exceeds the desired SLL. A comprehensive analytical study was undertaken to quantify the benefit of sub-array mirroring in edge slot waveguide antenna arrays for the mediation of second-order Cx-pol beams over a ±60° 1D electronic scan. The theoretical results of that study are presented herein.

1 INTRODUCTION

Second-order beams in the Cx-pol radiation pattern of edge slot waveguide arrays can often exceed the desired side lobe level (SLL) of the array. There are three common techniques utilized to suppress the level of these second-order Cx-pol beams [1]: (1) decrease the average edge slot tilt angle, (2) employ a choke between waveguides to suppress Cx-pol surface currents, and (3) employ baffles between waveguides to force the E-field to orient itself along the Co-pol regardless of slot orientation.

Decreasing the average slot tilt angle to lower the Cx-pol requires one to either increase the length of the waveguide or deal with matching to a slotted waveguide impedance that is greater than that of the characteristic impedance of the guide. Increasing guide length is a nice solution if the space is available, but it does have the undesirable effect of lowering the operating bandwidth of the array. Dealing with increased input impedance simply makes coupling energy into the guide more difficult. As a result, there is some practical limitation to the amount which one can increase the impedance.

Employing a choke to suppress Cx-pol currents simply requires one to place a metal bridge between waveguides approximately 0.2 – 0.25 wavelength down from the face of the array. The effectiveness of the choke in mitigating the Cx-pol radiation is maximum when the Cx-pol currents of adjacent waveguides are in phase. As the Cx-pol currents of

the adjacent waveguides become less in phase, the effectiveness of the choke diminishes to the point where the choke has no effect when the Cx-pol currents are out of phase. As a result, the choke is not effective across the entire electronic scan region.

Employing baffles between waveguides to force the E-field to orient itself along the Co-pol regardless of slot orientation is a very effective way to mitigate the Cx-pol level across the entire electronic scan region. However, this technique increases the depth and weight of the array as the baffles extend approximately one-half wavelength out in front of the array. Depending on the application, baffles are typically undesirable as a result of this increased weight and depth.

In order to help overcome some of the shortcomings of the aforementioned edge slot waveguide array Cx-pol mitigation techniques, a comprehensive analytical study was undertaken to quantify the benefits of sub-array mirroring to Cx-pol mediation over a $\pm 60^\circ$ 1D electronic scan.

2 ANALYTIC APPROACH

The full analytic approach is a two pronged effort consisting of a comprehensive theoretical analysis followed by an elaborate build and test for measurement verification. This approach should provide a high degree of confidence in the final results and conclusions, as well as verify the validity of the various theoretical methods employed.

The remainder of this paper presents the details of the theoretical analysis which utilized a combination of three different computational techniques to solve multiple variations of a common edge slot array model.

2.1 Computational Techniques

The benefits of sub-array mirroring to the Cx-pol performance of an edge slot waveguide array over a $\pm 60^\circ$ 1D electronic scan were investigated using three different computational techniques: (1) ideal array factor, (2) HFSS™ full wave electromagnetic (EM) [3], and (3) Hybrid HFSS™ / ideal array factor.

2.1.1 Ideal Array Factor

In the ideal array factor technique, the slot is treated as a point source with an E-field polarized perpendicular to the length of the slot. The magnitudes of the Co-pol and Cx-pol components are determined by multiplying the element excitation by the cosine and sine, respectively, of the average slot tilt angle. The Co-pol and Cx-pol radiation patterns are determined by squaring the ideal array factor formulation given in equation 2.1.1-1 [2]. The radiation patterns are then multiplied by $\cos^{1.75}(\theta)$ and subsequently converted to log scale. The $\cos^{1.75}(\theta)$ is used to approximate the roll off of the element radiation pattern, which in reality is much more complex and not azimuthally symmetric. In spite of the significant simplifications made with respect to element pattern and Co-pol and Cx-pol levels, the ideal array factor technique represents the most versatile computational model for the analysis of the benefit of sub-array mirroring.

$$AF(\theta, \phi) = \sum_{n=1}^N \sum_{m=1}^M I_{mn} e^{j(\beta \hat{r} \cdot \vec{r}'_{mn} + \alpha_{mn})} \quad (2.1.1-1)$$

where

$$I_{mn} = \begin{cases} a_{mn} \cos(\psi) & \text{co-pol slot excitation magnitude} \\ a_{mn} \sin(\psi) & \text{cx-pol slot excitation magnitude} \end{cases}$$

α_{mn} = slot excitation phase

$$\hat{r} = [\sin(\theta)\cos(\phi)]\hat{x} + [\sin(\theta)\sin(\phi)]\hat{y} + [\cos(\theta)]\hat{z}$$

$$\vec{r}' = x'_{mn}\hat{x} + y'_{mn}\hat{y} + z'_{mn}\hat{z} \quad (\text{slot location})$$

ψ = average slot tilt angle

2.1.2 HFSS™ Full Wave EM

In the HFSS™ full wave EM technique, the edge slot array models are solved completely in HFSS™. The size of the edge slot arrays (12 x 12) make it possible to solve on a high-end workstation with dual processors and 16 GB of RAM. A well converged solution is reached in approximately 4 hours. It is resource and time intense, but the results should be the most accurate of all computational techniques as everything is accounted for in the model.

2.1.3 Hybrid HFSS™ / Ideal Array Factor

The hybrid HFSS™ / ideal array factor technique utilizes HFSS™ radiation pattern results for the edge slot waveguide linear arrays shown in Figure 2.1.3-1. Master/slave boundary conditions are employed in HFSS™ to simulate a finite (12) x infinite array thus accounting for any guide to guide mutual coupling. Using the radiation patterns from HFSS™ as the element patterns for a linear array, the Co-pol and Cx-pol radiation patterns of the 12 x 12 array are determined. This method provides increased accuracy over the ideal array factor technique as it utilizes actual Co-pol and Cx-pol radiation pattern results from HFSS™ rather than simple cosine/sine approximations. The biggest simplification made in this technique is the fact that finite array edge effect is neglected in the H-plane.

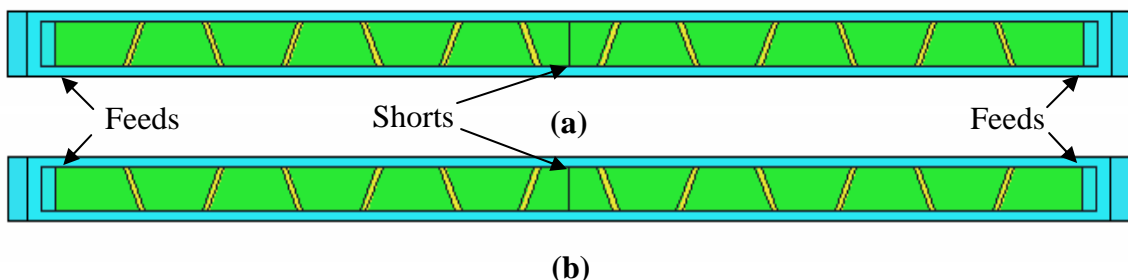


Figure 2.1.3-1 Edge slot linear array models: (a) tilt "A" and (b) tilt "B"

2.2 Edge Slot Array Model

Each computational technique solved multiple variations of the same X-band edge slot array model whose size was chosen such that it was large enough to yield meaningful results, yet small enough to be solved efficiently by each computational approach. The model consisted of 12 rows of resonant edge slot waveguide fed on both ends and shorted at the center as shown in Figure 2.1.3-1. Each row of edge slot waveguide had 12 slots along the waveguide, each having a tilt angle of 21.9° to achieve uniform aperture illumination. In order to generate the multiple sub-array mirroring variations, two slot tilt variations, “A” and “B” in Figure 2.1.3-1, were utilized. The “A” and “B” slot tilt variations are mirrors of one another and form the building blocks for investigating the five different sub-array mirroring configurations outlined in Table 2.2-1.

In addition to the planar 12 x 12 array, the ideal array factor technique was used to investigate a larger 24" x 20" planar array with 26 x 32 elements and a 24" circular array with 782 elements, both of which were assumed to have an average slot tilt angle of 10°.

Table 2.2-1 Planar 12 x 12 array configurations utilizing unit cell from Figure 2.1.3-1

Sub-Array Mirroring	Row Order (Top-to-Bottom)
Sub0	[A, A, A]
Sub1	[A, B, A, B, A, B, A, B, A, B, A, B]
Sub2	[A, A, B, B, A, A, B, B, A, A, B, B]
Sub3	[A, A, A, B, B, B, A, A, A, B, B, B]
Sub4	[A, A, A, A, B, B, B, B, A, A, A, A]

3 RESULTS

3.1 Planar 12 x 12 Edge Slot Array

The five sub-array mirroring variations outlined in Table 2.2-1 were solved using each of the three computational techniques. An example E-plane and H-plane 2D normalized radiation pattern of the Co-pol for the “Sub0” case is given in Figure 3.1-1. For the “Sub0” case with boresight ($\theta = 0^\circ$) beam, the undesired second order lobes in the Cx-pol are in the E-Plane pattern as shown, normalized to the maximum Co-pol, in Figure 3.1-2. These figures show excellent agreement between the three computational techniques in terms of the locations of the peaks and valleys of the pattern. The variations in absolute value are easily explained by simply considering the approximations made in the ideal array factor and hybrid computational techniques as discussed in Section 2.1.

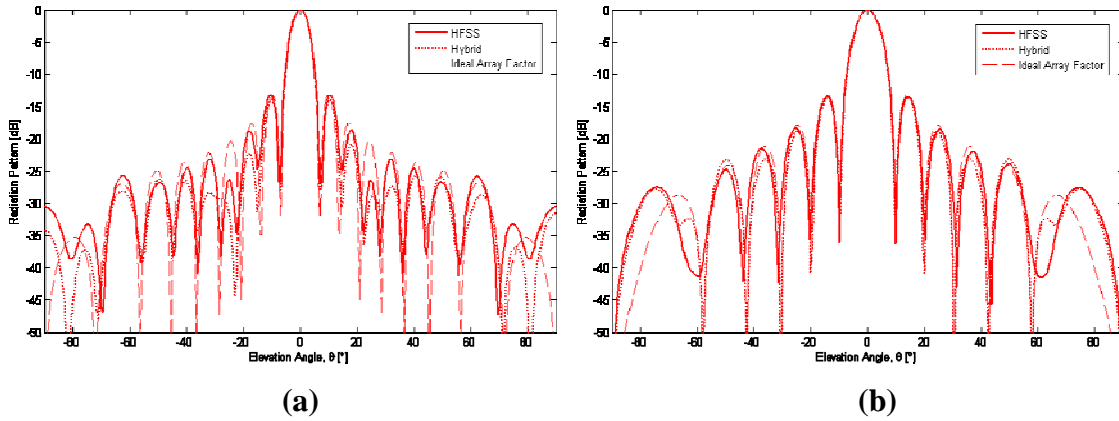


Figure 3.1-1 Planar 12 x 12 array Sub0 Co-pol pattern: (a) E-plane (b) H-plane

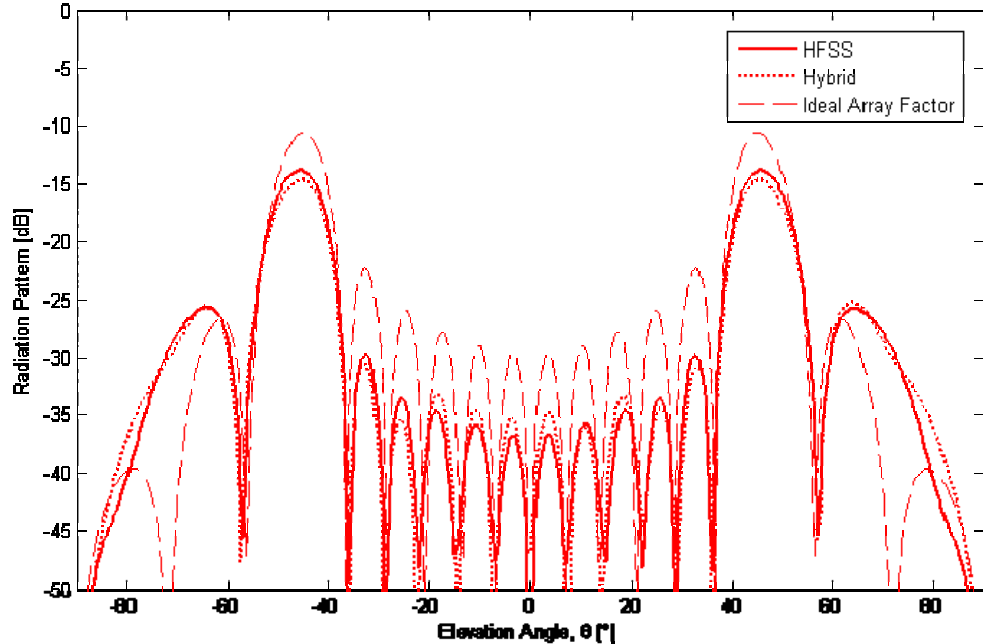


Figure 3.1-2 Planar 12 x 12 array Sub0 E-plane Cx-pol pattern

Having established excellent pattern correlation between the three computational techniques, each technique is now used to investigate the merits of each of the five sub-array mirroring variations in Table 2.2-1 with respect to the maximum Cx-pol as the antenna main beam is electronically scanned from boresight ($\theta = 0^\circ$) to $\theta = 60^\circ$ in 5° increments.

3.1.1 Sub-Array Mirroring = 0

For the “Sub0” case, the maximum Cx-pol versus main beam scan angle is shown in Figure 3.1.1-1. All three computational techniques indicate that the maximum Cx-pol level for low scan angles is rather high, -10 to -15 dB with respect to the Co-pol maximum. The Cx-pol level begins to decline as the main beam is scanned past 40° .

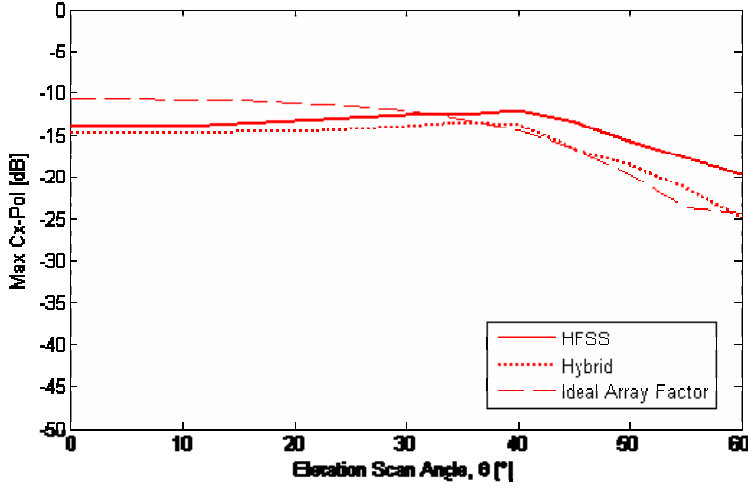


Figure 3.1.1-1 Planar 12 x 12 array Sub0 max Cx-pol vs. scan angle

3.1.2 Sub-Array Mirroring = 1

For the “Sub1” case, the maximum Cx-pol versus main beam scan angle is shown in Figure 3.1.2-1. All three computational techniques indicate that the maximum Cx-pol level for low scan angles has been dramatically reduced by over 20 dB compared to the “Sub0” case. However, unlike the “Sub0” case, the “Sub1” maximum Cx-pol level begins to rise as the main beam is scanned off boresight and even starts to exceed the Cx-pol level of the “Sub0” case after about 30° to 40° of scan.

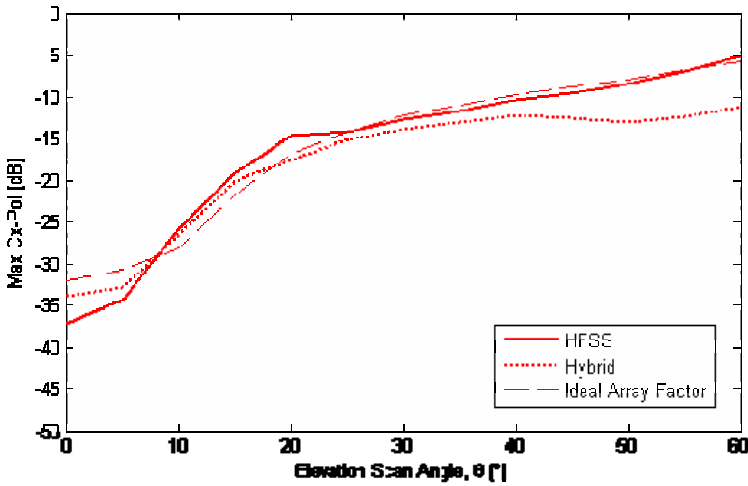


Figure 3.1.2-1 Planar 12 x 12 array Sub1 max Cx-pol vs. scan angle

3.1.3 Sub-Array Mirroring = 2

For the “Sub2” case, the maximum Cx-pol versus main beam scan angle is shown in Figure 3.1.3-1. All three computational techniques indicate that the maximum Cx-pol level for low scan angles, although better than the “Sub0” case by nearly 5 dB, is worse than the “Sub1” case. Similar to the “Sub1” case, the maximum Cx-pol level rises as the

main beam is scanned off boresight, but the increase is much slower such that the Cx-pol in the “Sub2” case is lower than the “Sub1” case after about 20° of scan. The “Sub0” case still has a lower Cx-pol beyond 40° of scan.

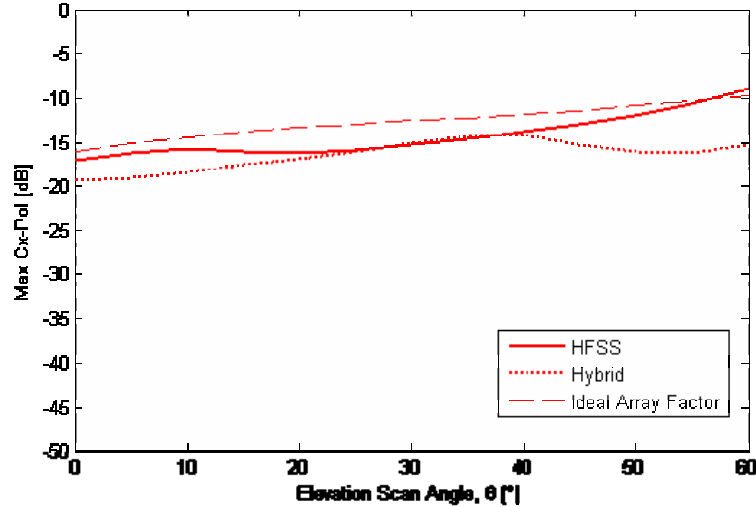


Figure 3.1.3-1 Planar 12 x 12 array Sub2 max Cx-pol vs. scan angle

3.1.4 Sub-Array Mirroring = 3

For the “Sub3” case, the maximum Cx-pol versus main beam scan angle is shown in Figure 3.1.4-1. The situation is almost identical to that of the “Sub2” case except that the maximum Cx-pol level is slightly higher at low scan angles and slightly lower at wide scan angles resulting in a minimal Cx-pol increase with scan.

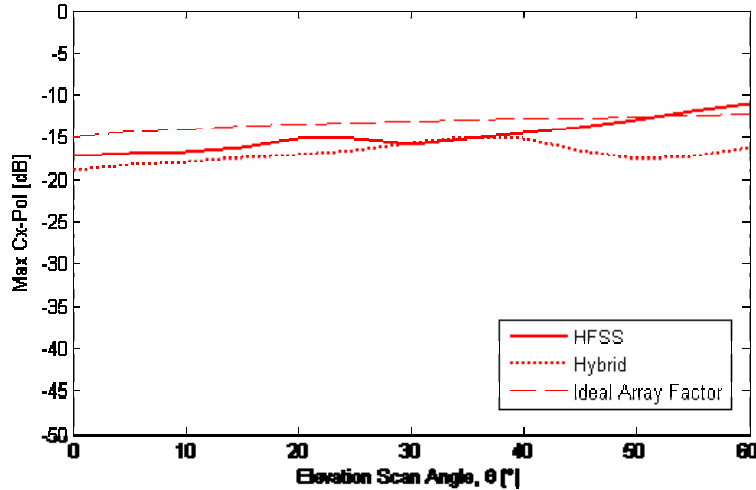


Figure 3.1.4-1 Planar 12 x 12 array Sub3 max Cx-pol vs. scan angle

3.1.5 Sub-Array Mirroring = 4

For the “Sub4” case, the maximum Cx-pol versus main beam scan angle is shown in Figure 3.1.5-1. The situation is almost identical to that of “Sub2” and “Sub3” except that

the maximum Cx-pol level is again slightly higher at low scan angles and slightly lower at wide scan angles. This results in a nearly constant Cx-pol level with respect to scan. The only computational technique that didn't show a nearly constant Cx-pol level was the HFSS full wave EM model, which shows an increase in the Cx-pol level after about 40° of scan.

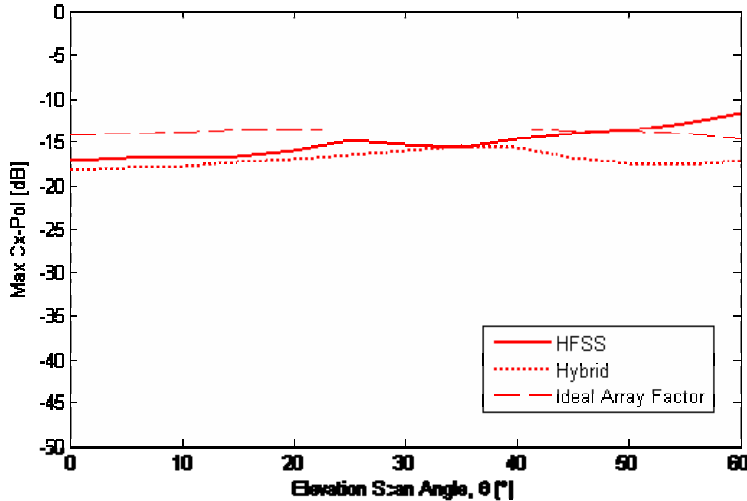


Figure 3.1.5-1 Planar 12 x 12 array Sub4 max Cx-pol vs. scan angle

3.2 Planar 26 x 32 Edge Slot Array

Having established the validity of the ideal array factor computational technique with respect to predicting trends in Cx-pol performance versus electronic scan, a larger approximately 24" x 20" planar array with 26 x 32 elements was analyzed with both a uniform excitation and a Taylor (30 dB $\bar{n} = 4$) excitation.

3.2.1 Uniform Excitation

For the uniform excitation case, the maximum Cx-pol versus main beam scan angle for all sub-array configurations is shown in Figure 3.2.1-1. The results are identical to those obtained for the 12 x 12 in terms of the maximum Cx-pol performance versus electronic scan angle for the various sub-array mirroring configurations. The overall level of the Cx-pol is lower, though, due to the lower average slot tilt used of 10° compared with 21.9° in the 12 x 12 array.

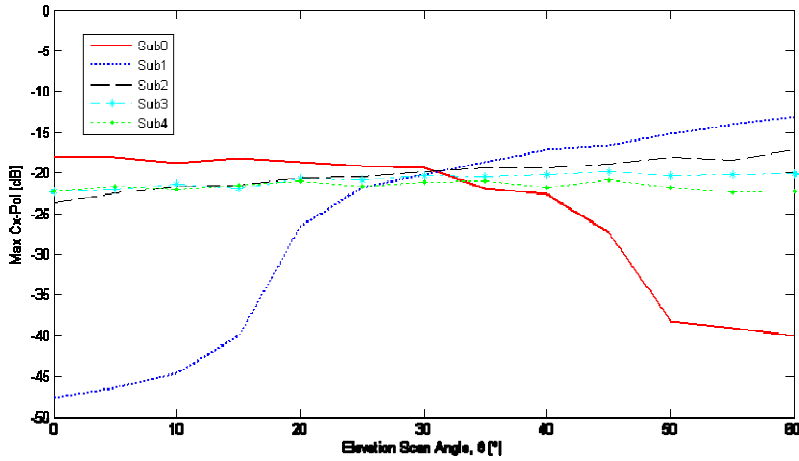


Figure 3.2.1-1 Planar 26 x 32 array uniform excitation max Cx-pol vs. scan angle

3.2.2 Taylor ($30 \text{ dB } \bar{n} = 4$) Excitation

For the Taylor 30 dB $\bar{n} = 4$ excitation case, the maximum Cx-pol versus main beam scan angle for all sub-array configurations is shown in Figure 3.2.2-1. The results show identical trends to those seen in the uniform excitation case. comparing Figures 3.2.1-1 and 3.2.2-1, the Taylor 30 dB $\bar{n} = 4$ excitation maximum Cx-pol results are nearly identical in magnitude to that of the uniform excitation for all sub-array mirroring configurations except “Sub0” at wide scan angles and “Sub1” at low scan angles. The maximum Cx-pol for these two cases is approximately 10 dB lower with a Taylor 30 dB $\bar{n} = 4$ excitation.

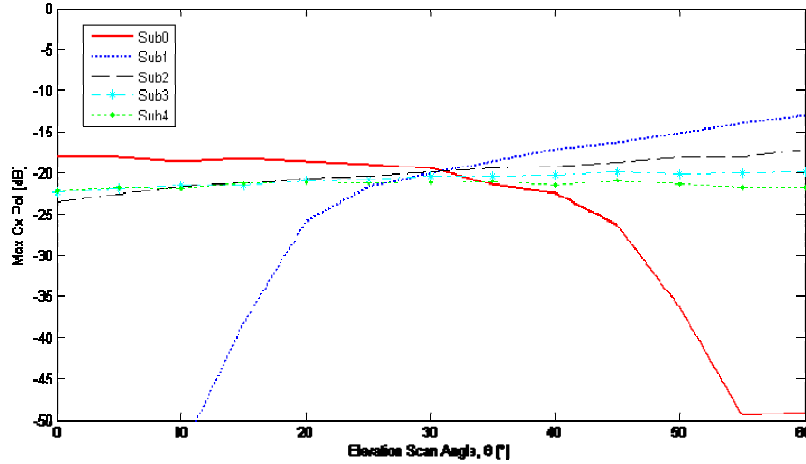


Figure 3.2.2-1 Planar 26 x 32 array Taylor 30 dB $\bar{n} = 4$ max Cx-pol vs. scan angle

3.3 Circular 24" Edge Slot Array

Having established that the trends observed in the smaller planar 12 x 12 array hold true for the larger 24" x 20" planar array with 26 x 32 elements excited with both a uniform and Taylor distribution, a large circular 24" aperture with 782 elements was analyzed with both a uniform excitation and a Taylor (30 dB $\bar{n} = 4$) excitation.

3.3.1 Uniform Excitation

For the uniform excitation case, the maximum Cx-pol versus main beam scan angle for all sub-array configurations is shown in Figure 3.3.1-1. The results are significantly different from those obtained for a planar rectangular array. All sub-array mirroring configurations had a higher Cx-pol at wide scan angles, but there was no more than an 8 dB difference in Cx-pol level over the entire 60° electronic scan. Also, “Sub0” and “Sub1” did not exhibit the significant reduction in Cx-pol seen in the planar rectangular arrays at wide scan and low scan angles respectively.

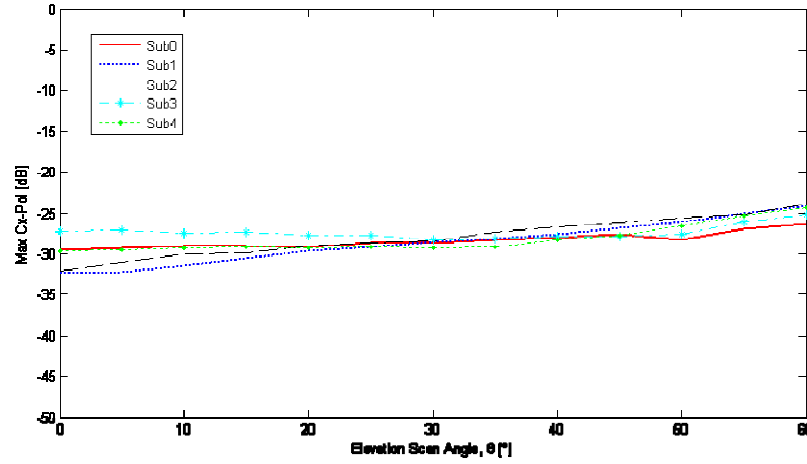


Figure 3.3.1-1 Circular 24" array uniform excitation max Cx-pol vs. scan angle

3.3.2 Taylor (30 dB $\bar{n} = 4$) Excitation

For the Taylor 30 dB $\bar{n} = 4$ excitation case, the maximum Cx-pol versus main beam scan angle for all sub-array configurations is shown in Figure 3.3.2-1. For all practical purposes, there is no significant difference between the Taylor 30 dB $\bar{n} = 4$ excitation and the uniform excitation when it comes to maximum Cx-pol for the different sub-array mirroring variations across 60° of electronic scan.

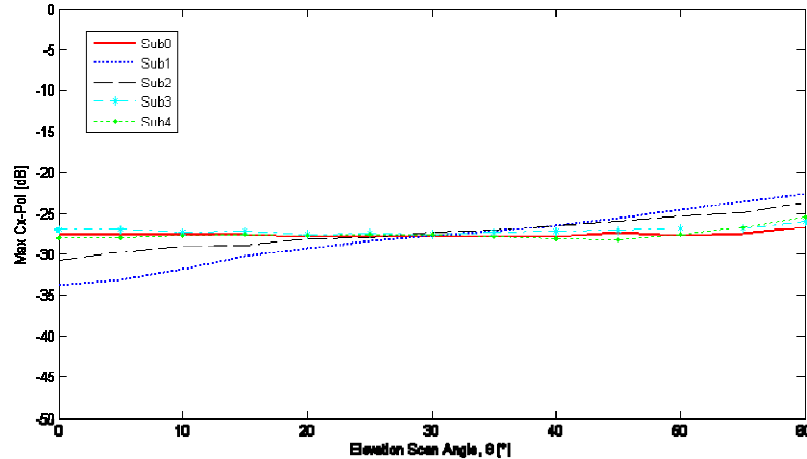


Figure 3.3.2-1 Circular 24" array Taylor 30 dB $\bar{n} = 4$ max Cx-pol vs. scan angle

4 CONCLUSIONS AND FUTURE WORK

The three computational models showed excellent agreement with respect to the effectiveness of sub-array mirroring in the mediation of second-order beams in the Cx-pol of a 12 x 12 edge slot waveguide array.

For a planar rectangular array, the results of both the 12 x 12 and a larger 26 x 32 array indicate that the best choice for 1D electronic scan under 30° is “Sub1”. For electronic scan beyond 30°, the choice for a planar rectangular edge slot array is less clear and would depend on the specific application requirements. The lowest maximum Cx-pol level when scanning from boresight to beyond 30° is likely to be the “Sub3” or “Sub4” variation. Based on the trends of the sub-array mirroring variations, it appears that going beyond a sub-array mirroring of “Sub4” would yield little improvement in the suppression of the max Cx-pol versus electronic scan.

For a circular array, the results of a 24" diameter array with 782 elements indicate that “Sub1” is once again the best choice for 1D electronic scan under 30°. However, its benefit at the low scan angles was not nearly as pronounced as it was in the case of the planar rectangular array. The lowest maximum Cx-pol level when scanning from boresight to beyond 30° is likely to be the “Sub1”, “Sub3” or “Sub4” variation. Again, based on the trends seen in the sub-array mirroring variations, there would be little to no benefit gained by going beyond a sub-array mirroring of “Sub4”.

Future work will consist of building and testing the numerous sub-array mirroring variations described in Table 2.2-1. These tests will validate the results of the computational techniques employed herein. Additionally, the use of a choke in combination with sub-array mirroring should yield even higher mitigation of the Cx-pol without adding to the depth of the array. Therefore, a similar analytical study of the benefit of sub-array mirroring in combination with a choke is warranted.

5 REFERENCES

- [1] L. A. Kurtz, J. S. YEE, “Second-order beams of two-dimensional slot arrays,” *IEEE Trans. Antennas and Propagation*, vol. 5, pp. 356 – 362, Oct. 1957.
- [2] W. L. Stutzman and G. A. Thiele, *Antenna Theory and Design*, 2nd ed. New York: John Wiley & Sons, Inc., 1998.
- [3] Ansoft Corporation; www.ansoft.com

Planar Edge Slot Waveguide Antenna Array Design using COTS EM Tools

M. W. Elsallal, B. J. Herting and J. B. West

Advanced Technology Center

Rockwell Collins, Inc. Cedar Rapids, IA 52498 USA

waelssall @ rockwellcollins.com, bherling @rockwellcollins.com, jbwest @rockwellcollins.com

Abstract: Edge slot waveguide antenna arrays have been extensively employed in surveillance radar application. Despite the long history and use of edge slot waveguide arrays, there still does not exist a comprehensive methodology utilizing commercial off the shelf (COTS) electromagnetic (EM) tools for the accurate and efficient design and analysis of such structures. In this paper, a detailed methodology for the design and analysis of edge slot waveguide antenna arrays is presented. A novel, yet simple, optimization routine that involves modulating the slot conductance by the square of the cosine of the slot tilt angle is shown to result in a better approximation of a given Taylor taper than traditional design techniques. An example is given in which the new optimized slot design results in a sidelobe level (SLL) of -27.7dB compared with -24dB for the traditional design using a desired Taylor 30dB $n_{\bar{n}}$ taper. The paper also extends the incremental slot conductance model suggested by Watson [7] from a regular single stick measured in an isolated environment to a stick inserted in an infinite array analyses that includes the ground plane choke to accurately account for mutual coupling. Such analysis would be time and cost prohibitive if done empirically, but an efficient method using modern COTS EM tools to perform this analysis is presented herein.

1. Introduction

Edge slot array antennas, sometimes called inclined transverse shunt slot antennas, have been used for a variety of radar, electronic warfare (EW) and communication applications because they are easy to fabricate, and they meet the low profile, low cost and low loss requirements [1-4]. Unfortunately, they are difficult to analyze rigorously with theoretical models due to problems in capturing the wall thickness effects and the exterior mutual coupling between slots [5]. Moreover, the published design data and techniques [6,7] are most useful for large edge slot arrays (i.e. many slots per waveguide). This is because the variation in the slot design parameters is minimal in large arrays; thereby the electrical characteristics of neighboring slots are very similar. However, in arrays with few slots, the design parameters can vary significantly from those obtained via traditional techniques making it very challenging to meet the design goals.

Todays' commercial off the shelf (COTS) computational EM (CEM) tools are helpful to gain a better understanding of the electrical characteristics of the edge slots arrays. This paper reports new sets of design guidelines and present several useful insights in how to accurately utilize the empirical incremental conductance models.

2. Design Parameters and Method of Analysis

The design parameters of the edge slot waveguide array are defined in figure 1. Each slot is turned around the center by a tilt angle, ϕ , which in practice could be machined with an end-mill cutter. The slots are excited by the transverse current and load the dominant TE_{10} mode as shunt admittances. In order to establish the pure shunt conductance, the slots are cut symmetrically into the broad faces of the waveguide by depth, δ . The WR90 waveguide wall has a uniform thickness, t , and the slot has a constant width, 62mils.

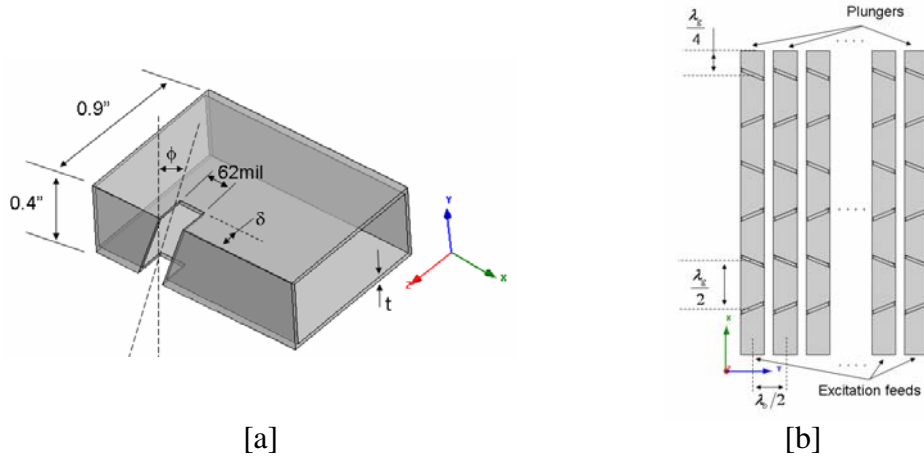


Figure 1: Waveguide antenna structure of inclined edge slots. [a] Isometric view showing the slot parameters in X-band waveguide (WR90). [b] Top view of a rectangular antenna array of edge slots. The E plane is along the waveguide axis (x-axis), while the H plane is along the perpendicular direction (y-axis).

In this paper, the edge slot antenna is a resonant/standing-wave structure, thus a plunger (short circuit) could be placed at multiple odd quarter guide wavelengths (λ_g) away from the center of the last slot. Therefore, the short circuit appears as an open-circuit, and doesn't change the impedance of the waveguide. The mid-band operating frequency is 9.35GHz. In order to feed the slots in phase, they are alternated $\pm \phi$ and spaced $\lambda_g/2$ apart along the waveguide. If the spacing varies, the slots will not be fed in phase and the main-beam along the E plane of the array will be tilted. A picture of the standing wave inside the waveguide where the E-field's maxima couples with the slots was depicted in reference [8]. The waveguide feed can be progressively phased to scan the array along its

H plane, therefore, the sticks are spaced half free-space wavelength ($\lambda_0/2$) apart at the highest operating frequency which is 9.5 GHz, to prevent grating lobes.

In traditional arrays, the antenna element and feed design can be decoupled from one another. However, in the edge slot waveguide array, these components are combined and strongly inter-related in one-body, thus the set of parameters need to be chosen carefully to satisfy all the design specifications.

Three different electromagnetic computational tools were employed to compute the input impedance and the radiation patterns. The primary computational tool for the simulations presented herein was Ansoft HFSS [9]. CST Microwave Studio [10], and Periodic Boundary Finite Difference Time Domain (PBFDTD) [11] were also used occasionally to verify the infinite x finite and the finite x finite array results from HFSS, respectively. All simulated designs were excited by a waveguide port. Perfectly matched layers (PML) were used as radiation boundary conditions.

3. Slot Impedance in Waveguide

The following discussion focuses on designing the slot excitations and calculating the input impedances using the equivalent transmission line model [7,8]. Figure 2 depicts the model of the end-fed resonant waveguide shown in figure 1. In order to calculate precise values for the normalized admittance of individual slots ($Y_n = g_n + b_n$), it is necessary to work with a large number of slots per waveguide. This empirical criterion is called the incremental conductance of the slot [7]. By a proper choice of the tilt angle, ϕ , and depth, δ , the slot admittance exhibits a pure conductance (g_n), figure 3. Based on figure 2, the total input conductance (G_{in}) is the sum of the individual slot conductance. Thus when $G_{in} = 1$, the waveguide is well-matched.

$$G_{in} = \sum_{n=1}^N g_n \quad (1)$$

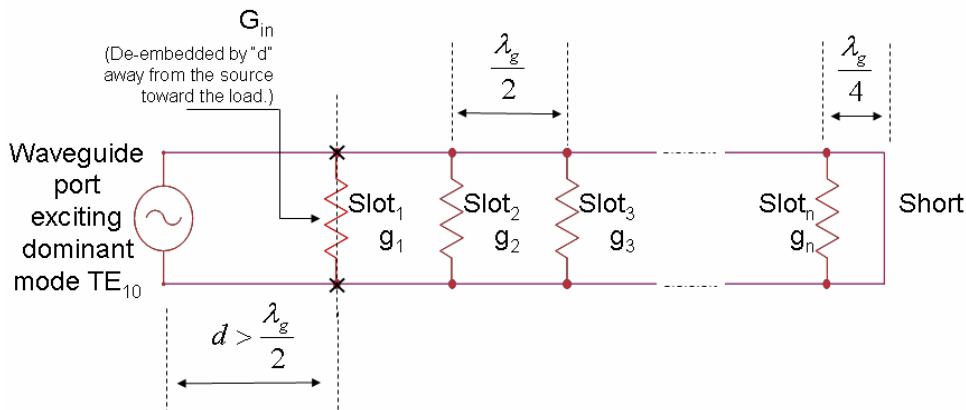


Figure 2: Circuit transmission line model of the edge slot waveguide array.

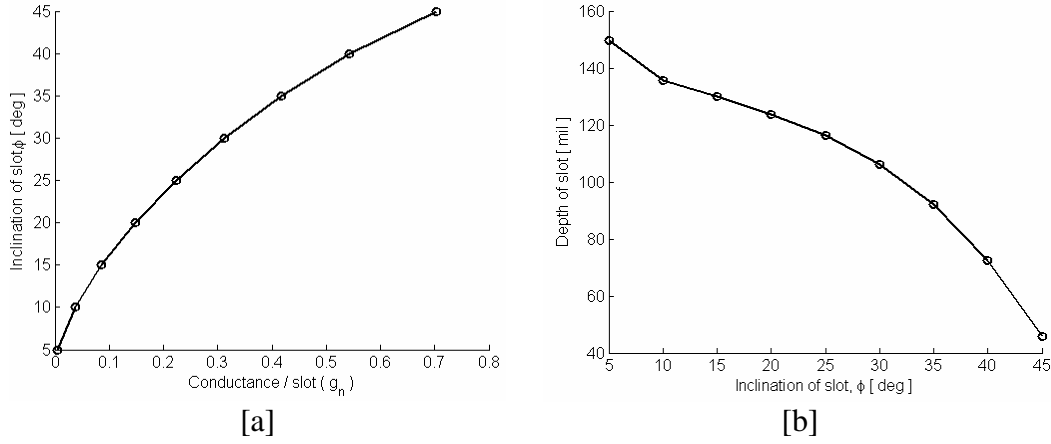


Figure 3: Variation of resonant conductance with: [a] slot tilt angle, and [b] depth. Data collected from HFSS model of single stick of WR90 waveguide (i.e. inside dimensions 0.9"x0.4") with 15 slots. The waveguide wall thickness, $t = 25\text{mils}$. The slot width is 62mils. Frequency of operating is 9.35GHz.

Since the slots should be located on maxima of the standing wave in the waveguide section, each slot radiates a portion of the power P_n . Equation (2) implies that the relative powers of the slots are in the same ratio as their conductance. Therefore the relative slot conductance can be determined from the desired amplitude taper, V_n , using equation (3) [8].

$$P_n = V_n^2 g_n \quad (2)$$

$$g_n = \frac{V_n^2}{\sum_{n=1}^N V_n^2} \quad (3)$$

4. Control of Amplitude and Phase Distribution in Edge Slot Waveguide

Equation (3) was used to determine the excitation coefficient in an edge slot array to realize a 30dB Taylor aperture. A linear array of 12 elements is subdivided into two halves. Therefore, each stick is end-fed and matched for a total of 6 slots, as is depicted in figure 5.

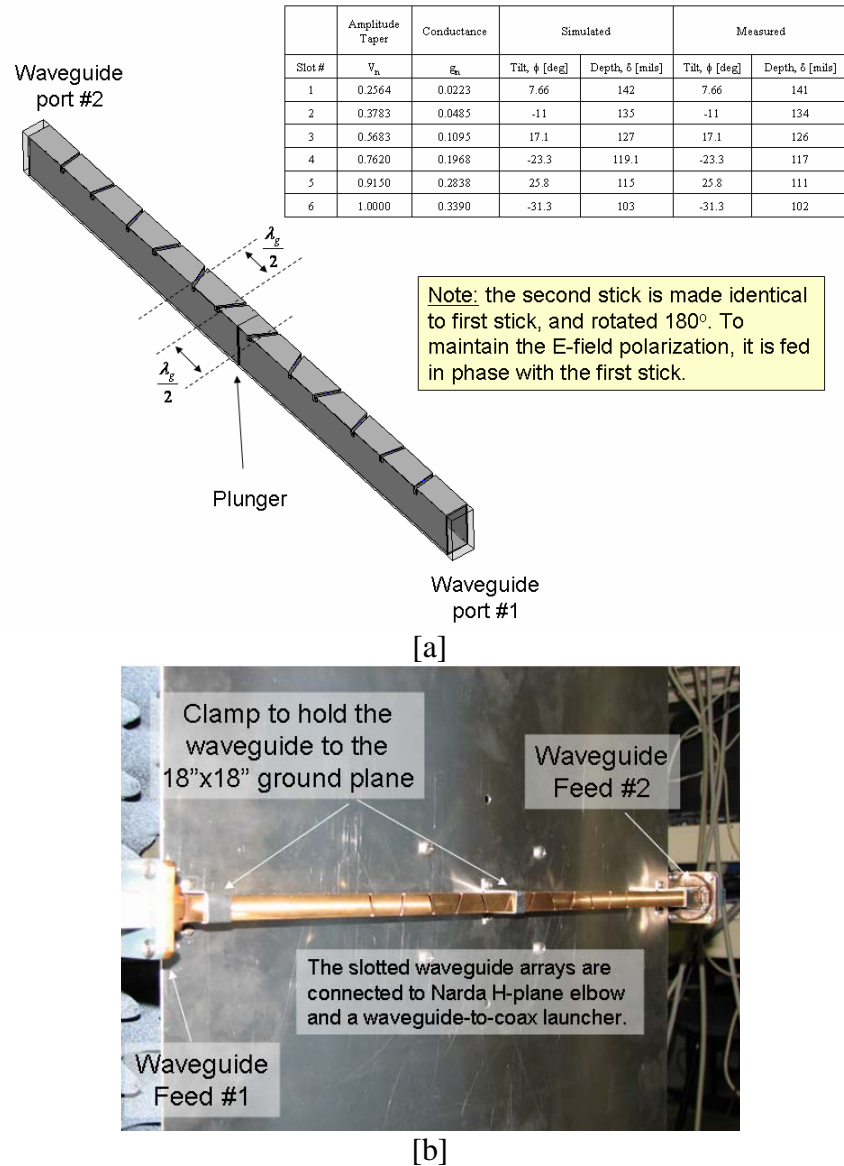


Figure 5: Linear array of 12 elements to realize 30dB n_bar 4 Taylor distribution. [a] Simulated aperture. [b] Fabricated aperture in the near-field range, where all the absorbers are removed for illustration purposes.

The input impedance and near-field and far-field patterns were measured and compared to the HFSS simulated data.

The array has good input impedance $VSWR < 1.2:1$ over the band 9.25 GHz to 9.5GHz, figure 6a. The simulated E-plane radiation pattern predicts a Co-Pol sidelobe (SLL) of about -25dB, while the measured patterns suggest a -20dB SLL, figure 6b. In the legend, the measured farfield (FF) from nearfield (NF) means that the FF pattern was calculated

using the Fourier transform of NF data. The 5dB difference in the SLL is attributed to the 15° phase mismatch at the input port elbows of the fabricated array. This also explains why the pattern is not symmetrical. The phase error was adapted in the HFSS simulated model, and the patterns agreed well. The Cx-Pol, figure 6c, depicts good measurement to simulation agreement. Nulls appear at the Cx-pol maxima ($\pm 45^\circ$), whose location are predicted by Kurtz and Yee [6], due to the rotation of the slots across the y-axis, which results in a difference beam in the Cx-pol.

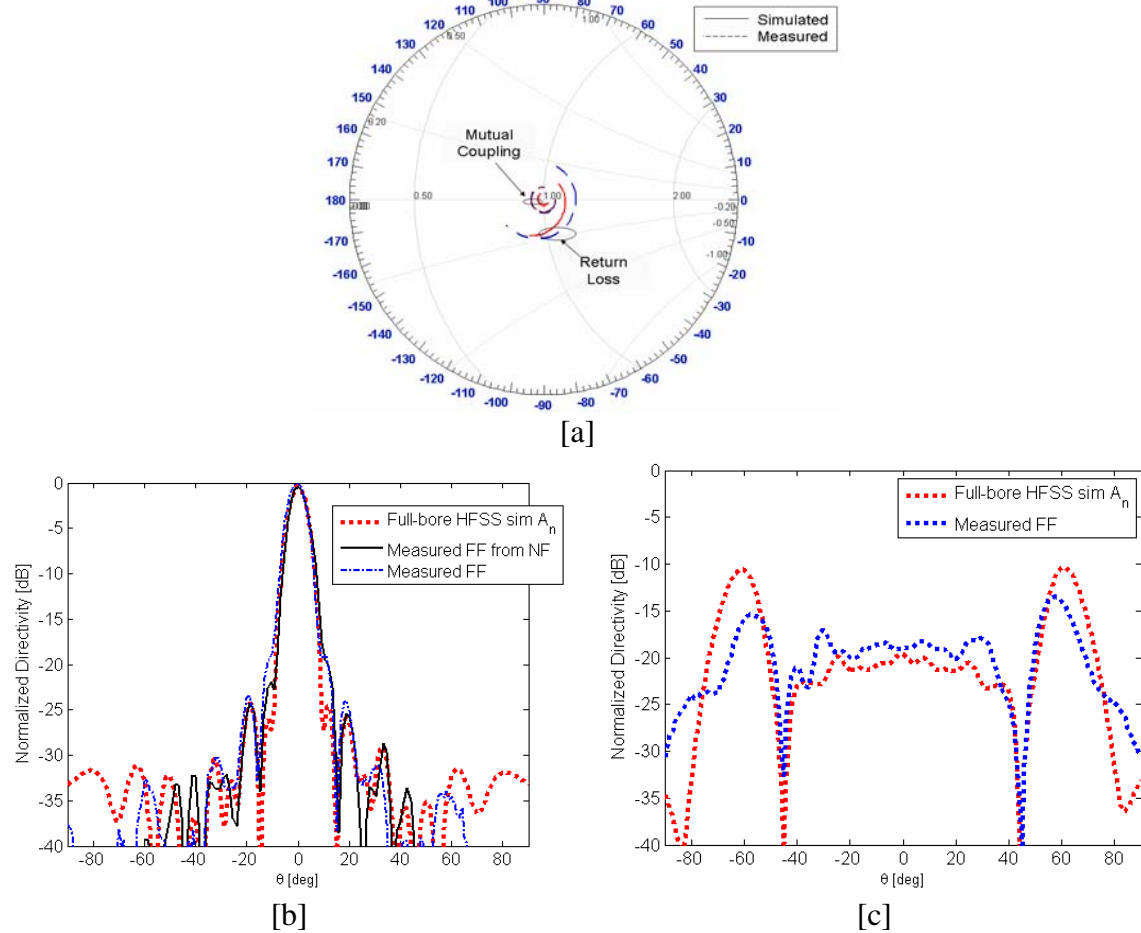


Figure 6: Linear array of 12 elements measurement. [a] Smith chart with return loss and mutual coupling. The scale is zoomed to $0.25 < r < 2$. [b] E plane Co-Pol radiation Pattern. [c] E plane Cx-Pol radiation Pattern.

The slot excitation coefficients (magnitude and phase) were calculated in the HFSS simulated model using Ampere's law, figure 7. The E-field integration line lies at the center of the slot and is tilted in the direction of maximum radiating E-field vectors. The array's NF data was processed along the Hologram at the aperture, and is compared to the calculated HFSS data, figure 8.

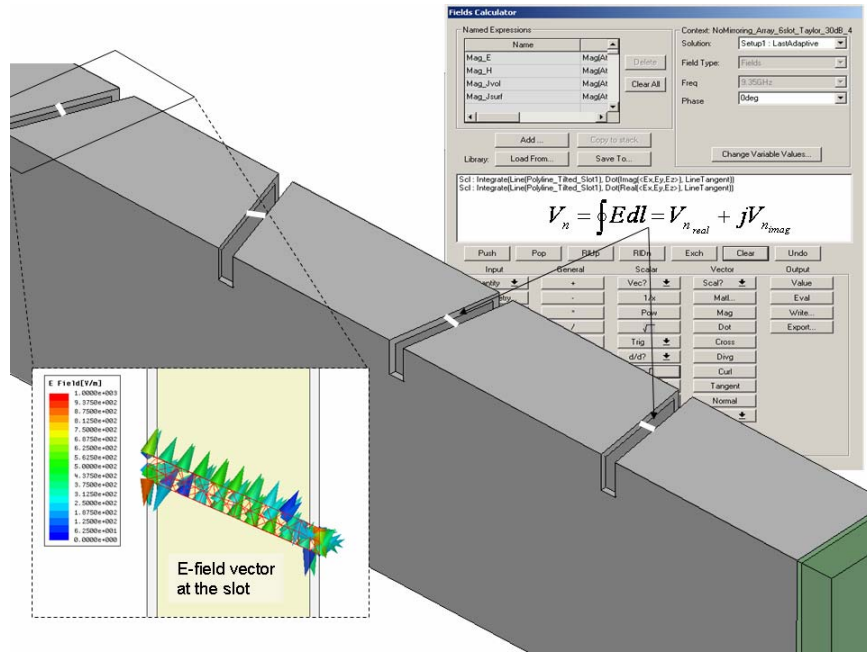


Figure 7: Calculating the excitation at the edge slot in HFSS model. The measurements were conducted at 9.35GHz.

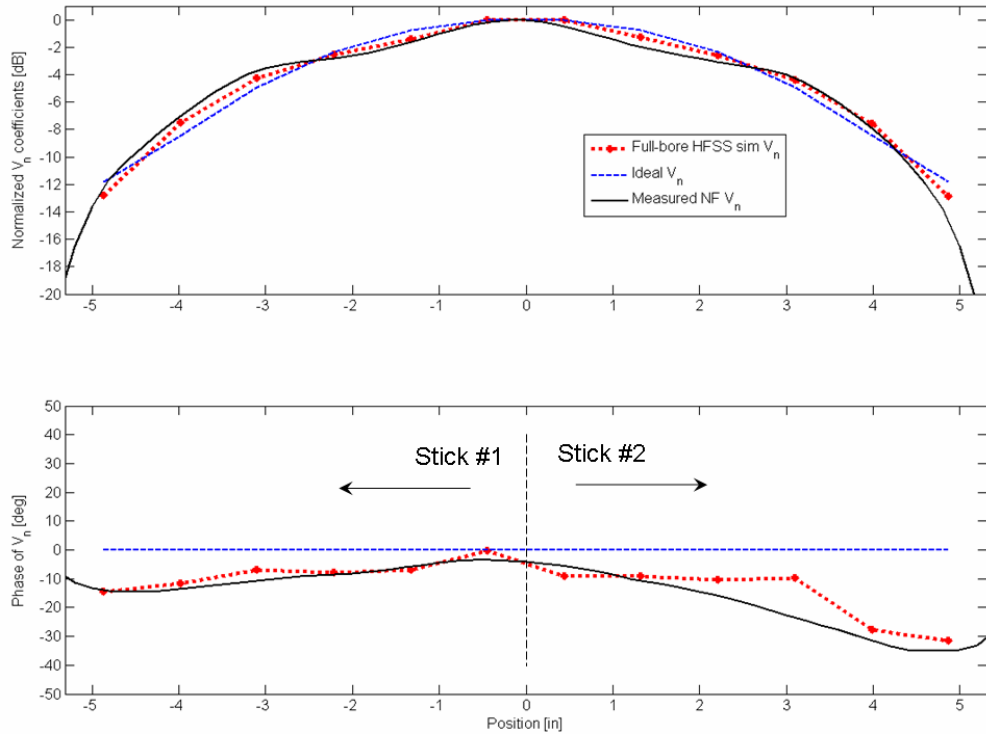


Figure 8: Measured and simulated excitation coefficients at the edge slot array.

The results in figure 8 explain why there is a higher SLL than the desired design-goal, which was -30dB. The conclusion is summarized as follows:

- Errors exist in the magnitude and phase of the slot excitations. When these values are incorporated in an ideal array theory formulation, equation 4, the calculated radiation pattern yields a -26dB SLL. Note, this formulation doesn't account for element pattern, mutual coupling, or slot orientation.

$$AF(\theta, \phi) = \sum_{n=1}^N I_n e^{j(\hat{r} \cdot \vec{r}_n + \alpha_n)} \quad (4)$$

where

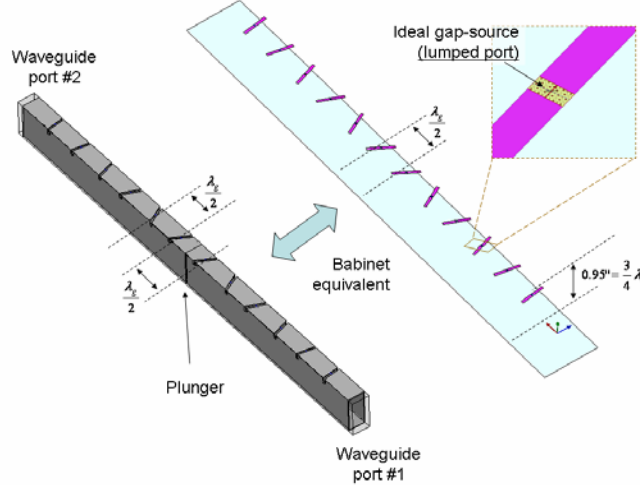
I_n = **magnitude of slot's excitation**

α_n = **slot excitation phase**

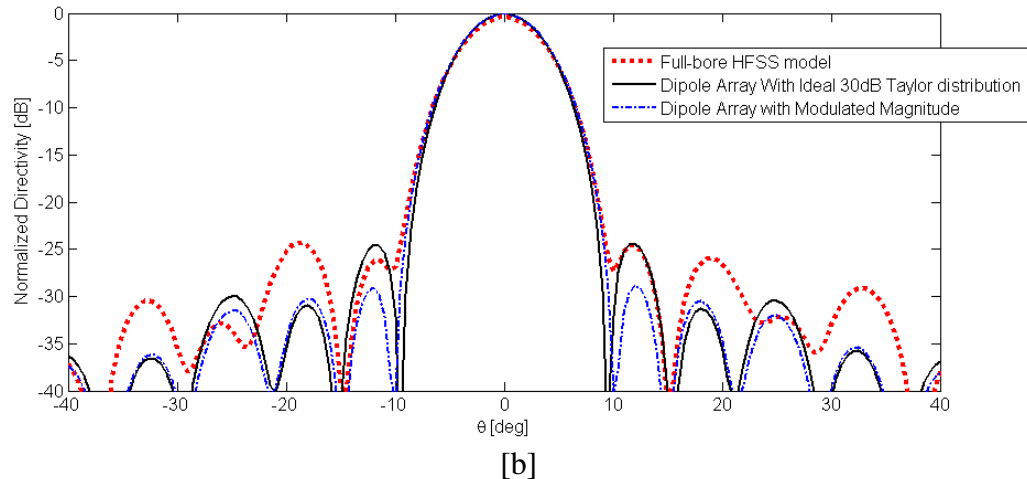
$$\hat{r} = \frac{2\pi}{\lambda_o} [\sin(\theta)\cos(\phi)]\hat{x} + [\sin(\theta)\sin(\phi)]\hat{y} + [\cos(\theta)]\hat{z}$$

$$\vec{r}' = x'_n \hat{x} + y'_n \hat{y} + z'_n \hat{z} \quad (\text{slot location})$$

- The slot excitation phases in the second stick confirm that there is an additional 15° phase mismatch between the sticks.
- In figure 7, it is obvious that the E-field vectors are tilted in conjunction with the slot. In the beginning, however, it was ambiguous whether this tilt would need to be compensated for or not. Thereby, it was necessary to model an array with tilted elements that had an ideal excitation vector, and then examine its radiation pattern. A dipole array suspended 0.95 inches above a ground plane serves as an excellent approximation for just such an experiment because it is the Babinet equivalent of the edge slot waveguide array. The two following studies were conducted:
 - First, the dipoles were tilted in the same fashion seen in figure 5, but excited using ideal-gap sources utilizing the ideal excitation magnitudes and phases of a 30dB Taylor, figure 9. The radiation pattern of this array has maximum SLL resting at -24.3dB.
 - The excitation magnitudes in the dipole array are now modulated by cosine of the tilt, i.e. $V_m = V_n / \cos(\phi_n)$. The new pattern has maximum SLL resting at -28.8dB. It is believed that the remaining 1.2dB variation from the -30dB design-goal is likely due to differences in the element patterns of the array due to the different tilt angles of each dipole (i.e. element pattern is azimuthally dependent).



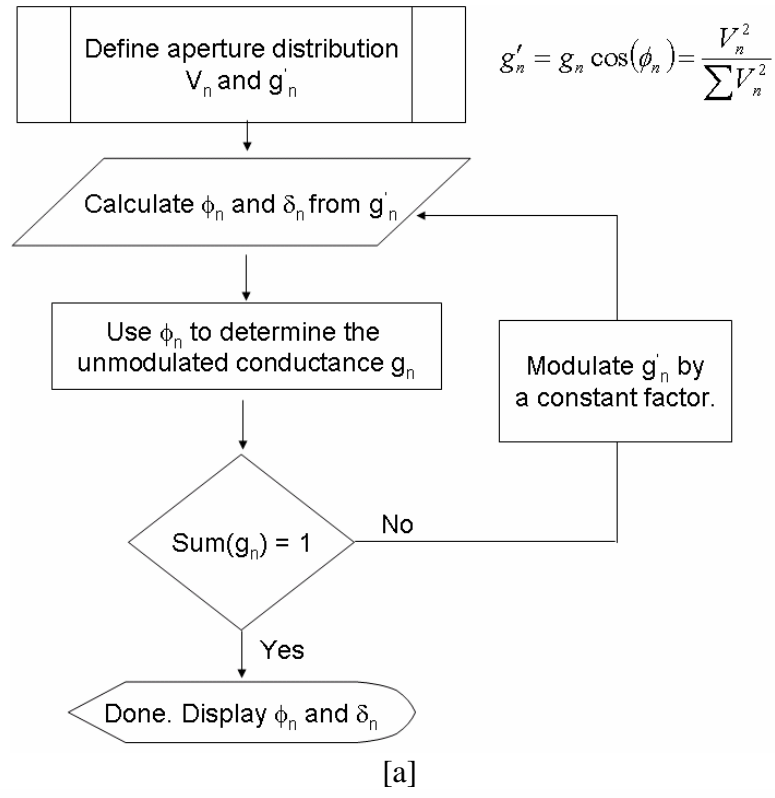
[a]



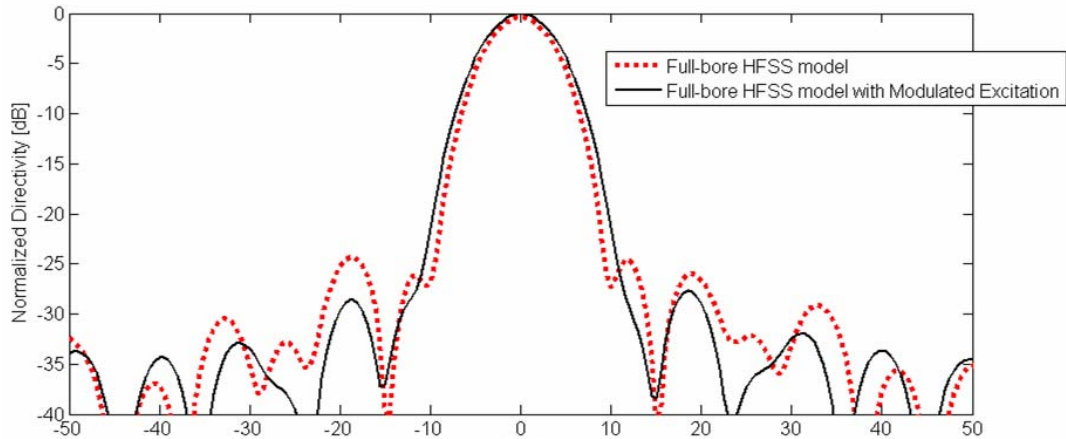
[b]

Figure 9: Investigation whether tilted E-field vector, that causes an increased SLL in the radiation pattern, should be compensated for or not. [a] Utilizing Babinet equivalent to simulate an array of dipole element excited by an ideal gap-sources. [b] Radiation patterns of the edge slot waveguide (E-plane is $\Phi=0\text{deg}$) and dipole (E-plane is $\Phi=90\text{deg}$) arrays. Frequency of operation = 9.35GHz

There is a difficulty in modulating the excited field at the waveguide slot aperture with the cosine of the tilt because the excitation magnitude is strongly related to the slot's tilt and depth. An optimization technique illustrated in figure 10a has helped to find an optimal tilt angle that reduces the maximum SLL from -24dB to -27.3dB. The magnitudes of the excited voltage track well with the ideal array, however the phase distribution is not flat. There is an ongoing investigation to vary the location of the slots to resolve the phase problem. In order to meet the design-goal of -30dB SLL, it is necessary to over-design the array with a -35dB Taylor.



[a]



[b]

Figure 10: An optimization technique to compensate for the tilt effect in the excited slot. [a] Optimization flow chart. [b] Radiation patterns of the edge slot waveguide before and after modulating the tilt effect. Frequency of operation = 9.35GHz

5. Suppression of Second Order Beams in Edge Slot Waveguide

When the linear array is inserted in a planar array environment, the mutual coupling is found to change the electrical characteristic of the excited field at the slot's aperture. Another component that will significantly change the environment surrounding the excited slots is the choke that is traditionally used to reduce the second order beams seen in the Cx-Pol of the array, figure 6. Therefore, the incremental slot conductance design curves presented in figure 3 are not valid for a planar array. Additionally, the curves must be generated with the correct choke height between adjacent waveguides. Therefore, a new model of an edge slot waveguide array is used with 15 slots in a finite x infinite array environment and the choke is also added to optimize the slot's depth and tilt angle for resonance, figure 11.

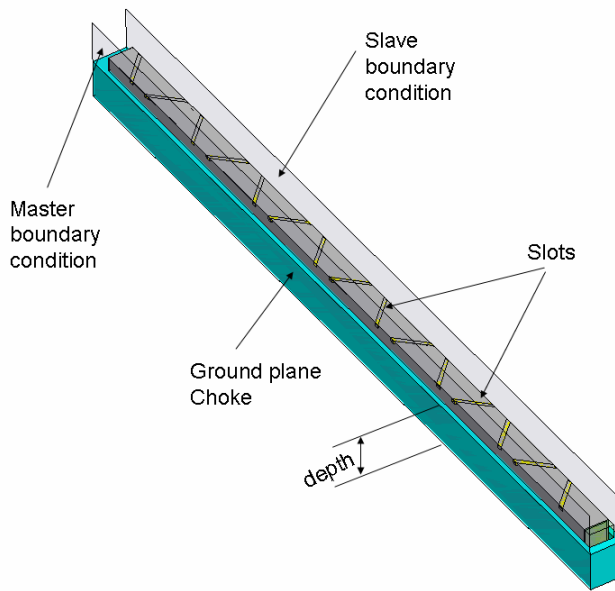


Figure 11: HFSS model for the incremental slot conductance including the mutual coupling from the neighboring waveguide, and the choke.

In order to accurately model all the effects of the surrounding environment, the depth of the choke has to be determined. Traditionally, it was said $\lambda_o/4$ is the optimal depth for the choke [6]. The authors didn't find in literature if this is also true for a small array (i.e. where there are few slots along the guide). Therefore, arrays of 5, 10, 12, 15, 20, 25, 30, 40 and 50 slots were simulated in HFSS using an adjusted depth for the ground plane. The simulations suggest that $0.2\lambda_o$ is the most optimal depth regardless of the size of the array. This depth has been incorporated in the model in figure 11, and the new design curves are depicted in figure 12. The radiation pattern of a 12 slot x 12 stick (similar to that in figure 5) array is shown in figure 13.

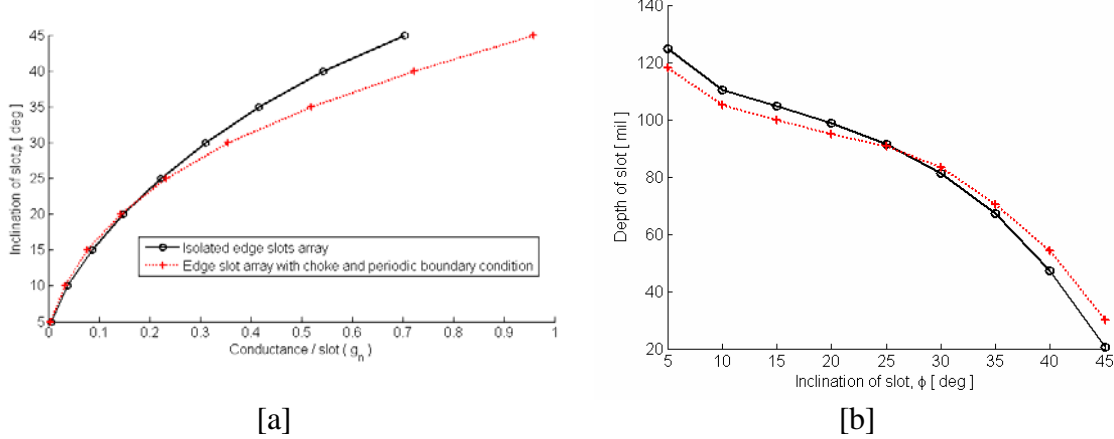


Figure 12: Variation of resonant conductance in the edge slot waveguide array with choke inside an infinite x finite array simulation. [a] conductance vs. slot tilt angle, and [b] slot tilt vs. depth. Data collected from HFSS model of WR90 waveguide (i.e. inside dimensions 0.9"x0.4"). The waveguide wall thickness, $t = 25$ mils. The slot width is 62mils. Frequency of operation is 9.35GHz.

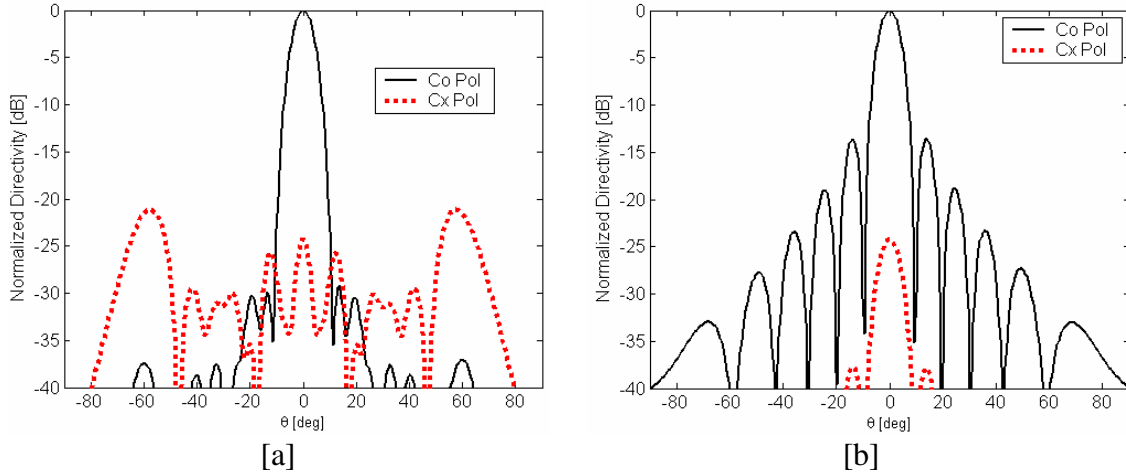


Figure 12: Radiation pattern of the 12x12 array using the incremental conductance model shown in figure 12, and the optimization technique described in figure 10. [a] E plane cut of the array. [a] H plane cut of the array. The array is uniformly excited in the H-plane, therefore, the sidelobe level is about -13.3dB.

6. Conclusion

Understanding the theory behind the edge slot waveguide array, and utilizing COTS EM tools to gain more insight, this paper suggested a new, yet simple design methodology for edge slot arrays that demand low sidelobe levels. A -30dB SLL was desired in a linear array of 12 slots. The Taylor amplitude coefficients were determined and the design was

performed using traditional text book techniques. The resulting array only had a -24dB SLL. When the optimization technique, proposed herein, was employed, the SLL was lowered to -27.7dB. Over-designing the array was suggested for meeting the SLL design-goal because of the presence of an error associated with an incorrect phase taper, as well as different element patterns due to the different tilts on the slots along the guide. This optimization technique is also believed to be applicable to large arrays. The paper concludes with recommendation to use CEM tools to model and design what seems to be time and cost prohibitive in the lab, i.e. the practical array environment: mutual coupling from neighboring waveguide elements, chokes, baffles .etc. Then the incremental slot conductance model should be utilized to obtain new design curves of the slot tilt and depth. The choke in the ground plane should always be set to $0.2\lambda_0$ to maximize the mitigation of the second order beams in the Cx-Pol, sometimes those beams are called the butterfly patterns. Finally, the optimization technique was used to design a finite 12 x 12 array with a ground choke to meet the design goal of -30dB SLL in the E-plane of the array.

7. Acknowledgment

The authors thank Bret Spars and Mike Davison who built and measured the arrays. Their contributions have been valuable in this work and are greatly appreciated.

References

- [1] D. J. Lewis, P. J. Gibson, and D. K. McCarthy, “A Single-Plane Electronically Scanned Antenna for Airborne Radar Application,” pp. 366-370 in “Practical Phased-Array Antenna Systems,” by Eli Brookner. Artech House. December 1991.
- [2] P. James, “A Waveguide Array for Unmanned Airborne Vechile (UAV),” IEE International Conference on Antennas and Propagation, 17-20 Apr. 2001, pp.810 – 813.
- [3] R. B. Gosselin, S. E. Seufert, L. R. Dod, “Design of Resonant Edge-Slot Waveguide Array for Lightweight Rainfall Radiometer (LRR),” IEEE Proceeding of Geoscience and Remote Sensing Symposium, v.1, 21-25 Jul. 2004, pp. 509-511.
- [4] R. Kinsey, “Monopulse Stick Phased Array,” Antenna Application Symposium, 20 Sept. 1995..
- [5] J. C. Young, J. Hirokawa and M. Ando, “Analysis of a Rectangular Waveguide, Edge Slot Array With Finite Wall Thickness,” IEEE Trans. on Antennas and Propagation, Vol. 55, No. 3, Mar. 2007, pp.812-818.
- [6] L. A. Kurtz, and J. S. Yee, “Second-Order Beams of Two-Dimensional Slot Arrays,” IEEE Trans. on Antennas and Propagation, Vol. 5, No. 4, Oct. 1957, pp.356-362.

- [7] W. H. Watson, "Resonant Slots," IEE Journal, Vol. 93, Part 3A, pp.747-777.
- [8] R. B. Gosselin, "A Computer-Aided Approach for Designing Edge-Slot Waveguide Arrays," Antenna Application Symposium, 20 Sept. 2001.
- [9] Ansoft Corporation; www.ansoft.com
- [10] CST, Inc.; www.cst.de
- [11] PBFDTD v4.0 by Dr. Henry Holter.
- [12] B. N. Dan, J. Ramakrishna and B. K. Sarap, "Resonant Conductance of Inclined Slots in the Narrow wall of Rectangular Waveguide," IEEE Trans. Antenna Propagation, vol.32. pp. 759-761. July 1984.

A Cross-Flux Method for Coupling Prediction of Two Installed Antennas

C. C. Lu

University of Kentucky

Lexington, KY 40506

Abstract

Prediction of two installed antenna's coupling is important for antenna placement, installation, and interference analysis. The coupling can be described in several different ways, such as the mutual impedances, etc. In this paper, a cross-flux approach is presented to predict the coupling coefficients of two normalized antennas (one transmitter and one receiver). This coefficient is expressed as a cross flux integration of two fields over a closed surface that encloses the receiving antenna. One field is generated by the receiving antenna in stand alone status, and the other is generated by the transmitting antenna in the presence of the platform on which the two antennas are installed. The first field is either user-provided or determined by a full-wave solver, and the second field may be determined by a full-wave solver or by other asymptotic methods when needed. The multilevel fast multiple is applied to calculate the near-field from the currents on the antennas as well as on the platform. This coupling coefficient is very close to the mutual impedance provided by the formula of induced EMF. Numerical results are provided to demonstrate the effectiveness and applications in solving large scale antenna coupling problems.

I. Introduction

Antenna coupling prediction is useful for EMC/EMI and antenna placement applications. The coupling between two antennas is generally described using circuit parameters such as the mutual impedance (Z_{12}) or S-parameter (S_{12}) [1-8]. These parameters are well defined and easy to evaluate for wire antennas or for antennas with a known driving mechanism. They are often expressed as integrations over the antennas' surface with the assumption of known antenna surface current. For example, in [10], the mutual impedance of two slender wire antennas is derived as a line integration of the product of transmission antenna's field and the current over the receiving antenna. For near-field coupling of two antennas, reference [8] presented an efficient method which can be applied to calculate coupling of two antennas in arbitrary orientation and distances using far-field information. However, it is not applicable to antennas that are installed on complex platforms. In some applications, one may not have an explicitly defined driving point (such as an ideal dipole) or it is simply unknown. For example, when antenna radiation patterns are given instead of the detailed antenna structure, one cannot use the traditionally defined mutual impedance or S-parameter to predict the coupling. In this case, coupling defined by field alone shall be used. There are at least two such formulations. One formulation, developed by Richmond [15], defined the mutual impedance in terms of two fields of the two coupling antennas; the other one defined a coupling coefficient in terms of the cross-flux integration over the fields of transmitting and receiving antennas. The results from the two formulations are essentially proportional to each other.

The cross-flux formulation [11-14] is applied in this paper to predict the coupling of two installed antennas. This formulation is based on the field concept, and hence, it can be used to a broader range of cases compared with the formula based on the circuit parameters. The definition uses the fields of the two antennas involved, and the antennas' detailed structures are not necessarily needed. In particular, it can define the far-field coupling when only the antenna patterns are given (this is not the restriction of cross-flux formulation, though; it is the restriction of the pattern definition). Moreover, it can be shown that cross-flux definition of coupling is related, or proportional to that given by circuit definition for many antennas. In the following, we first present the coupling formulation based on the cross-flux concept, and then discuss several

special cases and derive simplified coupling coefficient expressions associated with those cases. Numerical results will be provided to show some applications as well as to compare with the mutual impedance results. The equations in the formulation are given in frequency domain with an implied time factor of $\exp(-j\omega t)$.

II. Formulation

We use the ideal sources and ideal meters as defined in [11, p.2-29, p.2-30] to explain the field formulation of antenna coupling. The connections of the source to a transmit antenna and the meter to a receiving antenna are shown in Fig. 1. Let (a, b) be the two opposite directed wave amplitudes in the feed line of an antenna. Here a is for the wave from source to the antenna, and b for the reflected wave (from antenna to the source). When an ideal amplitude source is connected to a Tx antenna, we have $a = 1, b = 0$ (the source's output impedance is matched to the feed line, but the Tx antenna input impedance is not necessarily matched with the feed line). When an ideal amplitude meter is connected to an Rx antenna, we have $a = 0, b = \text{received wave amplitude}$ (again, the amplitude meter is matched with the feed line, but the Rx antenna input impedance is not necessarily matched with the feed line).



Fig. 1. The definition of (a) an ideal amplitude source (circle) connected to a Tx antenna by a feed line; and (b) an ideal amplitude meter (square) connected to an Rx antenna via a feed line. Both meters are matched to the feed line (antenna impedances are not necessarily matched to the feed line).

Consider the configuration in Fig. 2, in which two antennas (one as a transmitter and the other as a receiver) are installed on or placed near a complex platform. Both the antennas and the platform are placed in a free-space with background material of ϵ_0, μ_0 . For the purpose of

illustration, it is assumed that the receiving antenna (Rx) is not in direct contact with the platform. This restriction will be removed later when a deformed surface is introduced. The dash line in the figure around the Rx antenna indicates an artificial 3D that satisfies two conditions: (a) it is a closed surface, (b) it encloses Rx, but excludes the transmitting (Tx) antenna and the platform. Both the transmitting antenna and the receiving antenna are normalized in such a way that each will radiate one watt of power when operates alone in free-space.

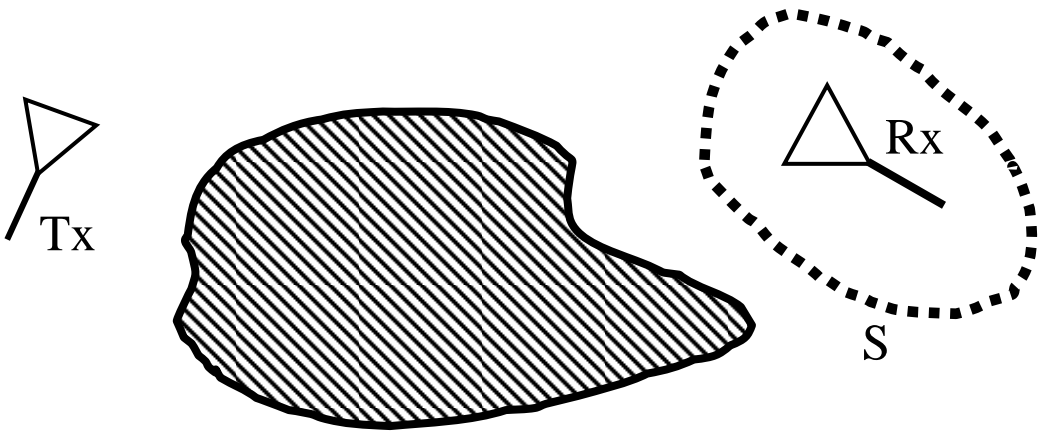


Fig. 2, Sketch of a transmitting antenna (Tx) and a receiving antenna (Rx), both are installed on a platform. The dash line indicates an artificial closed surface S which encloses Rx, but does not include the platform and the Tx.

We consider two situations: (1) Tx in transmission situation (Fig. 3a). In this case, the Rx is removed, and the Tx is connected to an ideal source, radiates in the presence of the platform. The field generated in this situation is (\vec{E}_1, \vec{H}_1) . (2) Rx in transmission situation (Fig. 3b), in which Tx and the platform are removed, and Rx radiates alone in free-space. The field produced is (\vec{E}_2, \vec{H}_2) . The cross-flux of the two fields on an artificial surface, which encloses the Rx antenna but excludes Tx and the platform, is the coupling between the two installed antennas. It is given as a surface integration in [11],

$$b_4 = \frac{1}{4a_1} \oint_S (\vec{E}_1 \times \vec{H}_2 - \vec{E}_2 \times \vec{H}_1) \cdot d\vec{S} \quad (1)$$

where, b_4 (Watt) $^{1/2}$ is the output (reading) of an ideal amplitude meter connected to Rx. It is a complex number that has both amplitude and phase. The coefficient a_1 is the excitation amplitude of Tx antenna which is set to 1 (Watt) $^{1/2}$ by definition. It is placed in the equation to indicate the unit of b_4 . Since $a_1 = 1$ by definition, it will be ignored in the following expressions. The elementary vector surface $d\vec{S} = \hat{n}dS$, with \hat{n} directing outward the surface. A factor of (1/4) appeared in Equation (1) instead of the (1/2) coefficient as in Equation (84) in [11, p. 2-32]. This is due to the fact that the rms values were used in [11], and the peak values are used in this paper for the electric and magnetic fields. It is emphasized that the integration in (1) does not depend on the shape and size of the surface, as long as it satisfies the conditions (closed surface enclosing Rx but excluding Tx and the platform). An example is given in the next section to verify this. Except for a scaling constant, Equation (1) also resembles the mutual impedance formula derived by Richmond in [15, Equation.(8)].

Since there are no analytical expressions for the fields in practical applications, the surface integral in Equation (1) is often evaluated numerically. A straightforward approach for performing the integration is to represent the surface as a mesh, i.e., a collection of many small elementary shapes such as triangles and quadrangles. Let S_n be an element, then, $S = \bigcup S_n$.

Under this circumstance, we have

$$b_4 = \frac{1}{4} \sum_{n=1}^N \oint_{S_n} [\vec{E}_1 \times \vec{H}_2 - \vec{E}_2 \times \vec{H}_1] \cdot d\vec{S} \quad (2)$$

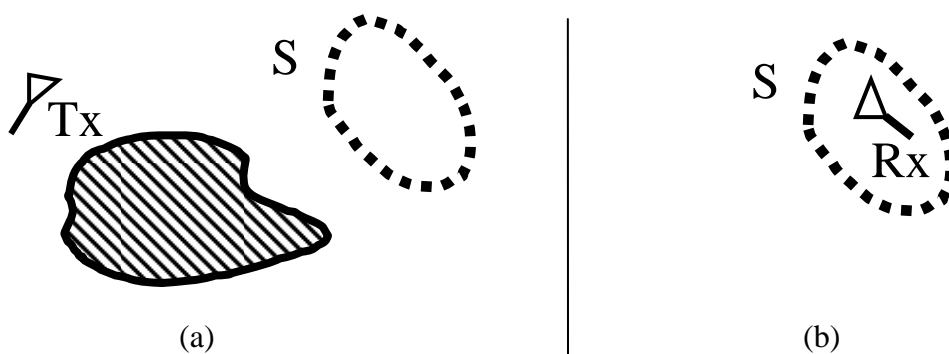


Fig. 3. Definition of two fields on the artificial surface S : (a) Field (\vec{E}_1, \vec{H}_1) is generated by Tx in the presence of the platform (but in the absence of Rx), (b) Field (\vec{E}_2, \vec{H}_2) is the radiation by Rx alone.

It must be pointed out that

- (1) The coupling coefficient b_4 is derived for two antennas radiating alone in free space. When they are installed on or placed near a complex platform, the formula still applies when the platform is lossless and contains only linear material (for which the reciprocity theorem holds). When the platform contains lossy material, the coefficient given by Equation (1) is only an approximation. However, in this case, modification can be made to remove this restriction, i.e., we treat the platform as part of the Tx antenna, and hence the Tx normalization coefficient has considered the power absorption of the platform material.
- (2) The surface enclosing the Rx antenna can be union of multiple closed surfaces. This is useful when Rx is an antenna array that is made of multiple elements. In this case, we can use one closed surface to enclose the entire array, or use one closed surface for each of the elements of the array. In the latter option, the surface S in Equation (1) is the union of all the sub-surfaces for each element.
- (3) Moreover, in case the Rx is in contact with the platform (which is true in many applications), part of the integration surface will coincide with the platform surface. Under this circumstance, the integration over the coincided portion of the surface will be expressed using the surface current on the platform. Depending on the boundary condition, the electric current, magnetic current, or both may be used to replace the tangential field on the surface.

The cross-flux integration surface may be deformed so that it coincides in part or fully with that of the Rx surface. If Rx antenna surface is perfectly electrically conducting (PEC), then the electric field (\vec{E}_2, \vec{H}_2) satisfies the boundary condition, $\hat{n} \times \vec{E}_2 = 0$ (on S). In this case, the magnetic field boundary condition gives rise to $\vec{J}_2 = \hat{n} \times \vec{H}_2$. As a result, using a vector identity $\vec{A} \cdot (\vec{B} \times \vec{C}) = \vec{C} \cdot (\vec{A} \times \vec{B})$, we can show that

$$b_4 = -\frac{1}{4} \oint_S (\vec{E}_1 \cdot \vec{J}_2) dS \quad (3)$$

where \vec{J}_2 is the surface current density of Rx when it is connected to an ideal amplitude source. The above can often be utilized to simplify the cross-flux integration for antennas with known current distribution. In particular, if Rx is an ideal electric dipole (infinitely short current element) located at \vec{r}_2 , then we have

$$b_4 = -\frac{1}{4} \vec{E}_1(\vec{r}_2) \cdot \hat{p}_2 I_2 dl_2 \quad (4)$$

where \hat{p}_2 is a unit vector that stands for the orientation of the dipole, and $I_2 dl_2$ is the dipole moment. For an ideal dipole of moment $I_2 dl_2$, the radiated power is $P_{rad} = (\eta_0/12\pi)(k_0 I_2 dl_2)^2$ [10]. Since Rx antenna radiation power is normalized to 1 Watt, we can easily determine the dipole moment as $I_2 dl_2 = \sqrt{12\pi/(\eta_0 k_0^2)}$.

Using Equation (4), we can obtain a closed form expression of the coupling coefficient of two ideal dipoles when they are in the far-field of each other. Let Tx dipole be located at the origin and z-directed, and the Rx dipole be located at \vec{r}_2 , then we have

$$\vec{E}_1(\vec{r}_2) = -jk_0 \eta_0 \frac{I_1 dl_1}{4\pi r_2} e^{-jk_0 r_2} \sin \theta \hat{\theta} \quad (5)$$

Using the normalized amplitudes of both dipoles, and applying Equation (4), we get

$$b_4 = j \frac{3 \sin \theta}{4k_0 r_2} \hat{\theta} \cdot \hat{p}_2 e^{-jk_0 r_2} \quad (6)$$

In the above, r_2 is the distance between Tx and Rx. The maximum coupling occurs when Rx dipole is in x-y plane and is also z-directed. In this case, the coupling coefficient is simplified as $b_4 = 0.75 j \exp(-jk_0 r_2)/(k_0 r_2)$, or $|b_4| \approx 0.119 \lambda_0 / r_2$, here λ_0 is the free-space wavelength at operating frequency. As is expected, the coupling amplitude is inversely proportional to the electrical distance of the two antennas if they are in the far-field of each other. This is a useful formula for verification of computer codes.

It is worthwhile to point out that Equation (3) is very similar in format to the expression of the mutual impedance of two wire antennas. In fact, the mutual impedance of two center feed thin wire antennas is given by [9,10,15],

$$Z_{12} = -\frac{1}{I_1(0)I_2(0)} \oint_S (\vec{E}_1 \cdot \vec{J}_2) dS \quad (7)$$

where $I_1(0)$ and $I_2(0)$ are the currents at driving points of the two antennas, \vec{E}_1 is the field generated by I_1 in antenna 1 (Tx), and \vec{J}_2 is the current density on antenna 2 (Rx). Since the electric field \vec{E}_1 by antenna 1 is related to its current by an integral, the mutual impedance in Equation (7) is in fact expressed as a two-fold line integral. It is clear that the coupling coefficient expressed by cross flux for PEC antennas is proportional to the mutual impedance. The proportional constant is

$$\frac{|b_4|}{|Z_{12}|} = \frac{|I_1(0)I_2(0)|}{4} \quad (8)$$

For a center feed half-wave dipole with sine-distributed current, the radiation power is $36.54|I_1(0)|^2$. If the radiation power is set to 1 (Watt) as is defined for the cross-flux formulation, then $I_1(0) = 0.1654$ (A). Hence, the proportional constant given by Equation (8) for two half-wave dipoles is $|b_4/Z_{12}| = 0.00684$, which is -43.3 dB. Result in one of the examples in the next section will verify this fact.

We use a hybrid surface-volume integral equation approach [16,17] to solve the problem of Tx radiation in the presence of a complex platform, and hence to determine the near-field (\vec{E}_1, \vec{H}_1) over the integral sampling points on surface S. One important feature of the hybrid integral equation is the flexibility in handling thin layers of dielectric materials such as appeared as antenna radome. If the platform size is electrically large, a fast iterative solver based on the multilevel fast multipole algorithm [18] is applied.

III. Numerical Results

In this section, some numerical examples are presented as verification and application of the coupling coefficient using cross-flux integration. If not specified, all length units are in meters. The first example considers three simple cases as listed below and shown in Fig. 4. The frequency of operation is 300 MHz for all the three cases.

Case-1: Two infinitely short dipoles. The Tx is at (0,0,0), and the Rx is at (2,0,0). Both are oriented in z-directions. Dash line shows the profile of cross-flux surface.

Case-2: Two wire antennas, both have the same length of 0.48m and with a sine-shaped current distribution: Tx at (0,0,0), Rx at (2,0,0). Both are oriented in z-directions

Case-3: Two wire antennas, both have the same length of 0.48m that are 1.5m above a PEC plate (4m by 4m in size, parallel to x - y plane at $z = -1.5$ m). The Tx is at (0,0,0), and the Rx is at (2,0,0). Both antennas are oriented in x-directions.

For each case, we use seven different cross-flux surfaces to evaluate the coupling coefficient. Among them, three are cubic boxes of different sides, three are spheres of different radii, and one is a conformal surface (the surface that coincide with the antenna surface, in this case, equation (3) is used). The calculated results are listed in Table 1. We can see that for each case, the results are very close to each other for various cross-flux surfaces, indicating that the integration is very stable when surfaces of different shape and size are used for the integration.

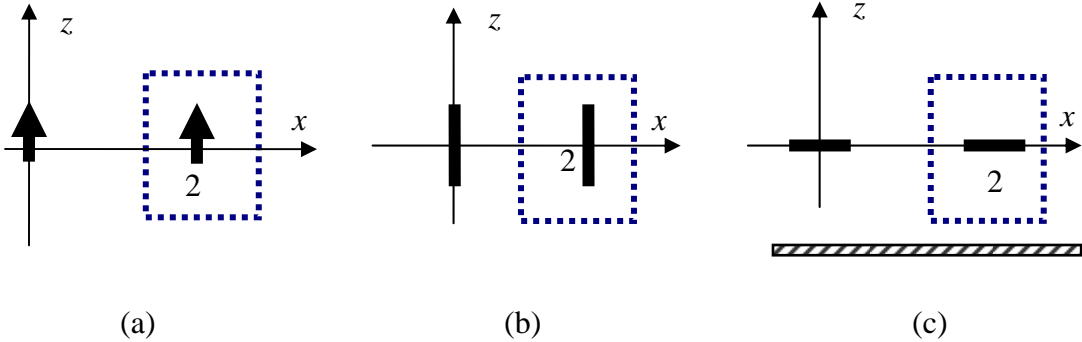


Fig. 4. Three configurations for program verification: (a) Two parallel dipoles, (b) Two parallel wire antennas, (3) Two parallel (co-linear) wire antennas that are 1.5m above a PEC plate of 2 by 2 meters in size. In all three cases, antenna separations are the same and is equal to 2 meters.

Table 1. The coupling coefficient of the antennas in Fig.4.

	CASE-1	CASE-2	CASE-3
Box (Side=1.0m)	-24.76	-24.10	-34.23
Box (Side=1.5m)	-24.60	-23.96	-34.02
Box (Side=2.0m)	-24.33	-23.69	-34.67
Sphere (R=0.5m)	-24.81	-24.17	-34.38
Sphere (R=0.75m)	-24.64	-24.01	-34.37
Sphere (R=1.0m)	-24.52	-23.88	-34.53
Conformal Surface	-24.49	-24.05	-34.33

In the second example, we consider two center-feed half-wave dipoles that are placed near a circular PEC cylinder, as shown in Fig. 5. The cylinder's radius and height are both 1.5m, and is centered on z-axis. At a frequency of 2.0 GHz, the cylinder is modeled by 90,000 flat triangles and 135,000 basis functions are used to express the induced current. The Tx antenna is fixed at (-1.5,0,0), and the Rx antenna shifted from (1.5,0,0) to (1.5,1.5,0). Both of the two dipoles are assumed to have a fixed sine-shaped current distribution (the influence of the antenna-dipole interaction on the current distribution can be considered as small in this case, and hence is ignored). Fig. 6 shows the couplings as function of y-position for two orientations of the antennas. Also shown in the figure are the results when the circular cylinder is absent. It can be

seen that the cylinder significantly affected the coupling between the two antennas. Because of the block by the cylinder, the couplings are very weak. The couplings when the two antennas are in the deep shadow region are more than 20 dB smaller than that when cylinder is absent. The weak coupling is mostly due to the creeping waves excited on the cylinder by the Tx antenna.

In order to compare the coupling coefficient from the cross-flux integration to that of mutual impedance or S-parameter, we use a similar configuration as the previous example. In this case, we use a thinner cylinder (of radius 0.075m) and move Rx antenna along x-axis from $x=0.5\text{m}$ to 2.0m . The frequency of operation is also set to 2.0GHz . We calculate the mutual impedances for the two antennas using the method of moments. Fig. 7 shows the calculated mutual impedance and the cross-flux integration using Equation (1). The mutual impedance is plotted as $20\log|Z_{12}| - 44.1$ (The shift of -44.1dB accounts for the proportional constant. The difference of the proportional constant from that predicted using Equation (8) may due to the facts that (a) the MoM is used in mutual impedance calculation (the current on the dipoles may slightly differ from that of the sine-shaped fixed current for cross-flux calculation), and (b) the prediction in Equation (8) assumes infinitely thin wires. In the MoM modeling in this example, the wire thickness for both the dipoles are the same and equal to 0.0015m (or 0.01 wavelength at 2.0GHz).

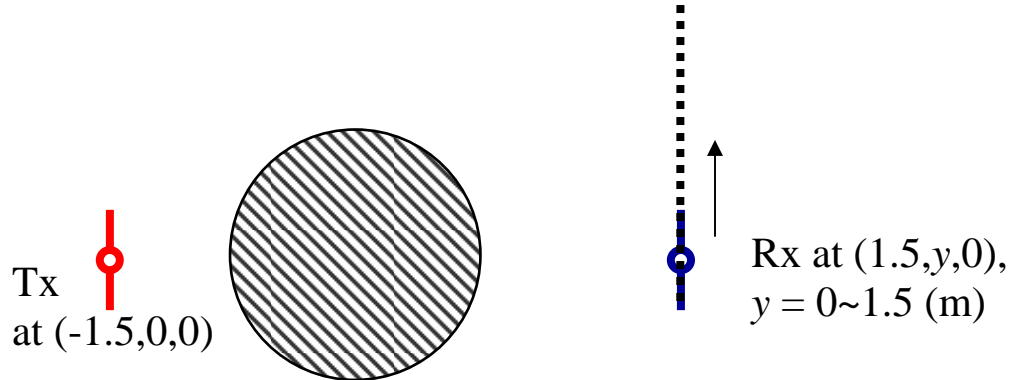


Fig.5. Two half-wave dipoles are placed near a circular PEC cylinder (top view).

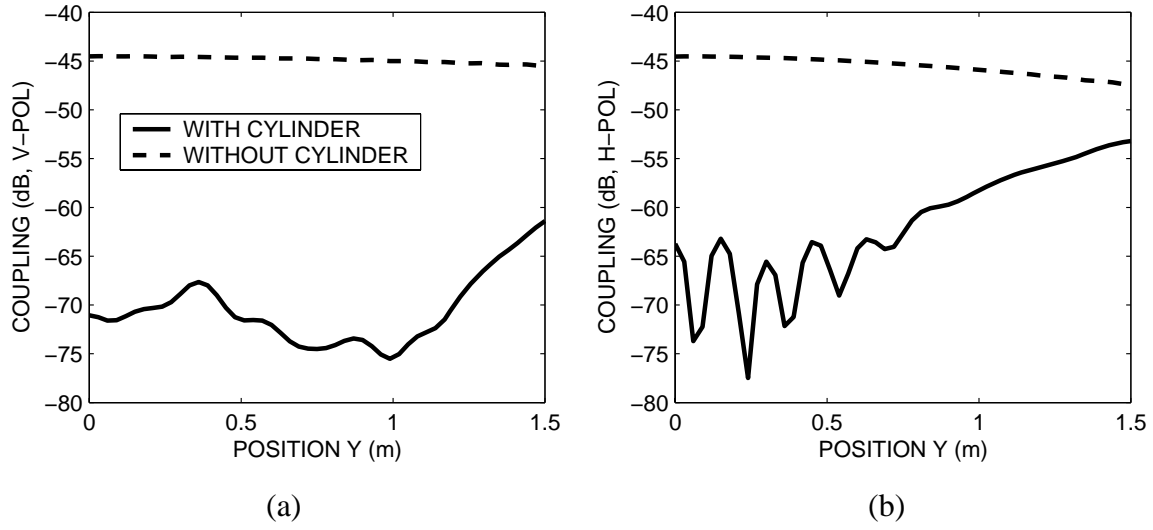


Fig. 6. The couplings of two half-wave dipoles that are placed near a circular cylinder as configured in Fig. 5.

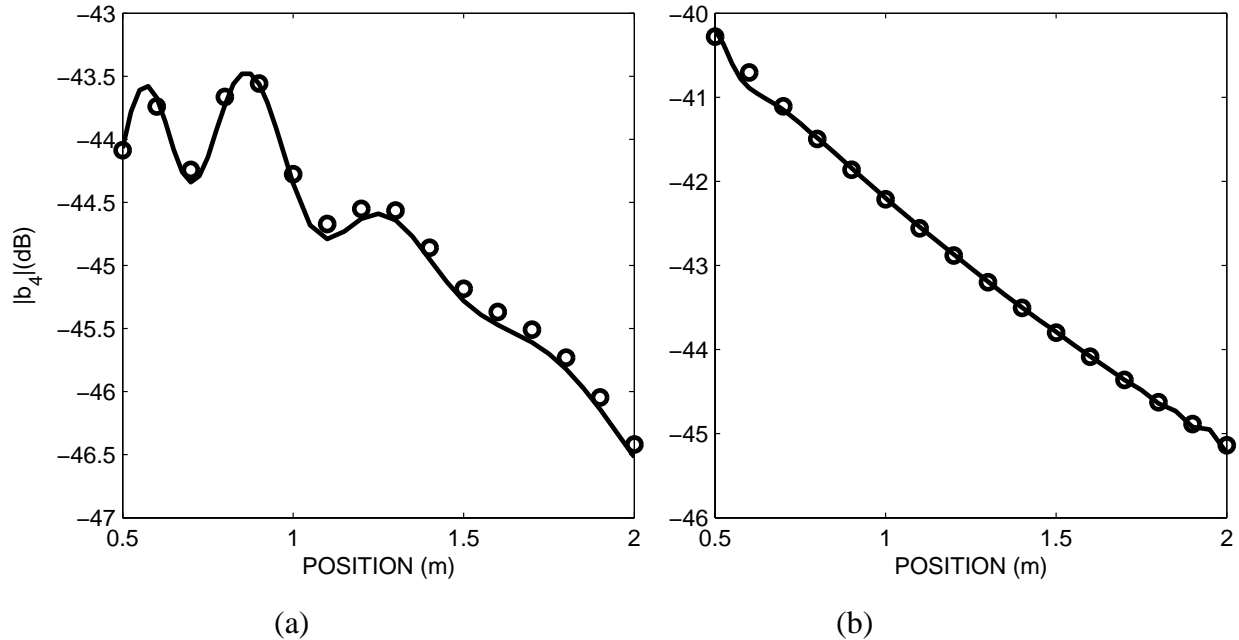


Fig. 7. The comparison of couplings as function of separation distance calculated using cross-flux integral (solid line) and the $|Z_{12}|$ (circles, shifted by -44.1dB) calculated by MoM: (a) dipoles are parallel to z-axis (also the cylinder axis), (b) dipoles are parallel to y-axis (perpendicular to x-z plane).

In the last example, we show the coupling of antennas that are near to a model airplane (VFY218). As shown in Fig. 8, the Tx antenna is a z-directed dipole that is placed a quarter wavelength above a PEC circular plate of radius 0.203m. A hemispherical dielectric shell is placed above the plate to serve as an antenna radome. The shell has inner radius 0.203m, and a thickness of 0.0254m. The dielectric's relative permittivity is (2.3,-0.5). The integral equation of the airplane-plate-radome system used 193,864 triangles (for the airplane and the plate) and 225 hexahedron element for the radome material. Total number of unknowns is 291,696. The Tx is fixed on top of the fuselage of the model at a coordinate (-1.27,0,0.58). Rx moves along a straight line from (-8.89, 2.286, -1.3716) to (8.89, 2.286, -1.3716). This receiving path is just slightly above the left wing and is slightly below the canard wing. We consider two cases of Rx antenna: (a) a half-wave dipole oriented in z-direction, and (b) an array of two half-wave dipoles oriented in z-direction. In the array case, the two elements are of the same amplitude, separated by a quarter of a distance, and with a phase difference of 90 degrees. In this case, the array pattern has a peak in $-x$ direction, and a null in $+x$ direction. The calculated coupling coefficients are shown in Fig. 9. The coupling coefficients in the absence of the airplane are also plotted in the figures. It can be seen that the coupling is greatly reduced in the position range from 0 to 2m. This is due to the blockage by the canard wing. It can also be seen that due to the non-symmetric pattern of Rx, the coupling is very small in the first half of the path when directed array is used as a receiver and the pattern is pointing toward $-x$ directions.

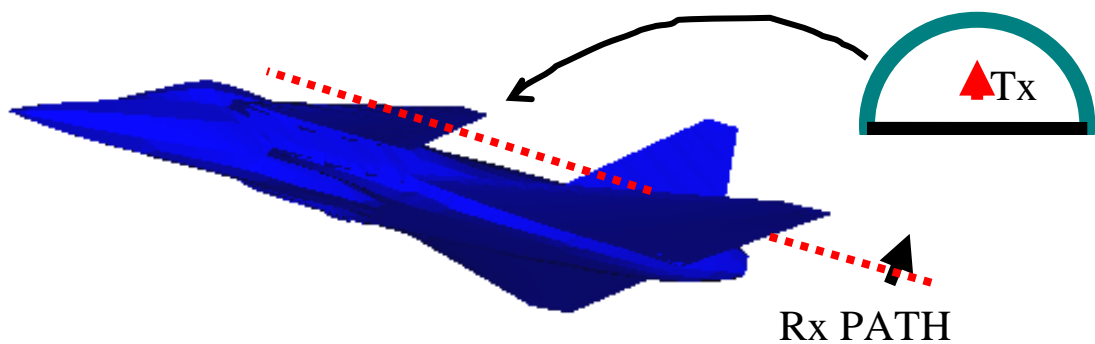


Fig. 8. Two antennas near a model airplane (VFY218). The dash line indicates the path of the receiver (Rx) which is just slightly above the left wing. The Tx is located inside a hemispherical dielectric shell which is closed at the bottom by a circular PEC plate of the same radius.

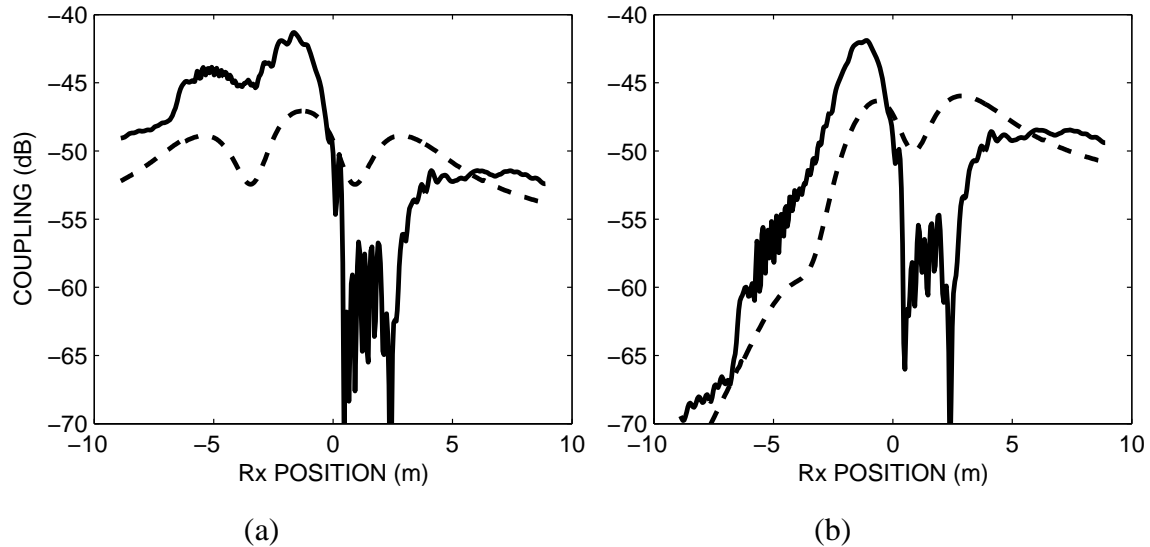


Fig. 9. The coupling of two antennas that are installed on a model airplane: (a) Rx is a half-wave dipole directed in z-direction, (b) Rx is an array of two half-wave dipoles. Dash lines represent the result when the airplane is absent. The x-coordinate of Tx antenna is at -1.27m

IV. Summary

A cross-flux approach is applied to calculate the antenna coupling between two installed antennas. The formulation expresses the coupling as an integral of two fields, one of the field is the radiation of Tx in the presence of the platform, and one by the radiation of the Rx in stand-alone mode. The formulation is valid and accurate if the platform is lossless. For lossy platform, the Tx antenna normalization shall include the absorption of the platform. The cross-flux expression of coupling can be applied to a broader range of applications. It can be used to predict the coupling of two antennas when only the patterns are known. In case of conducting wire antennas, the cross-flux integral is proportional to the mutual impedance integral. Numerical results are provided that show the coupling coefficients from the cross-flux approach are comparable with the mutual impedance.

V. References

1. P. Persson, L. Josefsson, "Calculating the mutual coupling between apertures on a convex cylinder using a hybrid UTD-MoM Method," *IEEE Trans. Antennas and Propagat.*, vol. 49, no. 4, pp. 672-677, April 2001.
2. S. V. Georgakopoulos, C. A. Balanis, and C. R. Birtcher, "Coupling Between transmission Line Antennas: Analytic Solution, FDTD, and Measurements," *IEEE Trans. Antennas Propagat.*, Vol. 47, no. 6, pp. 978-985, June 1999.
3. S. V. Georgakopoulos, C. A. Balanis and C. R. Birtcher, "Coupling Between Wire Antennas: Analytic Solution, FDTD, and Measurements," *IEEE 1998 Antenna and Propagation Society Symposium*, vol. 1, pp. 504-507, June 1998.
4. P. S. Carter, "Circuit relations in radiating systems and application to antenna problems," *Proc. IRE*, vol. 25, pp. 1004–1041, June 1932.
5. S. V. Georgakopoulos, "Coupling between multiple wire antennas on complex structures," M.S. thesis, Arizona State University, Tempe, 1998.
6. E. H. Van Lil, and A. R. Van De Caf'elle, "Transmission Line Model for Mutual Coupling Between Microstrip Antennas," *IEEE Trans. Antennas Propagat.*, Vol. 32, no. 8, pp. 816-821, Aug. 1984.
7. D. Pozar, "Input impedance and mutual coupling of rectangular microstrip antennas," *IEEE Trans. Antennas Propagat.*, vol. AP-30, no. 6, pp. 1191-1196, Nov. 1982.
8. A. D. Yaghjian, "Efficient Computation of Antenna Coupling and Fields Within the Near-Field Region," *IEEE Trans. Antennas Propagat.*, Vol. 30, no. 1, pp. 113-127, Jan. 1982.
9. C. A. Balanis, *Antenna Theory: Analysis and Design*. New York: Wiley, 1997.
10. R. S. Elliott, *Antenna Theory and Design*, IEEE Press, John Wiley & Sons, Inc., 2003.
11. Y. T. Lo and S. W. Lee, *Antenna Handbook*, Vol. 1, Van Nostrand Reinhold, New York, 1993.
12. G. A. Deschamps, "Scattering diagrams in electromagnetic theory," in *Electromagnetics Theory and Antennas*, Part I, E. C. Jordan, Ed., Pergamon Press, pp. 235-251, 1963.
13. M. Gerwell, H. Ling, and S. W. Lee, "Solution of two part scattering problems via the cross-flux," 2004 IEEE Antenna and Propagation Society Symposium, vol. 4, pp. 4164-4167, June 2004.

14. S. W. Lee, H. Ling, C. Lu, and J. Moore, "Cross-flux: a method for hybridizing Xpatch and other codes," *International IEEE AP-S Symposium*, paper no. S001p02a, 4, Washington, DC, July 2005.
15. J. H. Richmond, "A reaction theorem and its application to antenna impedance calculations," *IRE Trans. Antennas. Propagat.*, vol. AP-9, pp. 515-520, Nov. 1961.
16. **C. C. Lu**, "Volume-surface integral equation," Chapter 11 in "Fast and efficient algorithms in computational electromagnetics," Edited by W. C. Chew, John Wiley and Sons, Inc., July 2001.
17. **C. C. Lu** and W. C. Chew, "A coupled integral equation technique for the calculation of electromagnetic scattering from composite metallic and dielectric targets," *IEEE Trans. Antenna Propagat.*, vol. 48, no. 12, pp. 1866-1868, Dec. 2000.
18. J. M. Song, **C. C. Lu**, and W.C. Chew, "MLFMA for electromagnetic scattering by large complex objects," *IEEE Trans. Antennas Propagat.*, vol. 45, no. 10, pp. 1488-1493, Oct. 1997.

Proposed Coincident Phase Center Orthogonal Dipoles

W.R. Pickles and W.M. Dorsey
United States Naval Research Laboratory
Washington D.C. 20375
pickles@radar.nrl.navy.mil and dorsey@radar.nrl.navy.mil

Abstract: Several approaches to designing coincident phase center array antennas are surveyed. A concept for designing orthogonal dipoles with a coincident phase center is investigated. A double Marchand balun is investigated in conjunction with the concept dipole design. Data for a wide range of simulated balun dimensions is presented. The double Marchand balun dipole is investigated outside an array environment without the benefit of mutual coupling. It is found that the double Marchand balun affords very wide bandwidth and flexibility.

1. INTRODUCTION

This paper presents the results of an informal investigation into the possibility of designing coincident phase center dipole antennas. This implies that two “coincident phase center dipoles” can be situated perpendicular to each other with a common physical center, and by extension a common phase center.

There has been an increasing interest in Coincident phase center elements for electronically steered, polarization diverse, ultra wideband array antennas in recent years. This interest has arisen from the difficulty in maintaining the axial ratio of circularly polarized beams when scanning off-axis. When the constituent linear polarizations used to form circular polarization have adjacent phase centers, an angle dependant path length difference is introduced upon scanning. With increasing bandwidth, compensating for this path difference becomes more difficult. The motivation for developing ultra wideband coincident phase center antennas is to eliminate the scan dependant path length difference associated with adjacent phase center antennas.

Once the techniques for coincident phase center design have been developed for ultra wideband antennas, they can be used to redesign narrow band dual polarized antennas. This method is applied to dipoles in this paper. At the same time, some emphasis will be placed on keeping the resulting design simple.

A way to simplify the design of wideband antenna arrays is to use elements which do not

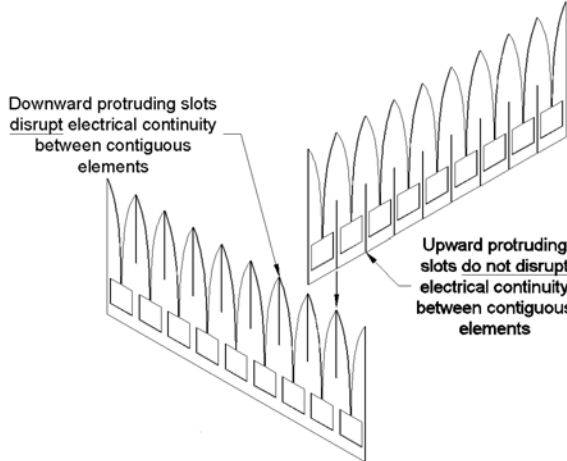


Figure 1 - Interleaving panels of flared notches.

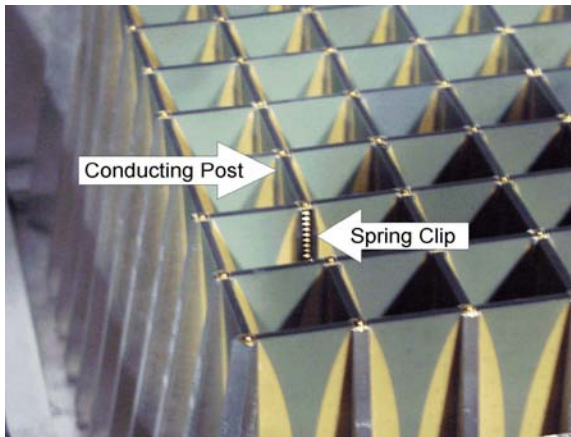


Figure 2 - Flared notch array with spring loaded posts.

have equal continuity and equal performance. The difficulty of this approach is that the posts tend to twist or spread. Regardless of what method is used to maintain electrical continuity between contiguous elements it becomes more difficult at higher frequencies. Manufacturing processes do not scale with frequencies as the frequency becomes too high. For example, consider a flared notch antenna designed for 5 GHZ.

It might have internal striplines with characteristic impedances of 100 ohms that are 6 mils wide, and beryllium copper fingers that are 2 mils thick may be used to fill the interleaving slots between contiguous elements.

Such an antenna could not be scaled to 20 GHZ because 1.5 mil wide stripline, and 0.5 mil thick beryllium copper fingers are prohibitively expensive to manufacture and handle. Herein lies the advantage of dipole elements - there is no conductive contact between

require electrical continuity between contiguous cells. Dual polarized flared notch arrays are commonly constructed in singly polarized panels which are then interleaved. At the lines of intersection between orthogonal panels, slots are cut to permit interleaving. As shown in Figure 1, one polarization has the slots cut from the bottom up to some midpoint while the other polarization has slots cut from the top down to the same midpoint. However, flared notch elements rely on conductive coupling between contiguous elements to achieve wide bandwidths[1]. The polarization with interleaving slots cut from the bottom up has good electrical continuity between contiguous elements. However, the downward protruding interleaving slots in the second polarization disrupt the electrical continuity between contiguous elements in that panel. Some extra effort is required to restore continuity.

Another approach to the continuity problem, employed by NRL and shown in Figure 2, is to construct all flared notches as single polarization modules. At the flare tips where contiguous and adjacent orthogonal elements meet spring loaded posts are introduced. Both polarizations

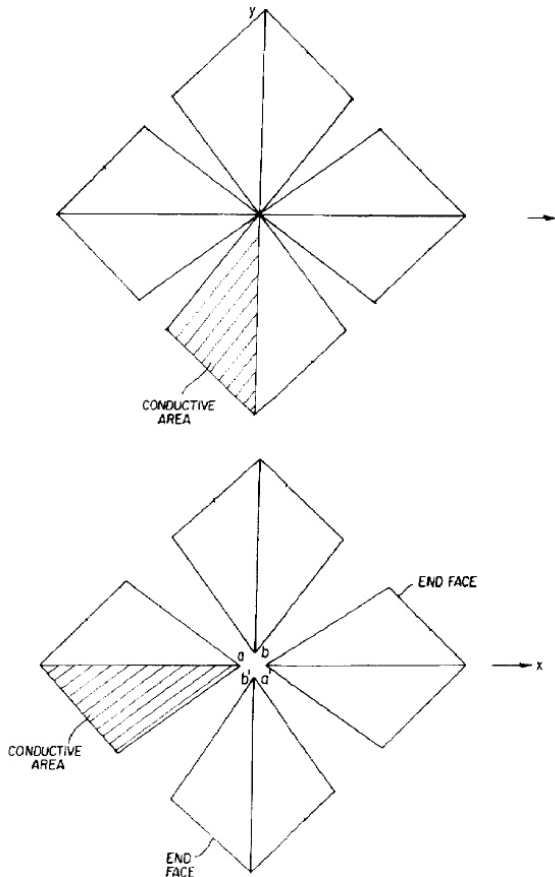


Figure 3 - Elliot's Folded Cross Grid Dipole

In addition, by removing the baluns from the region where they might interfere with the antenna, he obtains another degree of simplification.

The next design to consider is the Wideband Phased Array Radiator by Trott et. al[3]. It is shown in Figure 4. The basic unit cell consists of two orthogonal flared notch elements above a ground plane.

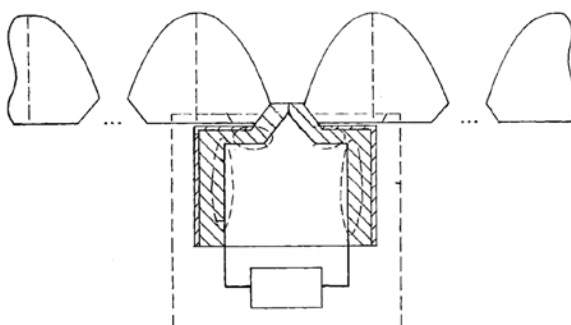


Figure 4 - Trott's Wideband Phased Array Radiator.

adjacent elements, simplifying construction. Unit cells of array can be constructed individually.

2. SURVEY of COINCIDENT PHASE CENTER TECHNIQUES

There are several coincident phase center antennas which might be considered as starting points for a coincident phase center dipole antenna. The first design to consider is Elliot's Folded Cross Grid Dipole[2] shown in Figure 3. Elliot does not refer to his design as a coincident phase center antenna, rather he mentions that it is useful for generating circular polarization. The terminals of Elliot's antenna are a pair of coincident balanced transmission lines which come out from behind the ground plane but he does not include a balun. Since Elliot claims to achieve an octave bandwidth, designing baluns or 180 degree hybrid couplers for his antenna should not be difficult. With a moderate dielectric constant substrate, there is plenty of space.

The next design to consider is the Wideband Phased Array Radiator by Trott et. al[3]. It is shown in Figure 4. The basic unit cell consists of two orthogonal flared notch elements above a ground plane. The feed network for the flared notches is located in a cavity in the ground plane behind the flared notches. Feed lines run up the sides of the cavity to the edges of the flared notches to provide excitation. Trott's design is a masterpiece of meticulous engineering and craftsmanship, but “simple” and “meticulous” are antithetical concepts.

The third design to consider is Mohuchy's Broadband Dual-polarized Microstrip

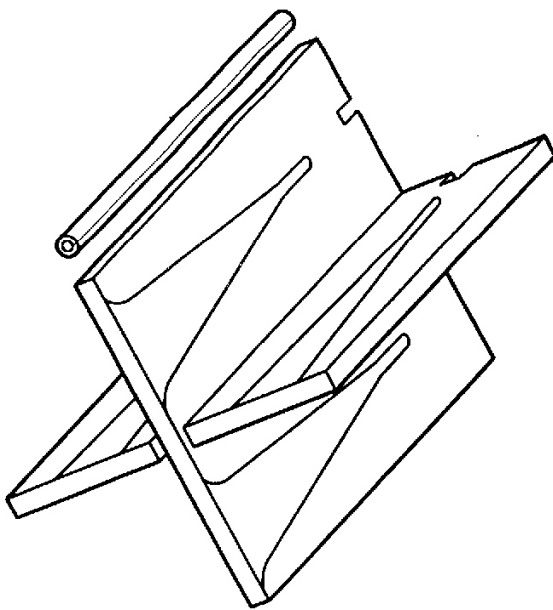


Figure 5 - Mohuchy's Broadband Dual-polarized Microstrip Notch Antenna

Notch Antenna[4], shown in figure 5. Normally flared notch elements for electronic steering applications are a half wavelength in width at their highest operating frequency. Mohuchy reduced the size of his flares by half and fed each pair of flares in tandem as a single element. The phase center of the element is between the flares, which corresponds to the location of the orthogonally polarized element. It is constructed exactly the same way as the first element except for the orientation of the interleaving slot. Some special effort is required to restore continuity for the polarization with the downward protruding slot. Mohuchy's design is impressive for its simplicity but it requires basic elements which are a quarter wavelength long at the highest operating frequency, not a suitable option for dipole elements.

The next design to consider is Smith's Radio Frequency Antenna[5], shown in Figure 6. It consists of a flared notch which is terminated in an E-plane tee instead of a balun. The two output arms of the E-plane tee feed counter-phased Marchand baluns, and the outputs of the baluns are combined remotely, away from the center of the antenna. An E-plane tee is a symmetrical device, so two orthogonal E-plane tees can be co-located with a common physical center. This allows a second set of Marchand baluns to be employed which do not interfere with the first.

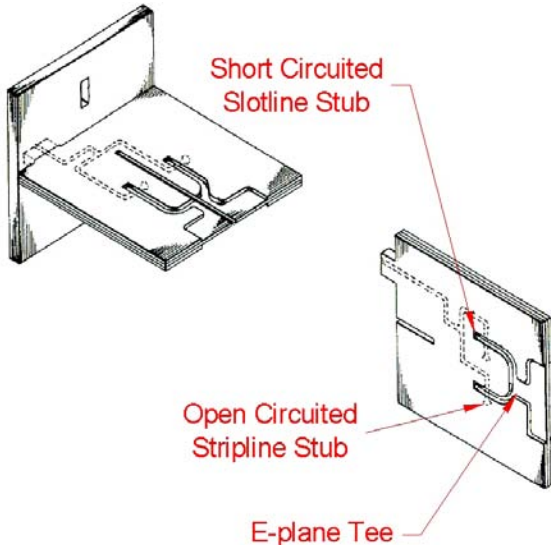


Figure 6 - Smith's Radio Frequency Antenna.

This is a good place to pause to review Marchand baluns because they will be referred to either directly or indirectly throughout the rest of this paper. A typical Marchand balun[6] is shown in Figure 7. It consists of a transition from unbalanced transmission line to balanced transmission line with intervening open circuit and short circuit stubs. The open circuit stub is in series with the unbalanced transmission line and is implemented in an unbalanced transmission line topology. The short

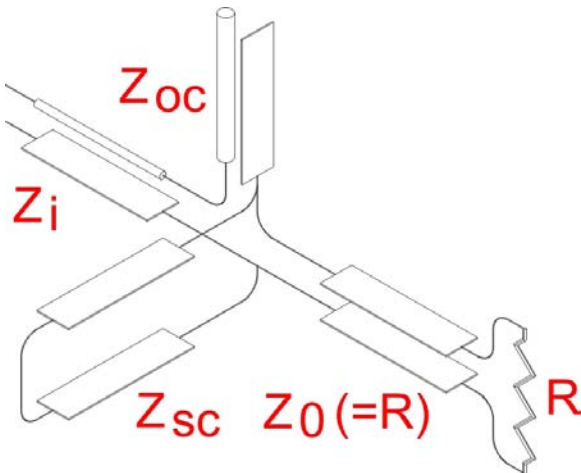


Figure 7 - Marchand Balun.

in Figure 7. The dipoles to be considered next have similar circuitry. In an attempt to simplify terminology, short circuited slot line stubs will be referred to as "slots" and open circuited stripline stubs will be referred to as "stubs." The use of the word "slotline" will be reserved to mean the short sections which go from the E-plane tee at the opening of the dipole to the short circuited stubs. The intersection with stripline occurs in the middle of the slotlines. The short section of slotline between this intersection and the short circuited stub adds a little bit of electrical length to the short circuited stub.

3. STUDY of an ARRAY ELEMENT

As shown in Figure 8, it is a fairly straight forward procedure to adapt Smith's design to a dipole configuration. A typical dipole with one quadrant cut away to show internal details is shown in the center. Other dipoles in the array are shown in gray to emphasize the infinite array aspects of the analysis. The slot lines emanating from the E-plane tee are shortened. The matching stubs are reoriented to fit in the dipole stem. One stub crosses its associated slotline from the top down and is straight. The second crosses its associated slotline from the bottom up and is bent over, around and behind the slot. The bent stub has the same electrical length as the straight stub. This makes setting up the simulations tedious. The stubs are not mirror images of each other. Rather, they have different coordinates which must be calculated for each iteration of a parametric study. It should be noted that knowledge of Edward's Microstrip Fed Printed Dipole with an Integral Balun[7], shown in Figure 9 aided us in make the mental transition from Smith's design to the dipole shown in Figure 8.

Essentially, the balun in Edward's design is doubled to arrive at the design shown in Figure 8.

circuit stub is in parallel with the balanced transmission line and is implemented in a balanced transmission line topology. In addition to transforming between balanced and unbalanced transmission line modes, Marchand baluns can also transform between a wide range of impedances. Referring to Figure 6, the portion of the slotlines below the points where they cross the striplines may be identified with the short circuit stub in Figure 7. Similarly, the portion of the striplines in Figure 6 following the intersection with the slotlines may be identified with the open circuit stub

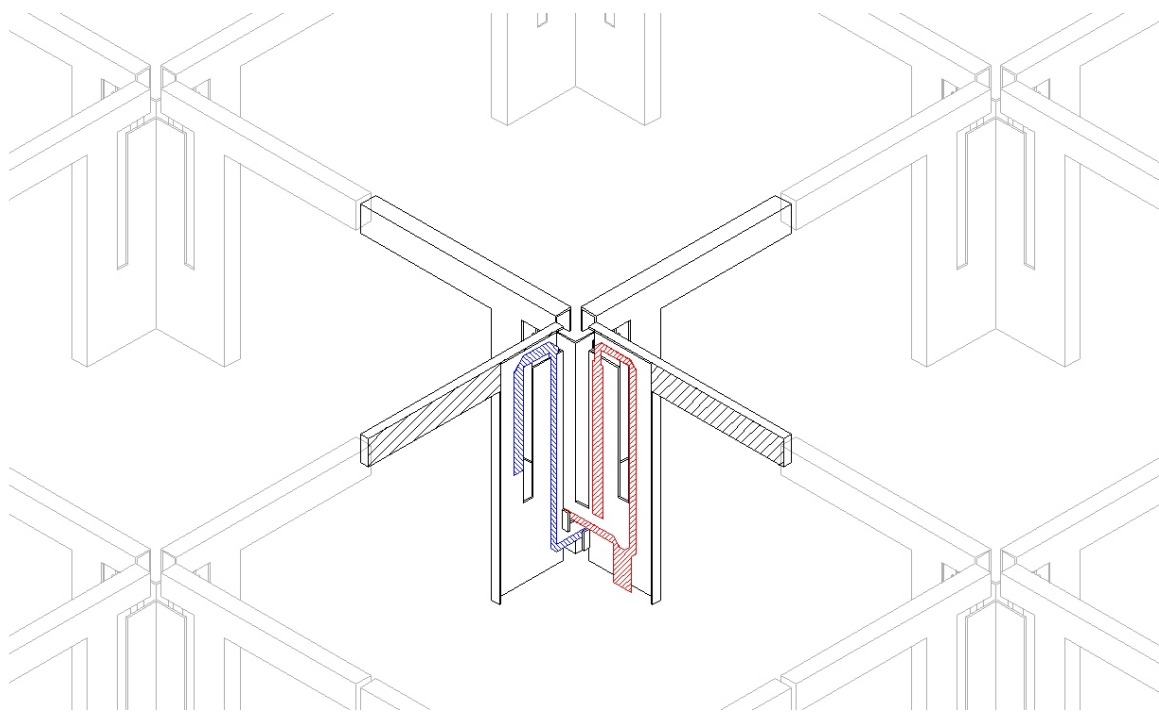


Figure 8 - Coincident phase center dipole, cutaway isometric view.

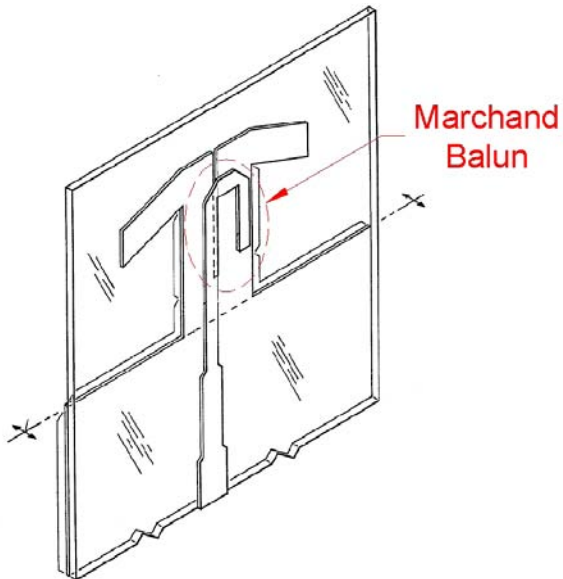


Figure 9 - Edward's Microstrip Fed Printed Dipole with an Integral Balun.

A significant simplification can be achieved by simulating just one quarter of the element as shown in Figure 10. The effects of the other three quarters of the unit cell and the infinite array are induced by the use of perfect electric and magnetic walls. There are

two of each employed in the model - one symmetry plane, and one cell boundary. The plane of the perfect magnet wall symmetry plane is coincident with the plane of the feed circuit, and the plane of the perfect electric wall symmetry plane bifurcates the dipole between the two arms. Note that in the quarter cell simulation model, the virtual balun is the mirror image of the object balun, but the virtual currents flow in the opposite direction from the object currents so everything is phased correctly. Unfortunately the perfect electric wall symmetry plane short circuits the feed circuit of the orthogonal dipole. Coupling between polarizations cannot be determined with this model. However, symmetry arguments hold that the orthogonal polarization is isolated from the first, and spot checks of the full model have verified this. The shell of the orthogonal element is added to the model to include any effects it may have on the impedance match of the first polarization. The feed line is 63 mils wide, and the space between dipole faces is 125 mils which gives a characteristic impedance of 100 ohms. Thus when both halves of the dipole are combined, the overall impedance will be 50 ohms.

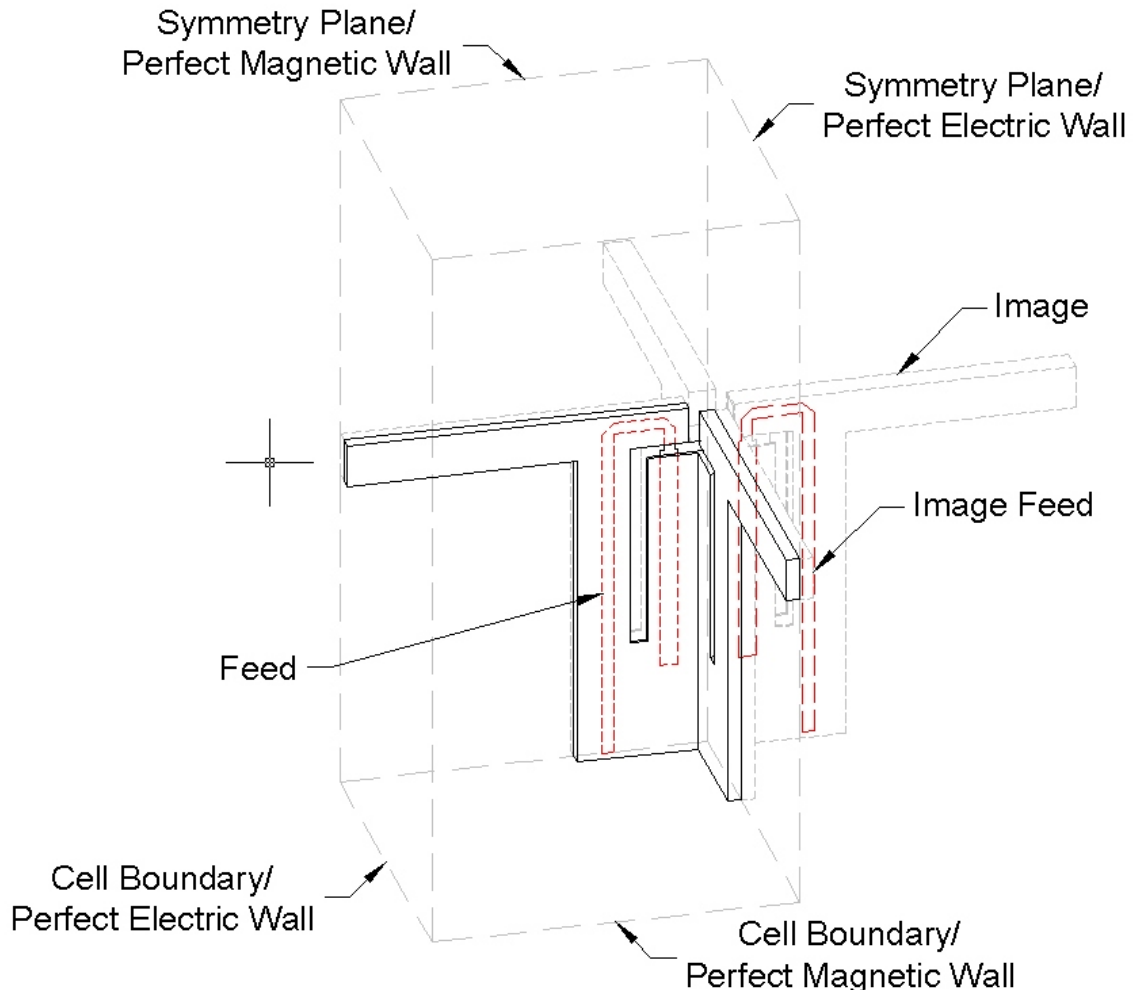


Figure 10 - One quarter of coincident phase center dipole array unit cell.

Having settled on the double marchand balun feed concept employed by Smith, the next step is to specify dipole dimensions. For scanning applications the maximum element spacing d to avoid grating lobes is given by (1)

$$d = \frac{\lambda}{1 + \sin(\theta)}, \quad (1)$$

where θ is maximum angle of scan from broadside. Briefly an application at 1.41 GHZ which required scanning to 45 degrees was considered. A half wavelength spacing was chosen which results in a cell size of 4200 mils. Intuitively it might be expected that longer dipole arms will extend the band of operation towards lower frequencies, which is desirable. On the other hand, the original intent of simple construction through modular design suggests that the dipole arms should have some mechanical clearance from

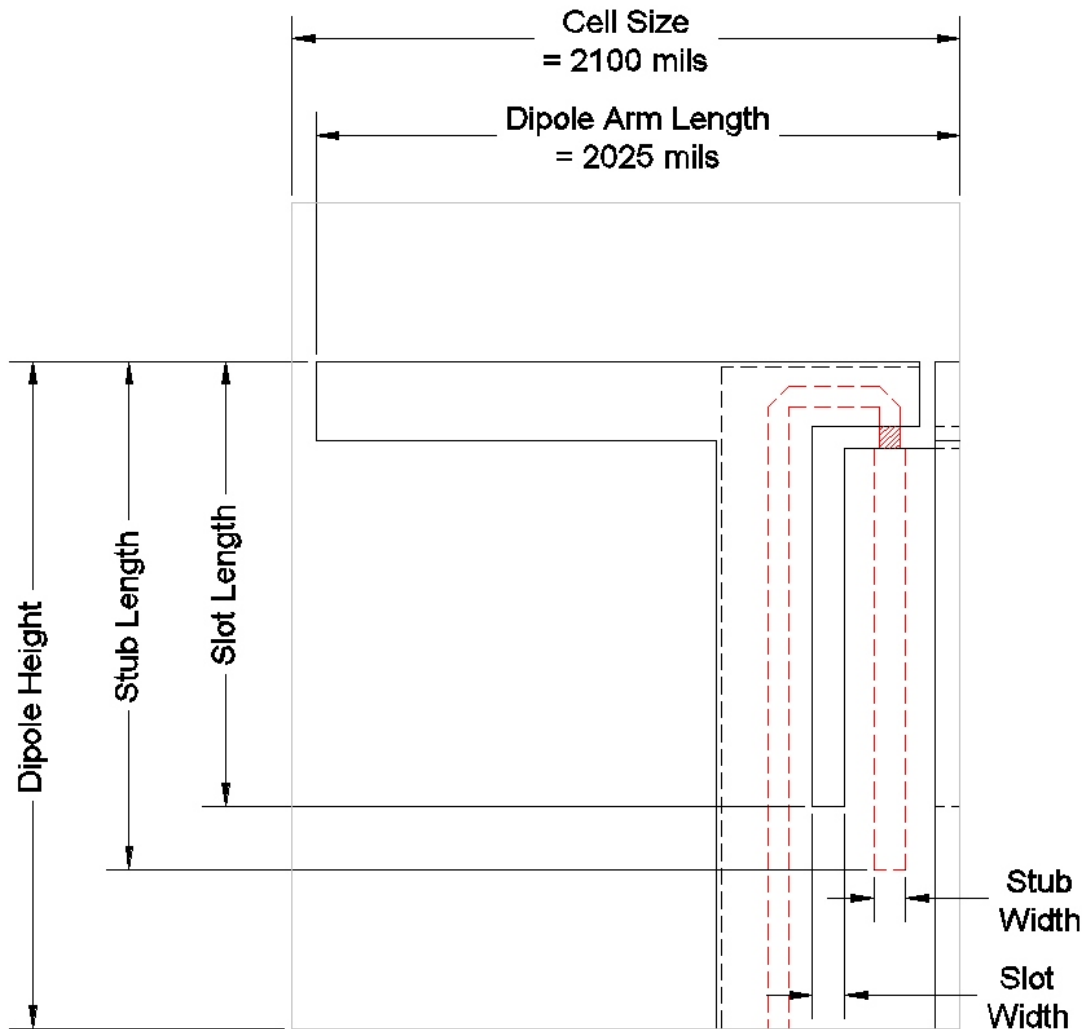


Figure 11 - Coincident phase center dipole dimensions.

adjacent dipoles. A dipole arm length of 2025 mils was selected which gives 150 mils clearance from adjacent dipoles.

There are several dimensions which can be varied to achieve a good impedance match. Parametric studies of the slot width, slot length, stub width and stub length will be performed while fixing dipole arm length, dipole arm width, and throat width. Two different values of dipole height will be compared. These dimensions are shown in Figure 11. Note that the lengths of the slot and stub are measured from the top of the dipole rather than the actual beginning of the slot and stub. This was done so that round numbers could be used in the plots and graphs which follow.

Vacuum was used as the only dielectric in all simulations. Although this leads to the unphysical condition of an unsupported center conductor, it ensures that the slots and stubs have the same propagation velocity, simplifying comparison of their lengths.

The first parametric study was performed for a dipole 2100 mils above a ground plane, a quarter wavelength at 1.41 GHZ. The study was conducted in two stages. First the stub and slot widths were fixed at intermediate values of 70 mils, and the stub and slot lengths were varied from 400 mils to 1800 mils in 200 mil steps, for a total of 64 different cases. A program written in C++ was used to extract the stored results from the simulation data file and plot them in AutoCAD. In AutoCAD all the results were compared simultaneously. In the first winnowing process all the results which did not have a VSWR less than 2:1 between 1.0 and 1.5 GHZ were eliminated. The remaining results were graded by setting limits at lower frequencies, and lower reflection levels with the goal of having most results graded satisfactory, a few graded as good, and a couple graded as very good. Then a map was constructed of the graded results with each cell representing a particular combination of stub length and slot length. Cross hatches were placed in the cells of the map to indicate the grade assigned to the results corresponding to that cell, with coarse hatching indicating the worst performance and progressively finer hatching indicating better results. After the best results were located on a 200 mil search grid, the search interval was refined to 100 mil steps in the vicinity of those results. The resulting map is shown in Figure 12.

The rows and columns that are only partially filled show where the search grid was refined. Several selected results from Figure 12 are plotted in Figure 13. The labels on the curves in Figure 13 indicate which squares in Figure 12 they correspond to. Curve 72 was selected as the best results from the parametric study of slot and stub length. A second study was performed in which the slot and stub widths were varied from 50 mils to 100 mils in 5 mil steps. Those results were extracted, plotted in AutoCAD and graded in a similar exercise. The map of those results are shown in Figure 14. All the results from this run were at least satisfactory. The plots of all results are shown in Figure 15, with the best shown as heavy lines. The label at 0.809 GHZ marks the lowest frequency

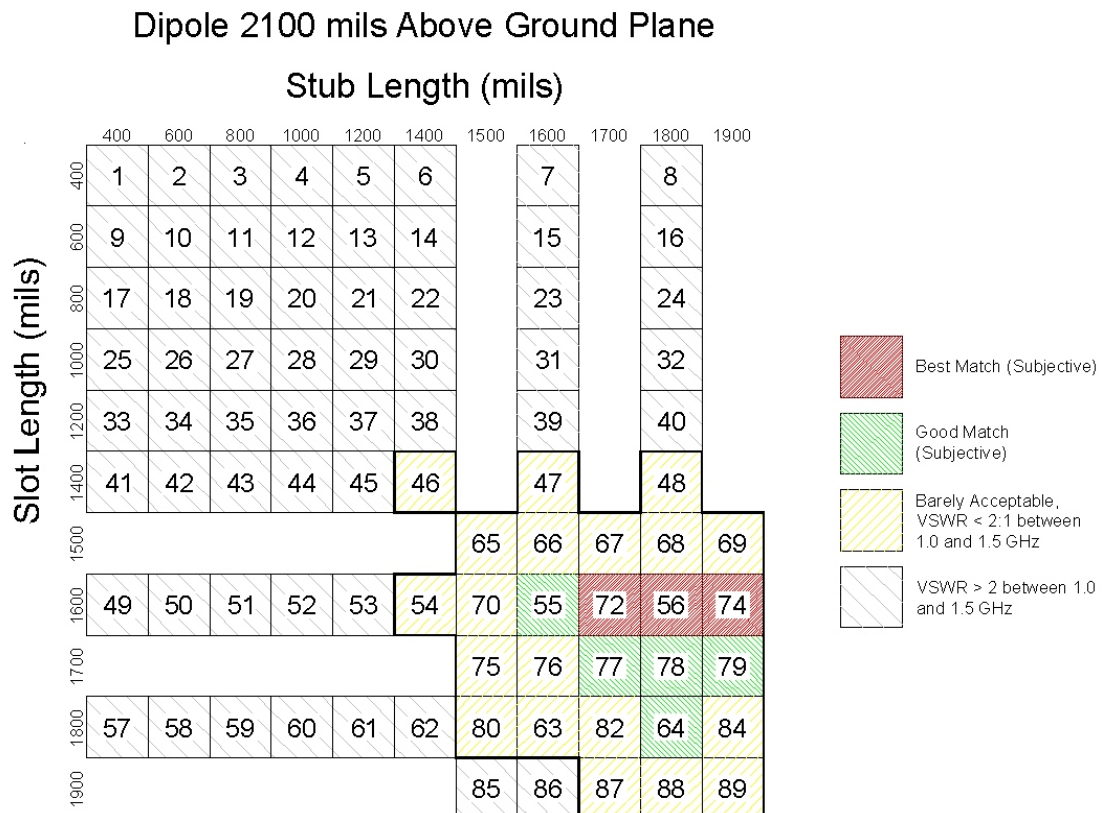


Figure 12 - Map of dipole match quality vs. slot and stub length. Slot and stub width set to 70 mils.

at which the selected best curves have a VSWR < 2:1. Note that some curves indicate

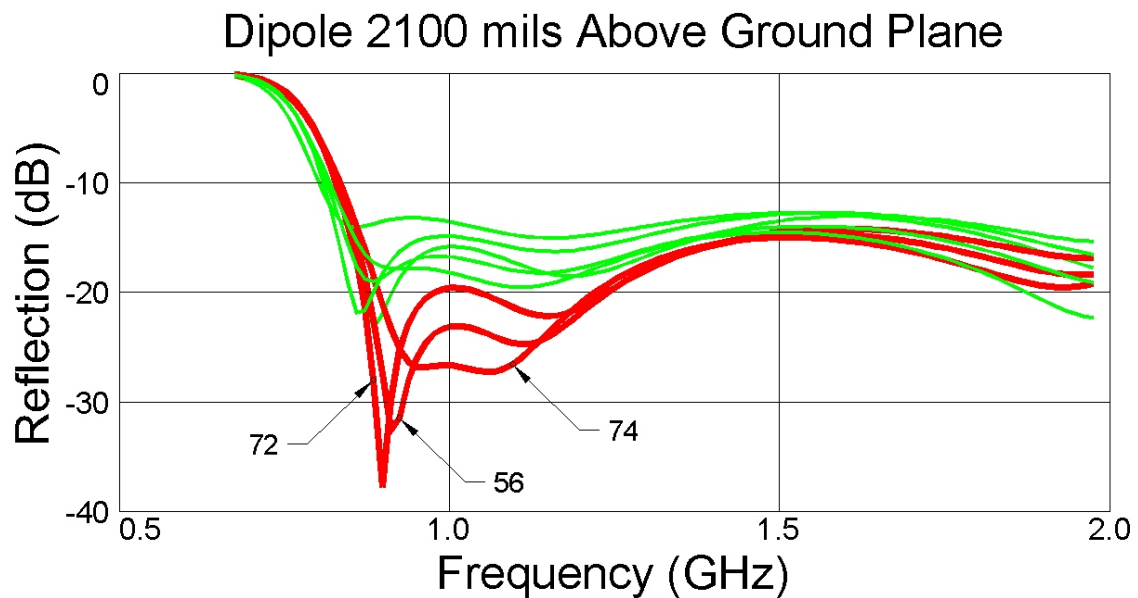


Figure 13 - Selected better curves for dipole dimensions from Figure 12. The best curves have numbers corresponding to squares in Figure 12.

Dipole 2100 mils above ground plane

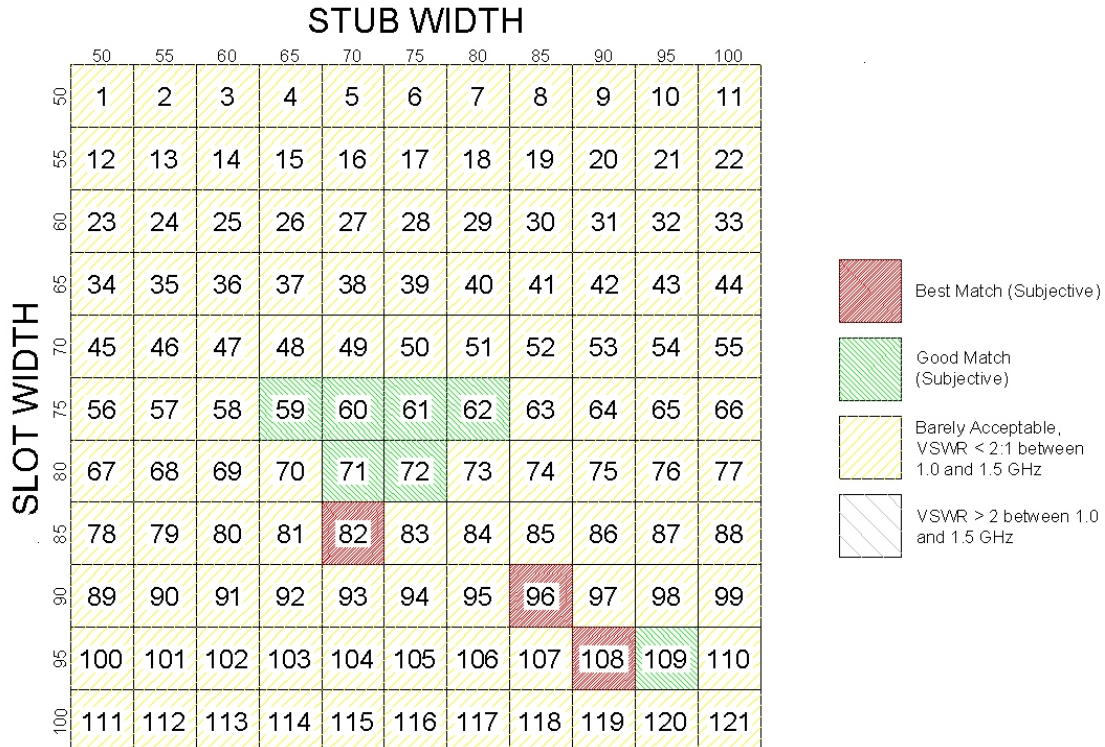


Figure 14 - Map of dipole match quality vs. slot and stub width. Slot and stub lengths set to 1600 and 1700 mils respectively.

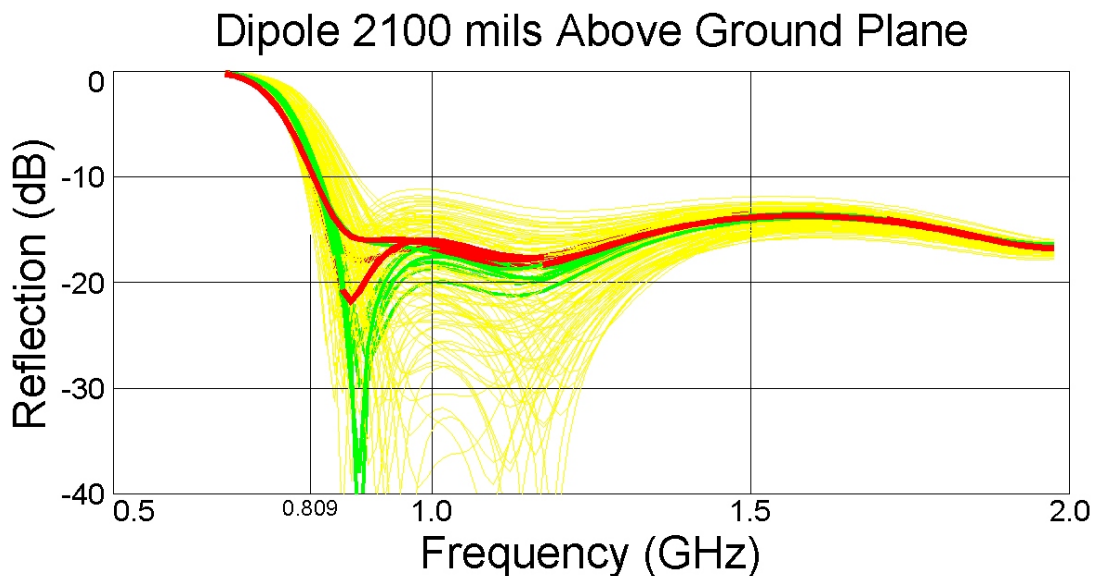


Figure 15 - Plot of all impedance curves used to generate map in Figure 14. The darkest curves correspond to squares 82, 96, and 108 in Figure 14 but are not labeled individually.

at which the selected best curves have a VSWR < 2:1. Note that some curves indicate slot and stub dimensions which would yield a good performance to lower frequencies than the selected best. Also note that some curves indicate slot and stub dimensions which would yield a better match in the middle of the band than the selected best. None do both simultaneously. Deciding how to balance low frequency performance against mid band performance is subjective.

The maps in Figures 12 and 14 indicate a 4 dimensional volume in which a satisfactory match can be obtained. It can be seen that there is considerable latitude, particularly with respect to slot and stub width. Figures 13 and 15, which show selected impedance curves are more striking. They show that a half wave dipole array, one quarter wavelength above a ground plane with a double Marchand balun can operate over a 100% bandwidth. Furthermore this is not hard to do as indicated by the large number of curves, corresponding to large variations in dimensions, which are satisfactory.

No radiation patterns have been presented because the simulators, one based on finite element analysis, and one based on FDTD analysis produced different radiation patterns for a cell in an infinite array. Also, at the time of this report, a method for automatically extracting radiation patterns from simulations, similar to the method used for impedance data, had not been perfected.

The simulations were run from 675 MHz to 1.975 GHZ. It can be seen in Figure 15 that many of the results were good from 1.41 GHZ up to the 1.975 GHZ. Obtaining a good impedance match for element spacing greater than $\lambda/2$ spacing does not seem to be a problem. The difficulty is in obtaining a good match for element spacings of $\lambda/4$ and less. A good impedance match at lower frequencies, however, is more interesting for scanning applications.

In an attempt to increase the bandwidth in the low frequency direction, the exercises just described were repeated for the same dipole 2500 mils above a ground plane, 400 mils higher. The stub and slot length search intervals were also increased by 400 mils; from 400 - 1800 mils to 800 - 2200 mils. The map for these results are shown in Figure 16 and the selected best impedance plots are shown in Figure 17. Curve 77, corresponding to slot and stub lengths of 1700 and 1900 mils respectively, was chosen as the best. A search for best slot and stub widths was performed as before. The map of the search results is shown in Figure 18, and the collection of all impedance curves is shown in Figure 19. The label at 0.788 GHZ marks the lowest frequency at which the selected best curves have a VSWR < 2:1. Comparing Figures 15 and 19, it can be seen that increasing the dipole height only marginally decreased the lowest frequency limit. The more noticeable effect it had was to decrease the upper frequency limit which is off the graphs to the right. In Figure 15, all the curves have slight downward slope at 1.975 GHZ, while in Figure 19 all the curves have a distinct upward slope at 1.975 GHZ. If there is any benefit to be obtained by increasing the dipole height in an array environment, 400 mils is probably too much.

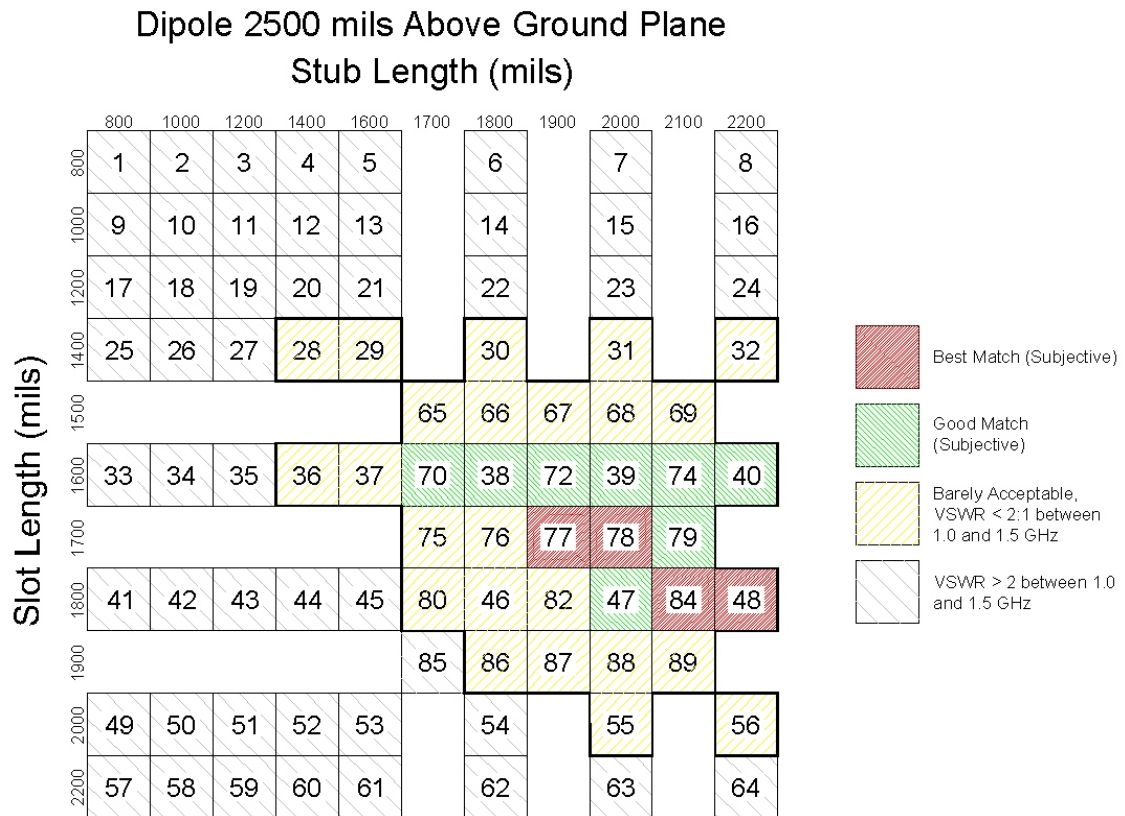


Figure 16 - Map of dipole match quality vs. slot and stub length. Slot and stub width set to 70 mils.

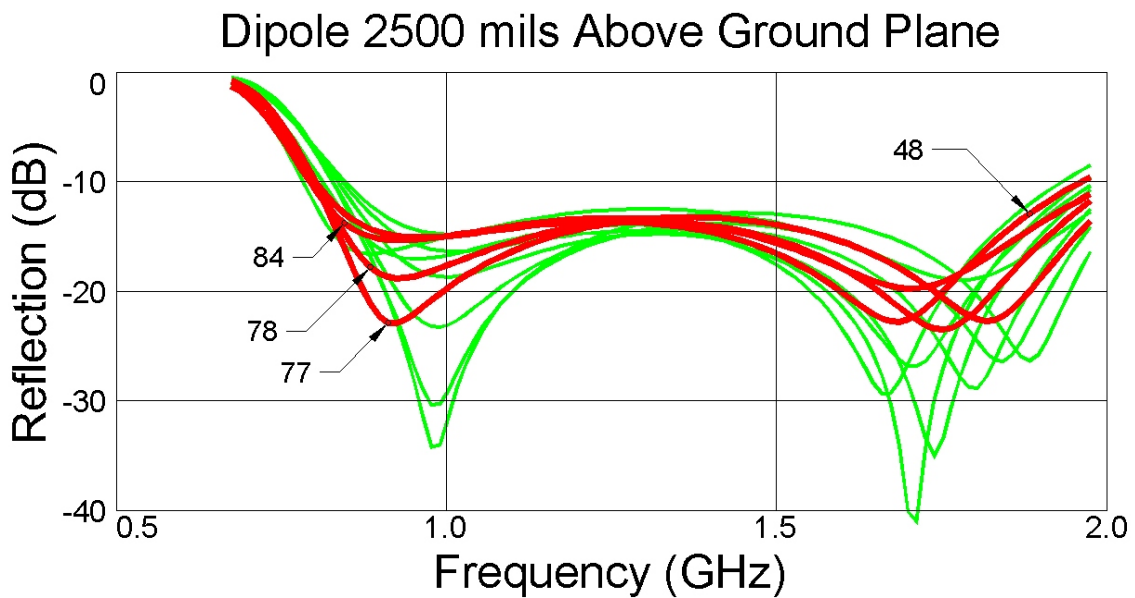


Figure 17 - Selected better curves for dipole dimensions from Figure 16. The best curves have numbers corresponding to squares in Figure 16.

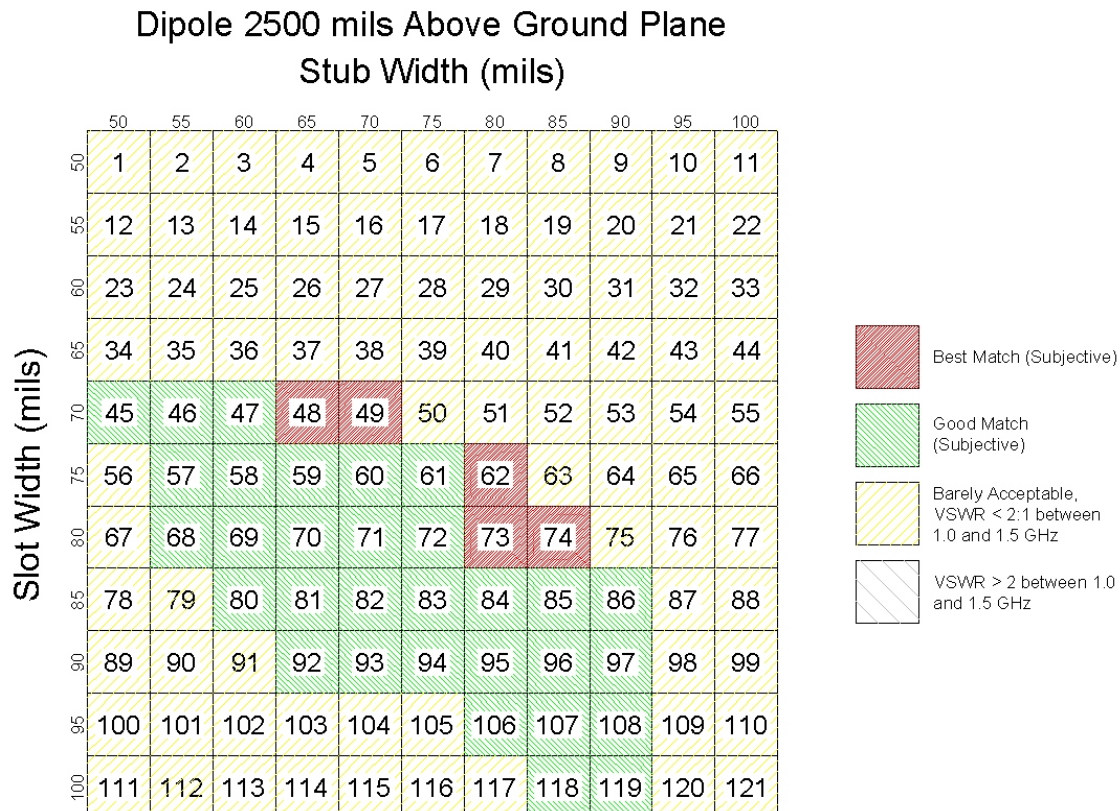


Figure 18 - Map of dipole match quality vs. slot and stub width. Slot and stub lengths set to 1700 and 1900 mils respectively.

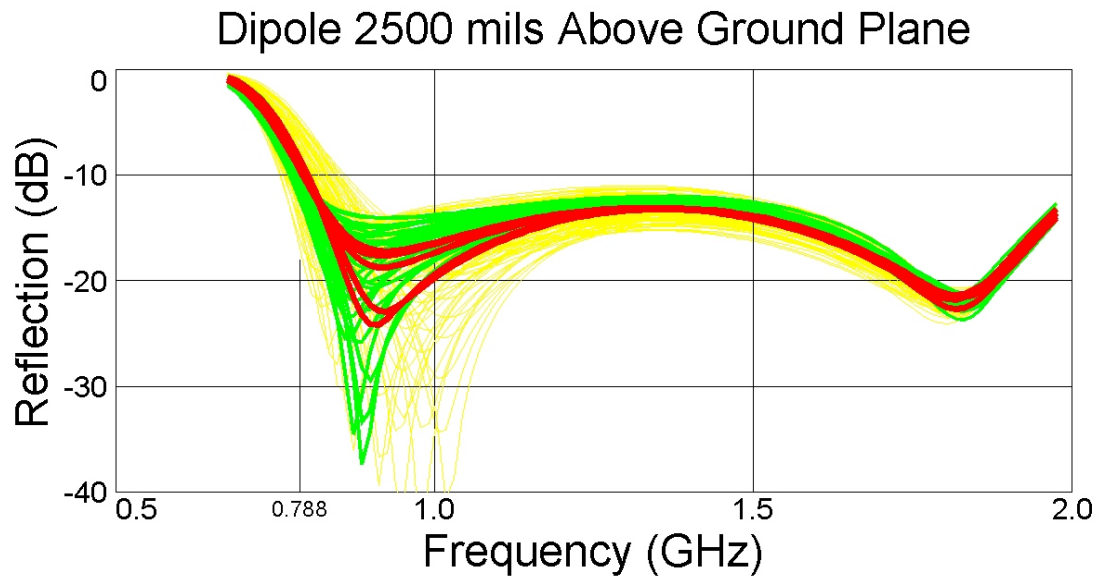


Figure 19 - Plot of all impedance curves used to generate map in Figure 18. The darkest curves correspond to squares 48, 49, 62, 73 and 73 in Figure 18 but are not labeled individually.

4. STUDY of an ISOLATED ELEMENT

All the simulations performed thus far were for a double marchand balun coincident phase center dipole operating in an infinite array environment. The bandwidths achieved are wider than what would be expected from dipoles. However, the parametric studies were all performed for dipoles with mutual coupling. This leads to the question of how the same dipoles will perform if mutual coupling is removed. The best 2100 mil high dipole from Figure 15 and the best 2500 mil high dipole from Figure 19 were modeled as free standing isolated crossed dipole pairs above an infinite ground plane. All the parametric studies conducted so far were for a quarter of a unit cell. A half unit cell, shown in Figure 20, was used for the free standing dipole simulations. The required the addition of a

Dipole Height	2100	2500
Straight Stub Length	1700	1900
Bent Stub Length	1130	1332
Slot Length	1600	1700
Stub Width	70	80
Slot Width	85	80

Table 1 - Numerical values, in mils, for dipole shown in Figure 20.

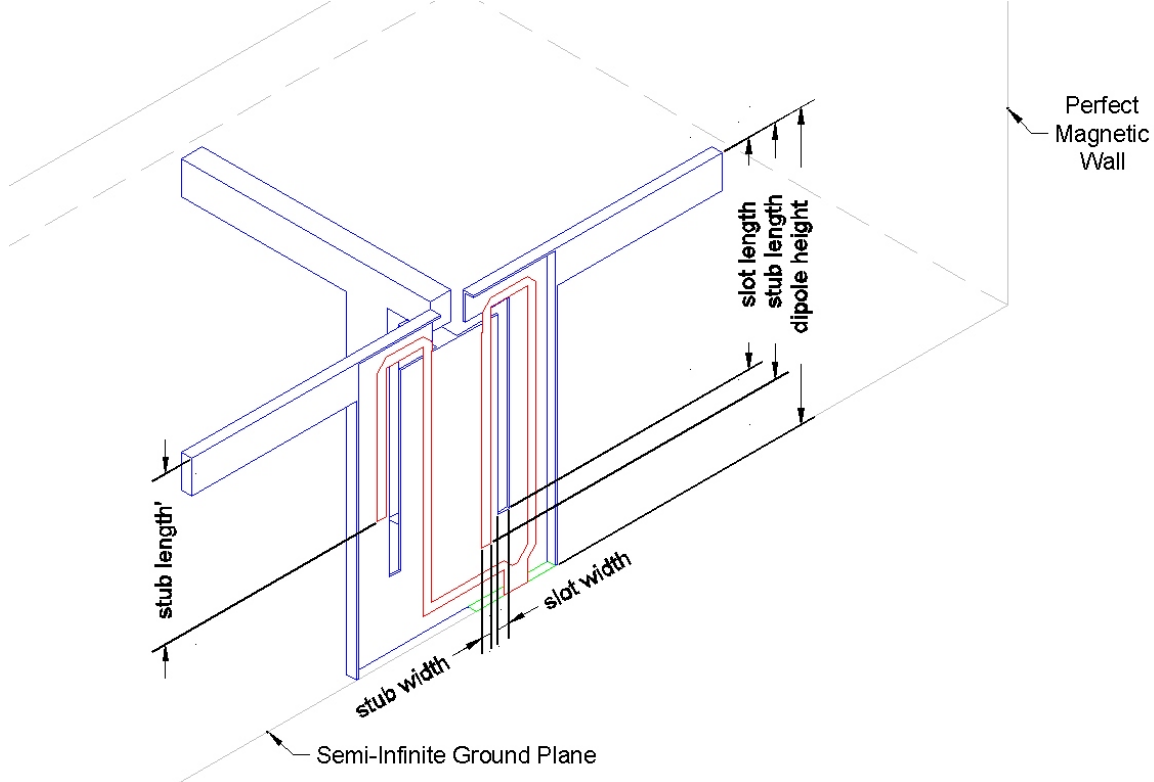


Figure 20 - Simulation model for free standing coincident phase center dipole. Only the polarization in the plane of the perfect magnetic wall is active.

second slot and stub. This change also had the beneficial side effect of reconciling differences between the finite element simulator and the FDTD simulator. All results presented so far were from the finite element simulator. The impedance plots to follow are from both simulators. The radiation patterns presented are from the finite element simulator but the patterns generated by the FDTD simulator were very similar.

The half unit cell and pertinent dipole dimensions used in the free standing dipole simulations are shown in Figure 20 and tabulated in Table 1. Note that the difference in lengths between the straight and bent stubs is not quite the same for the 2100 mil and 2500 mil dipoles. This is caused by the differences in slot and stub widths for the two cases. The simulation model was set up to keep the slots and stubs as far apart as possible within the available space. This was done to minimize interaction between the two. Simple miters were used on the stubs which have the same width as the stubs. If optimum miters had been used, calculation of the bent stub length would have been even more complicated. This is why quarter unit cell simulations instead of half unit cells were used for most of the investigations documented in this report.

The input reflection for the two dipoles are shown in Figures 21 and 22. It appears that increasing the height of the dipoles improves the match, but the radiation patterns also need to be considered. The radiation patterns for the 2100 mil high dipole at 1.38 GHZ and 1.975 GHZ are shown in Figure 23. 1.38 GHZ is the lowest frequency, from Figure 21, at which the VSWR < 2:1 and 1.975 GHZ is the highest frequency in the simulation. Note that a null is beginning to form on axis at 1.975 GHZ. This is caused by the image of the dipole which lies 2100 mils below the ground plane. The radiation patterns for the 2500 mil high dipole at 1.28 GHZ and 1.675 GHZ are shown in Figure 24. 1.28 GHZ is lowest frequency, from Figure 22 at which the VSWR < 2:1 and 1.675 GHZ is the maximum frequency at which the null on axis is less than 1 dB deep.

Inter element mutual coupling is strongly associated with the low frequency bandwidth enhancement obtained with the double Marchand balun dipole. Figure 21 shows that an isolated half wavelength long double Marchand balun dipole a quarter wavelength above a ground plane is not well matched for frequencies below resonance. Figure 15 shows that the same dipole with inter element mutual coupling does not have a half wave length resonance and stays well matched down to frequencies close to where it is a quarter wavelength long. A comparison of Figures 15 and 21 shows that for higher frequencies the effect of mutual coupling is less significant. At some frequencies it improves the match and at others it degrades the match.

However, the effects of the double marchand balun are important too. A dipole with a split sleeve balun has about a 10% bandwidth. Parametric studies of isolated double Marchand balun dipoles above a ground plane can be expected to improve the results shown in Figures 21 and 22. Time did not permit it for this report.

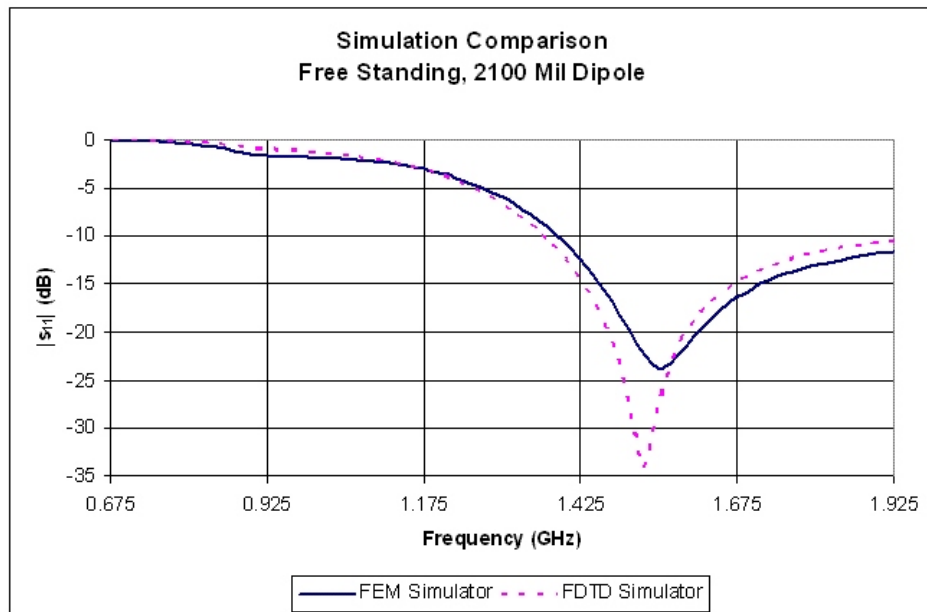


Figure 21 - Reflection vs. frequency for free standing coincident phase center dipole 2100 mils above ground plane. Dipole dimensions optimized for array environment.

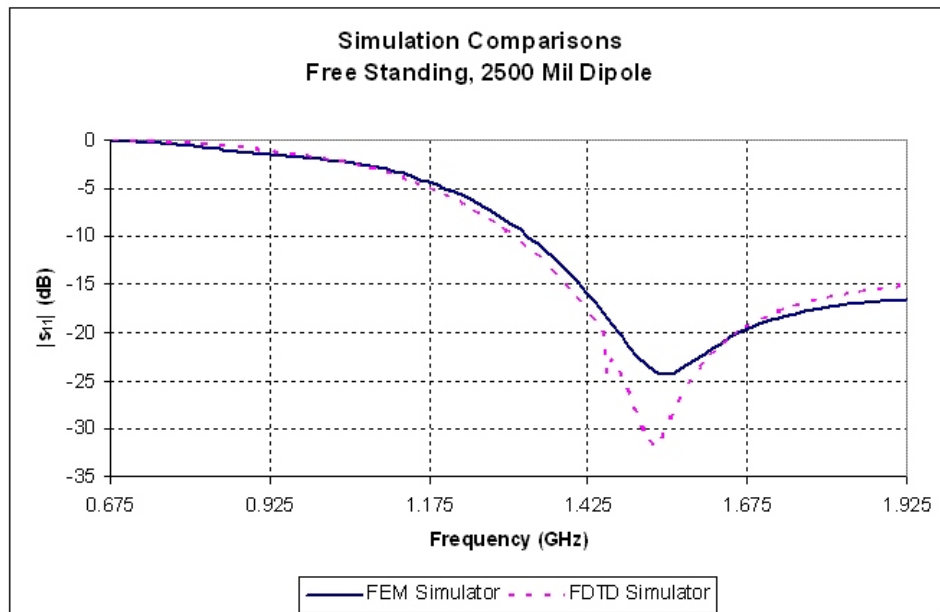


Figure 22 - Reflection vs. frequency for free standing coincident phase center dipole 2500 mils above ground plane. Dipole dimensions optimized for array environment.

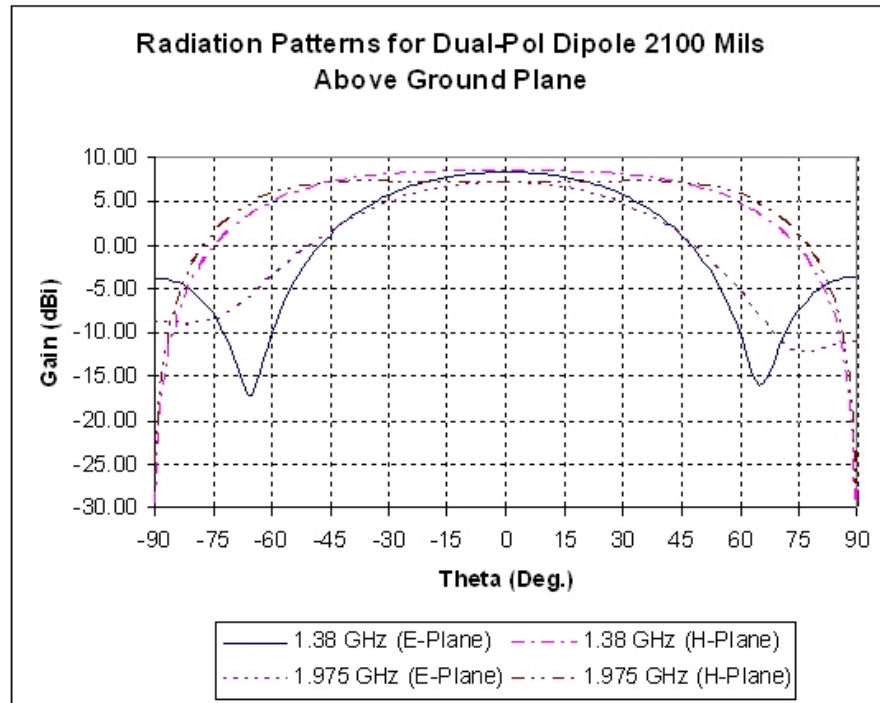


Figure 23 - Selected radiation patterns for free standing coincident phase center dipole 2100 mils above ground plane. Dipole dimensions optimized for array environment.

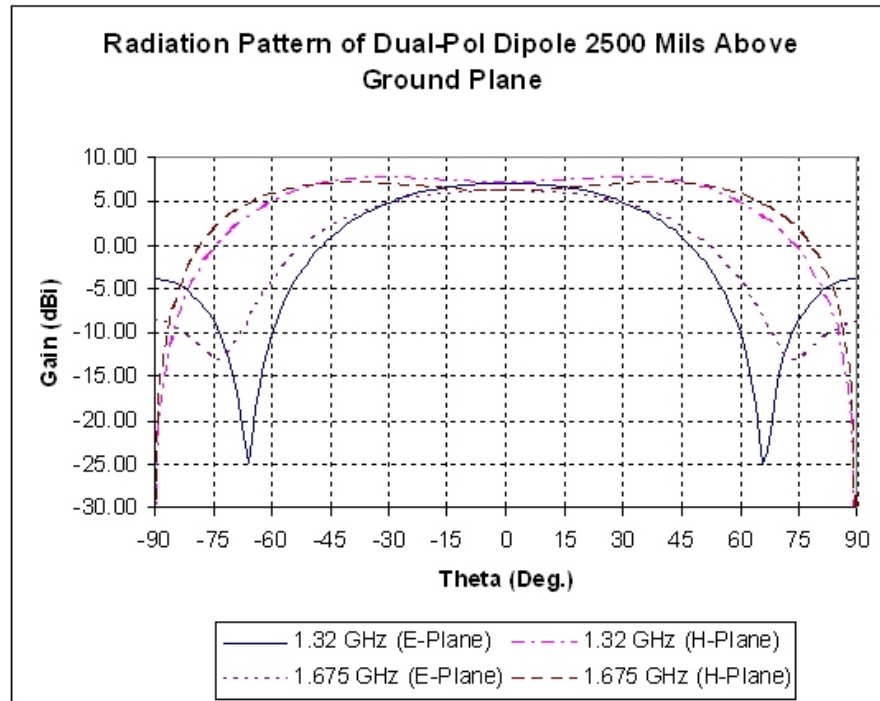


Figure 24 - Selected radiation patterns for free standing coincident phase center dipole 2500 mils above ground plane. Dipole dimensions optimized for array environment.

5. CONCLUSIONS

This investigation was begun to look for a simpler method to construct coincident phase center antennas. Current ultra wideband methods employ flared notch elements which require electrical continuity between contiguous elements. This complicates the design because mechanical clearance for the orthogonally polarized element is required in the same location. It was anticipated that if dipoles were substituted for flared notches the construction could be simplified at the expense of bandwidth. Quite unexpectedly, it was found that dipoles with double Marchand balun feeds can attain bandwidths close to one hundred percent.

It is anticipated that double Marchand balun dipoles will be useful in cost sensitive coincident phase center applications as well as more traditional moderately wideband applications.

A singly polarized test array is being designed at this time.

6. REFERENCES

1. M. Kragalott, W.R. Pickles, and M.S. Kluskens, "Design of a 5:1 bandwidth stripline notch array from FDTD analysis," IEEE Trans. Antennas Propagat., vol. 48, pp. 1733 – 1741, Nov. 2000
2. "Folded cross grid dipole antenna," U.S. Patent #5796372; Elliot, Paul G., Aug. 18, 1998
3. "Wideband phased array radiator," U.S. Patent #7180457; Trott, Keith D., Biondi, Joseph P., Cavener, Ronni J., Cummings, Robert V., McGuinnis, James M., Sikina, Thomas V., Yurteri, Erdem A., Beltran, Fernando; Feb. 20, 2007
4. "Broadband dual-polarized microstrip notch antenna," U.S. Patent #6552691; Mohuchy, Wolodymyr; Beyerle, Peter A.; MacFarland, Andrew B.; April 22, 2003
5. "Radio frequency antenna," U.S. Patent #5268701; Smith, Keith C., Dec. 7, 1993
6. Oltman, George, "The Compensated Balun," IEEE Trans. Microwave Theory Tech, vol. MTT-14, no. 3, pp. 112 – 119, March 1966
7. "Microstrip Fed Printed Dipole with an Integral Balun," U.S. Patent #4825220; Edward, Brian J, Rees, Daniel F., April 25, 1989

Scan impedance for an infinite dipole array: Hansen's formulas vs. Ansoft HFSS simulations

Sergey N. Makarov

Worcester Polytechnic Institute, Worcester, MA 01609
makarov@wpi.edu

Abstract: The present study reviews some results for the well-known case of an infinite array of center-fed strip dipoles above a ground plane. No dielectric sheet is included into consideration. In particular, we are interested in the test of simple equations for the scan (or active) impedance given by R. C. Hansen in his monograph *Phased Array Antennas*, Wiley, 1998 on pp. 236-238. The analytical method used in this study is the canonical Floquet expansion approach. It leads us to the results obtained by Oliner and Malech, and Stark ['Mutual coupling in infinite scanning arrays,' in *Microwave Scanning Antennas*, Vol. II, R.C. Hansen, ed., Academic Press, 1966, Chapter 3, pp. 195-335], and allows us to establish the domain of validity for Hansen's formulas. Simultaneously, we compare the analytical data with the Ansoft HFSS simulations, which use the periodic boundary conditions for a vertical unit cell. It is found that the agreement is quite good for the *E*-plane scan but the results may be significantly different for other scan planes.

Keywords: Phased arrays, Scanning antennas, Finite element methods

1. Problem statement

A motivation for this work was the necessity to program and test the standard scan impedance results for an infinite array of strip dipoles above a ground plane. The geometry is given in Fig. 1 [1]. We consider an infinite linearly-polarized array of planar strip dipoles above a ground plane separated by h . The unit cell size is $d_x \times d_y$; all dipoles have length l and width t . The (a priori estimated or known [1]) surface current distribution [A/m] on the central strip is given by a separable vector function in the xy -plane. The phasor current will have the form:

$$J(x, y) = x J_0 f(x) g(y) \quad (1)$$

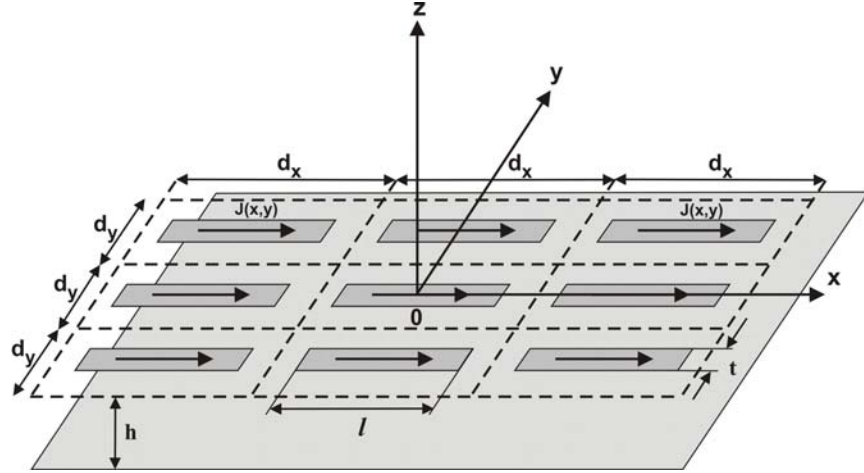


Fig. 1. Geometry of an infinite array with strip dipole elements (single polarization).

Thus, we assume that the surface current has only the vector component x in the E -plane (the xz -plane). The transversal current distribution $g(y)$ is constant, but the longitudinal distribution $f(x)$ may vary. The current distribution on other strips is the same, to within a complex phase shift factor.

A set of very appealing and elegant closed-form formulas is given for the present problem in Ref. [1], pp. 236-238. These formulas were obtained based on the unit-cell waveguide approach and a subsequent waveguide modal expansion, subject to the appropriate boundary conditions – see Ref. [2] and the discussion in Section 8 that follows. Unfortunately, the corresponding derivation procedure has not been given. We tested the formula for the scan resistance and found that it gives the expected results for the H -plane scan, but disagrees with the E -plane and D -plane scans depicted later in the same monograph [1] in Chapter 7. The subject of the present work will therefore be to carefully review the results for the scan impedance presented in Ref. [1] and establish their domain of validity. We will use the well-known Floquet expansion method that is very similar to that given in [2]-[4], but will rather follow a more formalized scheme of the recent monograph [5].

2. Current expansion

Three possible types of electric current distribution along the strips (phasor of the total current on both sides of the strip) are shown in Fig. 2. The former case (case A) corresponds to the uniform distribution considered in particular in Ref. [5]. The second case is the analytical model for the current distribution for an arbitrary non-resonant dipole around the first resonance – see [6], p. 170. The third case is exactly the resonant

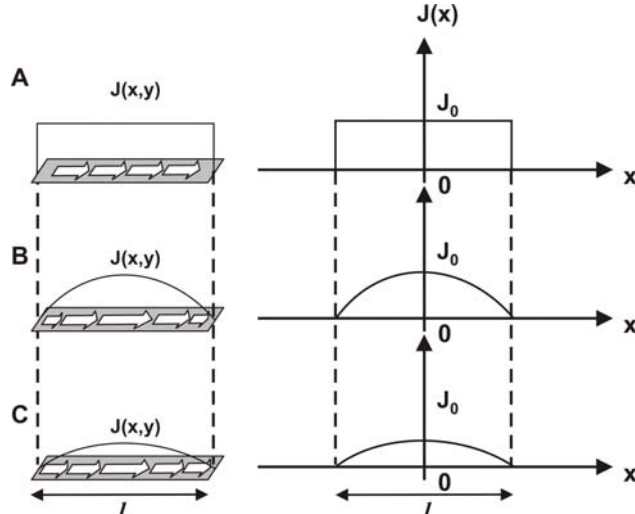


Fig. 2. Electric current distribution along the metal strip.

$(\lambda_0/2)$ dipole, similar to that considered in Ref. [1], pp. 236-238 – see the subsequent discussion¹.

One thus has -see Eq. (1)

$$J(x, y) = x J_0 f(x) g(y), \quad f(x) = \begin{cases} \Pi\left(\frac{x}{l}\right) & \text{case A} \\ \sin\left(k_0\left[\frac{l}{2} - |x|\right]\right) & \text{case B, } g(y) = \Pi\left(\frac{|y|}{t}\right) \\ \cos(k_0 x) & \text{case C} \end{cases} \quad (2)$$

where $k_0 = \omega/c_0$ is free-space wavenumber and $\Pi(x/a) = 1$ for $|x| < a/2$ is the rectangular function. The case-B current distribution is reduced to the resonant dipole (Case C) when $\lambda_0 = 2\pi/k_0 = l/2$. All dipoles are assumed to be center-fed. The feed gap is ignored when the continuous current distribution is considered - see below.

3. Fourier transform of current expansion

We shall derive Hansen's formulas using the elementary Floquet modal approach for the planar phased arrays [5]. This approach starts with the spatial Fourier transform of the surface/volume current distribution. Denoting the Fourier transform by superscript “~” one has

¹ Ref. [1] is apparently using the current distribution $\cos(\pi x/l)$, in accordance with the preceding sources [2, 3]. This current distribution is different from the non-resonant case in Eq.(2) but gives the same result at the resonance.

$$\tilde{J}(k_x, k_y) \equiv x J_0 \tilde{f}(k_x) \tilde{g}(k_y), \tilde{f}(k_x) = \frac{1}{2\pi} \int_{-\infty}^{+\infty} f(x) \exp(jk_x x) dx, \tilde{g}(k_y) = \frac{1}{2\pi} \int_{-\infty}^{+\infty} g(y) \exp(jk_y y) dy$$
(3)

The calculation of the Fourier transform is straightforward but lengthy, especially for case B in Eq. (2). It is performed by expressing the cosine functions in the complex exponential form and using integration by parts. The final result is

$$\tilde{g}(k_y) = \frac{\sin k_y t / 2}{\pi k_y} = \frac{t}{2\pi} \text{sinc}\left(\frac{k_y t}{2}\right)$$
(4)

$$\tilde{f}(k_x) = \frac{l}{2\pi} \text{sinc}\left(\frac{k_x l}{2}\right)$$
(5a)

$$\tilde{f}(k_x) = \frac{1}{2\pi} \frac{2k_0}{k_x^2 - k_0^2} \left[\cos\left(\frac{k_0 l}{2}\right) - \cos\left(\frac{k_x l}{2}\right) \right] = \frac{l^2 k_0}{8\pi} \text{sinc}\left(\frac{(k_x + k_0)l}{4}\right) \text{sinc}\left(\frac{(k_x - k_0)l}{4}\right)$$
(5b)

$$\tilde{f}(k_x) = \frac{1}{\pi k_0} \frac{\cos \pi z}{1 - 4z^2} \quad z = \frac{lk_x}{2\pi}$$
(5c)

Here, $\text{sinc}z \equiv \sin z / z$. Eqs. (5a-c) correspond to cases A, B, and C for the dipole current distribution considered above, respectively. Note that, by analogy with the *sinc* function,

Ref. [7] defines the *coscz* function in the form $\text{coscz} \equiv \frac{\cos \pi z}{1 - 4z^2}$, which allows us to express

the above result for case C as $\tilde{f}(k_x) = \frac{1}{\pi k_0} \text{coscz}$, i.e. as the Fourier transform of the cosine current distribution [1]. This definition is different from another one, $\text{coscz} = \frac{\cos \pi z - \text{sinc}z}{z}$, which is also found in the literature.

4. Floquet series for current expansion –[2,5]

For any dipole strip numbered (m, n) in Fig. 1, the current distribution is still given by Eq. (1), where the phasor current $J(x, y)$ is now multiplied by the phase factor:

$$\exp(-jk_{x0}x_{mn} - jk_{y0}y_{mn}), \quad x_{mn} = m dx, \quad y_{mn} = n dy, \quad m, n = 0, \pm 1, \pm 2, \dots, \text{etc.}$$
(6)

Here, k_{x0}, k_{y0} are two arbitrary constant phase factors – the “phase progression factors”. In particular, in order to scan in the direction θ_0, φ_0 in the spherical coordinates (with elevation angle measured from zenith) it is necessary to choose

$$k_{x0} = k_0 \sin \theta_0 \cos \varphi_0, \quad k_{y0} = k_0 \sin \theta_0 \sin \varphi_0 \quad (7)$$

The presence of two indices in Eq. (5) for x_{mn}, y_{mn} is redundant for a rectangular array, but may be meaningful for a triangular or a hexagonal array lattice [5].

The total current distribution everywhere in space is thus expressed by

$$J(x, y, z) = x J_0 \delta(z) \sum_{m=-\infty}^{m=+\infty} \sum_{n=-\infty}^{n=+\infty} f(x - x_{mn}) g(y - y_{mn}) \exp(-jk_{x0} x_{mn} - jk_{y0} y_{mn}) \quad (8)$$

A solution to Maxwell's equations (usually the equation for the magnetic vector potential, A) with the right-hand side given by Eq. (8) is cumbersome. The benefit of the Floquet theory is in representing Eq. (8) in a more convenient form, i.e. in the form of the so-called Floquet series,

$$J(x, y, z) = x \frac{4\pi^2}{d_x d_y} J_0 \delta(z) \sum_{m=-\infty}^{m=+\infty} \sum_{n=-\infty}^{n=+\infty} \tilde{f}(k_{xmn}) \tilde{g}(k_{ymn}) \exp(-jk_{xmn} x - jk_{ymn} y) \quad (9)$$

that is an extension of the Fourier series to the case of a function with a periodic amplitude but aperiodic progressive (increasing or decreasing) phase. The 2D current distribution given by Eq.(8) is exactly a function of such kind. The arguments are

$$k_{xmn} = k_{x0} + \frac{2\pi m}{d_x}, \quad k_{ymn} = k_{y0} + \frac{2\pi n}{d_y}$$

A Helmholtz equation for the magnetic vector potential (only the x -component exists)

$$\nabla^2 A_x + k_0^2 A_x = -J(x, y, z) \quad (10)$$

is then easily solved with the right-hand side given by Eq. (8); the solution is given by a series similar to Eq. (8), with the same exponential factors – Floquet modes – see the next Section.

5. Radiated electric field and scan impedance

The electric field is obtained from the Maxwell curl equation expressed in terms of the magnetic vector potential in the form $E = \frac{1}{j\omega\epsilon_0} \nabla \times H = \frac{1}{j\omega\epsilon_0} \nabla \times \nabla \times A$. This result is valid everywhere in space except the current sheet itself. The electric field has in general

three nontrivial components. Only one component, which is collinear to the current distribution, is of interest to us, namely [5]²

$$E_x(x, y, z) = -\frac{2\pi^2}{dxdy\omega\epsilon_0} J_0 \sum_{m=-\infty}^{m=+\infty} \sum_{n=-\infty}^{n=+\infty} \frac{k_0^2 - k_{xmn}^2}{k_{zmn}} \tilde{f}(k_{xmn}) \tilde{g}(k_{ymn}) \exp(-jk_{xmn}x - jk_{ymn}y - jk_{zmn}z) \quad (11)$$

where the exponential z -factor appears as a fundamental solution of the Helmholtz equation to the delta function, $\delta(z)$, and the dispersion relation has the usual form

$$k_{zmn}^2 = k_0^2 - k_{xmn}^2 - k_{ymn}^2 \quad (12)$$

A Floquet mode is propagating when the solution to Eq. (12), k_{zmn} , is real. When the unit cell size in Fig. 1 does not exceed $\lambda_0/2$ in size, one can easily show using (7), (9) and (12) that only one fundamental mode with $m=n=0$ can propagate – no grating lobes exists. When the unit cell size exceeds $\lambda_0/2$, there is at least one grating lobe, in quadrature with the main beam [2].

The scan impedance, Z_S , is the impedance of one array element with all other elements excited in the proper phase/amplitude [1]. It is most simply obtained through a complex power P delivered through the surface of a unit cell by current I_0 in the antenna feed (the so-called induced *emf* method – see [8], p. 349). The starting point for obtaining the impedance is identical to the expression for an impedance of a lumped circuit element S with phasor voltage V_0 and phasor current I_0 , expressed through the complex power delivered to this element in the form:

$$Z_S \equiv \frac{P}{I_0 I_0^*} = \frac{VI_0^*}{I_0 I_0^*} = Z_S \quad (13)$$

For the unit cell, the complex power P now becomes an integral over the unit cell so that one has ([8], p. 349)

$$Z_S \equiv \frac{P}{I_0 I_0^*} \equiv \frac{- \iint_{\text{unit cell}} E \cdot J^* ds}{\left| I_0 \right|^2} = - \frac{\iint_{\text{unit cell}} E_x(x, y, z=0) \cdot J_x^*(x, y) dxdy}{I_0^2} \quad (14)$$

with $I_0 = J_0 t$ being the total current in the feed (center of the dipole) and $J_x^*(x, y)$ given by Eq. (9)

² For unidirectional dipole currents, there is no magnetic field component in the x -direction and all field components are derivable from E_x only [2].

$$J_x(x, y) = \frac{4\pi^2}{dxdy} J_0 \sum_{m=-\infty}^{m=+\infty} \sum_{n=-\infty}^{n=+\infty} \tilde{f}(k_{xmn}) \tilde{g}(k_{ymn}) \exp(-jk_{xmn}x - jk_{ymn}y) \quad (15)$$

Whilst the total current in Eq. (14) is given as real – see Eqs. (2) – we still keep the complex conjugate of current in Eq. (14) to simplify operations on individual Floquet modes. An example is given by the next step, which implies a substitution of Eqs.(11), (15) into Eq. (14). This operation creates a combination of two double sums over indexes m, n and m', n' , respectively. Only the diagonal terms with $m = m', n = n'$ are retained after taking complex conjugate and integration, due to orthogonality of the corresponding Floquet modes over the unit cell. The result has the form

$$Z_s = \frac{2\eta\pi^2}{t^2 D_x D_y k_0^2} \sum_{m=-\infty}^{m=+\infty} \sum_{n=-\infty}^{n=+\infty} \frac{1 - k_{xmn}^2 / k_0^2}{k_{zmn} / k_0} |k_0 \tilde{f}(k_{xmn})|^2 |k_0 \tilde{g}(k_{ymn})|^2 \quad (16)$$

where $D_x = d_x / \lambda_0$, $D_y = d_y / \lambda_0$ and η is the free-space impedance.

6. Effect of ground plane

When a PEC ground plane is introduced at the distance $z = -h$, the electric field for every Floquet mode is the original field plus the one reflected from the ground plane, i.e.

$$E_x \rightarrow E_x + E_x [-\exp(-jk_{zmn} 2h)] \quad (17)$$

The second term in Eq. (17) is usually only significant when $m = n = 0$, i.e. for the propagating mode. Otherwise, the reflected evanescent waves will decay very fast – an estimate for the $h = \lambda_0 / 4$ -separation gives the minimum possible decay factor as $|\exp(-jk_{zmn} 2h)| \leq \exp(-\pi\sqrt{3}) \approx 0.004$ for $m = 0, n = 1$ or $m = 1, n = 0$ modes.

Note that the minus sign (phase reversal) in front of the exponential factor in Eq. (17) would be missing if a perfect magnetic conductor (PMC) ground plane were used. Eq. (17) allows for any surface impedance to be included into consideration, such as that for a frequency-selective surface. A simple transformation yields

$$1 + [-\exp(-jk_{zmn} 2h)] = 2 \sin^2 k_{zmn} h + 2j \sin k_{zmn} h \cos k_{zmn} h \quad (18)$$

Still, the final result for the scan impedance, which implies the use of Eq. (17) or (18), is written in the form

$$Z_s = \frac{2\eta\pi^2}{t^2 D_x D_y k_0^2} \sum_{m=-\infty}^{m=+\infty} \sum_{n=-\infty}^{n=+\infty} \frac{1 - k_{xmn}^2 / k_0^2}{k_{zmn} / k_0} |P(k_{xmn}, k_{ymn})|^2 [1 - \exp(-jk_{zmn} 2h)] \quad (19)$$

since, numerically, it is much more convenient to handle the simple complex exponential factor instead of sine functions that create large singularities for complex arguments. According to Eqs. (5),

$$P(k_{xmn}, k_{ymn}) = \frac{tlk_0^2}{4\pi^2} \text{sinc}\left(\frac{k_{xmn}l}{2}\right) \text{sinc}\left(\frac{k_{ymn}t}{2}\right) \quad (20a)$$

$$P(k_{xmn}, k_{ymn}) = \frac{tl^2 k_0^3}{16\pi^2} \text{sinc}\left(\frac{(k_{xmn} + k_0)l}{4}\right) \text{sinc}\left(\frac{(k_{xmn} - k_0)l}{4}\right) \text{sinc}\left(\frac{k_{ymn}t}{2}\right) \quad (20b)$$

$$P(k_{xmn}, k_{ymn}) = \frac{tk_0}{2\pi^2} \text{cosc}\left(\frac{k_{xmn}l}{2\pi}\right) \text{sinc}\left(\frac{k_{ymn}t}{2}\right) \quad (20c)$$

for the uniform, sinusoidal, and resonant current distribution, respectively. Furthermore,

$$k_{zmn} = \begin{cases} +\sqrt{k_0^2 - k_{xmn}^2 - k_{ymn}^2} & \text{for } k_0^2 - k_{xmn}^2 - k_{ymn}^2 > 0 \\ -j\sqrt{k_{xmn}^2 + k_{ymn}^2 - k_0^2} & \text{for } k_0^2 - k_{xmn}^2 - k_{ymn}^2 < 0 \end{cases} \quad (21)$$

Eqs. (19)-(21) describe a rather general situation that implies an arbitrary unit cell size, arbitrary (non-resonant) length of the strip dipole, and arbitrary position of the ground plane (arbitrary surface impedance). These equations are indeed equivalent to the classic result of Oliner and Malech, and Stark – see Eqs. (122)-(125) of Ref. [2] – for the resonant dipole with the cosine current distribution. They have been programmed in MATLAB; a short script `imp1.m` is given in Appendix A.

An alternative approach to the scan impedance would be to use the solutions of Dr. Ben Munk and coauthors [9], [7], which are based on the impedance matrix consideration and Carter's mutual impedances between two isolated dipoles – see also [6], p.471-478. Such an approach is also applicable to finite arrays. In the following Section, we consider additional simplifications of Eqs. (19)-(21) that lead to more elegant and simple expressions for the scan impedance [1].

7. Comparison with Hansen's formulas (Ref. [1], p. 237)

In order to further proceed with the comparison, we will consider the case of the resonant dipole (Eq. (20c)) only. We will take the effect of the ground plane into account only for the fundamental propagating mode. Then, the impedance expression Eq. (19) after substitution of Eq. (20c) and using Eqs. (7), (9), (12), and some straightforward manipulations yields

$$Z_S = R_S + jX_S, \quad R_S = \frac{\eta/\pi}{\pi D_x D_y} H_{00} \csc^2\left(\frac{k_{x00}l}{2\pi}\right) \text{sinc}^2\left(\frac{k_{y00}t}{2}\right) \sin^2 k_{z00} h$$

$$X_S = \frac{0.5\eta/\pi}{\pi D_x D_y} \left[H_{00} \csc^2\left(\frac{k_{x00}l}{2\pi}\right) \text{sinc}^2\left(\frac{k_{y00}t}{2}\right) \sin 2k_{z00} h - \sum_{N^2} \sum_{[m=0, n=0]} H_{mn} \csc^2\left(\frac{k_{xmn}l}{2\pi}\right) \text{sinc}^2\left(\frac{k_{ymn}t}{2}\right) \right] \quad (21)$$

where (see [1], p. 236)

$$H_{00} = \frac{1 - k_{x00}^2 / k_0^2}{k_{z00} / k_0} = \frac{1 - (\sin \theta_0 \cos \varphi_0)^2}{\cos \theta_0}$$

$$H_{mn} = j \frac{1 - k_{xmn}^2 / k_0^2}{k_{zmn} / k_0} = \frac{\left(\sin \theta_0 \cos \varphi_0 + \frac{m}{D_x} \right)^2 - 1}{\sqrt{\left(\sin \theta_0 \cos \varphi_0 + \frac{m}{D_x} \right)^2 + \left(\sin \theta_0 \sin \varphi_0 + \frac{n}{D_y} \right)^2} - 1} \quad (22)$$

and

$$k_{xmn} = k_0 \left(\sin \theta_0 \cos \varphi_0 + \frac{m}{D_x} \right), \quad k_{ymn} = k_0 \left(\sin \theta_0 \sin \varphi_0 + \frac{n}{D_y} \right) \quad (23)$$

Eqs. (21) should be the equivalent of Eqs. (7.41), (7.42) on p. 237 of Ref. [1]. For the purposes of comparison, one notes that η has approximately the value of 120π . Further, the ratio of dipole length to wavelength on p. 237 is replaced by $1/2$ for the resonant dipole. The results then become identical, to within two minor misprints that are as follows:

1. A factor of π is missing in the denominator of the argument of the \csc function. This circumstance does not affect the scan resistance in the H-plane ($k_{x00} = 0$).
2. A sine of the double argument should be used instead of the sine square in the first term for the scan reactance³.

Note that the corresponding result of Ref. [2] (Eqs. (127), (141) on p. 253 and p. 255, respectively) does not have these misprints. Eqs. (21)-(23) are also programmed in MATLAB in Appendix A – see the script `imp2.m`. The scan impedances as a function of the scan angle θ_0 are shown in Fig. 3 in three different planes – E-plane ($\varphi_0=0\text{deg}$); D-plane ($\varphi_0=45\text{deg}$); and H-plane ($\varphi_0=90\text{deg}$). The unit cell size is $0.5\lambda_0 \times 0.5\lambda_0$. The

³ Corrected in *Errata and Additions List* to Ref. [1] at <http://www.rchansen.com/paaerrat.htm>

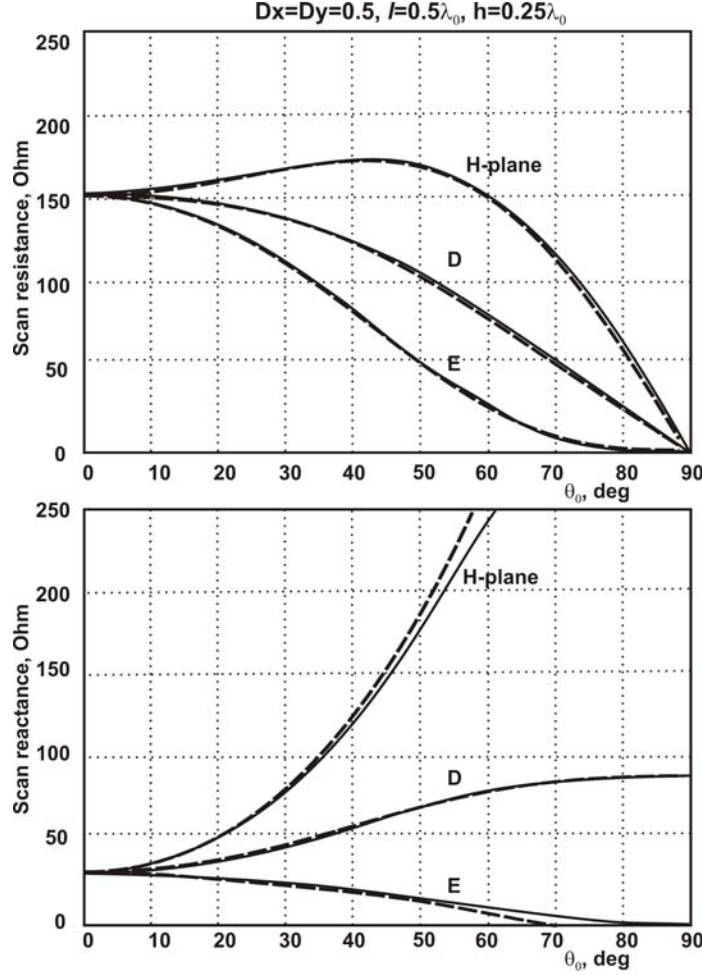


Fig. 3. Scan resistance/reactance as a function of the scan angle θ_0 in three different planes – E-plane ($\varphi_0 = 0\text{deg}$); D-plane ($\varphi_0 = 45\text{deg}$); and H-plane ($\varphi_0 = 90\text{deg}$). The unit cell size is $0.5\lambda_0 \times 0.5\lambda_0$. Solid curves – Hansen’s [1] plots – figures 7.18, 7.19; dashed curves –results from script `imp2.m`, with 30 terms in every sum.

dipole length is exactly $0.5\lambda_0$. The dipole width (it has a rather insignificant influence on the scan impedance) is chosen as $0.001\lambda_0$ in accordance with Ref. [1], p. 244. Dashed curves are those obtained from Eqs. (21)-(23) using script `imp2.m`; solid curves show the data *directly* adopted from Ref. [1] – see figures 7.18 and 7.19.

Some disagreement between two sets of results for reactance may be seen, at larger scanning angles. It is probably due to the simplified treatment of the ground plane in Eqs. (21)-(23); the textbook figures most likely follow to the more general scheme (19)-(21). To support this conclusion, Fig. 4 shows the scan impedance behavior for the same configuration, but for the unit cell size of $0.7\lambda_0 \times 0.7\lambda_0$, when a grating lobe appears at approximately 25.4 deg from zenith. Those results are obtained with script `imp1.m`. The

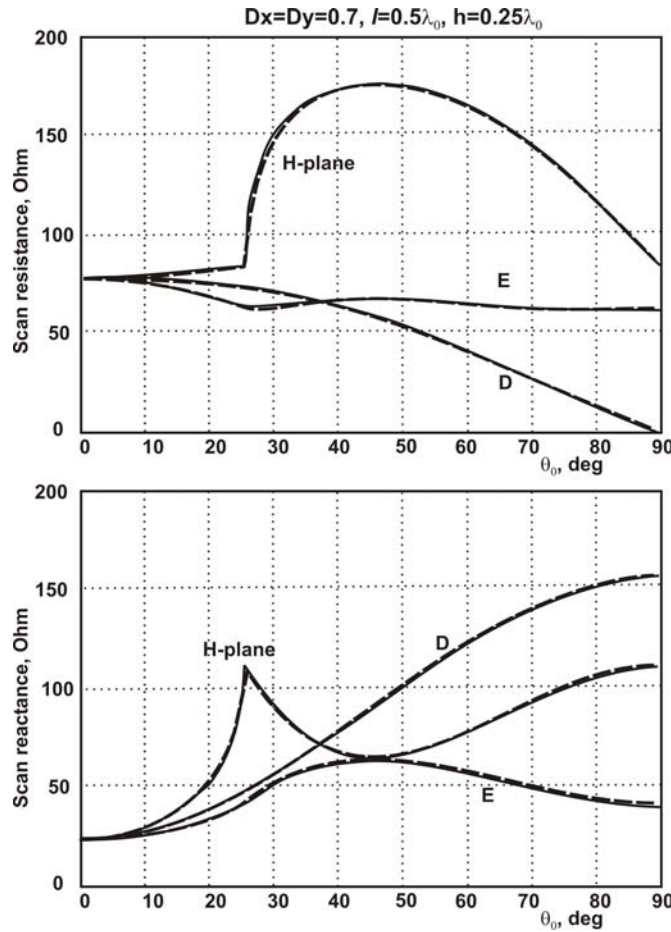


Fig. 4. Scan resistance/reactance as a function of the scan angle θ_0 in three different planes – E-plane ($\varphi_0=0\text{deg}$); D-plane ($\varphi_0=45\text{deg}$); and H-plane ($\varphi_0=90\text{deg}$). The unit cell size is $0.7\lambda_0 \times 0.7\lambda_0$. Solid curves – Hansen’s [1] plots – figures 7.24, 7.25; dashed curves – results from script `imp1.m`, with 30 terms in every sum.

solid curves again indicate the corresponding scan data *directly* adopted from textbook [1] - see figures 7.24 and 7.25. Both sets of results are now nearly identical.

The value of the scan resistance at zenith ($\theta_0 = 0, \varphi_0 = 0$) in Fig.3, $R_s \approx 153\Omega$, is originally that of Wheeler [10]. In [10], this value is established analytically, for an array of half-wave dipoles with half-wave separation; each dipole has an effective length of $a_{\text{eff}} = \frac{2}{\pi} \frac{\lambda_0}{2} = \frac{\lambda_0}{\pi}$. The scan resistance at zenith therefore becomes [10]

$$R_s = \eta \frac{a_{\text{eff}}^2}{dx dy} = \eta \frac{(\lambda_0/\pi)^2}{(\lambda_0/2)^2} \approx 153\Omega \quad (24)$$

Thus, the assumption of effective resonant dipole length being equal to λ_0/π is equivalent to the assumption of the exactly cosine current distribution along the dipole. The real current distribution in the infinite dipole array may be significantly different from that – see below. Also, in order to replicate this resistance value in a full-wave dipole array numerical model, we should use not exactly the $\lambda_0/2$ dipoles but rather the *resonant* thin dipoles, whose length is slightly less than $\lambda_0/2$, namely $0.48\lambda_0$ [6] – see below.

Another argument supporting the importance of the current distribution lies upon the inspection of the scan impedances obtained with the uniform current distribution model (20a). For half wave dipoles, they have almost nothing in common with the more realistic data from Eqs.(20b,c) – all Floquet modes are being excited in this case– but start to approach those for rather small dipoles.

8. Ansoft HFSS numerical model

The corresponding Ansoft HFSS v. 10 project is shown in Fig. 5. It was created by the author, then corrected by the Ansoft staff, and finally slightly modified in order to ensure the proper parameter and boundary setup.

The Ansoft HFSS setup uses the fixed waveguide approach to the unit cell, discussed in [2] and in preceding references. The simplest way to understand this approach is to consider scanning at zenith, when every array element becomes equivalent to an isolated element in a hypothetical rectangular waveguide having two PEC walls (parallel to the H -plane) and two PMC walls (in the E -plane), due to symmetry reasons. At other scanning angles, one may consider a similar rectangular skew waveguide, now deformed in the scanning direction, with the same pairs of PEC/PMC walls.

Alternatively, one may still consider the fixed vertical waveguide but with the mixed boundary conditions on two pairs of the walls. The boundary conditions on one wall replicate the boundary conditions on the opposite wall to within a phase shift that is a function of the scanning angles – the periodic boundary conditions. In Ansoft HFSS, the pair of the walls with the periodic boundary conditions is designated as *master* and *slave* – see Fig. 5 – the order of them unimportant. However, they need to be aligned with respect to each other as shown in Fig. 5. This is done by a proper choice of two directional unit vectors u, v .

If the upper top of the waveguide were using the simple radiation boundary then the waveguide itself would need to be infinitely long - some numerical experiments with the waveguide lengths of $3-5\lambda_0$ indicated very poor convergence. Instead, a Perfectly Matched Layer (PML) box should be used as shown in Fig. 5. The critical point is to introduce the same periodic boundary conditions on the vertical side walls of the PML box – see Fig. 5. Otherwise, the results become nearly as inaccurate as those for the

radiation boundary. The PEC ground plane can be either finite or infinite; the results are not affected by that choice.

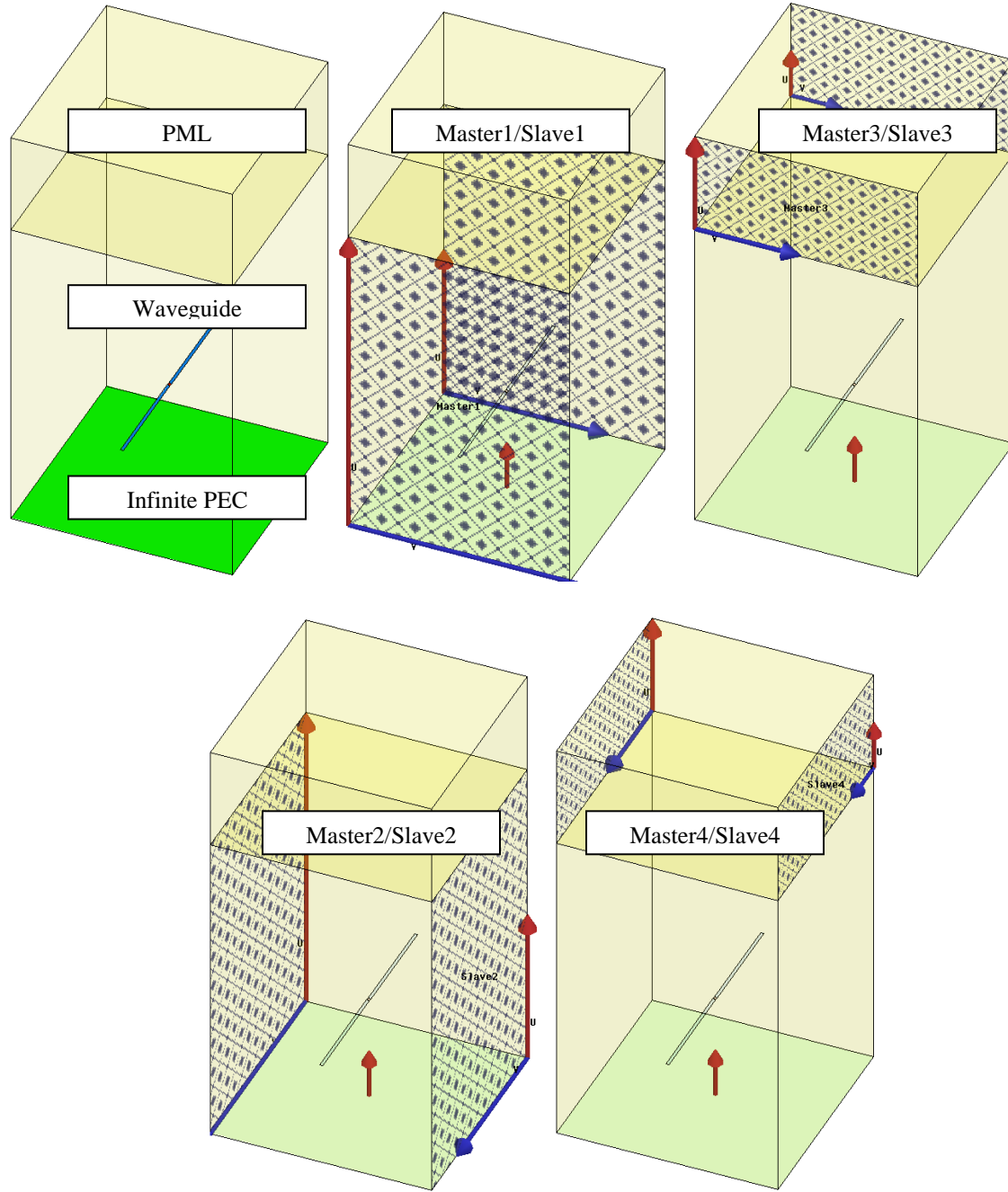


Fig. 5. Boundary conditions for the unit cell approach to a dipole array over a ground plane in Ansoft HFSS. The desired scanning angles are specified for every boundary and should be the same.

The following parameters have been chosen:

Center frequency,	$f_0 = 10 \text{ GHz}$
Wavelength,	$\lambda_0 = 30.0 \text{ mm}$
Total dipole length (from end to end),	$l = 0.495\lambda_0 \text{ or } l = 0.48\lambda_0$
Dipole strip width,	$t = \lambda_0 / 160$
Feed length (included into dipole length),	$l_s = \lambda_0 / 160$
Unit cell size,	$0.5\lambda_0 \times 0.5\lambda_0 \text{ or } 0.7\lambda_0 \times 0.7\lambda_0$
Unit cell height H (without PML),	$0.75\lambda_0 \text{ or } \lambda_0$; ground plane at $\lambda_0 / 4$
PML thickness,	$\approx 0.25\lambda_0$
Final meshes, tetrahedra,	$18 - 37e3 H = 3/4\lambda_0 \text{ or } 31 - 50e3 H = \lambda_0$
Iterative convergence	good in all cases; 17 to 20 refinement passes
Sweep for all periodic boundaries	over scan angle θ_0 from 0 to 90 deg over scan angle φ_0 from 0 to 90 deg

The dipole feed was modeled by a lumped port. The scan impedance as a function of the scan angle θ_0 was found as a dipole input impedance, for the different values of θ_0 and φ_0 . Three azimuthal angles corresponding to three different scan planes – E-plane ($\varphi_0=0\text{deg}$); D-plane ($\varphi_0=45\text{deg}$); and H-plane ($\varphi_0=90\text{deg}$) – have been considered. It has also been found that the results are weakly affected by the unit cell height. Therefore, only two values of the height are considered in this text.

The number of adaptive passes was adjusted in order to have the final mesh sizes on the order of 20,000-50,000 tetrahedra; further mesh refinement up to 100,000 tetrahedra did not alter the results significantly. The impedance curves were then exported to MATLAB and processed, along with the analytical results.

9. Comparison of analytical results with simulations

9.1 Comparison for a $0.5\lambda_0$ array – $0.495\lambda_0$ long dipoles

Comparison results are shown in Fig. 6 that follows. The value of dipole length is chosen as $0.495\lambda_0$. It is only slightly less than $0.5\lambda_0$, which nevertheless ensures the necessary physical separation of the dipole from the periodic boundary. Fig. 6 depicts the data for an array of dipoles spaced by $0.5\lambda_0$ in both dimensions and separated by $0.25\lambda_0$ from the ground plane (no scan blindness).

The agreement between theory and simulations for the scan resistance/reactance is marginally acceptable, except the *H*-plane case in Fig. 6. However, the numerical resistance data typically shows a large deviation from the theoretical value (Eq. (24)) at zenith. The scan resistance at zenith in Fig. 6 is not 153Ω (cf. Eq. (24)) but is rather about 188Ω . Such a difference becomes understandable if we remember that the $\lambda_0/2$ dipole is in fact not the *resonant* thin dipole. The resonant thin dipole should have the length of about $0.48\lambda_0$ - see, for example, [6], p. 184.

9.2 Comparison for a $0.5\lambda_0$ array – $0.480\lambda_0$ long dipoles

We could now try to align the scan resistance at zenith by choosing a resonant dipole of the total length $0.48\lambda_0$. All other parameters remain the same. Fig. 7 gives the results. Whilst the resistance results (except the *H*-plane) are now much closer (as expected) in theory and simulations, the reactance data shows a larger deviation compared to the previous case of the exactly half wave dipoles.

9.3 Comparison for a $0.7\lambda_0$ array – $0.495\lambda_0$ long dipoles

Comparison results are shown in Fig. 8 that follows. The dipole length is again $0.495\lambda_0$. Fig. 8 depicts the data for an array of dipoles spaced by $0.7\lambda_0$ in both dimensions and separated by $0.25\lambda_0$ from the ground plane (scan blindness). The grating lobe at 25.4 deg from zenith is identified quite well but otherwise the agreement between theory and simulations is not very impressive. The best agreement is again observed in the *E*-plane.

9.4 Comparison for a $0.7\lambda_0$ array – $0.480\lambda_0$ long dipoles

For the purposes of completeness, we present in Fig. 9 results for $0.48\lambda_0$ -long dipoles. The resistance results are again much closer in theory and simulations; however, the reactance data shows a larger deviation compared to the previous case of the exactly half wave dipole.

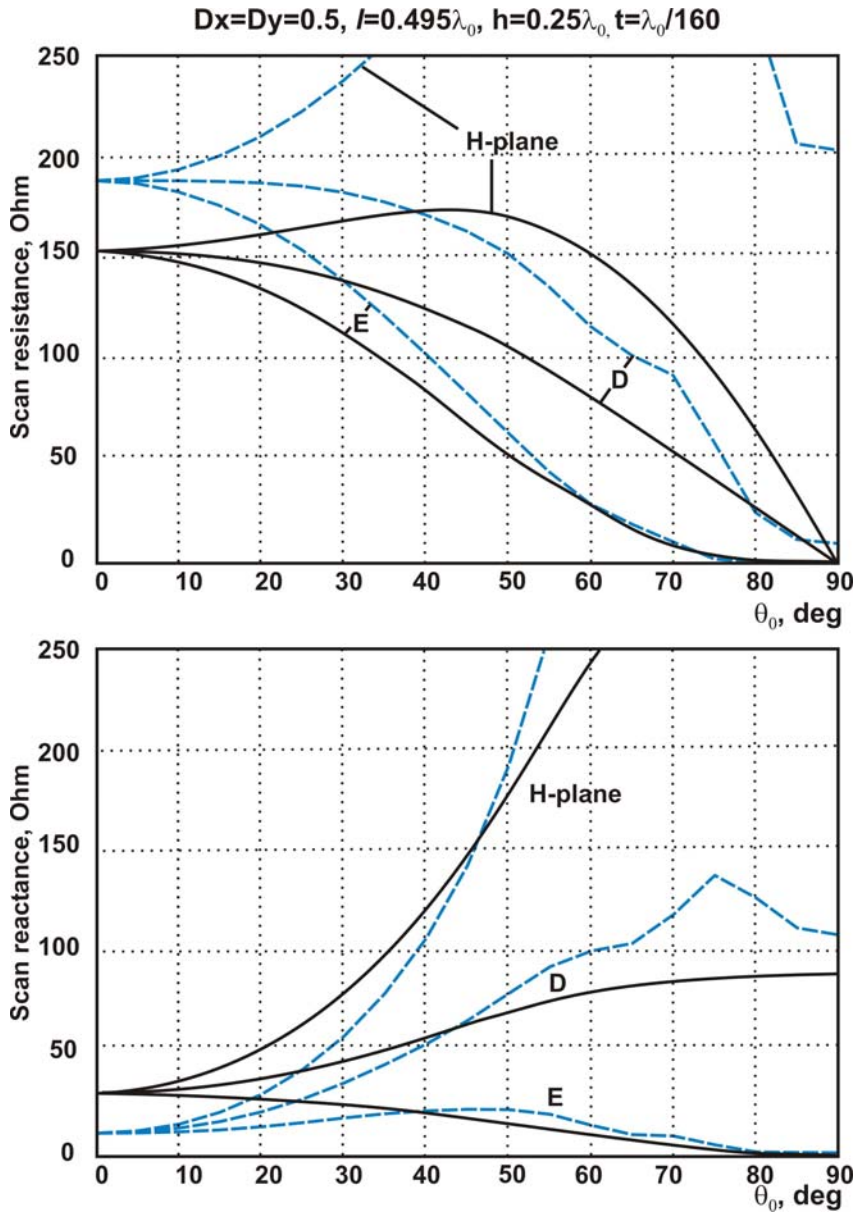


Fig. 6. Scan resistance (top) and reactance (bottom) as a function of the scan angle θ_0 in three different planes – *E*-plane ($\varphi_0=0$ deg); *D*-plane ($\varphi_0=45$ deg); and *H*-plane ($\varphi_0=90$ deg). The unit cell size is $0.5\lambda_0 \times 0.5\lambda_0$. Solid curves –analytical solutions for a $\lambda_0/2$ -dipole; dashed curves – the corresponding Ansoft HFSS numerical model with dipole length $0.495\lambda_0$, dipole width $\lambda_0/160$, and unit cell height of $0.75\lambda_0$ (18,000 tetrahedra). θ_0 -step is 5 deg.

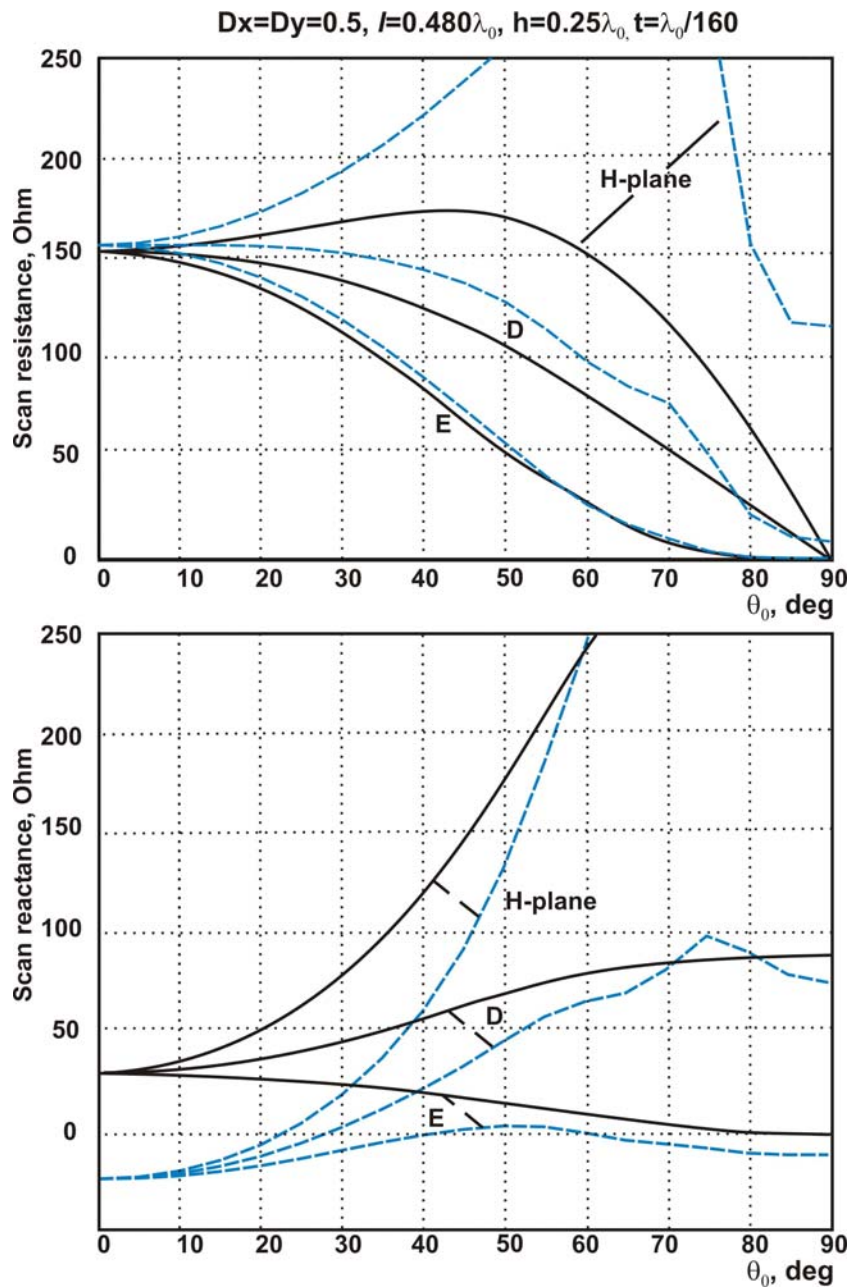


Fig. 7. The same results as in Fig. 6 but the simulated dipole length is now $0.48\lambda_0$.

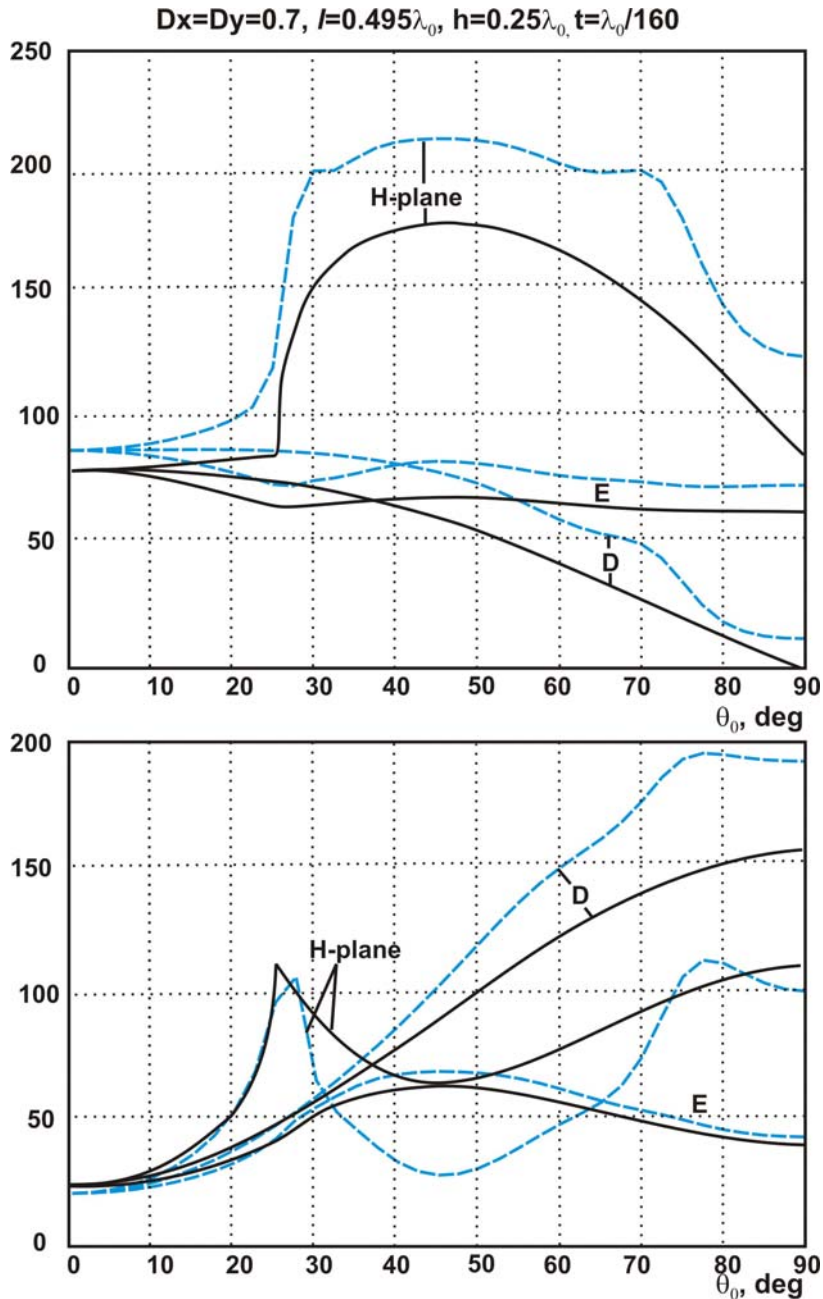


Fig. 8. Scan resistance (top) and reactance (bottom) as a function of the scan angle θ_0 in three different planes – E -plane ($\varphi_0=0\text{deg}$); D -plane ($\varphi_0=45\text{deg}$); and H -plane ($\varphi_0=90\text{deg}$). The unit cell size is $0.7\lambda_0 \times 0.7\lambda_0$. Solid curves –analytical solutions for a $\lambda_0/2$ -dipole; dashed curves – the corresponding Ansoft HFSS numerical model with dipole length $0.495\lambda_0$, dipole width $\lambda_0/160$, and unit cell height of $0.75\lambda_0$ (37,000 tetrahedra). θ_0 -step is 2.5 deg.

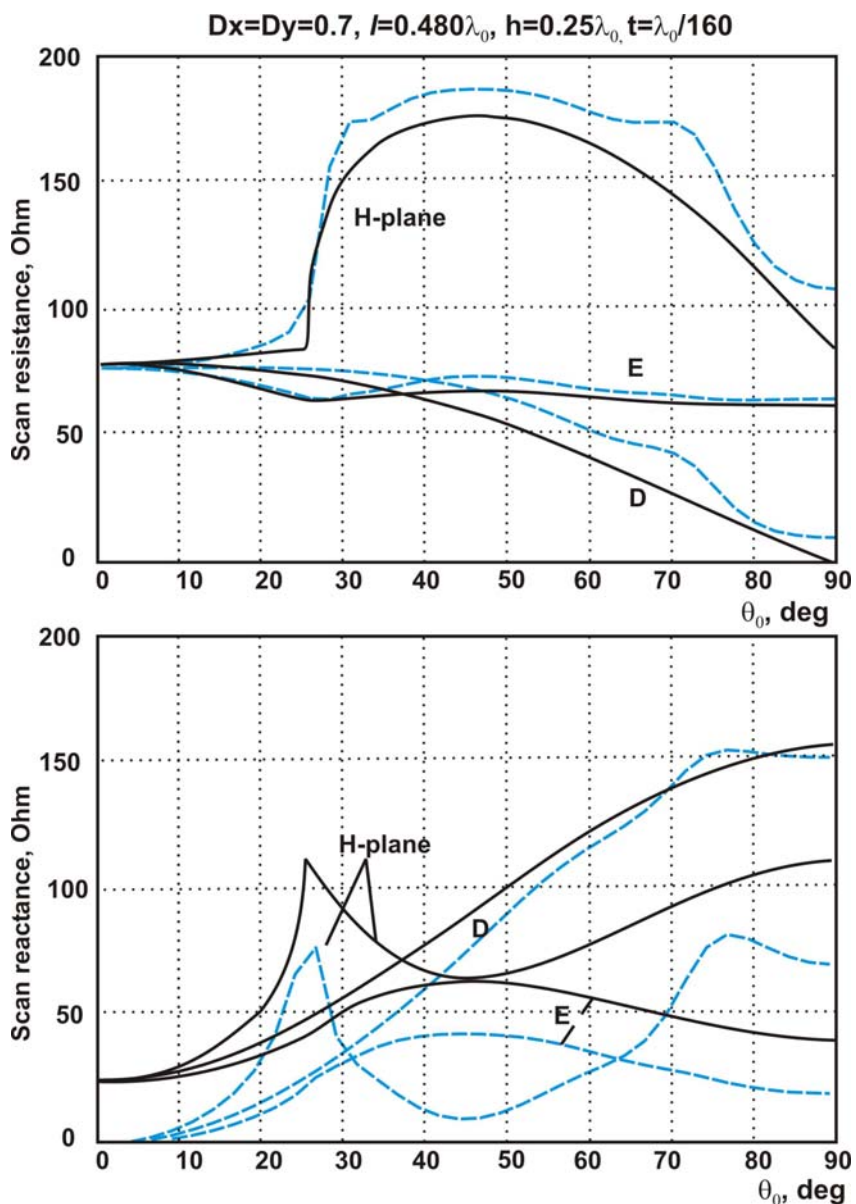


Fig. 9. The same results as in Fig. 8 but the simulated dipole length is now $0.48\lambda_0$.

10. Conclusions

It may become apparent from these sets of data that both the theory results and numerical simulations have their weaknesses and strength for this particular problem. The best agreement between the present canonical theory and the FEM modeling is obtained in the *E*-plane, which points us to some potential problems with this particular implementation of periodic BCs for a fixed-waveguide geometry at different azimuthal angles – see Fig. 5. Note that the numerical results do not vary significantly if we change (increase) the height of the unit cell. Also note that the MoM numerical solutions typically show a better agreement with the spectral analytical approaches – see, for example, [13] and [1], p. 231.

The value of the existing analytical model should be in a rapid estimation of the antenna array performance over a frequency band of interest, whilst the value of the numerical simulations is in the fine tuning of the model. Indeed, more realistic array elements may be considered numerically, with comparably little efforts, such as printed dipoles [11,13], patch antennas [12], etc. [5].

Acknowledgements

The author is thankful to Ms. Shu Li of Ansoft Burlington for the help with periodic BCs for the PML box. The author also values discussions with Mr. Angelo Puzella of Raytheon Company, Dr. Reinhold Ludwig, Mr. Vishwanath Iyer, and Mr. Christopher Hamman, of Worcester Polytechnic Institute, MA. Interest and help of Dr. Robert C. Hansen and of Dr. Hans Steyskal are highly appreciated.

References

1. R. C. Hansen, *Phased Array Antennas*, Wiley, New York, 1998.
2. A. A. Oliner and R. G. Malech, "Mutual coupling in infinite scanning arrays," in *Microwave Scanning Antennas*, Vol. II, R.C. Hansen, ed., Academic Press, 1966, Chapter 3, pp. 195-335.
3. L. Stark, *Radiation Impedance of a Dipole in Infinite Arrays*, Hughes Aircraft Company Technical Report No. FL60-230, 1960.
4. L. Stark, "Radiation impedance of a dipole in an infinite planar phased array," *Radio Science*, vol. 1, March 1966, pp. 361-377.
5. A. K. Bhattacharyya, *Phased Array Antennas: Floquet Analysis, Synthesis, and Active Array Systems*, Wiley, New York, 2006.
6. C. A. Balanis, *Antenna Theory*, Wiley, New York, 2005, 3rd ed.
7. R. C. Hansen, "Cross polarization of microstrip patch antennas," *IEEE Trans. Antennas and Propagation*, vol. AP-35, no. 6, June 1987, pp. 731-732.
8. R. F. Harrington, *Time-Harmonic Electromagnetic Fields*, McGraw Hill, New York, 1961 (Reprinted IEEE-Wiley, New York, 2001).
9. Ben A. Munk, *Frequency Selective Surfaces – Theory and Design*, Wiley, New York, 2000, Ch. 3, Ch. 4.
10. H. A. Wheeler, "The radiation resistance of an antenna in an infinite array or waveguide," *Proceedings of the I.R.E.*, April 1948, pp. 478-487.
11. D. M. Pozar and D. H. Schaubert, "Scan blindness in infinite phased array of printed dipoles," *IEEE Trans. Antennas and Propagation*, vol. AP-32, no. 6, June 1984, pp. 602-610.
12. D. M. Pozar and D. H. Schaubert, "Analysis of an infinite array of rectangular microstrip patches with idealized probe feeds," *IEEE Trans. Antennas and Propagation*, vol. AP-32, no. 10, Oct. 1984, pp. 1101-1107.
13. J.-P. R. Bayard, M. Cooley, and D. H. Schaubert, "Analysis of infinite arrays of printed dipoles on dielectric sheets perpendicular to the ground plane," *IEEE Trans. Antennas and Propagation*, vol. AP-39, no. 12, Dec. 1991, pp. 1722-1732.
14. R. C. Hansen, Private communication, July 6th 2007.

Appendix A

Script `imp1.m` – Scan impedance for an array of planar dipoles with arbitrary parameters (Floquet model)

```

clear all
const.epsilon      = 8.85418782e-012;                      % ANSOFT HFSS value
const.mu          = 1.25663706e-006;                     % ANSOFT HFSS value
const.c           = 1/sqrt(const.epsilon*const.mu);
const.eta         = sqrt(const.mu/const.epsilon);

f0      = 10*1e9;
lambda0 = const.c/f0;
k0      = 2*pi*f0/const.c;
Dx      = (0.7*lambda0)/lambda0;
Dy      = (0.7*lambda0)/lambda0;
h       = lambda0/4;
dlength = lambda0/2;
t       = lambda0/1000;

theta0  = [0:89]/180*pi;
phi0    = [0:45:90]/180*pi;
color   = ['r' 'g' 'b'];

% Scan impedance
M = [-15:15]; N = [-15:15]; % Size of the Floquet series
for k =1:3
    DUMMY = 0;
    for m=1:length(M)
        for n=1:length(N)
            kxmn   = k0*(sin(theta0).*cos(phi0(k)) + M(m)/Dx);
            kymn   = k0*(sin(theta0).*sin(phi0(k)) + N(n)/Dy);
            for p =1:length(theta0)
                temp = k0^2-kxmn(p)^2-kymn(p)^2;
                if temp>0
                    kzmn(p)= +sqrt(temp);
                else
                    kzmn(p)=-j*sqrt(-temp);
                end
            end
            Hmn     = (1-kxmn.^2/k0^2)./(kzmn/k0);
            %-----uniform-----
            % P      = (t*dlength*k0^2/(4*pi^2))*sinc(kxmn*dlength/2/pi).*sinc(kymn*t/2/pi);
            %-----resonant-----
            % P      = (t*k0/(2*pi^2))*cosc(kxmn*dlength/(2*pi)).*sinc(kymn*t/2/pi);
            %-----arbitrary-----
            P      = (t*dlength^2*k0^3/(16*pi^2))*...
                     sinc((kxmn+k0)*dlength/4/pi).*sinc((kxmn-...
                     k0)*dlength/4/pi).*sinc(kymn*t/2/pi);
            %-----
            DUMMY   = DUMMY +(2*const.eta*pi^2)./(t^2*Dx*Dy*k0^2).*Hmn.*P.^2.* (1-exp(-j*kzmn*2*h));
        end
    end
    Zs(k,:) = DUMMY;
end

Rs = real(Zs); Xs = imag(Zs);
f1 = figure; grid on; hold on;
for k =1:3
    plot(theta0*180/pi, Rs(k,:), color(k), 'LineWidth', 2);
end
axis([0 90 0 200]);
f1 = figure; grid on; hold on;
for k =1:3
    plot(theta0*180/pi, Xs(k,:), color(k), 'LineWidth', 2);
end
axis([0 90 0 200]);

```

Script **imp2.m** – Scan impedance for an array of planar resonant dipoles (Floquet model)

```

clear all
const.epsilon      = 8.85418782e-012;                      % ANSOFT HFSS value
const.mu          = 1.25663706e-006;                      % ANSOFT HFSS value
const.c           = 1/sqrt(const.epsilon*const.mu);
const.eta         = sqrt(const.mu/const.epsilon);

f0      = 10*1e9;
lambda0 = const.c/f0;
k0      = 2*pi*f0/const.c;
Dx      = (0.5*lambda0)/lambda0;
Dy      = (0.5*lambda0)/lambda0;
h       = lambda0/4;
dlength = lambda0/2;
t       = lambda0/1000;

theta0  = [0:89]/180*pi;
phi0    = [0:45:90]/180*pi;
color   = ['r' 'g' 'b'];

% Scan resistance
f1 = figure; hold on; grid on;
for k=1:3
    kx00   = k0*(sin(theta0).*cos(phi0(k)));
    ky00   = k0*(sin(theta0).*sin(phi0(k)));
    kz00   = k0*cos(theta0);
    H00    = (1-(sin(theta0).*cos(phi0(k))).^2)./cos(theta0);
    Rs     = (const.eta/pi)./(pi*Dx*Dy).*H00.*...
              (cosc(kx00*dlength/(2*pi)).^2).*...
              (sinc(ky00*t/2/pi).^2).* (sin(kz00*h).^2);
    plot(theta0*180/pi, Rs, color(k), 'LineWidth', 2);
    axis([0 90 0 250]);
end

% Scan reactance
f2 = figure; hold on; grid on;
for k=1:3
    kx00   = k0*(sin(theta0).*cos(phi0(k)));
    ky00   = k0*(sin(theta0).*sin(phi0(k)));
    kz00   = k0*cos(theta0);
    H00    = (1-(sin(theta0).*cos(phi0(k))).^2)./cos(theta0);
    Xs     = (0.5*const.eta/pi)./(pi*Dx*Dy).*H00.*...
              (cosc(kx00*dlength/(2*pi)).^2).*...
              (sinc(ky00*t/2/pi).^2).* (sin(2*kz00*h));
    M = [-20:20]; % Size of the Floquet series
    N = [-20:20]; % Size of the Floquet series
    for m=1:length(M)
        for n=1:length(N)
            if ((M(m)==0)&(N(n)==0)) continue; end;
            kxmn   = (sin(theta0).*cos(phi0(k)) + M(m)/Dx);
            kymn   = (sin(theta0).*sin(phi0(k)) + N(n)/Dy);
            Hmn   = (kxmn.^2-1)./sqrt(kxmn.^2 + kymn.^2 - 1);
            Xs     = Xs + (-1)*...
                      (0.5*const.eta/pi)./(pi*Dx*Dy).*Hmn.*...
                      (cosc(k0*kxmn*dlength/(2*pi)).^2).*...
                      (sinc(k0*kymn*t/2/pi).^2);
        end
    end
    plot(theta0*180/pi, Xs, color(k), 'LineWidth', 2);
    axis([0 90 0 250]);
end

```

Script **cosc.m** [14]

```

function [y] = cosc(x)
y = cos(pi*x)./(1-4*x.^2);

```

High Performance Phased Arrays of Doubly Mirrored Balanced Antipodal Vivaldi Antenna (DmBAVA): Current Development and Future Considerations

M. W. Elsallal^(1,2) and D. H. Schaubert⁽¹⁾

(1) Center for Advanced Sensor and Communications Antennas

Department of Electrical and Computer Engineering

University of Massachusetts, Amherst, MA 01003

w.elsallal @ ieee.org and schaubert @ ecs.umass.edu

(2) Advanced Technology Center

Rockwell Collins, Inc. Cedar Rapids, IA 52489

waelsall @ rockwellcollins.com

Abstract: In this paper, the Single Polarized DmBAVA infinite array that was presented last year has been fabricated and measured in an H plane parallel plate waveguide simulator to resemble an infinite x finite array analysis. The array confirmed high performance capabilities being electrically short ($\sim \lambda_{\text{Highest-Frequency}}/2$), broadband (3:1), and capable of wide scan volume (+/- 45°). Furthermore, it was found that adding metallic posts placed strategically in the unit cell will tune the antenna performance. Finally, a magnetic current slot was created inside the metallic flare to enhance the impedance match. Both techniques have extended the operating bandwidth in E-plane to more than two octaves (5.4:1) without sacrificing the modularity feature in the array.

1. Introduction

The growth in the demand for low profile, light weight and high performance phased arrays has led to more interest in developing modular types of radiating elements to reduce the array's fabrication and maintenance costs [1, 2]. The authors surveyed the literature and have identified six radiating elements that may meet the demand: the short Vivaldi antennas [3], the Bunny-Ear antenna [4], the Body of Revolution (BOR) antenna [5], the interlaced printed dipole antennas [6], the fragmented aperture [7], and the Doubly-mirrored Balanced Antipodal Vivaldi Antenna (DmBAVA) [8]. The latest development of DmBAVA is of particular interest in this paper because it naturally is not connected to its neighbors, electrically and mechanically (hence ensuring modularity) and it does not require impedance transformation nor close spacing between elements.

The DmBAVA is a variation of the conventional Balanced Antipodal Vivaldi Antenna (cBAVA) that was first introduced in reference [9]. When the broadband single element of cBAVA is inserted in a planar array environment as a modular element with no contiguous electrical connection to the adjoining elements, two impedance anomalies limit the operating bandwidth to less than 1.4:1 [10]. Numerical studies suggest that the BAVA element's depth should be made as short as possible to move high frequency anomaly above the grating lobe frequency. Also, the low frequency anomaly was found to be sensitive to element parameters and array spacing. When metallic crosswalls are inserted parallel to the H plane of the array, they alter the mutual coupling, and suppress the monopole radiation from the triline feed section; hence they eliminate the low frequency anomaly [2,11]. This configuration is called conventional BAVA with metallic crosswalls (cBAVAm).

If the metallic walls of the cBAVAm were made infinitely high, the elements of each row would be mirrored in these walls so that adjacent rows are images in the E-plane direction. Adopting this type of mirror symmetry in the array with finite height walls and also reversing adjacent elements along the H-plane creates a doubly mirrored BAVA array, DmBAVA, as is shown in figure 1 and reference [8]. To maintain the radiation pattern of the array, adjacent elements are excited 180° out of phase yielding in-phase parallel electric field vectors at the element apertures.

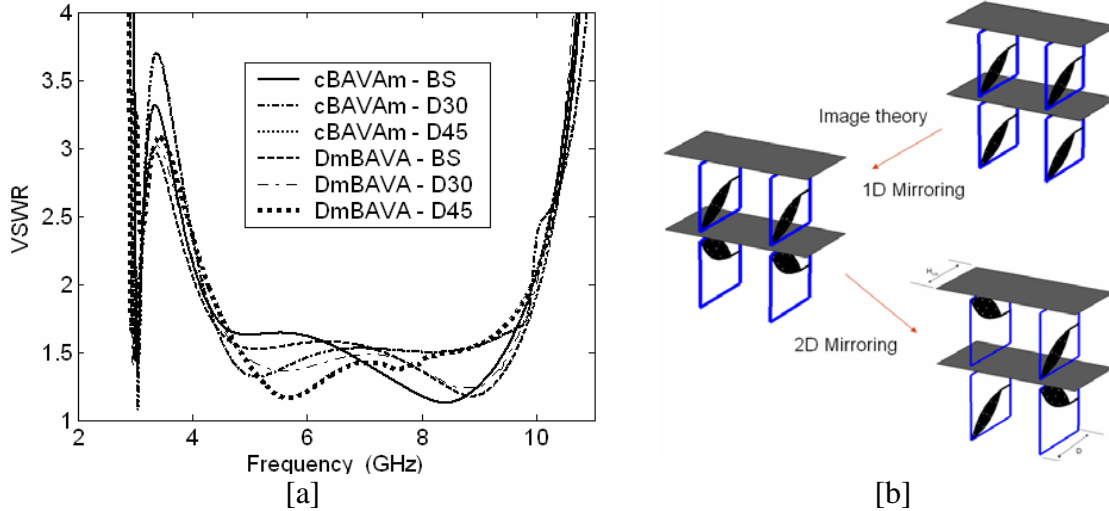


Figure 1: [a] Active VSWR performance of Doubly mirrored BAVA (DmBAVA) in diagonal plane vs. the conventional BAVA with metallic cross walls (cBAVAm). Grating lobes enter visible space at frequencies above 10 GHz. [b] Only the outer conductors of BAVA are shown to simplify illustration. $D=1.5\text{cm}$, $A=B=1.51\text{cm}$, $H_a=1.26\text{cm}$, $\epsilon_r=3.0$, $t=90\text{mils}$. Vias are inserted in the substrate.

In last year's symposium, the single polarized (SP) DmBAVA array shown in figure 1 was transformed into a dual-polarized (DP) version, and has retained similar bandwidth performance and modular features [12,13]. Note that in figure 1, there is not much

difference in the bandwidth performance of the SP array realized by cBAVAm or DmBAVA unit cells. However, the DmBAVA unit cell in DP array has wider utilization of the bandwidth its' double-mirroring symmetry eliminates a high frequency resonance appear at all scan-angles in the DP array that uses the cBAVAm configuration [11].

The trade-off associated with air gap periodicity between individual elements and subarrays of the SP-DmBAVA was discussed, resulting into an introduction of a 2x2 modular subarray that is capable of 3.75:1 bandwidth over more than 30° scan volume [13]. Most recently, this modular subarray was fine-tuned to create a DP version that has bandwidth as wide as 4.4:1 at broadside and up to 4:1 bandwidth for 45° scan-volume [3].

This paper confirms the numerical analyses presented last year and introduces a new variation of DmBAVA with more than two octave bandwidth 5:1 over wide scan angles.

2. Measurement of DmBAVA in Parallel Plate Waveguide Simulator

In the past, the DmBAVA performance was evaluated in PBFDTD [14], and was occasionally validated in Ansoft HFSS [15] and CST MWS [16]. In this section, the numerical analyses are validated against measurement.

The double-mirroring technique of the asymmetric BAVA (i.e. center conductor inside the dielectric substrate and outer conductors are exposed to air) makes this antenna well suited for phased array measurement in a metallic waveguide simulator [17] to verify the PBFDTD simulations. Figure 2 depicts the asymmetry of BAVA element and the E-plane mirror symmetry of a waveguide simulator. Note that this was not possible in conventional BAVA array configuration [10].

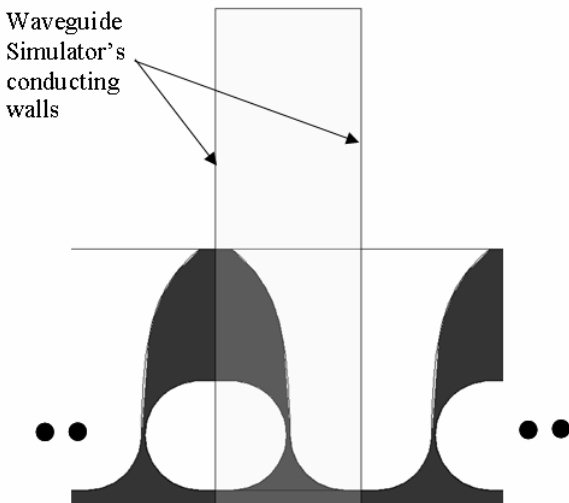


Figure 2: Equivalent infinite array of BAVA modeled inside the waveguide simulator.

The parallel plate waveguide simulator, which was built by the Center of Advanced Sensor and Communication and Antennas (CASCA) at University of Massachusetts, has been utilized in this work. The basic concepts of how the parallel plate waveguide works was reported in [18]. The physical structure of the parallel plate waveguide simulator is shown in figure 3. It consists of three modules. The height and length of each module are 2 cm and 10 cm respectively, and it can house 16 elements in grooves spaced 2 cm apart. This spacing corresponds to a square grid with highest operating frequency of 7.5 GHz for half – wavelength spacing. The distribution of the BAVA elements inside the first module is shown in figure 3b-c. The elements are mirrored along the upper and lower waveguides walls to reproduce the DmBAVA configuration.

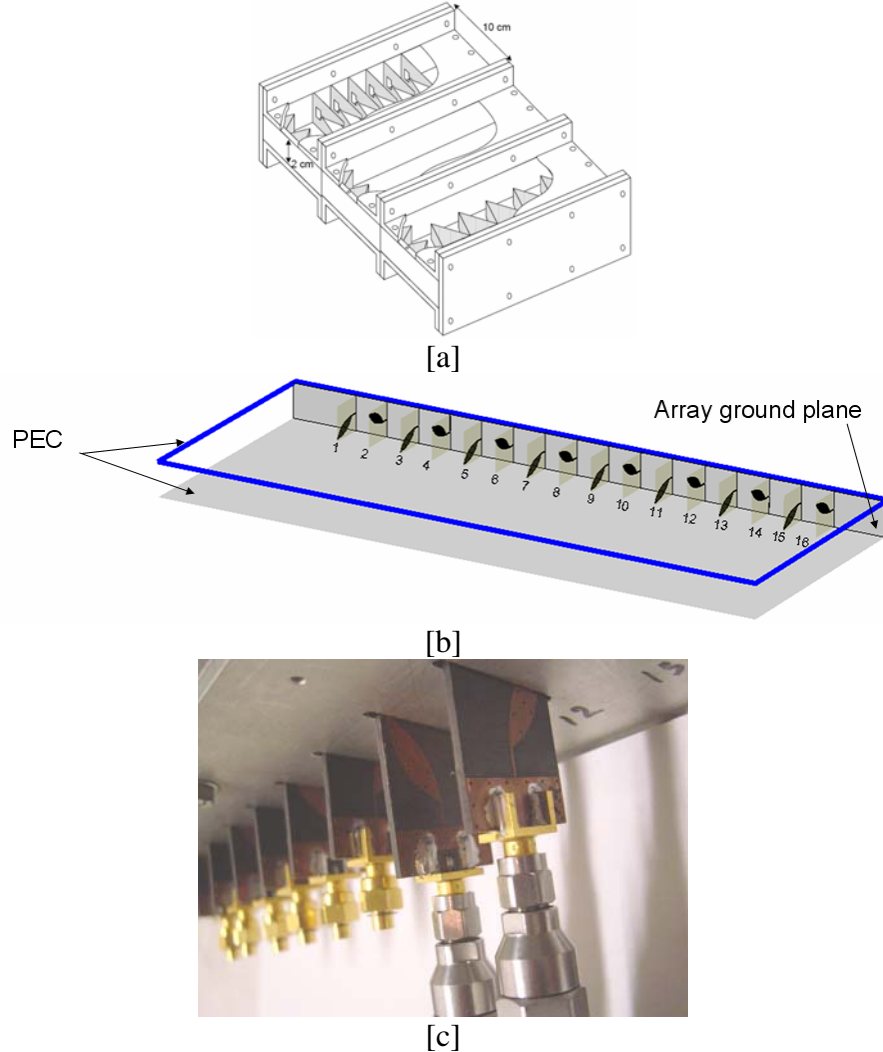


Figure 3: Measuring performance of DmBAVA configuration in parallel plate waveguide simulator. [a] Modular structure of the waveguide simulator with Vivaldi antennas. Foams are placed on the side to absorb any reflection. [b] Distribution of the H-plane 16xinfinite mirrored DmBAVA array. [c] Photo of alternating BAVA distribution along H plane.

The BAVA elements were fabricated on 60mils Duriod 5880 substrate with a stripline feed. The antenna design parameters were discussed in [8], where the overall dimensions of the radiating element are about 2.00cm width by 2.025cm depth.

The S-parameters coupling matrix of all 16 elements inside the parallel plate waveguide simulator has been measured. Thus from the S-matrix, the active reflection coefficient of an element can be computed using the relation below. The [S] parameters of the odd-numbered elements are modulated by 180° phase shift to maintain the radiation pattern of the array as was discussed earlier. The results are presented in figure 4.

$$\Gamma_{active_m} = \sum_{n=1}^{16} (-1)^n S_{mn} e^{j(m-n)d_y \sin \theta_0} \quad (1)$$

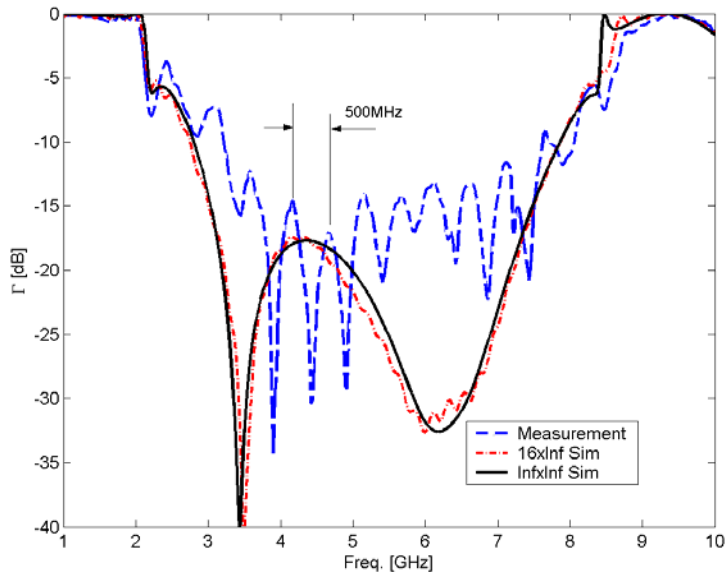


Figure 4: Active reflection coefficient of the measured and simulated infinite \times 16 DmBAVA elements in parallel plate waveguide simulator at broadside. Response calculated for the center element. $D=2.025\text{cm}$, $A=B=2.00\text{ cm}$, $H_a=1.8\text{cm}$, $\epsilon_r=2.2$, $t=60\text{mils}$. Vias are inserted in the substrate.

The antenna has a good impedance match between 2.5 GHz – 7.8 GHz that is 3:1 bandwidth for a grating-lobe free operation. Simulated and measured results have agreed on the frequencies of the anomalies occurring at 2 GHz and 9.5 GHz. The 500MHz ripples in the measured data are associated with reflection from the foam because they scale $\lambda/2$ with the depth of the waveguide simulator's module. This has been further verified when the experiment was repeated using 8 DmBAVA elements in three and four modules (i.e. longer waveguides) yielding different depth of the simulator, 30cm and 40cm, and different oscillation characteristics as depicted in figure 5. This concludes that the oscillations/ripples correspond approximately to the changes in the depth of the waveguide and not the width of the array. Another observation is that the impedance match quality (i.e. gain) has been improved in the longer module, probably because of reduced effects from the more-distant absorber.

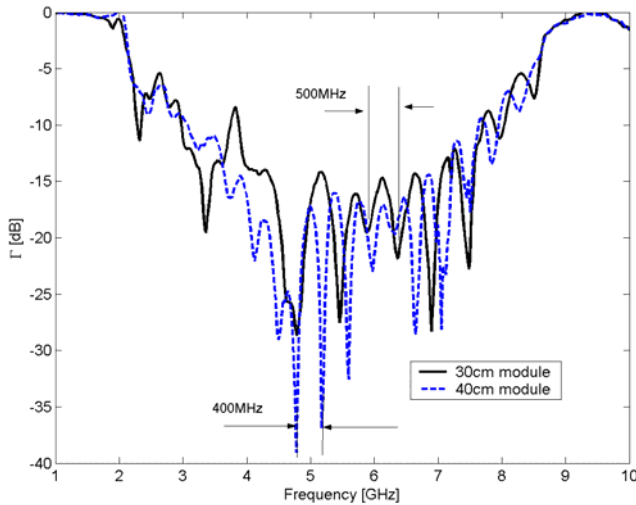


Figure 5: Active reflection coefficient of the measured and simulated infinite \times 8 DmBAVA elements in parallel plate waveguide simulator at broadside. Measurement conducted in a 30cm long module and 40cm long module. Response calculated for the center element. $D=2.025\text{cm}$, $A=B=2.00\text{cm}$, $H_a=1.8\text{cm}$, $\epsilon_r=2.2$, $t=60\text{mils}$. Vias are inserted in the substrate.

A TEM horn has replaced the foam at the end of the parallel plate waveguide simulator, and is inserted in a mini-range chamber, as shown in figure 6. The TEM horn is believed to provide a very good impedance match to the parallel plate waveguide thereby reducing the reflection effects observed in figures 4 and 5. The new [S] has been measured and active reflection coefficient has been calculated at several scan angles. Figures 7-9 depict better agreements between the simulated and measured data.

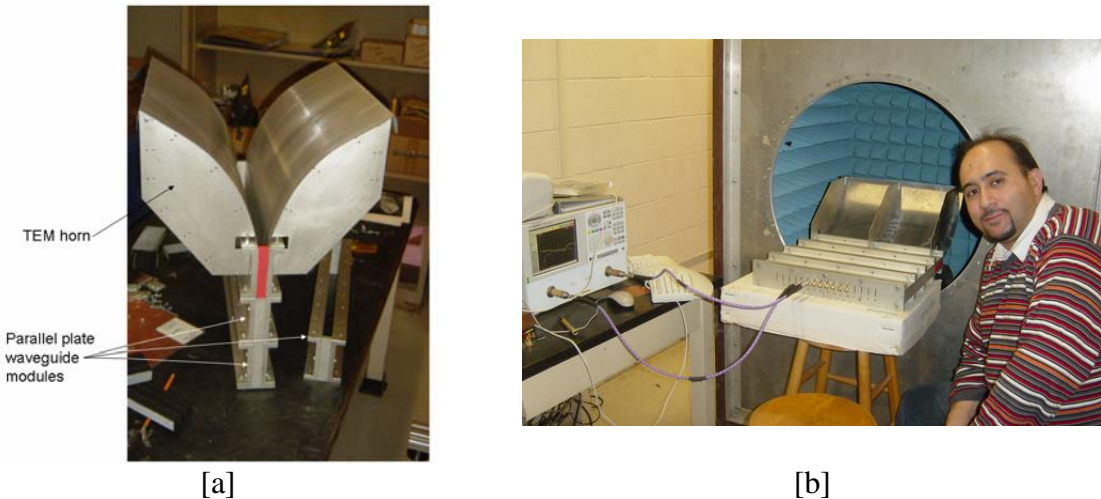


Figure 6: Measuring infinite \times 8 DmBAVA array with TEM horn “load”. [a] Parallel plate waveguide simulator with TEM horn extension. [b] The final measurement setup: mini-range chamber, parallel plate waveguide simulator with TEM horn, 2Ports HP Power Network Analyzer (PNA).

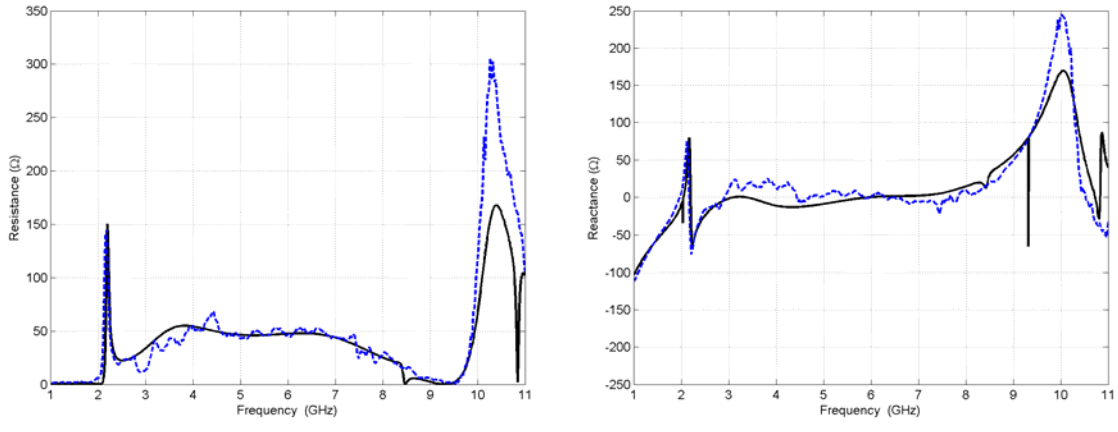


Figure 7: Active input impedance of the measured and simulated infinite \times 8 DmBAVA elements in parallel plate waveguide simulator with TEM horn at broadside. Response calculated for the center element. [a] Resistance. [b] Reactance. $D=2.025\text{cm}$, $A=B=2.00\text{ cm}$, $H_a=1.8\text{cm}$, $\epsilon_r=2.2$, $t=60\text{mils}$. Vias are inserted in the substrate.

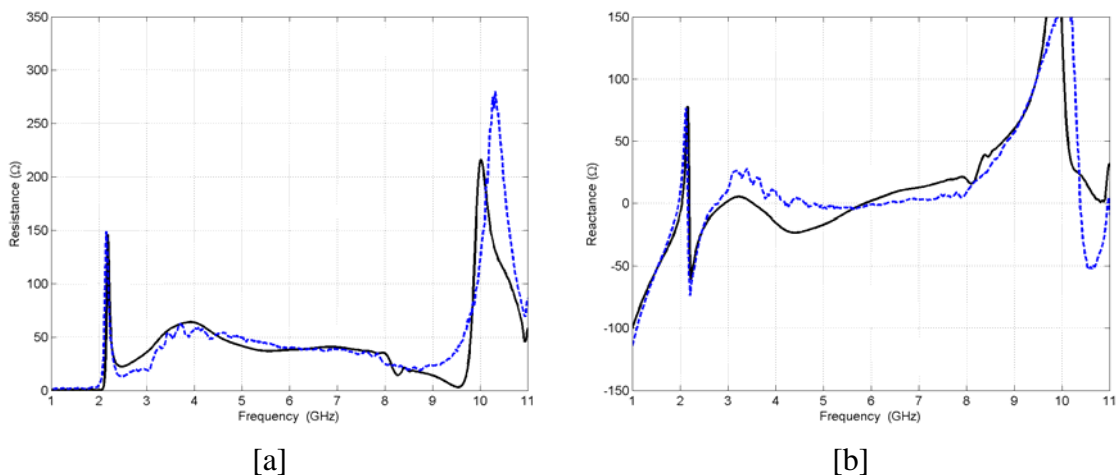


Figure 8: Active input impedance of the measured and simulated infinite \times 8 DmBAVA elements in parallel plate waveguide simulator with TEM horn at 30° in H plane. [a] Resistance. [b] Reactance. $D=2.025\text{cm}$, $A=B=2.00\text{cm}$, $H_a=1.8\text{cm}$, $\epsilon_r=2.2$, $t=60\text{mils}$. Vias are inserted in the substrate.

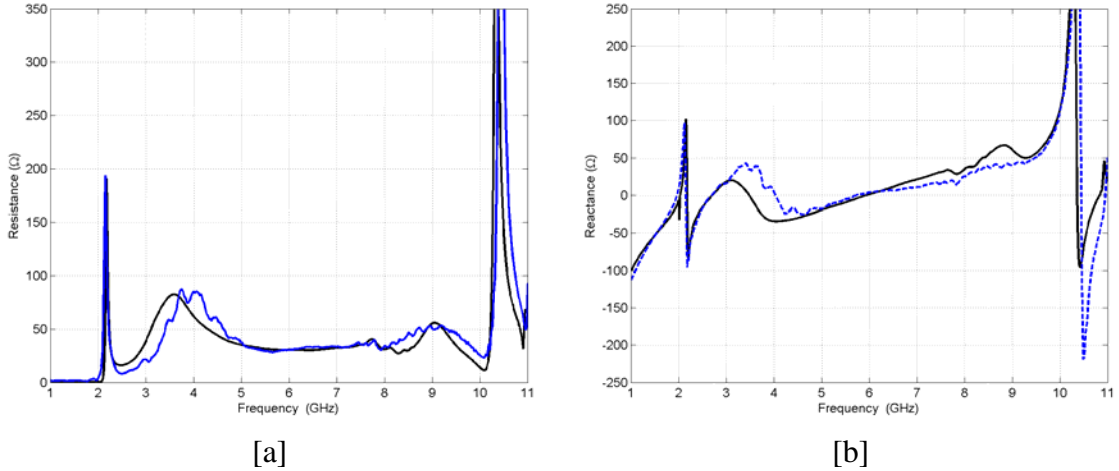


Figure 9: Active input impedance of the measured and simulated infinite \times 8 DmBAVA elements in parallel plate waveguide simulator with TEM horn at 45° in H plane. [a] Resistance. [b] Reactance. $D=2.025\text{cm}$, $A=B=2.00\text{ cm}$, $H_a=1.8\text{cm}$, $\epsilon_r=2.2$, $t=60\text{mils}$. Vias are inserted in the substrate.

3. DmBAVA with Magnetic Current Slot (DmBAVA-MAS)

The new antenna and array's unit cell structure used for the PBFDTD simulations in this section is depicted in figure 10. Most of the design parameters and equations were defined in [13]. In this paper, two new components to the design of DmBAVA unit cell are added where their contributions to enhance the performance are described as follows:

- *Metallic poles:* Adding metallic poles (or posts) between adjoining DmBAVA elements widens the operational bandwidth because it moves the low-frequency cut-off down. The poles have width, W_{poles} , and height, H_{poles} . Thus, they can be optimized for best scan impedance. Note the metallic poles are neither mechanically nor electrically connected to the neighboring antenna elements. However, they are terminated at the array's ground plane. An example of how much could those poles affect the performance is shown in figure 11. The original DmBAVA design that was presented in figure 1 had a little bit over an octave 2.5:1 bandwidth [8]. When the metallic poles are added, the antenna has a boresight bandwidth about 3.3:1 for a VSWR < 2.2.
- *Magnetic slot:* Selective removal of portions of the element's metallic fins has created a magnetic slot in the middle of the fins. It is defined by two heights, Cr_5 and Cr_6 , and two opening rates, R_3 and R_4 . Those parameters determine the profile of the slot in the fin, where there is an optimal shape at which they most improve the gain of the antenna, i.e. the 2:1 VSWR curve. Following the example shown in figure 11, the slot is added to the fin of the DmBAVA antenna, and now the array has 4:1 bandwidth for VSWR less than 2.

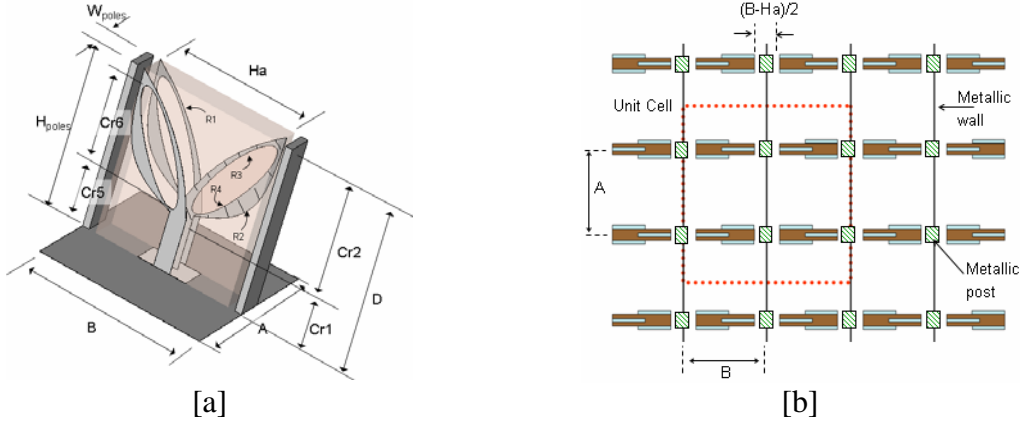


Figure 10: Structure of DmBAVA-MAS. [a] Front view of a single element of the modified BAVA. The hatched area is a conductor embedded in the middle of the substrate. The solid and slightly shaded shapes are identical conductors forming the ground plane of the stripline on the upper and lower surfaces of the substrate. [b] The DmBAVA-MAS array's unit cell.

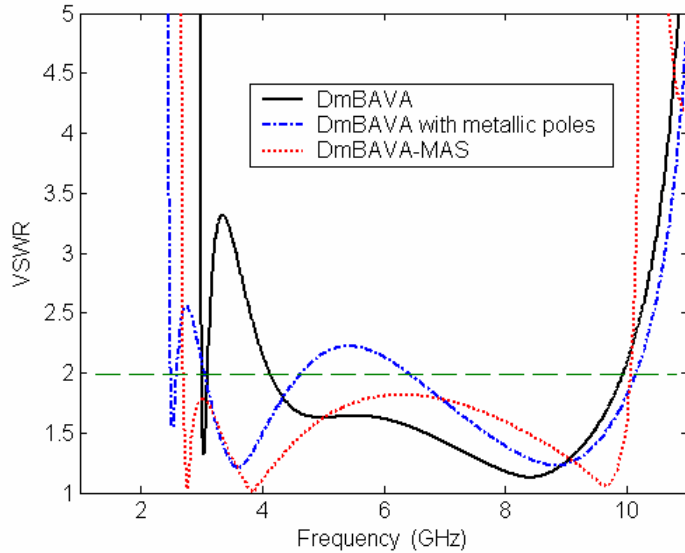


Figure 11: Active reflection coefficient at broadside of the DmBAVA-MAS compared with performance of DmBAVA that was shown in figure 1 in this paper, and with the DmBAVA that has metallic post only. $D=1.5\text{cm}$, $A=B=1.51\text{cm}$, $H_a=1.26\text{cm}$, $\epsilon_r=3.0$, $t=90\text{mils}$. Vias are inserted in the substrate. Grating lobe is at 10GHz.

When these techniques are applied to the antenna that was presented last year [13], the new antenna is now operating with a bandwidth of 5.4:1 at broadside, and up to 5:1 bandwidth when is scanned along E plane $< 45^\circ$, figure 12a. The performance in the H plane (figure 12b) is not as good as it should to be, but there is an ongoing effort to optimize the design further to get a full 5:1 scan-volume bandwidth.

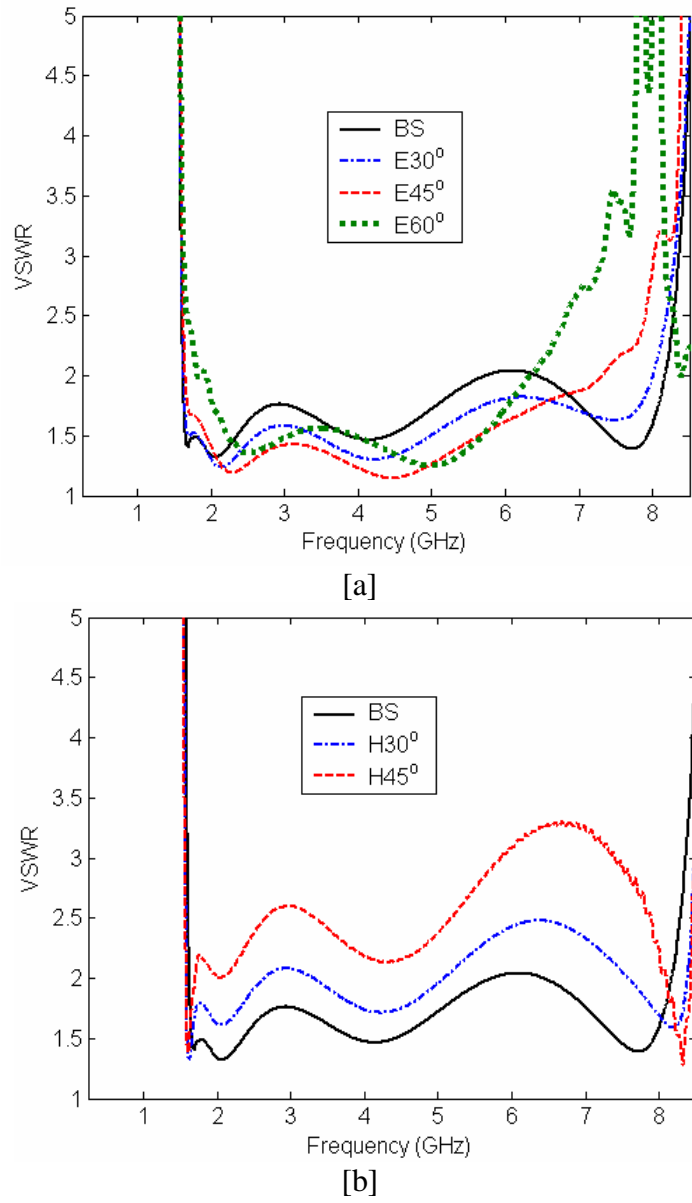


Figure 12: Active reflection coefficient in the optimized DmBAVA-MAS array. [a] E plane scan performance. [b] H plane scan performance. $D=2.00\text{cm}$, $A=B=2.00\text{cm}$, $H_a=1.8\text{cm}$, $\epsilon_r=2.2$, $t=80\text{mils}$. Vias are inserted in the substrate. Grating lobe is at 7.5GHz.

4. Summary

The doubly-mirrored technique for the conventional BAVA has been explored through numerical simulations and verified in measurements. A decent agreement was obtained using the parallel plate waveguide and a TEM horn to emulate a finite x infinite array. A newer configuration for DmBAVA arrays has been also explored through numerical

simulations. The new array and unit cell includes metallic poles placed strategically in the gaps between doubly-mirrored elements to push down the lowest operation frequency of the antenna. Furthermore, introducing a magnetic slot into the metallic fin of the DmBAVA provides good scan performance greater than 5:1 bandwidth for an E plane scan. Further numerical studies are being conducted to improve the scan performance in the H plane of the new array.

The addition of the metallic poles and magnetic slots had not sacrificed the modularity feature in the array. The array can be realized as individual elements that are fabricated and inserted into a supporting structure comprised of the metallic poles, metallic walls (in case of single polarized) and ground plane. The BAVA element makes electrical contact only to the ground plane, but not to the metallic poles, to the metallic crosswalls nor to the adjacent elements.

Acknowledgment

The authors thank several individuals whose contributions have been valuable in this work. Mr. James West and the Advanced Technology Center of Rockwell Collins for providing financial support and access to computational resources. Mr. Gene Losik for building the antenna, and CASCA for sponsoring the measurement efforts. The contributions are greatly appreciated.

References

1. R. P. Owens and A. Smith, "A dual band, dual polarized array antenna of modular construction," IEE Colloquium on Circularly Polarized Elements and Arrays. 13 Jun 1991.
2. D. Schaubert, S. Kasturi, M.W. Elsallal and W Cappellen, "Wide bandwidth Vivaldi Antenna Arrays – Some Recent Developments," EuCAP 2006. Nov 06 – 10, 2006. Nice, France.
3. D. Schaubert, S. Kasturi, A. Boryssenko1 and M.W. Elsallal, "Vivaldi Antenna Arrays for Wide Bandwidth and Electronic Scanning," to appear at EuCAP 2007. Nov 11 – 16, 2007. Edinburgh, UK.
4. J. J. Lee, S. Livingston and R. Koenig, "Performance of a Wideband (3-14 GHz) Dual-pol Array," IEEE Antenna Propagation Symposium, pp. 551-554, 20-25 June 2004.
5. H. Holter, "Dual-Polarized Broadband Array Antenna with BOR-Elements, Mechanical Design and Measurements," IEEE Transaction on Antennas and Propagation. Volume 55, Issue 2, Feb. 2007. pp. 305 – 312
6. B. Munk, R. Taylor, T. Durharn, W. Croswell, B. Pigon, R. Boozer, S. Brown, M. Jones, J. Pryor, S. Ortiz, J. Rawnick, K. Kerbs, M. Vanstrum, G. Gothard and D.

- Wiebelt, "A Low-Profile Broadband Phased Array Antenna," IEEE Antenna Propagation Symposium, pp. 448-451, 22-27 June 2003.
7. B. Thors, and H. Steyskal, "Synthesis of Planar Broadband Phased Array Elements with a Genetic Algorithm," 2005 Antenna Applications Symposium, pp. 324 – 344, 21-23 September, 2005.
 8. M.W. Elsallal and D. H. Schaubert, "Reduced-Height Array of BAVA with Greater Than Octave Bandwidth," 2005 Antenna Applications Symposium, pp. 226 – 242, 21-23 September, 2005
 9. J. D. Langely et al, "Balanced Antipodal Vivaldi Antenna for Wide Bandwidth Phased Arrays," IEE Proceeding of Microwave and Antenna Propagations, Vol. 143, No. 2 Apr 1996, pp. 97-102.
 10. M.W. Elsallal and D. H. Schaubert, "Parameter study of single isolated element and infinite arrays of balanced antipodal Vivaldi antennas," 2004 Antenna Applications Symposium, Allerton Park, Monticello, Illinois, pp. 45 – 69, 15-17 September, 2004.
 11. M.W. Elsallal, "Doubly-mirrored Balanced Antipodal Vivaldi Antenna (DmBAVA) for High Performance Arrays of Electrically Short, Modular Elements," Ph.D. Dissertation Thesis, Department of Electrical and Computer Engineering, University of Massachusetts, Amherst. To be presented in October 2007.
 12. M.W. Elsallal and D. H. Schaubert, "Electronically Scanned Arrays of Dual-Polarized, Doubly-Mirrored Balanced Antipodal Vivaldi (DmBAVA) Based on Modular of Elements," IEEE Antenna and Propagation Symposium, pp. 887-889, 9-12 June 2006. Albuquerque, NM.
 13. M.W. Elsallal and D. H. Schaubert, "On the Performance Trade-Offs Associated with Modular Element of Single- and Dual-Polarized DmBAVA," 2006 Antenna Applications Symposium, pp. 166 – 187, 20-22 September, 2006.
 14. Periodic Boundary FDTD (PBFDTD) Program, written by Henrik Holter. Stockholm, Sweden.
 15. Asnsoft HFSS, version 11, www.ansoft.com.
 16. MWS CST, version 2006B, www.cst.de.
 17. P. W. Hannan et al, "Simulation of a phased-array antenna in a waveguide," IEEE Trans. Antenna and Propagation, Vol. AP-13, pp 475-476, May 1965.
 18. S. Kasturi, "Design Parameters in Single Polarized, Infinite Arrays of Vivaldi Antennas," M.S. Thesis, University of Massachusetts, Amherst. Sept. 2004.

MINIATURIZATION OF CAVITY-BACKED SLOT ANTENNAS

Mudar Al-Joumayly and Nader Behdad

Department of Electrical Engineering and Computer Science
University of Central Florida, Orlando, FL, 32816-2362
maljouma@mail.ucf.edu, behdad@mail.ucf.edu

Abstract - A technique for miniaturization of cavity-backed slot antennas is presented. This is achieved first by inductively loading a cavity-backed slot antenna with a number of distributed inductors to increase its electrical length such that the resonant frequency of the antenna is decreased without increasing the occupied area by the antenna. Further reduction is achieved by modifying the ground plane around the slot by using a patterned ground plane composed of a series of meandered strip lines with a specific pattern placed around the slot antenna. The combination of these two miniaturization techniques allows for reducing the occupied area by the antenna by a factor larger than 82%.

1. INTRODUCTION

The rapid advancement of communication technology and the significant growth of consumer demands over the past couple decades have brought about a new age in wireless communication industry. The proliferation of personal wireless communication devices and the increased functionality of such devices have placed numerous constraints on their performance and capabilities. Characteristics such as small size, increased battery lifetime and improved reliability are commonly desired features. One of the challenges in reducing the size of any wireless communication device is the issue of antenna miniaturization. This problem must be properly addressed before a viable solution for size reduction of any wireless device can be developed. Antenna miniaturization is not a new topic and has been extensively studied over many decades [1]. One major disadvantage of antenna miniaturization is the substantial reduction in radiation efficiency of such miniaturized antennas that occurs as a consequence of miniaturization [1]. Recently, there has been a renewed interest in this subject and several miniaturized antennas with moderate to high radiation efficiency values have been reported [2]-[3]. In these studies, it has been shown that using a slot antenna topology, miniaturized antennas that are far more efficient than their printed wire or patch counterparts can be obtained. One problem with slot antennas, however, is their bi-directional radiation patterns. This creates a major problem in using these antennas in many of today's wireless communication devices, where more often than not the antennas need to be integrated with the rest of RF transceiver circuits in confined spaces. The problem of bi-directional radiation can be solved by using a cavity-backed slot

antenna (CBSA). However, to operate efficiently, cavity-backed slot antennas must have cavity dimensions in the order of half a wavelength squared ($\lambda/2 \times \lambda/2$). Therefore, this solution does not provide a practical means of alleviating the problem of bi-directional radiation in a miniaturized slot antenna, unless the cavity itself can also be miniaturized.

In [4], an attempt was made to reduce the size of cavity-backed slot antennas by patterning the ground plane around the slot. However, this approach is only partially successful, since only one of the dimensions of the cavity backed slot antenna was miniaturized. In this paper, the concept of distributed inductive loading [5], in conjunction with the patterned ground planes concept proposed in [4], are used to achieve a miniaturized cavity-backed slot antenna, in which both the length and width of the cavity can significantly be reduced compared to an ordinary cavity-backed slot antenna.

2. DESIGN PROCEDURE

Fig. 1 shows a cavity backed slot antenna fed with a microstrip line. The microstrip line and the slot antenna are printed on two different sides of a 0.5 mm thick RO4003 substrate (from Rogers Corp.). This substrate is then placed on a shallow cavity with a height of 6.35 mm, which is filled with a material with dielectric constant of $\epsilon_r=3.27$ (TMM3 from Rogers Corp.). The antenna is fed using 50 Ω off-centered open circuited microstrip line. The length of the open circuited microstrip line and its location are optimized such that the input impedance of the antenna is matched to the characteristic impedance of the feeding microstrip line. This optimization is performed using full-wave Method of Moments (MoM) simulations in IE3D [6]. The cavity width is chosen such that the distance from the cavity edge to the slot is effectively quarter wavelength at the center frequency of operation. The antenna is designed and simulated in IE3D and complete geometrical dimensions are listed in Table I. This cavity backed slot antenna is designed to operate at 1.5 GHz, and is used as a reference to compare the performance of the miniaturized cavity-backed slot antennas.

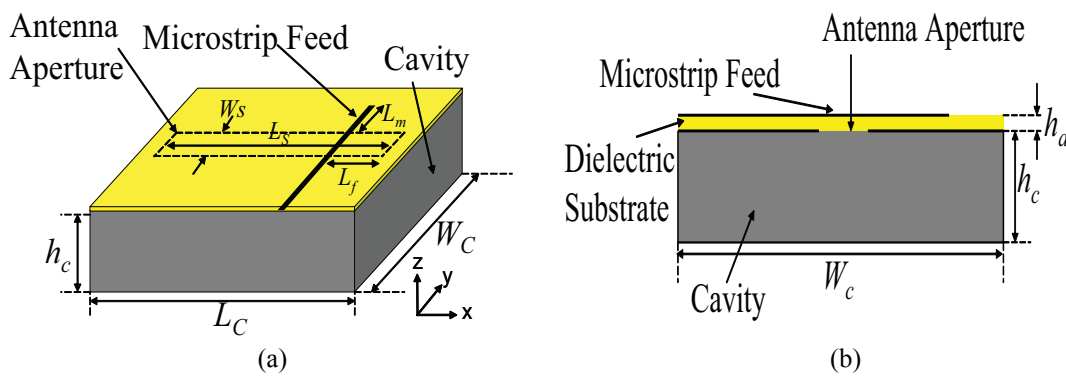


Fig. 1. Topology of a cavity-backed slot antenna, fed with a microstrip line. (a) 3D view, (b) Side view

TABLE I
Physical dimensions of a simple cavity-backed slot antenna studied in Section 2.

Parameter	L_C	W_C	L_m	L_f
Value	94mm	57mm	18mm	5.9mm
Parameter	L_S	W_S	h_c	h_a
Value	90mm	2mm	6.35mm	0.5mm

The length of the cavity-backed slot antenna, shown in Fig. 1, can be reduced by loading it with one or more inductive slits at one or more locations along the slot [5]. This can be explained by modeling the antenna as a transmission line with a length of $\lambda_g/2$ short circuited at both ends. The inductive loads can be obtained by adding slits with electrical lengths less than $\lambda_g/4$ [5]. This phenomenon can also be explained by studying the electric current distribution in the ground plane around the slot antenna. By creating a discontinuity in the path of the electric current circulating around the slot, the current is forced to circulate around this discontinuity creating a longer effective electrical length. This can be achieved using the topology shown in Fig. 2, where the lengths and the total number of the added slits determine the miniaturization factor that can be achieved. The length of the open circuited microstrip line, L_m , is optimized each time the slit lengths are changed to achieve the best impedance match. Fig. 3 shows a similar CBSA topology, where an off centered microstrip line is used to feed the antenna. A third slot is added at the feed end to help achieve a better impedance match.

Studying the electric current distribution in the ground plane around the slot reveals that the electric current has two different components. One that circulates around the slot and one that is perpendicular to it. The circulating component is mainly responsible for creating a resonant condition, whereas the normal component is the main contributor to the far field radiation [4]. Therefore the ground plane around the slot can be substituted with a patterned ground plane without significantly decreasing the radiation efficiency of

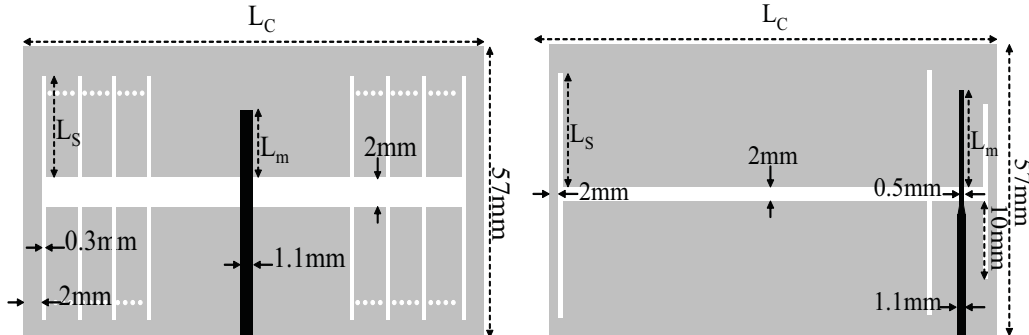


Fig. 2. Topology of a cavity-backed slot antenna, whose length is miniaturized using the distributed inductive loading technique [5]. The antenna is fed with microstrip line at the center of the aperture

Fig. 3. Topology of a CBSA miniaturized using the distributed inductive loading technique. The antenna is fed with an off-centered microstrip line.

the antenna, as long as a conductive path exists that can carry both components of the current. This can be done by substituting the ground plane around the slot with a number of parallel strips and a perpendicular strip that circulates around the slot. Fig. 4 shows the inductively loaded CBSA with a ground plane replaced by a number of parallel metal strips. As the number of the parallel strips increases, the antenna response becomes closer to that of the ordinary CBSA with such a ground plane. By meandering the parallel strips in the modified ground plane, as shown in Fig. 5, the cavity width can significantly be reduced. The meandered strips are carefully designed such that they have effectively the same electrical length as the straight parallel strips. This ensures that the effective electrical length of the meandered strips remains $\lambda_g/4$.

3. RESULTS AND DISCUSSION

The miniaturized cavity backed slot antennas described in the previous section are designed, fabricated, and their radiation patterns are measured and characterized. The microstrip line and the inductively loaded CBSA, shown in Fig. 2, are printed on two different sides of a 0.5 mm thick RO4003 substrate. This substrate is then placed on a cavity with a depth of a 6.35 mm, which is filled with a dielectric material with dielectric constant of $\epsilon_r=3.27$. The antennas are fed using center-fed 50 Ω open circuited microstrip lines with the width of 1.1 mm (an impedance of 50 Ω). The antennas are designed with different slit lengths, L_s , and then the antenna length is reduced to achieve resonance at 1.5 GHz. By reducing the length of the antenna, the cavity length can also be reduced. The simulated input reflection coefficients of several miniaturized CBSAs with different slit lengths are presented in Fig. 6. It can be seen from Table II that as L_s increases, the cavity length decreases. Using this technique, the cavity length can be reduced to 24 mm (25.5% of the volume occupied by the original CBSA studied in Section 2).

The modified ground plane of the miniaturized CBSA is then designed. This antenna is also fabricated using the same procedure as mentioned above. In these modified antennas, the width of the center-fed open circuited microstrip line is changed to 0.588 mm (an impedance of 72 Ω) such that its width is close to the strip width of the ground plane underneath it.

Table II
Parameters and cavity dimensions of a number of
Inductively Loaded miniaturized cavity-backed slot antennas

	L_s (mm)	L_c (mm)	L_m (mm)
Case 1	9.5	55	5.55
Case 2	13	41	5.5
Case 3	15.5	30	3.75
Case 4	18	24	3.75

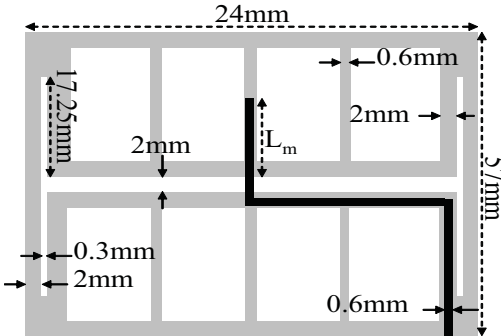


Fig. 4. Topology of miniaturized inductively loaded cavity-backed slot antenna. The antenna is fed with a microstrip line at the center and the ground plane around the slot is replaced with a number of parallel and perpendicular metal strips.

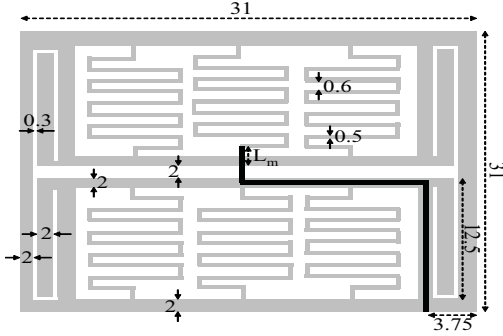


Fig. 5. Topology of a miniaturized, inductively loaded CBSA. The parallel strips of Fig. 4 are replaced with meandered strips to conserve space and achieve further miniaturization. All dimension are in mm.

The simulated input reflection coefficients of the miniaturized CBSA with different number of parallel strips are shown Fig. 7. The difference in the center frequency of operation can be attributed to the changes in the ground plane pattern as the number of strips changes. The antenna gain, efficiency, and bandwidth are affected by the number of strips. As the number of strips is increased, both the antenna gain and bandwidth increase [4]. The simulated and measured input reflection coefficients ($|S_{11}|$) of the miniaturized CBSA with three parallel strips (see Fig. 8) are shown Fig. 9. The difference observed between the measured and the simulated results can be explained by the fact that the antenna is simulated assuming infinite dielectric material outside the cavity, which is not the case in reality.

As mentioned in the previous section, the maximum miniaturization is achieved by meandering the metal strips. This way, both the length and width of the cavity can

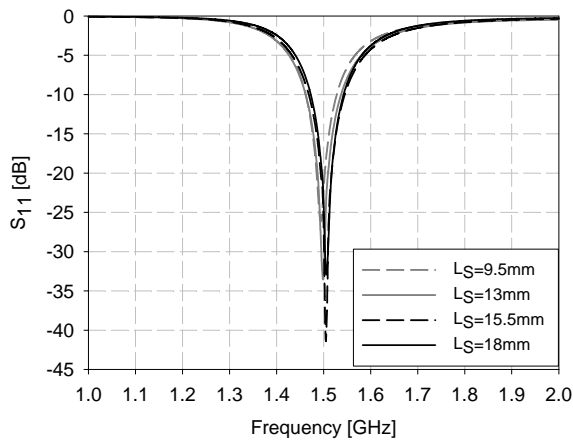


Fig. 6. Input reflection coefficient (S_{11}) of a number of inductively loaded cavity-backed slot antennas.

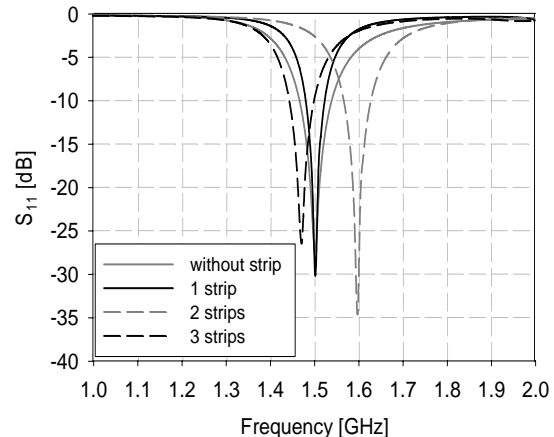


Fig. 7. Input reflection coefficient of a number of inductively loaded CBSA with patterned ground planes composed of a number of parallel strips.

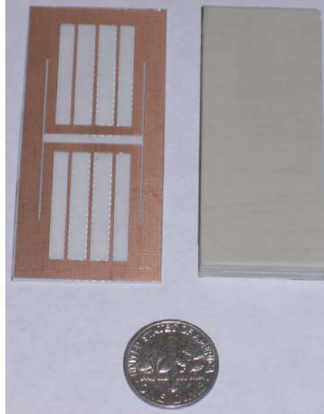


Fig. 8. Photography of the topology of miniaturized inductively loaded cavity-backed slot antenna. The ground plane around the slot is replaced with 3 parallel and perpendicular metal strips.

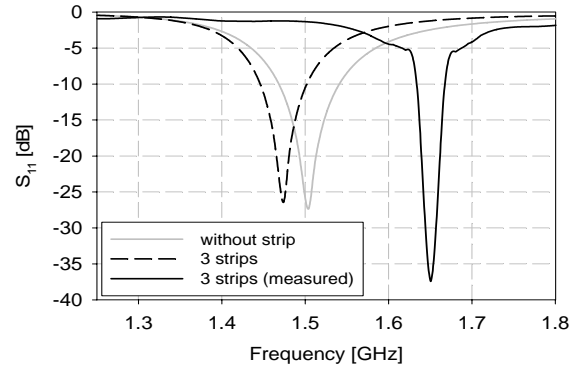


Fig. 9. Measured and simulated input reflection coefficients of inductively loaded CBSA with patterned ground planes composed of 3 of parallel strips compared with that of uniform ground plane.

significantly be reduced. The simulated input reflection coefficients of the miniaturized CBSAs with different number of meandered strips are shown Fig. 10. It is observed that a good impedance match in all three cases can be obtained. Regardless of the changes in the miniaturized CBSA structure, the impedance match can be optimized by changing the length of the open circuited microstrip line, L_m . The measured and simulated input reflection coefficients of both the traditional CBSA and the miniaturized CBSA with three meandered strips (see Fig. 11) are shown Fig. 12. A relatively good agreement between the simulation and measurement results are observed. It is also observed that all the measured antennas have non-zero input reflection coefficients outside the main band;

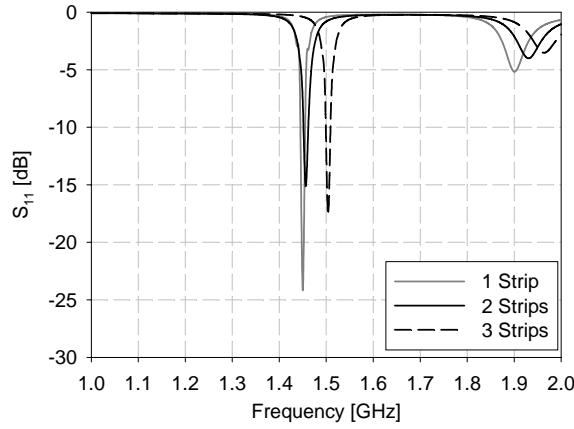


Fig. 10. Input reflection coefficient of miniaturized cavity-backed slot antennas, shown in Fig. 5, with different number of meandered strips.

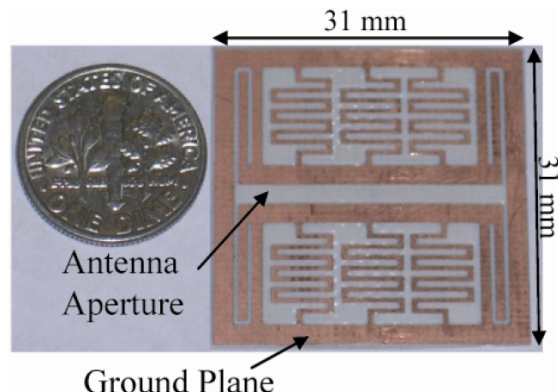


Fig. 11. Photography of the topology of miniaturized inductively loaded cavity-backed slot antenna. The ground plane around the slot is replaced with 3 meandered metal strips.

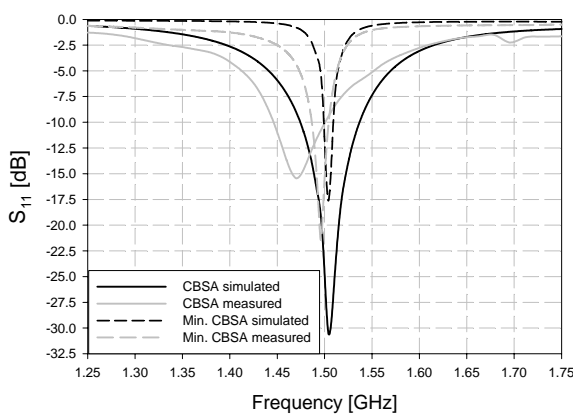


Fig. 12. Input reflection coefficients of a traditional CBSA and miniaturized cavity-backed slot antennas with 3 meandered strips, shown in Fig. 11.

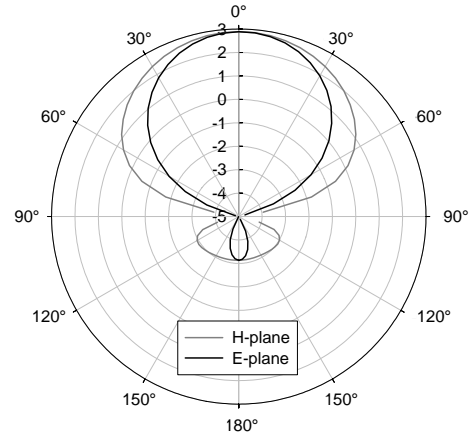


Fig. 13. Simulated Far field radiation patterns of the miniaturized cavity-backed slot antenna

this is caused by the losses of a semi-rigid coaxial cable that is used to feed the antenna. Since this cable is soldered to the antenna, its losses are not calibrated out. As can be seen from Fig. 12, the bandwidth of the miniaturized CBSA is narrower than that of the traditional CBSA, which is a consequence of miniaturization [1]-[3]. Fig. 13 presents the simulated radiation patterns of a miniaturized CBSA with 3 meanders in the H-plane ($|E_\phi|$ at $\varphi=0^\circ$) and E-plane ($|E_\theta|$ at $\varphi=90^\circ$). The radiation patterns of the miniaturized antennas with parallel strips ground plane and meandered strips ground plane are measured and are presented in Fig. 14 and 15, respectively. The difference observed between the measured and simulated radiation patterns of the antenna can be attributed to the presence of the relatively large semi-rigid coaxial cable feeding the antenna in close proximity to the electrically small radiator. Nevertheless, in spite of its miniaturized dimensions, the miniaturized CBSA demonstrates a front-to-back ratio (FTBR) of about 6 dB. More importantly, unlike bi-directional slot or dipole antennas, it is possible to place this miniaturized CBSA in close proximity to a large ground plane or earth. This does not adversely affect the response of the antenna and is particularly useful for systems that require low profile sensors which need to be placed near the earth or mounted on vehicular platforms. The final miniaturized CBSA occupies a volume that is only 18% of the volume occupied by the ordinary CBSA.

4. CONCLUSION

A technique for miniaturization of cavity-backed slot antennas is presented. The technique is based on the combination of two different miniaturization techniques: distributed inductive loading and modification of the ground plane. It is shown that, for a given physical dimension, inductively loading a cavity-backed slot antenna increases the electrical length of the antenna and reduces its frequency of operation. It is also shown

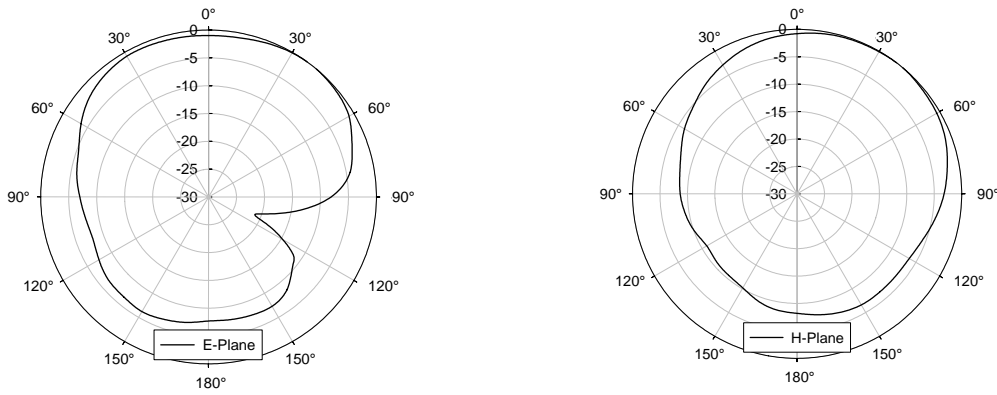


Fig. 14. Measured Far field radiation patterns of the miniaturized cavity-backed slot antenna (shown in Fig. 8)

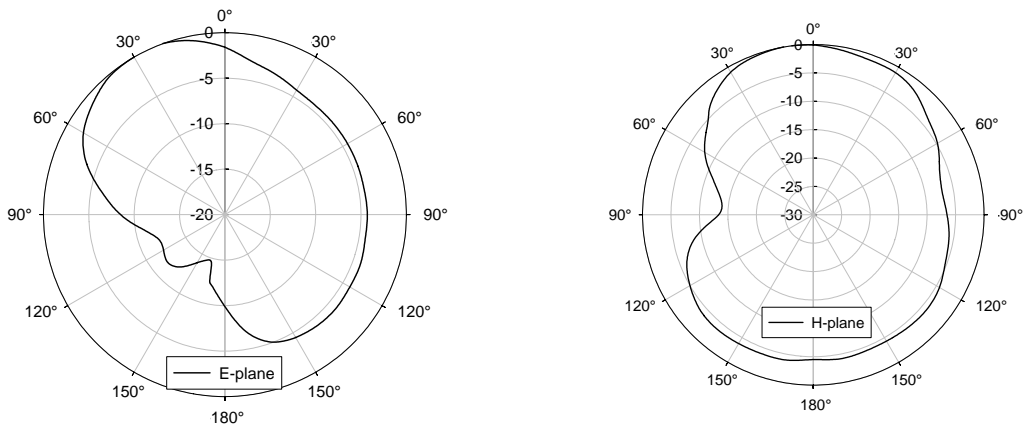


Fig. 15. Measured Far field radiation patterns of the miniaturized cavity-backed slot antenna (shown in Fig. 11)

that modifying the ground plane around the slot, by replacing it with a patterned ground plane utilizing a number of parallel meandered strips, can substantially reduce the cavity width. Using this technique, a miniaturized cavity-backed slot antenna is designed that occupies a volume, which is only 18% of an ordinary CBSA operating at the same frequency.

Reference:

- [1] L. J. Chu, "Physical limitations of omni-directional antennas," *J. Appl. Phys.*, vol. 19 pp. 1163-1175, Dec 1948.
- [2] R. Azadegan, K. Sarabandi, "Novel Approach for Miniaturization of Slot Antennas", *IEEE Trans. Antennas Propag.*, vol. 51, No. 3, pp: 421-429, March 2003.

- [3] K. Sarabandi, R. Azadegan, "Design of an efficient miniaturized UHF planar Antenna", IEEE Trans. Antennas Propag., vol. 51, No. 6, pp: 1270-1276, June 2003.
- [4] W. Hong, N. Behdad, K. Sarabandi, "Size reduction of cavity-backed slot antennas," IEEE Trans. Antennas Propag., vol. 54, No. 5, pp. 1461–1466, May 2006.
- [5] N. Behdad, K. Sarabandi, "Bandwidth Enhancement and Further Size Reduction of a Class of Miniaturized Slot Antennas," IEEE Trans. Antennas Propag., vol. 52, No. 8, pp. 1928–1935, August 2004.
- [6] IE3D Electromagnetic Simulation and Optimization Software, Zeland Software, Inc.

A Compact Ku/Ka Band Feed for Airborne Antenna Applications

J.P. Creticos and D.H. Schaubert

Center for Advanced Sensor and Communication Antennas

Department of Electrical and Computer Engineering

University of Massachusetts, Amherst, MA 01003

jcretico@ecs.umass.edu and schaubert@ecs.umass.edu

A compact Ku/Ka band antenna feed for use in reflector applications is presented. The feed consists of a corrugated horn primarily used to radiate Ku band, and a tapered dielectric rod inserted in a foam sleeve to radiate Ka band. The beamwidths in the two operating bands are independently controllable over a moderately wide range. The feed is unique in two ways: (1) the foam sleeve reduces the beamwidth and increases the usable range of beamwidths at Ka band and (2) a ridged waveguide transition is used to introduce the Ku band signal, reducing the size of the feed and increasing its bandwidth.

1. Introduction

Several reflector antenna designs currently being carried out at the University of Massachusetts Amherst require a feed capable of supporting Ku and Ka bands with center frequencies at approximately a 2.5:1 ratio. One of the designs, an offset-fed prime focus reflector, will be used in the High-Altitude Imaging Wind and Rain Airborne Profiler (HIWRAP) to be flown on the Global Hawk aircraft. The HIWRAP antenna must provide two beams, 30° and 40° incidence on the earth. Each beam is comprised of Ku and Ka band signals that are co-boresighted with peak sidelobes of -22 dB and diffraction limited gain at each frequency. Due to the tight space constraints, and the environmental conditions presented by an aircraft installation, the feeds must be compact, lightweight, rugged, and sealable to moisture.

To meet the dual beam requirement, the HIWRAP antenna consists of a reflector oriented to 33° off nadir fed by two compact feeds appropriately located to produce beams scanned to 30° and 40° incidence with maximum gain as shown in Figure 1. The antenna assembly spins about a vertical axis so the two beams sweep a conical scan with fixed angles of incidence on the ground. Table 1 outlines the feed requirements with an additional requirement that the return loss be at least 18 dB over a 100 MHz bandwidth at each band.

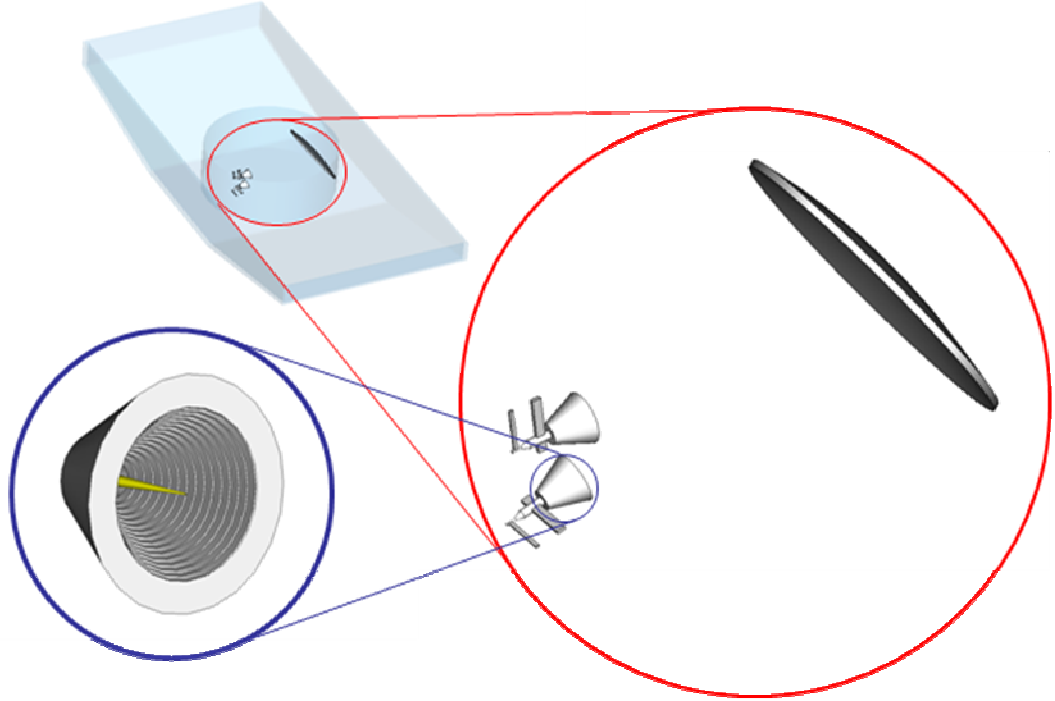


Figure 1: Layout of HIWRAP antenna within the Global Hawk payload compartment.
The shaded cylinder indicates the usable volume for the antenna.

Table 1: Performance requirements for feeds. Feed 1 provides the 30° beam and Feed 2 provides the 40° beam.

Feed	Band	Center Freq. (GHz)	Beamwidth	Edge Taper (dB)
Feed 1	Ku	13.91	52°	-14
Feed 1	Ka	35.56	52°	-13
Feed 2	Ku	13.35	50°	-12
Feed 2	Ka	33.76	50°	-13

A Ka/W band feed, previously developed at UMass [1], has been modified for use in this application [2]. Though the modified feed is viable for ground based applications, the space limitations and environmental conditions expected in an aircraft installation lead to concerns about the feed's suitability. Furthermore, the feed suffers from dissociation of the Ku and Ka band phase centers. In a standard reflector application this is a significant concern, in a scanned reflector application dissociated phase centers cause unacceptable degradation of the radiation patterns.

2. Previously Developed Feed

2.1 Design Overview

To understand the motivation for the present design, it is useful to review the previous design shown in Figure 2. The Ka band signal is introduced to the back of the feed through an air-filled circular waveguide that is then changed to a dielectric filled (Rexolite 1422, $\epsilon_r=2.53$) waveguide. A transition is made from completely filled waveguide to partially filled waveguide capable of supporting Ku and Ka bands. The transition is made gradually to keep the Ka band energy bound to the dielectric rod. A rectangular sidearm, used to introduce the Ku band signal to the feed, is placed approximately $1.25\lambda_g$ from the position where the Ka-to-Ku transition becomes cut-off to the Ku-band signal. Opposite the rectangular sidearm is a shorted rectangular stub used to improve the Ku transition bandwidth.

In the frontend of the feed, the dielectric rod is tapered leading to radiation of the Ka band signal while Ku band radiation is controlled by a corrugated horn. A meniscus lens, required because the appropriate Ka band beamwidth cannot be achieved with the tapered dielectric rod alone, is used to correct both beams. The corrugated horn is designed to use the lens following standard design procedures [3], [4]. To control the Ka beamwidth, the taper of the dielectric rod is changed and it is moved toward or away from the meniscus lens. Holes are drilled into the inner and outer surfaces of the lens so that a good match is achieved at both bands at both surfaces.

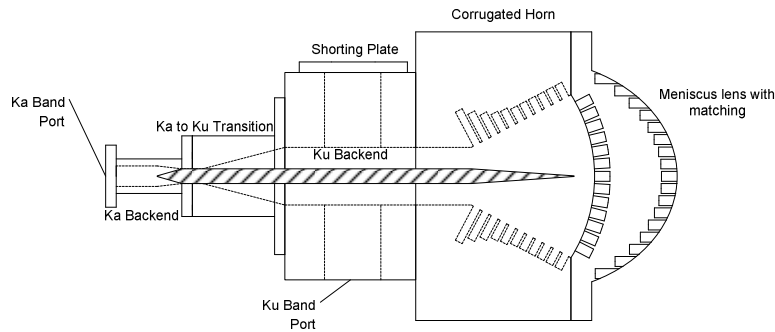


Figure 2: Schematic view of previously designed compact Ku/Ka feed.

2.2 Design Shortcomings

The design in Figure 2 has several electrical and mechanical problems:

- *Length:* The feed is long and needs an external circular-to-rectangular adapter and waveguide bend at Ka band adding at least 5 cm to the total feed length.
- *Mechanical Stability:* The use of only a small section of completely filled Ka

band waveguide does not provide the stability necessary to keep the dielectric rod properly positioned within the feed.

- *Condensation:* The feeds will be used in an unheated, unsealed, payload compartment in a high altitude flight. Condensation will likely form in the meniscus lens matching holes and severely affect feed performance.
- *Inter-band Electrical Alignment:* The strong dependency of both Ku and Ka bands on the meniscus lens for beam control leads to an inability to independently control radiation at each band which, in turn, leads to an inability to co-locate the Ku and Ka band phase centers.

3. New Feed Design

3.1 Design Overview

To address the problems with the previous design several changes were made. The new design, shown in Figures 3 and 4, incorporates the following key changes:

- The rectangular waveguide sidearms used in the Ku band section of the backend are replaced by double ridged waveguides allowing narrower sidearms that can be placed closer to the Ka-Ku taper resulting in a smaller Ku backend and greater Ku bandwidth.
- The Ka backend design is changed to a rectangular sidearm design similar to the Ku backend design of the previous feed. The new design reduces the length of the Ka backend, eliminates the need for external waveguide components, and provides better support for the dielectric rod as it is in a longer section of completely filled waveguide and is aligned by simply being placed against the back short.
- The meniscus lens is replaced by a flat Rexolite cap allowing condensation to be more easily shed. The required feed beamwidth at Ka band is now achieved through the use of a foam sleeve constructed from a medium density foam ($\epsilon_r=1.16$). The permittivity is chosen to be high enough to alter the Ka band radiation pattern but low enough to cause little impact on the Ku band signal. The Rexolite cap is designed to act as an A-sandwich radome at Ku band [5] and two resonant dielectric windows at Ka band. The foam sleeve is held in place with a low density ($\epsilon_r=1.04$) stabilization foam that is also used to properly align the inner Rexolite disc of the A-sandwich.
- A longer, larger aperture, profiled corrugated horn supports Ku band radiation. The longer horn section is allowed by the considerable length savings in the new Ku and Ka band backend designs.
- The use of the corrugated horn at Ku band and the foam sleeve at Ka band allows independent control of Ku and Ka band radiation and allows the phase centers of the two bands to be co-located.

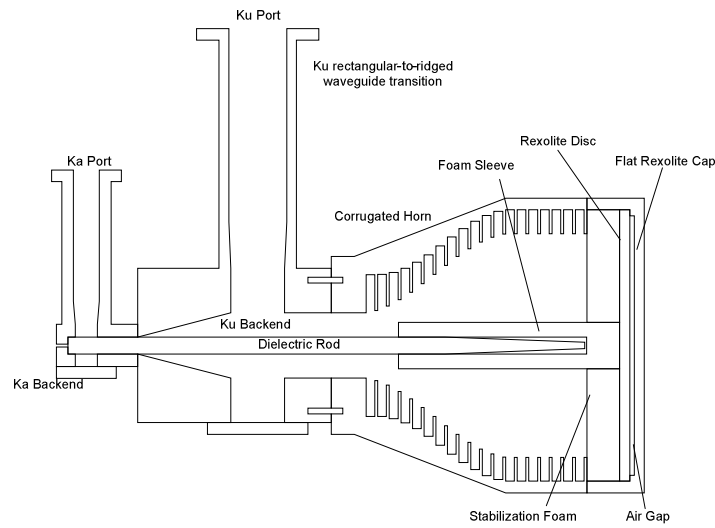


Figure 3: Cross-sectional view of new feed design.

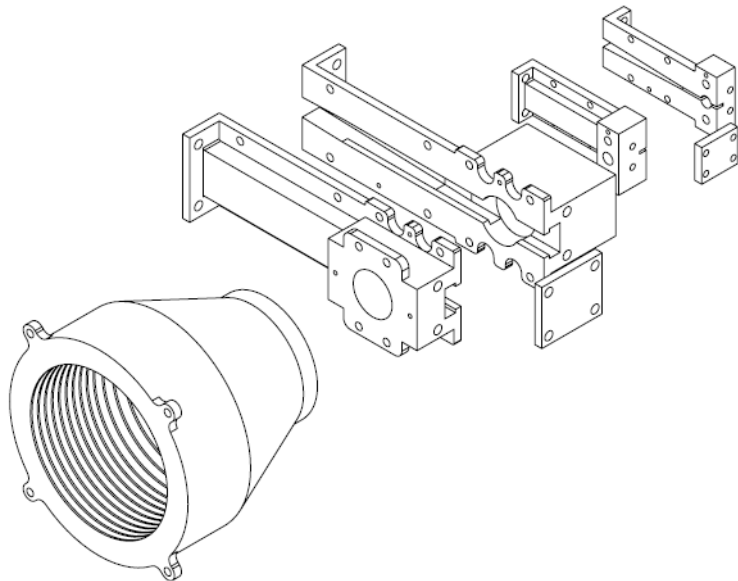


Figure 4: Exploded view of new design.

3.2 Foam Sleeve Design

Significant to the new feed design is the use of an $\epsilon_r=1.16$ foam sleeve to achieve the required Ka beamwidth. Two of the main sleeve parameters that affect performance are sleeve length and diameter. As the sleeve length increases, the beamwidth narrows (Figure 5a) and the phase center (Figure 5b) moves toward the front of the sleeve. At a point, longer foam sleeves do not bring the phase center any closer to the front of the

sleeve, though the beam continues to narrow. Increasing the diameter of the sleeve also narrows the beam and allows a phase center closer to the front of the foam sleeve to be achieved. By controlling the foam sleeve length and diameter, the beamwidth requirements of Table 1 are met and the phase center is located near the Ku band phase center of the corrugated horn.

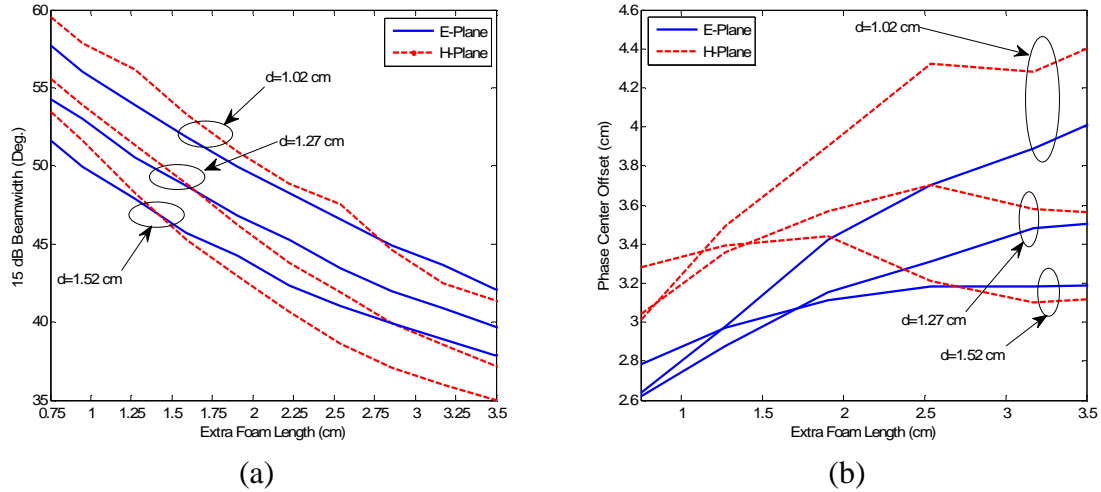


Figure 5: Variation of (a) 15 dB beamwidth and (b) phase center distance behind front of foam sleeve with sleeve length beyond end of tapered rod and sleeve diameter, d . The taper length of the rod is 3.81 cm and operates at 35 GHz.

3.3 Results

Feeds meeting the requirements in Table 1 were designed and prototyped. Using Ansoft HFSS v10.1, the feeds were simulated in sections. Where possible, one or two planes of symmetry were used to reduce simulation time and memory requirements. Ansoft Designer v3.5 was used to cascade the individual simulations. The prototype feeds shown in Figure 6 were fabricated from aluminum and passivated with a gold iridite finish and weigh approximately 0.5 kg each.

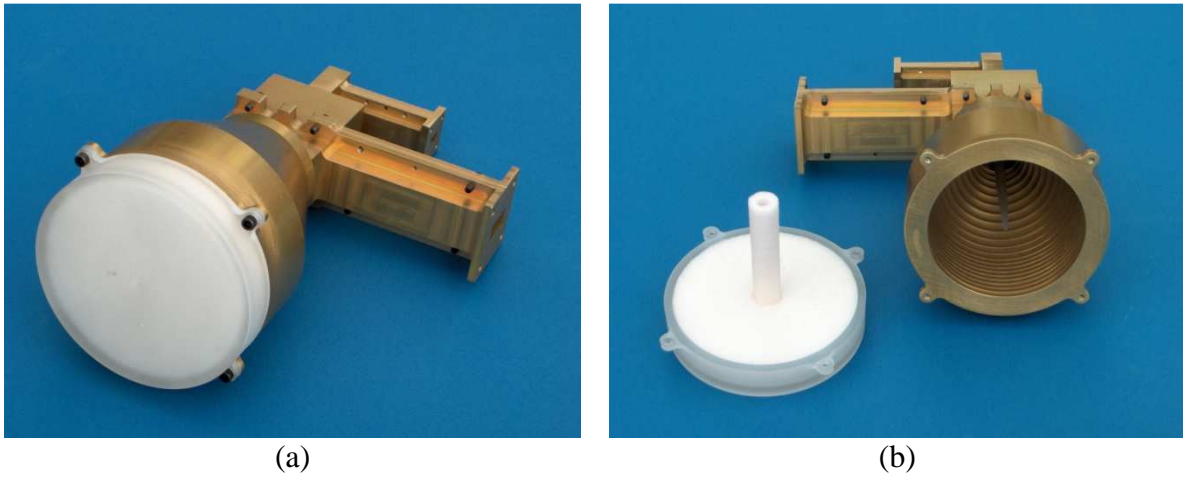


Figure 6: Photos of prototype feed with radome (a) attached and (b) removed.

The return loss of both feeds at Ku band meets system requirements (Figure 7a-b), but both feeds are tuned too high in frequency at Ka band (Figure 7c-d). Further testing of the feeds isolated the shift in tuning frequency to the Ka backend portion of the feed. Modified Ka backend designs that can replace the Ka backend portions on the current prototypes are being developed. The main change in the backend design is the lowering of the tuning frequency by lengthening the distance from the sidearms to backshort.

The E- and H-Plane radiation patterns (Figures 8-9, Table 2) of both feeds, at both bands, are very close to the specified values of Table 1. The Ku and Ka band phase centers of Feed 1 are measured to be 2.54 cm and 2.41 cm behind the outer surface of the radome respectively. The Ku and Ka band phase centers of Feed 2 are measured to be 2.26 cm and 2.44 cm behind the outer surface of the radome respectively.

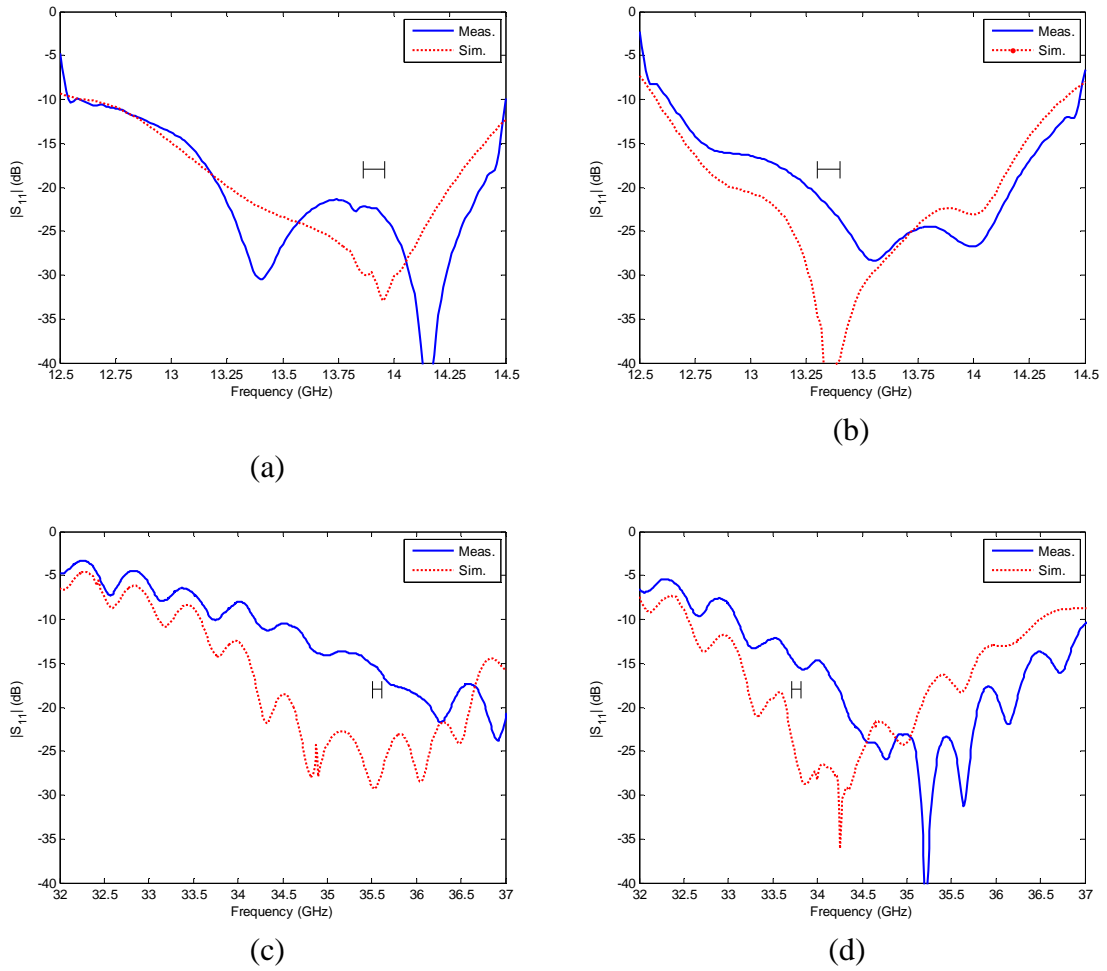


Figure 7: Return loss results (a) Feed 1, Ku band, (b) Feed 2, Ku Band, (c) Feed 1, Ka band, (d) Feed 2, Ka band.

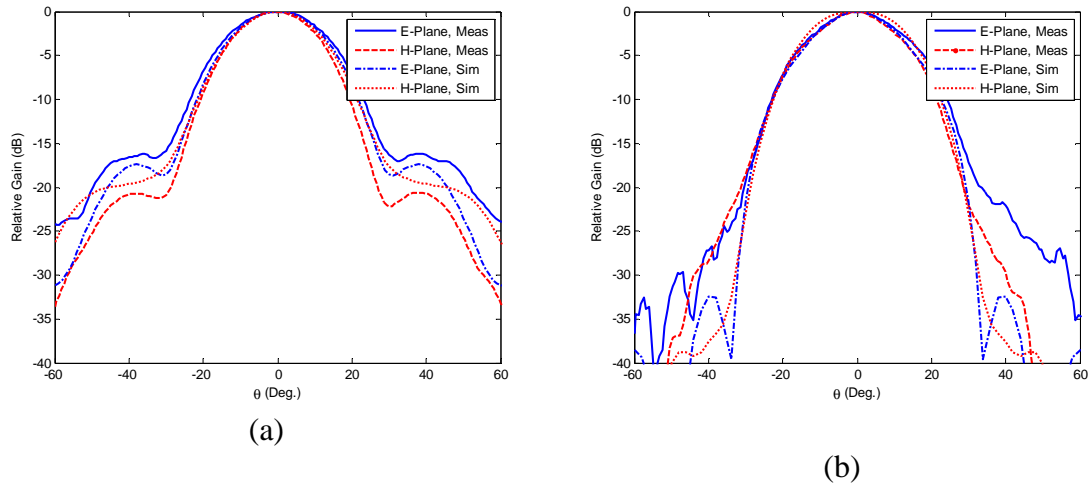


Figure 8: (a) Ku and (b) Ka band radiation patterns of Feed 1.

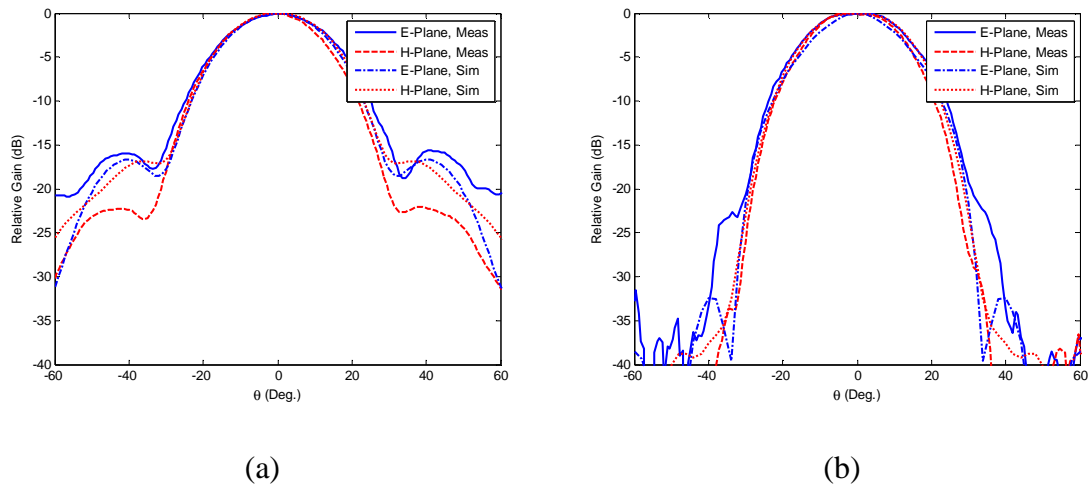


Figure 9: (a) Ku and (b) Ka band radiation patterns of Feed 2.

Table 2: Comparison of specified and measured feed pattern parameters.

Feed	Band	Edge Taper (dB)	Specified Beamwidth (°)	E-Plane Beamwidth (°)	H-Plane Beamwidth (°)
Feed 1	Ku	-14	52	54.6	46.6
Feed 1	Ka	-13	52	52.0	49.2
Feed 2	Ku	-12	50	53.8	49.2
Feed 2	Ka	-13	50	52.1	47.5

4. New Design Used as Reflector Feed

To judge the effectiveness of the new design, the performance of the feed when used with the HIWRAP reflector was simulated by using HFSS simulations of the feed in combination with physical optics analysis performed using FEKO 5.2. The HIWRAP reflector is an offset reflector with a diameter of 50.6 cm and a focal length of 47.6 cm. The F/D ratio of the parent parabola from which the offset section is cut is 0.36. Figures 10 and 11 show that the modeled feeds produce reflector radiation patterns that, in all cases, meet the 22 dB sidelobe requirements and are similar to the patterns expected from ideally located Gaussian sources. This indicates co-located Ku and Ka band phase centers and proper illumination of the reflector.

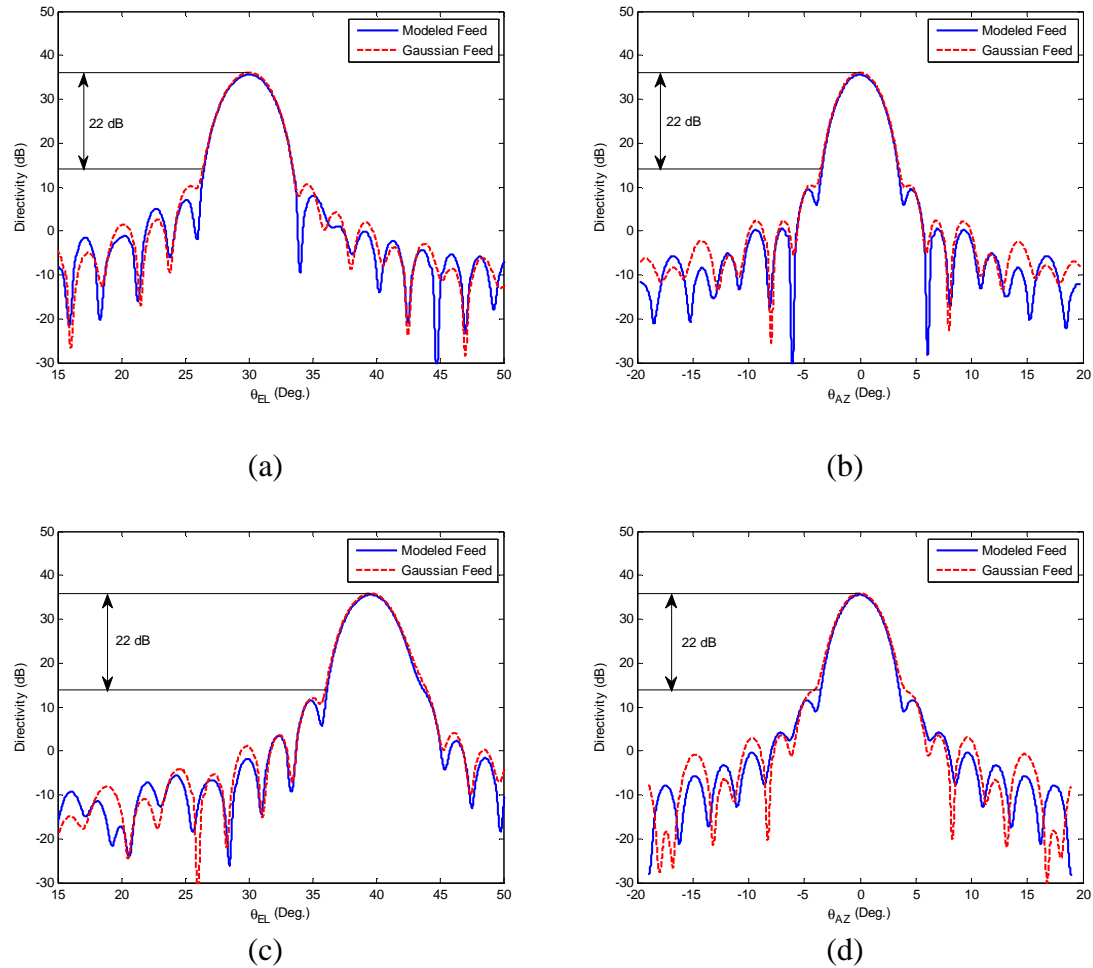


Figure 10: Secondary radiation patterns of HIWRAP reflector at Ku band fed by new feed design (a) Feed 1 elevation, (b) Feed 1 azimuthal, (c) Feed 2 elevation, (d) Feed 2 azimuthal

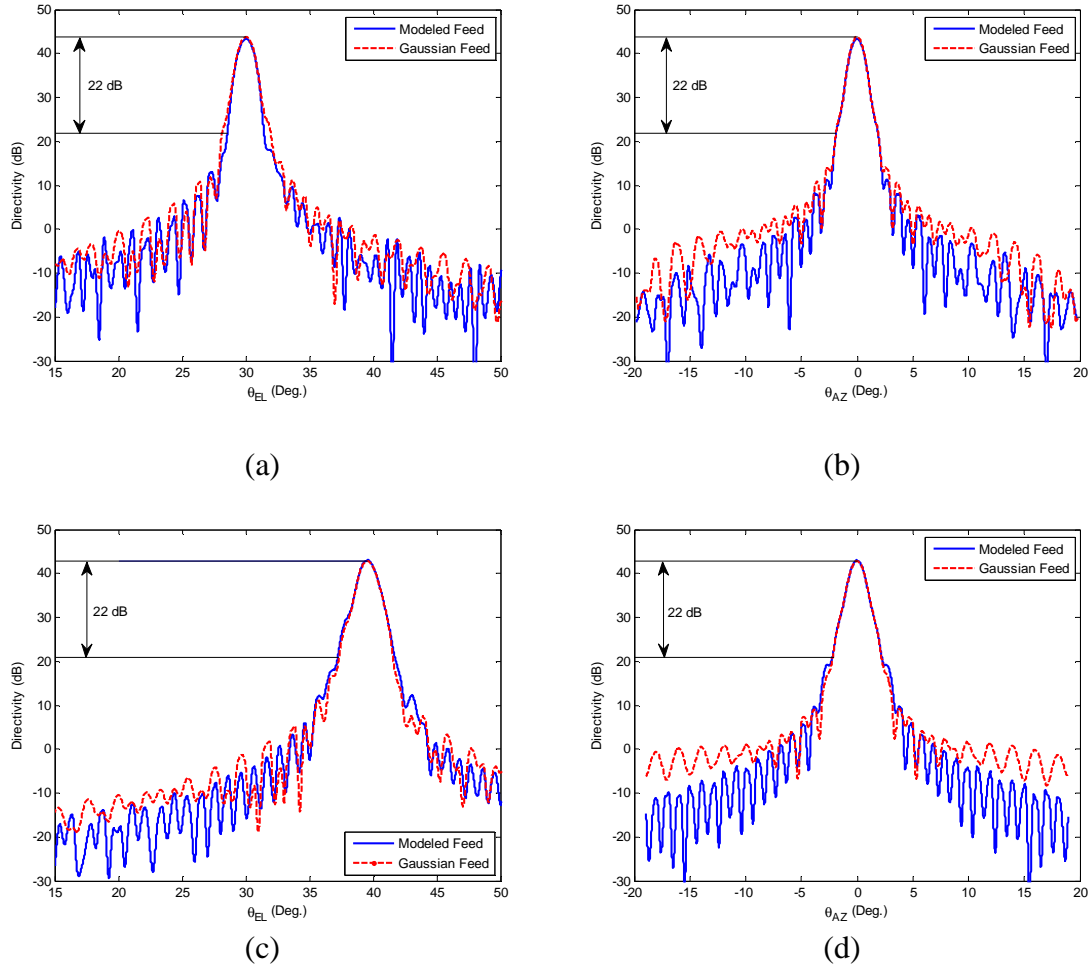


Figure 11: Secondary radiation patterns of HIWRAP reflector at Ka band fed by new feed design (a) Feed 1 elevation, (b) Feed 1 azimuthal, (c) Feed 2 elevation, (d) Feed 2 azimuthal

5. Conclusion

A compact, dual band feed capable of supporting Ku and Ka bands has been presented. Two designs have been detailed, with the second design incorporating two new developments – the use of ridged waveguides in the backend portion of the feed so it is shortened and has a larger bandwidth, and the use of a foam sleeve for reduction of the Ka band beamwidth beyond that achievable by a dielectric rod alone. These modifications lead to a smaller, more rugged feed, with better electrical characteristics.

Simulated and measured results for the new design have been presented. The measured return loss at Ku band meets system requirements while the return loss at Ka band is tuned slightly high for both feeds. A redesign of the Ka backend portion for each feed is

in progress that will correct this problem. Radiation pattern measurements indicate good agreement between the feed's phase center at Ku and Ka bands. Simulations using the modeled feeds show that, when feeding the HIWRAP reflector, the new feed designs perform extremely well, producing secondary reflector patterns that meet system requirements in all cases

6. Acknowledgments

This work is supported by NASA Goddard Space Flight Center grant number NNG05GQ52G.

7. References

1. D. Mooradd *et al.*, "Design of a Dual-Frequency, Dual-Polarized, High Power Millimeter Wave Radar Antenna", IEEE Int. Antennas and Propagat. Symp., pp. 584-587, June, 1993
2. J.P. Creticos and D.H. Schaubert, "A Compact Ku/Ka Band Feed", to be presented at IEEE Int. Antennas and Propagat. Symposium, June, 2007
3. P.J.B. Clarricoats and A.D. Olver, Corrugated Horns for Microwave Antennas, Peter Peregrinus Ltd., 1984
4. P.-S. Kildal, "Meniscus-lens-corrected horn: a compact feed for a Cassegrain antenna," IEE Proceedings, Vol. 131, Pt. H, No. 6, December 1984
5. S. Silver, *Microwave Antenna Theory and Design*, pp. 528-533, Peter Peregrinus Ltd., 1984

UWB Tapered Slot Antenna Array Using SIW Technology

Song Lin, Songnan Yang, Aly E. Fathy

EECS Department, University of Tennessee, Knoxville, TN, USA

Abstract --- A Significantly lower loss feed network for a tapered slot array antenna has been developed. The developed compact tapered slot antenna array is printed on a thick substrate and integrated with its feed-- a Substrate Integrated Waveguide (SIW) structure. The array utilizes a SIW binary splitter to minimize the feed structure insertion loss, and has a common Grounded Coplanar Waveguide (GCPW) feed to sustain a good input match while preventing higher order modes excitation over a wide frequency range. The antenna was designed, fabricated and thoroughly investigated as a part of a precise UWB localization and an UWB see through walls radar system currently being developed. Our studies have included the overall performance effects of using protruded polystyrene rods at the tips of the slots and placing the antenna between two flared metal plates to minimize sidelobe levels. Detailed simulations and measurements will be presented.

Introduction

Vivaldi antennas are extremely useful for ultra wide band antenna applications for their many features such as high gain, simple design, narrow beam width in the E-plane, and relatively wide operating bandwidth. They are excellent candidates for array manufacturing as they do not necessitate wide lateral dimensions [1]. However, their overall performance is generally hindered by the need for a wide band feed network which can cause significant insertion loss. Yang et al. [2] has utilized a multitude of wide band Wilkinson combiners to cover the 8-12 GHz bandwidth based on microstrip technology, but the overall insertion loss was substantially high (over 3.5 dB). Meanwhile, Hao et al. [3]-[4] utilized a SIW binary feed network that showed an improved performance, but its 2.5 dB insertion loss is still inadequate for developing high performance receivers. In this paper, we have improved their design to develop an efficient SIW feed network that has led to substantial performance improvements. Design improvements include the utilization of a thicker substrate to reduce the conductor loss, and developing an optimized GCPW feed to the binary SIW structure to improve both bandwidth and return loss performance while preventing the excitation of higher order modes associated with the use of microstrip lines on thick substrates. The proposed antenna array concept here consists of four parts: (1) an array of eight printed radiating elements (Vivaldi antenna) placed along the axis; (2) a feeding network printed on the same dielectric substrate integrated with the radiating elements; (3) two flared metal plates on top and bottom of the substrate; (4) different lengths of 0.5" diam polystyrene rods for gain control. Design details of

the proposed wideband transitions and feed networks together with its simulation and the experimental results of the fabricated structure will be presented in the following sections.

Substrate Integrated Waveguide Technology

Technology of Substrate integrated waveguide (SIWs) structures fabricated on printed circuit boards is a lower cost alternative. Where SIW sidewalls are constructed from lined via holes, as shown in Fig.1, rather than solid fences in conventional rectangular waveguides. This technology is simple, less expensive, and renders light structures. S. Yang et al. [5] have presented extensive full parametric study of the SIW structures that is based on a full wave 3D analysis using Ansoft HFSS. To simplify their design, S. Yang et. al [5] developed an equivalent conventional dielectric loaded rectangular waveguide to model the SIW structure (as shown in Fig.1). Similar steps have been utilized in our design including using a thick substrate to reduce conductor loss.

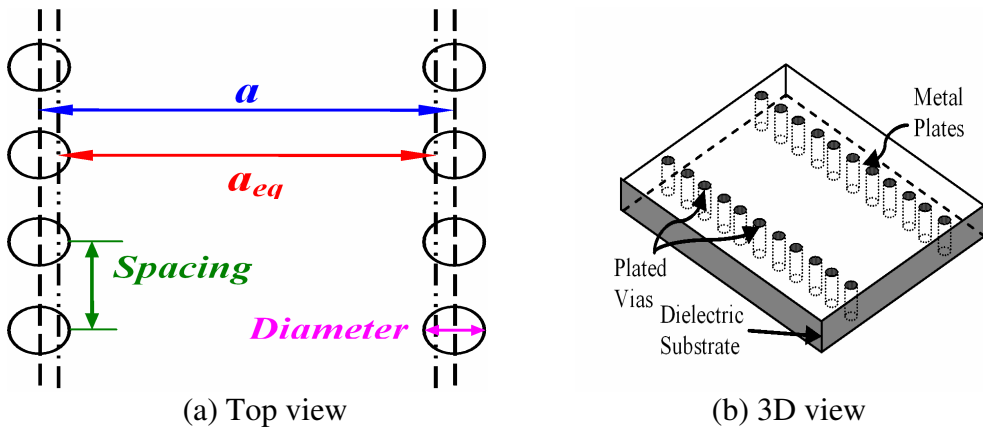


Fig.1. Substrate integrated waveguide on dielectric substrates.

Design of Wideband GCPW to SIW Transition

Use of thick substrate (as mentioned above) will reduce conductor loss, however, a microstrip feed structure in this case [3] is not appropriate, as the feed lines will be very wide and higher order modes may be easily excited. Therefore, a GCPW (Ground Coplanar Waveguide) has been adapted. The previously utilized transition from the GCPW to SIW in [7] has a narrow band performance. Here we have developed a novel wide band GCPW to SIW transition to circumvent such problems. The design covers over 2 GHz bandwidth and is centered around 8 GHz. Figs. 2a, 2b and 2c show the Ansoft HFSS model, its simulation, and the implemented circuit of the back-to-back GCPW to SIW transition. Fig. 2d is the measured result of the back-to-back test fixture, which shows an insertion loss of a single GCPW to SIW transition of less than 0.7 dB from 7 to 9 GHz which is slightly higher than the simulated results.

Feed Network

The developed binary feed network construction is based on an extensive use of optimized T-junction designs. These designs were previously developed by [7] through direct translation from its metallic waveguide version [8-9] to SIW. In our implementation, we have followed the design steps outlined in [7], and an equivalent “a” dimension of SIW has been selected to give us a relatively wide bandwidth for a single stage T-junction, as well as, a decent insertions loss values. Then the spacing between the combining stages is judiciously selected to achieve a wideband compact 1 to 8 power divider in three cascaded stages. A back to back 1 to 8 power divider is fabricated as shown in Fig. 3(a). It is very compact and the measured back-to-back insertion loss from 7.5 to 8.5 GHz is less than 2.5 dB which is much lower than similar measurements reported by [2] and [3]. As mentioned in [5], this kind of SIW feeding network can lead to a very balanced power division over a wide band. Both the balanced power split and low insertion loss should help in increasing the gain and overall efficiency of the antenna array. Meanwhile, the use of thick substrates and the optimized T-junctions has led to a performance improvement including a good input port return loss over the 7 to 9 GHz frequency range. Fig.3 (a, b) shows the return and the insertion losses of the shown structure.

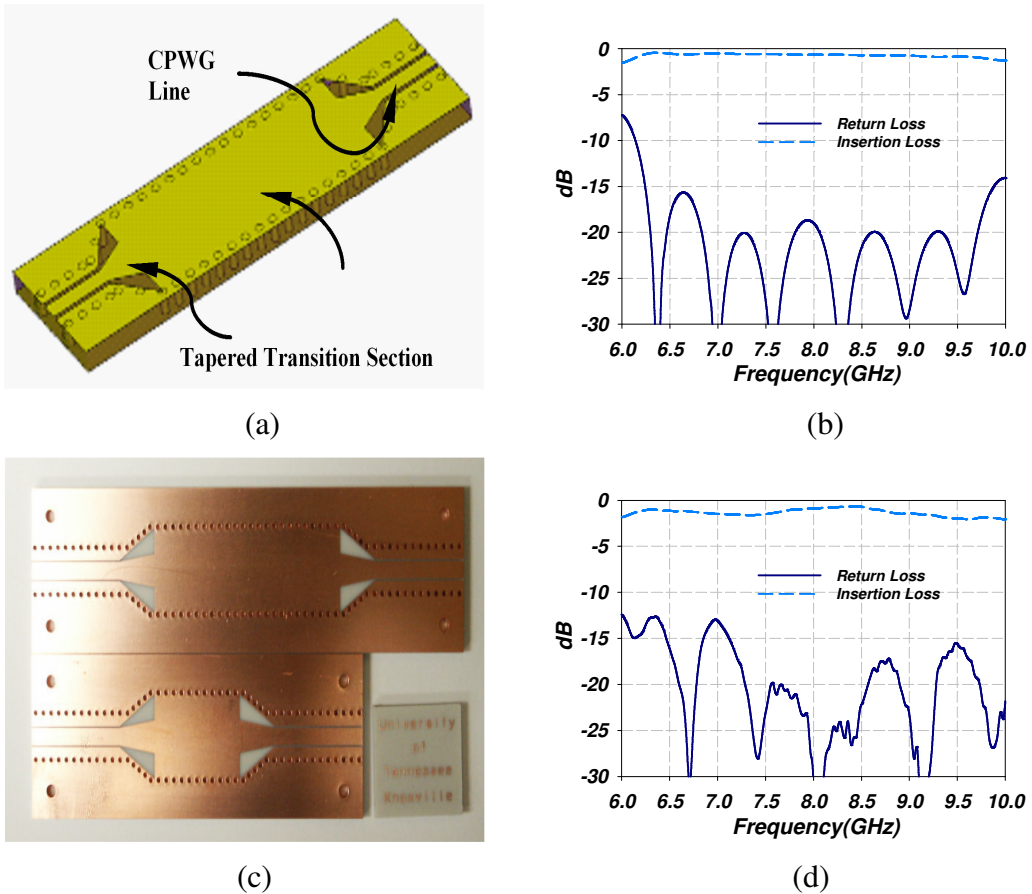


Fig.2. (a) GCPW to SIW back to back transitions model in Ansoft HFSS, (b) Simulation results, (c) Manufactured GCPW to SIW back to back transitions, (d) Measured results

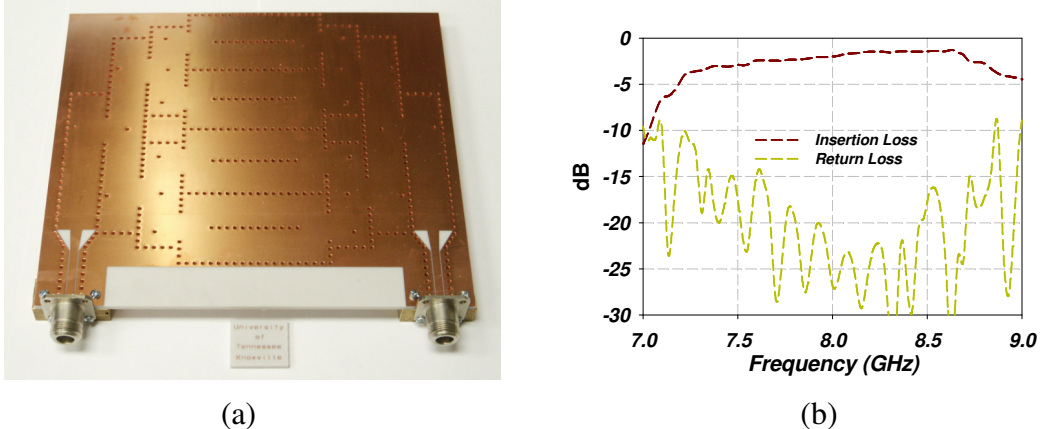


Fig.3. (a) Back to back 1 to 8 feed network, (b) Measured return loss and insertion loss of the back to back 1 to 8 feed network.

Single Antenna Element Design

For SIW technology, there are a number of antennas that can be used such as H-plane horns, slot antennas, tapered slot traveling wave antennas, etc. H-plane horns would require very thick substrates to have low return loss over a wide band, which would increase the overall system cost. Slot antennas, on the contrary, have the advantage of small size and can be used in a traveling wave array configuration to form a 2D array. However, the phase shift between the elements will change with frequency causing beam squint. This is undesirable for some UWB applications such as see through walls; where it is desirable to have the beam direction fixed with frequency. Thus we have chosen to use tapered slot antennas that are fed using SIW and would have minimal beam squint. The taper can be linear (LTSA), exponential (Vivaldi), elliptical or constant width (CWTSA) [10]. Linear elements are generally easier to design due to their relatively smaller number of parameters that need to be optimized. However they need to be long enough to have a good match over a wide band such as in [4], where an 80mm taper length was utilized. However, in our implementation, instead of using the wideband balun, we used a SIW to feed a Vivaldi antenna to minimize the losses. Here, we have investigated the use of three configurations (shown in Fig. 4), and their length is 27 mm-- to be compact while providing adequate wide band operation. The first element is a LTSA element, and it has demonstrated a good return loss; but only over a narrow band. The second element is an exponentially tapered element, whose exponential taper rate was optimized to obtain a low return loss. Meanwhile, the third element is an exponentially tapered slot antenna combined with a polystyrene rod. The power is coupled to the HE_{11} mode of the rod and radiates (leaks) from the surface of the rod. This allows for a significantly higher gain as compared to the original design (as shown in Fig. 5.b). We have achieved better than 10 dB return loss which is adequate, however, this return loss and gain performance can be further improved upon utilizing a tapered polystyrene rod design. The design detail of the single element is shown in Fig. 6. The dimensions of the single element are shown in Table 1. Fig.8a shows the fabricated single element Vivaldi antenna. Fig. 8b

demonstrates the return loss of the single element Vivaldi antenna which is less than 10dB over 5.5 to 9 GHz.

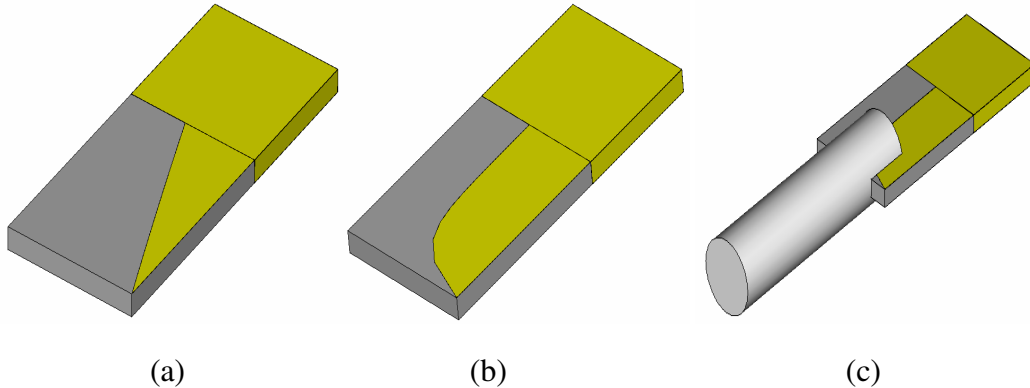


Fig.4. The three investigated elements (a) the linearly tapered slot antenna, (b) the exponentially tapered slot antenna and (c) the exponentially tapered slot antenna with the protruded dielectric rod.

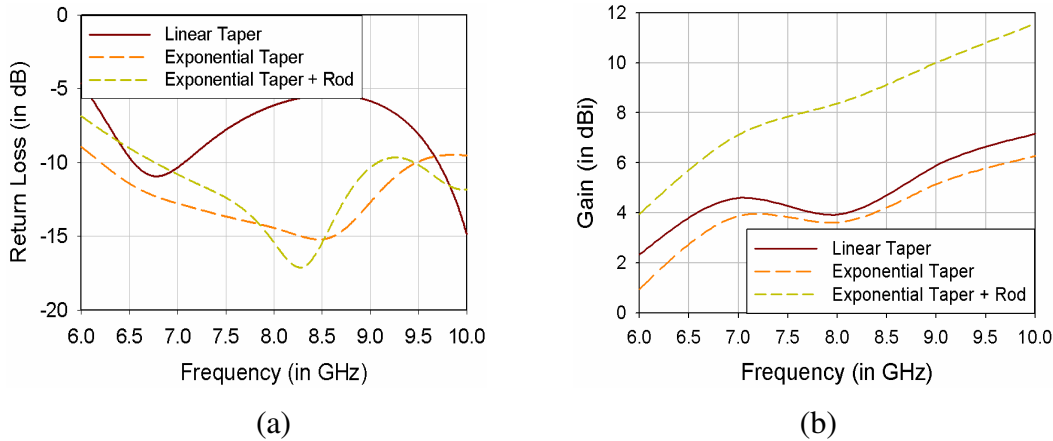


Fig.5. (a) Return loss the three elements, (b) Gains of the three elements.

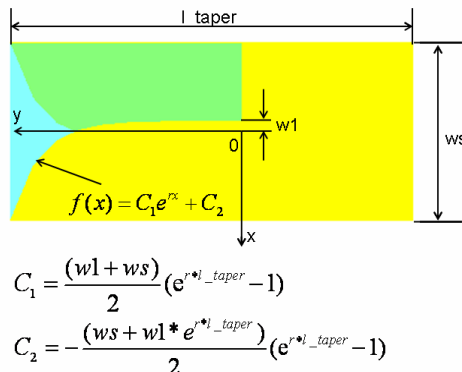


Fig. 6. Configuration of the proposed antipodal Vivaldi antenna.

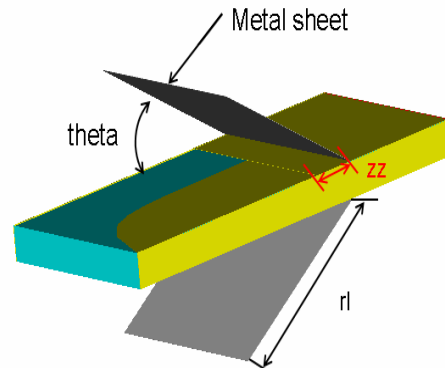


Fig.7. Configuration of the proposed antipodal Vivaldi antenna with flared metal sheets

Table 1 parameters of single element

l_taper (mm)	r	w1(mm)	ws (mm)
27	0.3	1.25	20.5

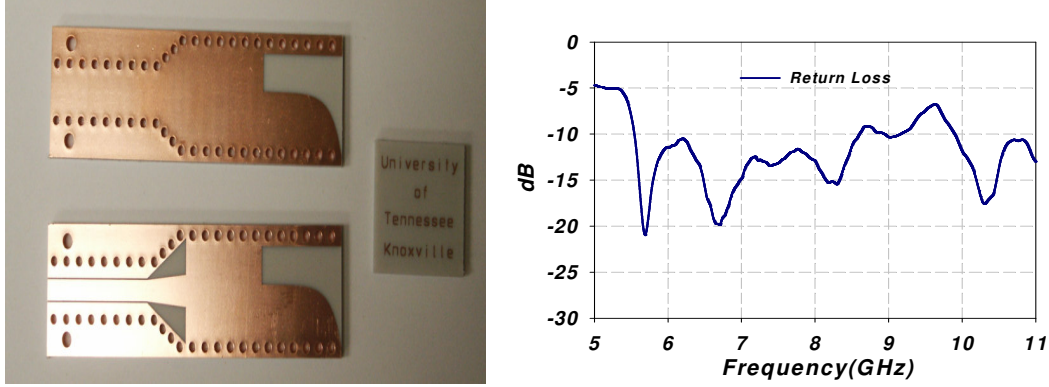


Fig.8. (a) Fabricated single element, (b) Measured return loss

In order to lower the sidelobe level of the antenna even further, two flared metal sheets are put along the antenna on both sides of the substrate with a flare angle less than 180^0 as shown in Fig. 7. Fig.9 (a) & (b) are the simulation results using CST Microwave Studio, which shows that the return loss of the antenna changes with the aperture angle (θ_1) and the gain increases with the length (r_1) of the two flared metal sheets. Since several adjacent arrays will be used in UWB see through walls radar in a 2D array configuration, the maximum height of the metal sheets measured from the substrate is severely limited to avoid grating lobes in the H-Plane (H-plane is the plane perpendicular to the substrate).

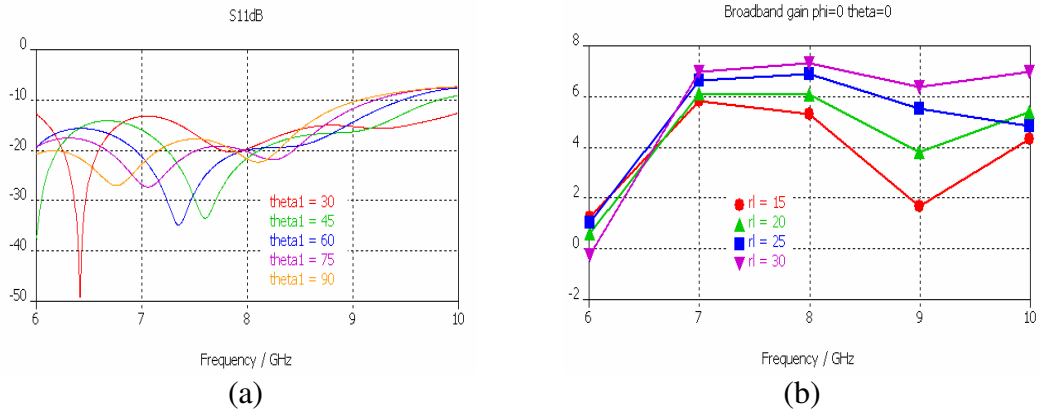


Fig.9.(a) Return Loss VS theta1, (b) Gain VS r1

Eight Elements Array Design

As part of our investigation to develop a see through wall system based on UWB technology, it is required to develop an antenna with an adequate gain (~ 12 dB) over the operating bandwidth in order to preserve an acceptable SNR at the

receiver side. This will reduce the amount of multi-path reflections that the DSP detection algorithm has to process, and will simplify the overall system design. It is also required that the array has a small return loss and minimal structure losses (i.e. achieve high radiation efficiency) in order to reduce the antenna noise temperature and obtain a high G/T ratio. As the developed synthetic aperture radar for our see through wall system requires a narrow E-plane beam width; therefore an E-plane linear uniform array will be pursued here. The amplitude distribution affects the side lobe level and the gain. For our application, since we need a wide band, using a constant tapered distribution is difficult to achieve over a wideband. Thus, we have chosen a uniform distribution with a binary feed network, which allows a uniform excitation over the required wide band. An optimum design would be to set the spacing between the elements such that it is $\sim 0.8\lambda$ at the highest operating frequency (λ_{\min}), which is based on a limited synthetic steering providing no grating lobes to appear over the operating band while achieving the maximum possible gain. Also, the increase in gain vs. frequency is partially compensated by the increase of the conductor and dielectric losses (which increase with frequency); thus allowing a better fidelity over the operating band. Another point to consider in this array design is mutual coupling between the elements which affects the return loss of the single element when it is placed in an array configuration. We have evaluated the use of 3 - 7 element array to check the mutual coupling between the elements, and the three element array structure is shown in Fig.10a-- as an example. As shown in Fig.10b, the mutual coupling as expected shifts the return loss center frequency of the array element and would require re-tuning; meanwhile the mutual coupling from non-adjacent element is very small here. Similar to the single element, after putting two pieces of metal around the Vivaldi array, the H-Plane sidelobes become smaller and the main beam angle increases as shown in Fig. 11.

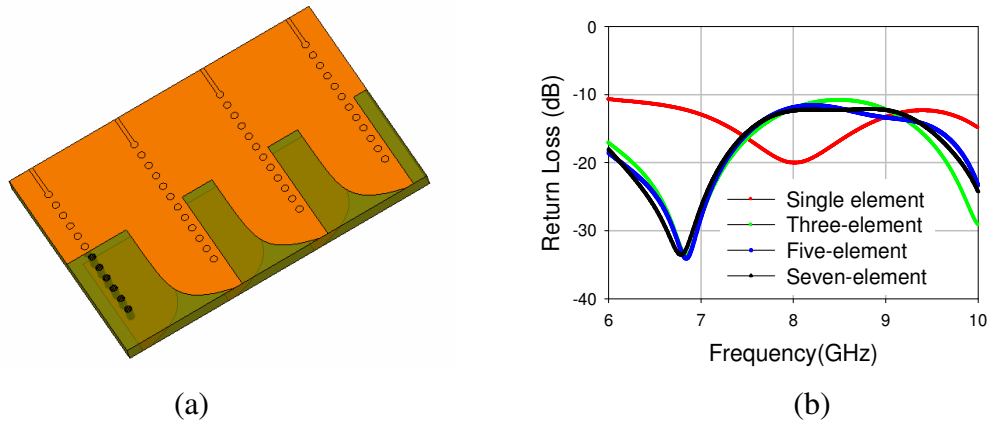


Fig.10. (a) Test structure for the mutual coupling effect, (b) Return Loss Vs element numbers

The Vivaldi antenna array is designed to operate over the 7 to 9 GHz frequency range, and was printed on a 125mil thick Neltec NY9208 substrate with a dielectric constant of 2.08 and loss tangent of 0.0006. Fig.12 shows the manufactured eight elements Vivaldi array, where fed using a SIW structure feed

network. Polystyrene rods can be added to the array (as shown in Fig.13a). Adding these dielectric rods to each element with optimized dimensions can reduce the H-plane beam width and improve the overall gain of the whole array by 2-3dB. Because of SIW feeding network, it is more convenient to add two flared metal sheets (see Aleksandar Negid et. al [11]). Fig. 13b shows the Vivaldi array with the two flared metal sheets.

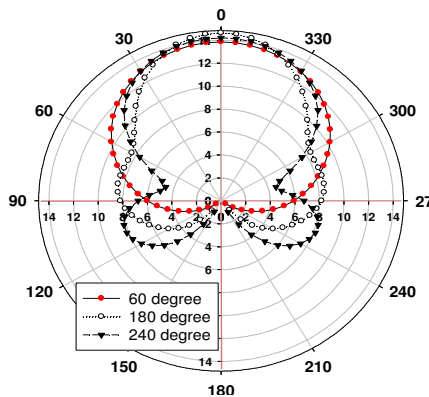


Fig.11 H-Plane radiation pattern

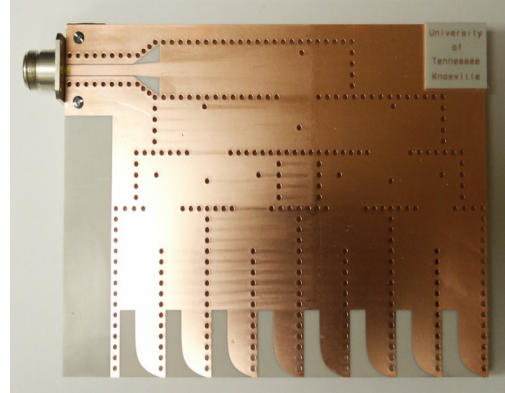
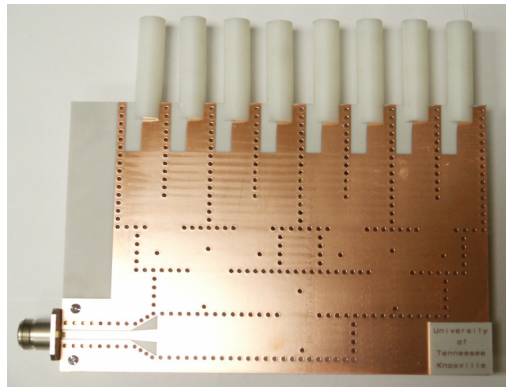
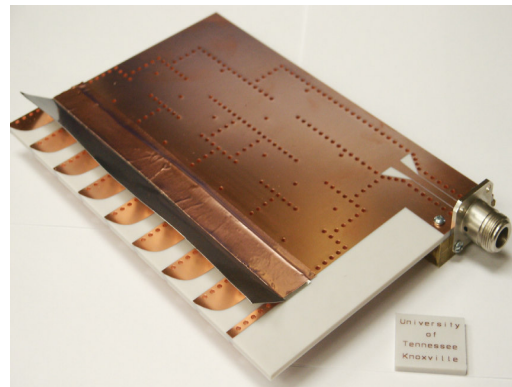


Fig.12 Eight elements Vivaldi array



(a)



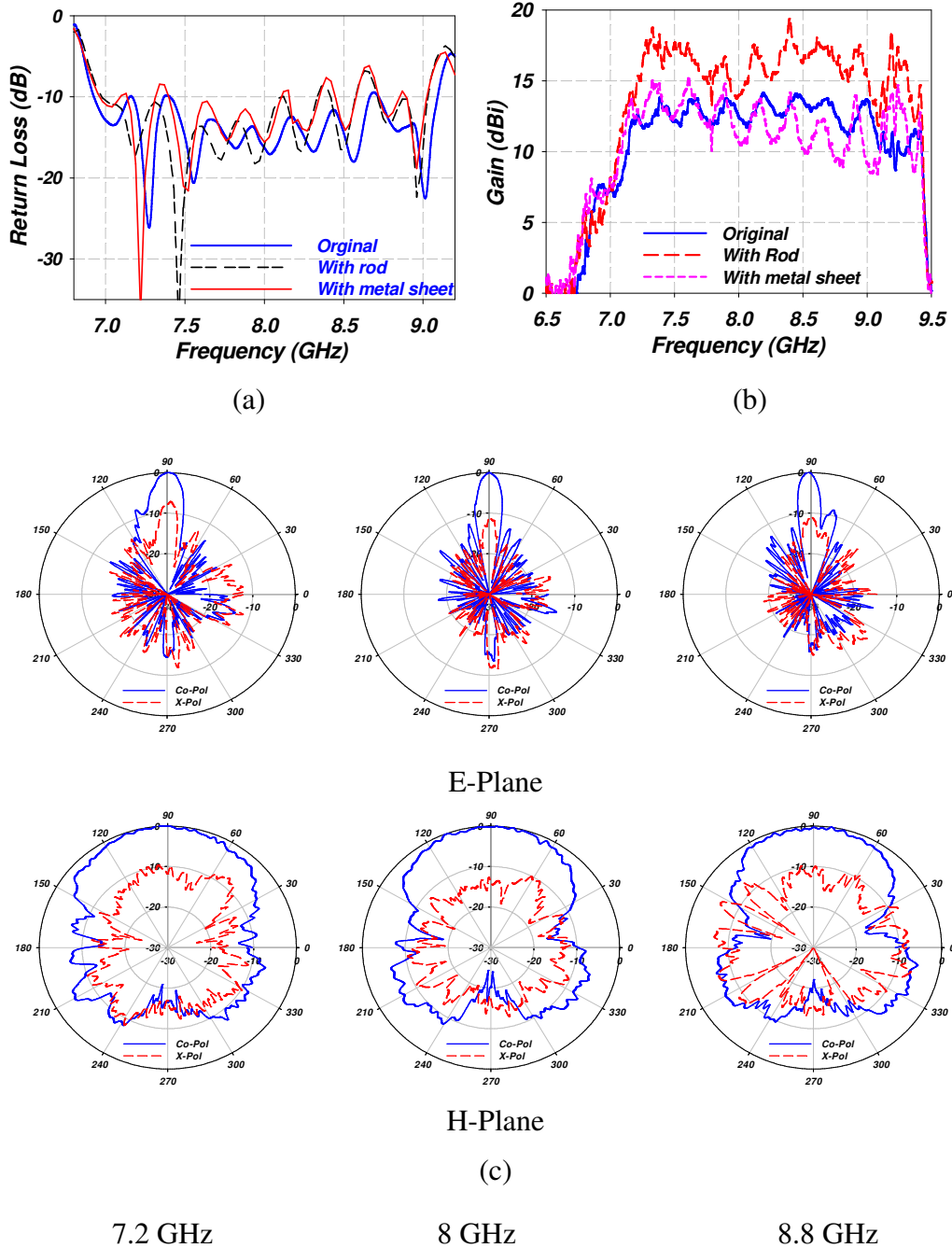
(b)

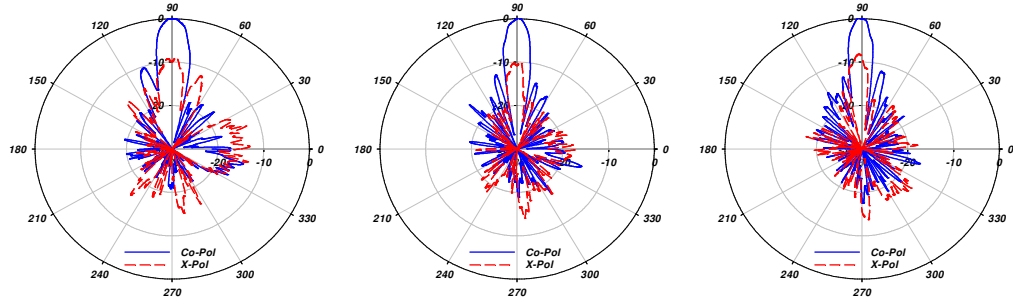
Fig.13. (a) Eight elements Vivaldi array with polystyrene rods, (b) Eight elements Vivaldi array with metal sheet

Array Measured Results

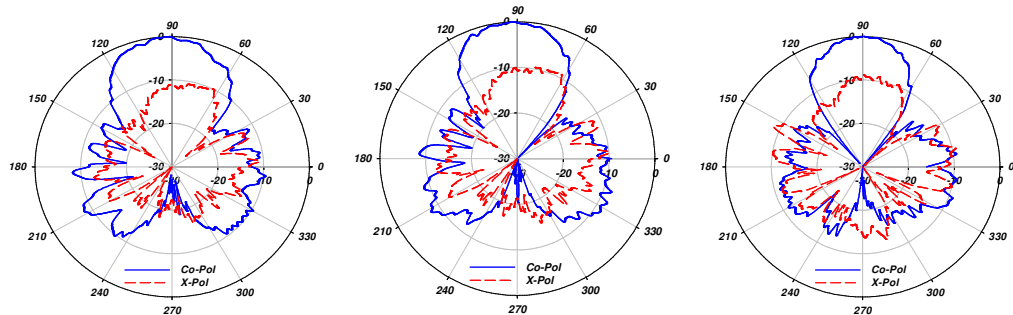
The measured input return loss and radiation patterns are shown in Figs. 14a, 14b & 14c. The return losses of the three arrays are mostly better than 10 dB over a 2 GHz bandwidth. A gain of 12.5 dB is sustained over the 1.8 GHz bandwidth for the eight-element array; meanwhile it is well over 15 dB in the case with the rods. The efficiency of the Vivaldi array without rods has exceeded 75% and only utilizes a 7×7 in² real-estate area as compared to [2] with a 12×18 in² area for a similar gain at the center frequency (10 GHz). Moreover, the array with rods possesses an efficiency of over 78% at the center frequency which is a pronounced improvement to the original Vivaldi array. It should be noted that the conductor loss has been significantly reduced in this case, and the reduction in the

radiation efficiency is actually due to the reflection loss rather than conductor loss. Thus, the array G/T ratio, should be significantly higher as compared to the previously developed one using Wilkinson power dividers [2]. Additionally, the H-plane beam width is narrower after adding the rods as shown in Fig. 14d. The H-plane side lobe levels become even lower after adding two flared metal sheets as shown in Fig. 14e.



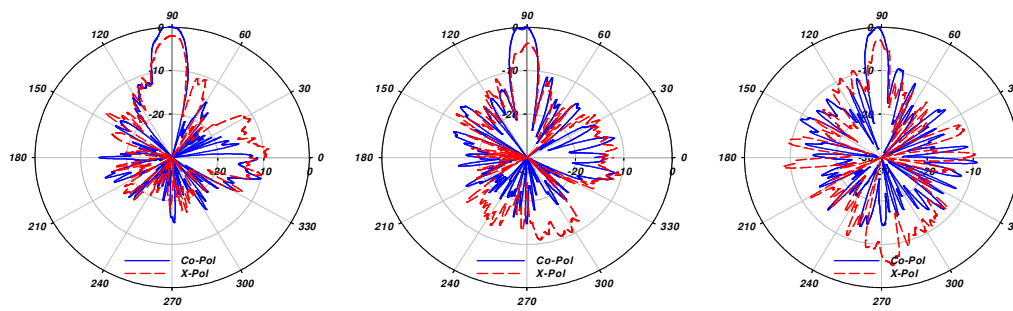


E-Plane

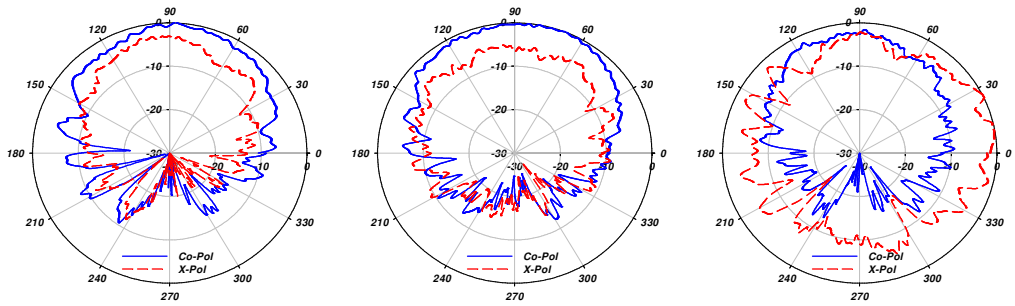


E-Plane

(d).



E-Plane



E-Plane

(e)

7.2 GHz

8 GHz

8.8 GHz

Fig 14. (a) Return loss of the arrays, (b) Gain VS. Frequency, (c) & (d) Radiation pattern VS. Frequency (original/with rod), (e) Radiation pattern VS. Frequency (with metal sheets)

Conclusion

Development of Vivaldi antenna array feeds to operate over a wide band with low insertion loss has previously hindered its use. In this paper, we use a SIW structure with an optimized design fabricated on a thick substrate to minimize conductor losses. The use of optimized T-junctions and the integration of a GCPW feed have led to even an improved performance with significant loss reduction. The novel design of the feeding network has helped in minimizing the size of the whole array. Insertion of dielectric rods into the flared notches of the Vivaldi antennas has led to an increase in the gain, meanwhile adding the flared metal helped in improving the performance in the H-plane. The developed Vivaldi antenna array, which has high gain, narrow beam width in the E-plane & H-plane and relatively wide bandwidth, is extremely useful for ultra wide band antenna applications such as see through walls and high precision localization.

References

- [1] Sang-Gyu Kim; Kai Chang; "A low cross-polarized antipodal Vivaldi antenna array for wideband operation" Antennas and Propagation Society International Symposium, 2004. IEEE; Volume 3, 20-25 June 2004 Page(s):2269 - 2272 Vol.3
- [2] Yunqiang Yang; Cemin Zhang; Song Lin; Fathy, A.E.; "Development of an ultra wideband Vivaldi antenna array" Antennas and Propagation Society International Symposium, 2005 IEEE; Volume 1A, 3-8 July 2005 Page(s):606 - 609 Vol. 1A
- [3] ZhangCheng Hao; Wei Hong; Hao Li; Hua Zhang; Ke Wu; "Multiway broadband substrate integrated waveguide (SIW) power divider" Antennas and Propagation Society International Symposium, 2005 IEEE; Volume 1A, 3-8 July 2005 Page(s):639 - 642 Vol. 1A
- [4] ZhangCheng Hao; Wei Hong; Ji Xin Chen; Xiao Ping Chen; Ke Wu; "A novel feeding technique for antipodal linearly tapered slot antenna array" Microwave Symposium Digest, 2005 IEEE MTT-S International
- [5] S.Yang, A.Elsherbini, S. Lin, A.Fathy, A.Kamel, H.Elhennawy, "A Highly Efficient Vivaldi Antenna Array Design on Thick Substrate and Fed by SIW Structure with Integrated GCPW Feed" Accepted for oral presentation at the *IEEE AP-S Symposium*, Hawaii, Jun. 2007
- [6] H. Uchimura and T. Takenoshita, "Wiring board equipped with a line for transmitting a high frequency signal," U.S. Patent 5 982 256, Nov. 9, 1999.
- [7] S. Yang, S. H. Suleiman, and A. E. Fathy, "Development of a Slotted Substrate Integrated Waveguide (SIW) Array Antennas for Mobile DBS Applications," presented at Proc. Antennas Applications. Symp., Montecello, IL, Sep. 2006.

- [8] T. Takahashi, J. Hirokawa, M, Ando and N, Goto, “A single-layer power divider for a slotted waveguide array using π -junction with an inductive wall,” *IEICE Trans. Commun.*, vol. E79-B, no. 1, pp. 57–62, Jan. 1996.
- [9] K. Fukazawa, J. Hirokawa, M, Ando and N, Goto, “Two-way power divider for partially parallel feed in single layer slotted waveguide arrays,” *IEICE Trans. Commun.*, vol. E81-B, no. 6, pp. 1248–1253, June. 1998.
- [10] Schaubert, D.; Kollberg, E.; Korzeniowski, T.; Thungren, T.; Johansson, J.; Yngvesson, K. “Endfire tapered slot antennas on dielectric substrates”, *IEEE Trans. Antenna and Prop.*, Volume 33, Issue 12, Dec 1985 Page(s): 1392 - 1400
- [11] Aleksandar Negid, Zoran Midid&, Siniga, Jovanovid&, Ivana Radnovic1, and Dugan Negid ; “Millimeter-Wave Printed Antenna Arrays for Covering Various Sector Widths” *IEEE Antennas and Propagation Magazine*, Vol. 49, No. 1, February 2007

A STUDY OF THE PERFORMANCE PROPERTIES OF SMALL ANTENNAS

Steven R. Best
The MITRE Corporation
202 Burlington Road
Bedford, MA 01730
sbest@mitre.org
(781) 271-8879

ABSTRACT: Electrically small antennas are of interest in a variety of applications, particularly where the antennas must be unobtrusive. The performance properties considered in the design of small antennas typically include impedance, radiation efficiency, pattern shape, polarization and particularly operating bandwidth and quality factor (Q). In this paper, we compare the performance properties of several fundamental small antenna designs as a function of overall height and size (ka). Antennas studied here include the multi-arm folded helix, the matched disk loaded dipole, the matched spherical-cap dipole and the multi-arm spherical resonator. The antennas are compared to determine which configuration offers the best performance in terms of pattern shape, radiation efficiency, and $\frac{1}{2}$ -power and 2:1 VSWR bandwidths.

1. Introduction

Optimization of the performance properties of electrically small antennas has been given considerable attention in recent years. Performance optimization goals generally include achieving a good impedance match (low VSWR), high radiation efficiency and low Q or wide operating bandwidth. In this optimization process, the small antenna's Q and bandwidth properties are typically compared against well defined fundamental limits.

Design approaches used in achieving the optimization goals stated above vary and include techniques such capacity or top-hat loading [1]-[2], the use of multiple folded arms in wire monopole or dipole antennas [2]-[3], inductive loading in wire antennas (an increase in conductor length) [4], and more recently the use of Metamaterials [5]-[7] and multi-arm coupled structures [8]-[10].

It is well known that any electrically small antenna can be impedance matched at any single frequency using an external matching network comprised of reactive matching components. One challenge in using an external matching network with an electrically

small antenna is that the loss resistance within the matching network often exceeds the radiation resistance of the antenna, resulting in low overall efficiency. In some cases, the reduction in mismatch loss achieved with the impedance match exceeds the increase in loss due to the matching components and better overall performance is achieved relative to the isolated mismatched antenna.

Impedance matching can also be accomplished within the antenna structure using a number of techniques that include but are not limited to the use of multiple folded arms [11]-[13] and shunt or parallel matching stubs [14]-[15]. These techniques are often more efficient than impedance matching the small antenna using an external matching network. Many electrically small antenna designs have been described which exhibit low VSWR and high radiation efficiency [8]-[9], [12]-[13], [15], [16]-[19].

The remaining challenge in designing a small antenna is optimizing the operating bandwidth, which is often characterized using the antenna's Q . Recent efforts in this area have demonstrated that small antennas can be designed to achieve a Q that closely approaches fundamental limits.

The objective of this work is to examine and compare the relative performance properties of a number of fundamental small antenna designs which include the folded spherical helix [11]-[12], the folded cylindrical helix, the disk-loaded dipole [20], the spherical-cap dipole [21]-[22] and the spherical resonator antenna [8]. The folded spherical helix is a single resonant antenna that exhibits a Q within 1.5 times the lower bound. The disk-loaded dipole and spherical-cap dipole are well known designs that are often assumed to be optimum approaches in achieving the lowest possible Q with a small antenna. The spherical resonator is of interest because it exhibits closely spaced resonances within its defined VSWR bandwidth and may offer wider bandwidths than can be achieved with small antennas that exhibit a single resonance.

The performance properties studied include impedance, radiation efficiency, pattern and polarization performance, Q and bandwidth.

2. Fundamental Limitations of Small Antennas

Most of what follows in this section has been presented in previous journal and/or conference publications. It is presented here for completeness of the work and as a necessary background discussion for the relative performance comparisons that are to be made between the different small antennas.

An antenna is considered to be electrically small as a function of its overall size or occupied volume relative to the wavelength. A small antenna is one where $ka \leq 0.5$, where k is the free space wavenumber, $2\pi/\lambda$, and a is the radius of an imaginary sphere circumscribing the maximum dimensions of the antenna.

The frequency dependent impedance of the electrically small antenna is given by $Z(\omega) = R(\omega) + j X(\omega)$, where ω is the radian frequency $2\pi f$, f is the frequency in Hz, $R(\omega)$ is the antenna's total feed point resistance (including both radiation and loss terms) and $X(\omega)$ is the antenna's feed point reactance. The bandwidth and Q of the small antenna are defined at radian frequency ω_0 , where the antenna is either naturally self-resonant or tuned to resonance with a lossless series reactance. In most instances, the tuned or self-resonant small antenna exhibits a single resonance within its defined VSWR bandwidth. The maximum extent of the defined bandwidth is typically limited to values of VSWR less than 5.828 ($\frac{1}{2}$ -power).

The bandwidth of the small antenna is often characterized by its Q because matched VSWR bandwidth and Q have been shown to be inversely related and a lower bound on the minimum achievable Q is defined and well known. No electrically small antenna will exhibit a Q less than the lower bound.

The exact Q of an electrically small antenna that is tuned or made to be self-resonant at a frequency ω_0 , is defined as [23]-[24]

$$Q(\omega_0) = \frac{\omega_0 |W|}{P} \quad (1)$$

where W is internal energy and P is the total power accepted by the antenna. If the tuned small antenna exhibits a single resonance within its defined VSWR bandwidth, its Q can be accurately approximated from its impedance properties using [24]

$$Q(\omega_0) \approx Q_Z(\omega_0) = \frac{\omega_0}{2R(\omega_0)} \sqrt{R'(\omega_0)^2 + \left(X'(\omega_0) + \frac{|X(\omega_0)|}{\omega_0} \right)^2} \quad (2)$$

where $R'(\omega_0)$ and $X'(\omega_0)$ are the frequency derivatives of resistance and reactance, respectively. The lower bound on Q is given by [25]

$$Q_{lb} = \eta_r \left(\frac{1}{(ka)^3} + \frac{1}{ka} \right) \quad (3)$$

where η_r is the antenna's radiation efficiency.

To characterize the antenna's bandwidth, it is necessary to define bandwidth in a manner such that Q and bandwidth are inversely related. The definition of bandwidth suitable for this purpose is fractional matched VSWR bandwidth, $FBW_V(\omega_0)$, where the VSWR of the tuned antenna is determined using a characteristic impedance, Z_{CH} , equal to the antenna's feed point resistance, $R(\omega_0)$. Fractional matched VSWR bandwidth is given by

$$FBW_V(\omega_0) = \frac{\omega_+ - \omega_-}{\omega_0} \quad (4)$$

where ω_+ and ω_- are the frequencies above and below ω_0 , respectively, where the VSWR is equal to any arbitrary value denoted by s . Fractional matched VSWR bandwidth and Q are related as [24]

$$Q(\omega_0) \approx \frac{2\sqrt{\beta}}{FBW_V(\omega_0)}, \quad \sqrt{\beta} = \frac{s-1}{2\sqrt{s}} \leq 1 \quad (5)$$

The approximations in Eqs. (2) and (5) were derived in [24] under the assumptions that the tuned antenna exhibits a single resonance within its defined VSWR bandwidth and that the $1/2$ -power matched VSWR bandwidth ($s = 5.828$) is not too large.

The minimum achievable Q of a tuned or matched small antenna exhibiting a single resonance is limited by the lower bound defined in Eq. (3). Since Q and matched VSWR bandwidth are inversely related, the matched VSWR bandwidth of the small antenna exhibiting a single resonance will not be greater than that predicted by the inverse of Q . Using Eqs. (3) and (5), an upper bound on the fractional matched VSWR bandwidth can be written as

$$FBW_{Vub} = \frac{1}{\eta_r} \frac{(ka)^3}{1+(ka)^2} \frac{s-1}{\sqrt{s}} \quad (6)$$

3. The Small Antennas

In this section, the basic configurations and performance properties of the small antennas are presented. These antennas include the folded spherical helix, the folded cylindrical helix, the disk-loaded dipole, the spherical-cap dipole and the multi-arm spherical resonator. Performance properties considered include the antenna's impedance,

radiation efficiency, pattern characteristics (including polarization), VSWR bandwidth and Q .

3.1 The Folded Spherical Helix

The first antenna considered is the 4-arm folded spherical helix [11]-[12] because it was specifically designed to exhibit a good impedance match in a 50Ω system, high radiation efficiency and a low Q . The folded spherical helix exhibits a single resonance and has a Q that is within 1.5 times the lower bound at a value of $ka \approx 0.263$. The folded spherical helix is considered the baseline antenna for this study. Other antennas compared to the folded spherical helix will be designed to have the same height, same value of ka or operate at (or very near) the same frequency. Here, the design objective is to operate all of the antennas as close to 300 MHz as possible.

The folded spherical helix, its impedance, matched VSWR ($Z_{CH} = 57.8\Omega$) and radiation patterns are presented in Fig. 1. Numerical results are obtained using the NEC4 engine of EZNEC/4 Pro [26]. Copper conductor loss is included in all of the numerical simulations. The antenna is operated as a dipole (no ground plane), has a single feed point and has an overall height and diameter of 8.36 cm. It has a conductor diameter of 2.6 mm. It is self-resonant at a frequency of 299.8 MHz.

The Q of the folded spherical helix, calculated using Eq. (2), is 84.78, which is approximately 1.5 times the lower bound of 57.39. Its radiation efficiency is 97.4%. Its $\frac{1}{2}$ -power and 2:1 VSWR bandwidths are 2.37% and 0.87%, respectively. The radiation pattern illustrates that the folded spherical helix primarily operates as an electric dipole with minimal cross-polarization.

3.2 The Folded Cylindrical Helix

The 4-arm folded cylindrical helix is designed based on the same principles as the folded spherical helix, with the exception that the conductors are wound on the outside volume of an imaginary cylinder rather than a sphere. In this instance, the cylindrical helix has the same overall height and diameter as the spherical helix, 8.36 cm. The conductor diameter is also the same, 2.6 mm. To maintain nearly the same operating frequency as the folded spherical helix, the total conductor length in each arm had to be adjusted. Since the cylindrical helix occupies a greater physical volume than the spherical helix, it is expected to have greater bandwidth and lower Q . However, since it occupies less of the spherical volume defined by the value of ka , its Q will not approach the lower bound as closely as that of the spherical helix. The cylindrical folded helix is self-resonant at 301.1 MHz, with a value of $ka = 0.373$.

The folded cylindrical helix, its impedance, matched VSWR ($Z_{CH} = 83.6\Omega$) and radiation patterns are presented in Fig. 2. Its resonant resistance is greater than that of the folded cylindrical helix and it exhibits a VSWR less than 2.0 in a 50Ω system. The Q of

the folded spherical helix is 53.5, which is approximately 2.5 times the lower bound of 21.35. Its radiation efficiency is 98.3%. Its $\frac{1}{2}$ -power and 2:1 VSWR bandwidths are 3.75% and 1.33%, respectively, both greater than those of the spherical helix. Similar to the folded spherical helix, the folded cylindrical helix primarily operates as an electric dipole with minimal cross-polarization.

3.3 The Disk-Loaded Dipole

Top, capacitive or disk-loading a straight-wire dipole or monopole antenna is a well known technique for size reduction [20]. A wire-grid and solid disk version of a disk-loaded dipole are depicted in Fig. 3. The wire grid version is modeled using EZNEC while the solid disk version is modeled using Microwave Studio [27]. Each of these antennas has the same overall height and diameter as the folded spherical helix, 8.36 cm. These antennas have the same value of ka as the folded cylindrical helix.

The impedances of these antennas are presented in Fig. 4. As expected, the impedances of these antennas are similar. The solid top-disk version of the antenna has less capacitive reactance since there is more capacitance between the upper and lower disks. Without tuning, neither is resonant near 300 MHz. The wire-grid top-hat version of the antenna is considered further since it can be easily modeled using EZNEC and the results can be more directly compared to the antennas constructed using only wires.

To tune the disk-loaded dipole for self-resonance near 300 MHz, a helical coil dipole is placed between the upper and lower plates as illustrated in Fig. 5(a). To then impedance match the antenna to 50Ω , a shunt or parallel stub is placed across the feed point as illustrated in Fig. 5(b).

The impedance, matched VSWR ($Z_{CH} = 50\Omega$) and radiation patterns of the matched disk-loaded dipole are presented in Fig. 6. The antenna is matched at a frequency of 294.4 MHz, where $ka = 0.365$. The Q of the disk loaded dipole is 48.0, which is approximately 2.14 times the lower bound of 22.27. Its radiation efficiency is 95.5%. Its $\frac{1}{2}$ -power and 2:1 VSWR bandwidths are 3.04% and 1.44%, respectively, both greater than those of the spherical helix, but slightly less than those of the cylindrical helix. The matched disk-loaded dipole operates as an electric dipole with minimal cross-polarization.

3.4 The Spherical-Cap Dipole

The spherical-cap dipole is also a top-loaded antenna similar to the disk-loaded dipole. With this design, the top-loading structure maintains a spherical shape so that the entire antenna structure fits within the spherical volume defined by the value of ka . In [21], Wheeler described the spherical-cap dipole in these terms: “*the best simple utilization of a spherical volume is achieved by spherical caps covering about one-half the surface, tuned by a distributed inductor.*” The distributed inductor Wheeler refers to

is the helical coil dipole that was used to tune the disk-loaded dipole as described in the previous section. In [22], Lopez modeled an untuned spherical cap dipole and achieved a Q that was within 1.75 times the lower bound. Lopez concluded that this was the lower achievable bound for electric antennas. We see that the folded spherical helix more closely approaches the lower bound, being within approximately 1.5 times its value. A theoretical design approaching within 1.5 times the lower bound was also presented by Stuart and Pidwerbetsky in [7]. As discussed by Thal in [28], the lower achievable limit for electric dipoles is 1.5 times the lower bound.

Here, a wire grid version of the spherical-cap dipole, having an overall diameter of 8.36 cm is considered. The matched spherical-cap dipole, its impedance, matched VSWR ($Z_{CH} = 50\Omega$) and radiation patterns are presented in Fig. 7. The antenna is matched at a frequency of 293.6 MHz, where $ka = 0.26$. The Q of the spherical-cap dipole is 95.29, which is approximately 1.68 times the lower bound of 56.86. Its radiation efficiency is 93.3%. Its $\frac{1}{2}$ -power and 2:1 VSWR bandwidths are 2.06% and 0.74%, respectively, both slightly less than those of the spherical helix. The spherical-cap dipole operates as an electric dipole with minimal cross-polarization.

3.5 The Spherical Resonator

The spherical resonator antenna was introduced by Stuart and Tran in [8] and [9]. It is comprised of a single-fed wire structure electromagnetically coupled to closely spaced identical wires as illustrated in Fig. 8, which depicts a 6-arm version of the antenna. At a frequency where strong coupling modes exist between the feed-arm and the parasitic arms, a tight (narrow band) coupling loop develops in the impedance of the antenna as illustrated in Fig. 9. In the region of this tight impedance loop, the frequency derivatives of the antenna's resistance and reactance are such that an accurate approximation of the antenna's exact Q may not hold and the value of approximate Q determined using Eq. (3) may be less than the lower bound [10]. When the spherical resonator is tuned and/or matched, the existence of the tight coupling loop results in closely spaced multiple resonances within the defined VSWR bandwidth. The expected advantage of these closely spaced multiple resonances is that greater bandwidth may be achieved with this antenna than can be achieved with small antennas that exhibit single resonances.

Following the approach in [8] and [9], the spherical resonator antenna considered here was designed without dielectric and scaled so that the impedance loop was centered near a frequency of 300 MHz. The resulting implementation of the spherical resonator considered here is a 6-arm version since it exhibits a resistance of approximately 50Ω near the center of the impedance loop. To operate at near 300 MHz, without dielectric loading, the overall dipole length of the antenna is 19.89 cm, a dimension substantially larger than the antennas considered in the previous sections. Since the antenna is not inherently matched to 50Ω , some method of impedance matching must be employed. Impedance matching can be achieved through tuning using an external matching network

[8], series inductors located at the feed point, or an increase in the feed-arm length using a meander-line technique. Here, the meander-line is chosen as the impedance matching technique.

The matched 6-arm spherical resonator, its impedance, matched VSWR ($Z_{CH} = 50\Omega$) and radiation patterns are presented in Fig. 10. The antenna is matched at a frequency of 298.2 MHz, where $ka = 0.622$. The estimated approximate Q of the spherical resonator is 1.64, which is substantially less than the lower bound of 5.66. This is an incorrect result since no small antenna can exhibit an exact Q that is less than the lower bound [10]. Additionally, it was shown in [10] that the exact Q does not as closely approach the lower bound as does the Q of the folded spherical helix. The antenna's radiation efficiency is 98%. Its $\frac{1}{2}$ -power and 2:1 VSWR bandwidths are 14.8% and 8.5%, respectively, both substantially greater than those of the spherical helix.

The 6-arm spherical resonator primarily operates as an electric dipole but there is a notable amount of power in the cross-polarized radiation pattern. For antennas that exhibit significant levels of cross-polarization, there must be a corresponding reduction in the lower bound on Q [12], [23], [25] and [29]. The lower bound on Q is reduced in direct proportion to the ratio of power contained in orthogonal polarizations, in which case Eq. (3) becomes [29]

$$Q_{lb} = \eta_r \left(\frac{1}{1+\gamma} \right) \left(\frac{1}{(ka)^3} + \frac{1}{ka} \right) \quad (7)$$

where γ is the ratio of power between orthogonal polarizations and γ is chosen such that $0 \leq \gamma \leq 1$. For example, if orthogonal polarizations have equal power, $\gamma = 1$ and the lower bound of Eq. (7) is $\frac{1}{2}$ the lower bound of Eq. (3). If one polarization has twice the power of the other, $\gamma = 0.5$ and the lower bound of Eq. (7) is $\frac{2}{3}$ the lower bound of Eq. (3).

From Fig. 10, it is evident that the vertical polarization contains substantially more power than the horizontal polarization and the lower bound for the antenna is not significantly reduced. If the orthogonal polarizations shared equal power, the calculated lower bound of 5.66 would be reduced to 2.83, a value still greater than the calculated approximate Q of 1.64.

3.6 Summary of Results

A summary of the results discussed in this section is presented in Table 1. The folded spherical helix antenna exhibits a Q that most closely approaches the lower bound. The spherical resonator antenna exhibits the largest bandwidth but also has the highest value of ka . Given the difference in the values of ka between the spherical resonator and the

other configurations, the obvious question to ask is how does the performance of each antenna compare when they are designed to have the same value of ka ? This is considered in the next section.

Table 1. Performance comparison of the folded spherical helix, the folded cylindrical helix, the matched disk-loaded dipole, the matched spherical-cap dipole and the spherical resonator antennas. All are designed to operate at or very near 300 MHz.

Antenna	Frequency (MHz)	Overall Height (cm)	ka	η_r (%)	Q_{lb} (includes loss)	Q_z	$\frac{1}{2}$ -Power VSWR Bandwidth (%)
Folded Spherical Helix	299.8	8.36	0.263	97.4	57.39	84.78	2.37
Cylindrical Folded Helix	301.1	8.36	0.373	98.3	21.35	53.5	3.75
Matched Disk Loaded Dipole	294.4	8.36	0.365	95.5	22.27	48.0	3.04
Matched Spherical Cap Dipole	296.3	8.36	0.26	93.3	56.86	95.29	2.06
Matched Spherical Resonator	298.2	19.89	0.622	98.0	5.66	1.64	14.8

4. The Small Antennas having the Same ka as the Spherical Resonator

In the previous section, a number of small antenna configurations were compared, where all were designed to operate at or very near 300 MHz. With the exception of the spherical resonator, all of the antennas had the same overall dipole length and, in some cases, the same value of ka . The spherical resonator exhibited the greatest bandwidth but it also had the highest value of ka . The question considered in this section is whether its greater bandwidth is a result of the higher value of ka (its larger volume) or whether the design itself offers more bandwidth when compared with the other antenna configurations modified to have the same value of ka ?

4.1 The Matched Disk-Loaded Dipole Antenna

The first antenna considered is the matched disk-loaded dipole. The size of the antenna was adjusted to achieve a value of ka as close to 0.622 as possible, matching that of the spherical resonator. In this adjustment process, the physical dimensions were also set so as to maintain an operating frequency as close to 300 MHz as possible. In this case, the overall height of the disk-loaded dipole is 18 cm and the disk diameter is 8.4

cm. The antenna is impedance matched to 50Ω using a shunt-stub. A helical coil is not necessary for tuning.

The matched disk-loaded dipole, its impedance, matched VSWR ($Z_{CH} = 50\Omega$) and radiation patterns are presented in Fig. 11. The antenna is matched at a frequency of 304.5 MHz, where $ka = 0.634$. The Q of the antenna is 11.21, which is approximately 2.05 times the lower bound of 5.48. Its radiation efficiency is 99.5%. Its $\frac{1}{2}$ -power and 2:1 VSWR bandwidths are 18.25% and 6.34%, respectively. Its $\frac{1}{2}$ -power bandwidth is greater than that of the spherical resonator but its 2:1 VSWR bandwidth is less. The matched disk-loaded dipole operates as an electric dipole with minimal cross-polarization.

4.2 The Matched Spherical-Cap Dipole Antenna

As with the matched disk-loaded dipole, the size of the spherical-cap antenna was adjusted to achieve a value of ka as close to 0.622 as possible and an operating frequency as close to 300 MHz as possible. In this case, the overall height of the spherical-cap dipole is 19.89 cm. The antenna is impedance matched to 50Ω using a shunt-stub. A helical coil is not necessary for tuning.

The matched spherical-cap dipole, its impedance, matched VSWR ($Z_{CH} = 50\Omega$) and radiation patterns are presented in Fig. 12. The antenna is matched at a frequency of 290.3 MHz, where $ka = 0.605$. The Q of the antenna is 11.92, which is approximately 2.02 times the lower bound of 5.89. Its radiation efficiency is 95.5%. Its $\frac{1}{2}$ -power and 2:1 VSWR bandwidths are 16.36% and 5.65%, respectively. Its $\frac{1}{2}$ -power bandwidth is greater than that of the spherical resonator but its 2:1 VSWR bandwidth is less. The matched spherical-cap dipole operates as an electric dipole with minimal cross-polarization.

4.3 The Folded Spherical Helix Antenna

Again, the size of the folded spherical helix antenna was adjusted to achieve a value of ka as close to 0.622 as possible and an operating frequency as close to 300 MHz as possible. The overall height of the folded spherical helix 19.89 cm. The significant design variables with the folded spherical helix are the number of arms, which determines the resonant resistance, and the length of each arm, which determines the operating frequency. As the number of arms increases, and the arm length is adjusted to maintain the same operating frequency, the resonant resistance increases. The optimum configuration for the folded spherical helix in terms of impedance matching to 50Ω is a 2-arm spherical helix. An increase in the number of arms decreases the antenna Q and increases the operating bandwidth. However, the resonant resistance increases and the antenna is no longer matched to 50Ω .

The 2-arm folded spherical helix, its impedance, matched VSWR ($Z_{CH} = 50\Omega$) and radiation patterns are presented in Fig. 13. The antenna is matched at a frequency of 298.2 MHz, where $ka = 0.621$. The Q of the antenna is 18.9, which is approximately 3.28 times the lower bound of 5.76. Its radiation efficiency is 99.3%. Its $\frac{1}{2}$ -power and 2:1 VSWR bandwidths are 12.43% and 4.37%, respectively. Its $\frac{1}{2}$ -power and 2:1 VSWR bandwidths are less than those of the spherical resonator. The folded spherical helix operates as an electric dipole, however, there is a higher level of cross-polarization than with the 4-arm configuration designed to operate with $ka \approx 0.26$.

The other folded spherical helix configurations considered were the 4, 5 and 6-arm configurations. These offered a substantial decrease in Q and increase in bandwidth but the antennas are no longer well matched to 50Ω . A summary of their performance properties is presented in Table 2.

Table 2. Summary of the performance properties of the multi-arm folded spherical helix antennas compared to the spherical resonator antenna.

Antenna	Frequency (MHz)	ka	Matching Impedance (Ω)	Q_{lb}^1 (includes loss)	Q_Z	$\frac{1}{2}$ -Power VSWR Bandwidth (%)	2:1 VSWR Bandwidth (%)
Matched Spherical Resonator	298.2	0.622	50	5.66	1.64	14.8	8.5
4-Arm Folded Spherical Helix	298.7	0.622	243.17	5.78	10.1	20.05	7.03
5-Arm Folded Spherical Helix	312	0.65	312.2	5.18	8.21	22.15	7.91
6-Arm Folded Spherical Helix	312	0.65	312	5.16	6.81	27.2	10.3

1. The stated lower bound includes the term for radiation efficiency but does not include the term that takes into account any power division between the vertical and horizontal polarizations. These configurations have some power delivered to the orthogonal polarization and the lower bound is slightly overstated.

4.4 Summary of Results

A summary and comparison of the results discussed in this section is presented in Table 3. The matched disk-loaded dipole exhibits the largest $\frac{1}{2}$ -power bandwidth. It also has the largest value of ka . The spherical resonator exhibits the largest 2:1 VSWR bandwidth.

Table 3. Performance comparison of the matched disk-loaded dipole, the matched spherical-cap dipole, the folded spherical helix and the spherical resonator antennas. All are designed to operate at or very near 300 MHz and have nearly equal values of ka .

Antenna	Frequency (MHz)	ka	η_r (%)	Q_{lb} (includes loss)	Q_z	$\frac{1}{2}$ -Power VSWR Bandwidth (%)	2:1 VSWR Bandwidth (%)
Matched Spherical Resonator	298.2	0.622	98.0	5.66	1.64	14.8	8.5
Matched Disk Loaded Dipole	304.5	0.634	99.5	5.48	11.21	18.25	6.34
Matched Spherical Cap Dipole	290.3	0.605	95.5	5.89	11.92	16.36	5.65
2-Arm Folded Spherical Helix	298.2	0.621	99.3	5.76	18.9	12.43	4.37

5. The Small Antennas having a ka less than 0.5

In the previous section, several of the small antennas were compared having nearly the same value of ka . The values of ka ranged between 0.605 and 0.634, all above the electrically small antenna limit of $ka \leq 0.5$. Here, versions of each antenna were designed to operate near 300 MHz with values of $ka \approx 0.45$. The matched disk-loaded dipole, matched spherical-cap dipole and folded spherical helix were designed and similar in configuration to those described in the previous section. Their impedance, matched VSWR bandwidths and patterns are not presented here in figures.

To achieve a value of $ka \approx 0.45$ with the spherical resonator, an 8-arm configuration loaded with dielectric is necessary [8]. The dielectric material is Rogers RO4003. This configuration is depicted in Fig. 14(a) and was modeled using Microwave Studio. Its impedance and matched VSWR are presented in Fig. 14(b) and 14(c), respectively. In this case, the matched VSWR is determined by simply tuning the antenna with an external tuning inductor that is assumed to be lossless. A comparison of the performance of these antennas is presented in Table 4. In this particular case, the matched spherical-cap dipole exhibits the greatest bandwidth.

Table 4. Performance comparison of the matched disk-loaded dipole, the matched spherical-cap dipole, the folded spherical helix and the spherical resonator antennas. All are designed to operate at or very near 300 MHz and have values of $ka \approx 0.45$.

Antenna	Frequency (MHz)	ka	η_r (%)	Q_{lb} (Lossless Antenna)	Q_z	$\frac{1}{2}$ -Power VSWR Bandwidth (%)	2:1 VSWR Bandwidth (%)
8-Arm Matched Spherical Resonator	297.5	0.424	98.0	15.5	31.1	6.1	2.1
Matched Disk Loaded Dipole	300	0.45	99.5	13.2	26.2	7.4	2.6
Matched Spherical Cap Dipole	300	0.45	95.5	13.2	19.5	10	3.52
3-Arm Folded Spherical Helix	297.1	0.446	99.3	13.5	24.6	6.7	2.2

6. Discussion

The radiation properties of several fundamental electrically small antennas were compared where each had the same overall length, the same value of ka or where they were designed to operate at the same frequency. For the small value of $ka \approx 0.26$, the folded spherical helix exhibits a Q that most closely approaches the lower bound. It also offers the largest bandwidth at this value of ka .

The spherical resonator antenna was of interest because when tuned or matched, it exhibits multiple resonances within its defined VSWR bandwidth, which may possibly lead to achieving greater bandwidth than can be achieved with single resonance antennas. For nearly the same value of ka , the matched spherical-cap dipole exhibits the largest $\frac{1}{2}$ -power bandwidth but a slightly lower 2:1 VSWR bandwidth than the spherical resonator. No attempt was made here to optimize the bandwidth of any of these configurations. At a value of $ka \approx 0.45$, the matched spherical-cap dipole offers the largest bandwidth.

With both the folded spherical helix and the spherical resonator antennas, designing for an impedance match ($Z_{CH} = 50\Omega$) at a specific value of ka can be a challenge. The design approach requires adjust of the number of arms, the arm length, and in some cases, may require dielectric loading. For example, with the folded spherical helix at value of $ka \approx 0.625$, a lower Q and larger bandwidth than the other configurations can be achieved but the antennas are not well matched to 50Ω . Optimization of these designs is a topic of current research.

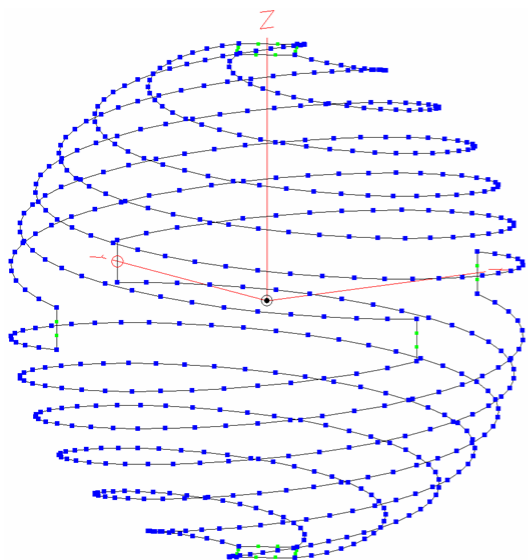
While the Q of the spherical-cap dipole may not closely approach the lower bound as desired at certain values of ka , it often may exhibit larger bandwidth than the other configurations. The design of the spherical-cap dipole is also quite straight-forward in that the resonant frequency can be adjusted using a helical coil dipole feed or an adjustment of the volume of the spherical-cap. Matching can be easily accomplished using a shunt stub, provided the resonant resistance is sufficiently lower than 50Ω .

In all cases, the specific value of ka may dictate the most suitable design approach from a physical perspective and it may also determine which design approach will provide the lowest Q and largest bandwidth.

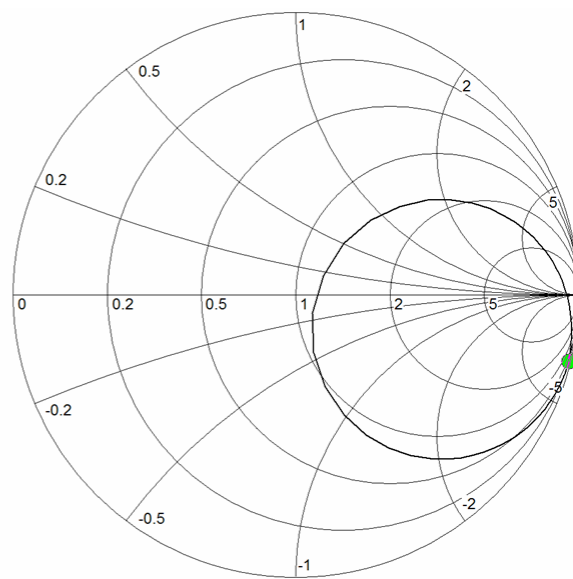
7. References

- [1] C. E. Smith and E. M. Johnson, "Performance of Short Antennas," *Proc. IRE*, Vol. 35, No. 10, pp. 1026-1038, Oct 1947.
- [2] E. W. Seeley, "An Experimental Study of the Disk Loaded Folded Monopole," *IRE Trans. Antennas Propag.*, pp 27 – 28, Jan 1956.
- [3] R. Guertler, "Impedance Transformation in Folded Dipoles," *Proc. IRE*, Vol. 38, No. 9, pp. 1042-1047, Sep 1950.
- [4] J. D. Kraus, "The Helical Antenna," *Proc. IRE*, Vol. 37, No. 3, pp. 263-272, Mar 1949.
- [5] R. W. Ziolkowski and A. D. Kipple, "Application of Double Negative Meta-Materials to Increase the Power Radiated by Electrically Small Antennas," *IEEE Trans. Antennas Propagat.*, Vol. 51, No. 10, pp. 2626-2640, Oct. 2003.
- [6] R. W. Ziolkowski and A. Erentok, "Metamaterial-Based Efficient Electrically Small Antennas," *IEEE Trans. Antennas Propagat.*, Vol. 54, No. 7, pp. 2113-2130, Jul 2006.
- [7] H. R. Stuart and A. Pidwerbetsky, "Electrically Small Antenna Elements Using Negative Permittivity Resonators," *IEEE Trans. Antennas Propagat.*, Vol. 54, No. 6, pp. 1644 – 1653, Jun 2006.
- [8] H. R. Stuart and C. Tran, "Subwavelength Microwave Resonators Exhibiting Strong Coupling to Radiation Modes," *Appl. Phys. Ltrs.*, 87, 151108, 2005.
- [9] H. R. Stuart and C. Tran, "Small Spherical Antennas Using Arrays of Electromagnetically Coupled Planar Elements," *IEEE Ant. Wireless Prop. Lett.*, vol. 6, pp. 7-10, 2007.
- [10] H. R. Stuart, S. R. Best, and A. D. Yaghjian, "Limitations in Relating Quality Factor to Bandwidth in a Double Resonance Small Antenna," *IEEE Ant. Wireless Prop. Lett.*, Accepted for Publication
- [11] S. R. Best, "The Radiation Properties of Electrically Small Folded Spherical Helix Antennas," *IEEE Trans. Antennas Propagat.*, Vol. 52, No. 4, pp. 953-960, Apr 2004.

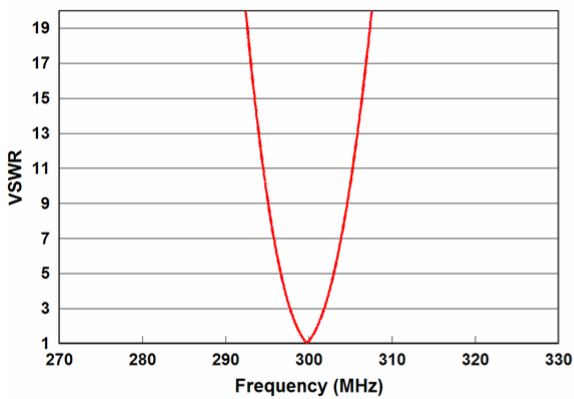
- [12] S. R. Best, "Low Q Electrically Small Linear and Elliptical Polarized Spherical Dipole Antennas," *IEEE Trans. Antennas Propagat.*, Vol. 53, No. 3, pp. 1047-1053, Mar 2005.
- [13] S. R. Best, "The Performance Properties of Electrically Small Resonant Multiple Arm Folded Wire Antennas," *IEEE Antennas Propagat. Mag.*, Vol. 47, No. 4, pp. 13-27, Aug 2005.
- [14] R. King, C. W. Harrison, and D. H. Denton Jr., "Transmission-line Missile Antennas," *IRE Trans. Antennas Propag.*, Vol. 8, pp. 88-90, Jan 1960.
- [15] S. R. Best, "A Discussion on the Quality Factor of Impedance Matched Electrically Small Antennas," *IEEE Trans. Antennas Propagat.*, Vol. 53, No. 12, pp. 502-508, Jan 2005.
- [16] J. A. Dobbins and R. L. Rogers, "Folded Conical Helix Antenna," *IEEE Trans. Antennas Propagat.*, Vol. 49, No. 12, pp. 1777-1781, Dec 2001.
- [17] E. E. Altshuler, "A Method for marching an Antenna Having a Small Radiation Resistance to a 50-Ohm Coaxial Line," *IEEE Trans. Antennas Propagat.*, Vol. 53, No. 9, pp. 3086-3089, Sep 2005.
- [18] A. Alu, N. Engheta, A. Erentok and R. W. Ziolkowski, "Single-Negative, Double Negative, and Low-Index Metamaterials and their Electromagnetic Applications," *IEEE Antennas Propagat. Mag.*, Vol. 49, No. 1, pp. 23-36, Feb 2007.
- [19] S. Lim and H. Ling, "Design of Thin, Efficient, Electrically Small Antenna using Multiple Foldings," *Elect. Lett.*, Vol. 42, Issue 22, pp. 1292-1293, Oct 26, 2006.
- [20] K. Fujimoto, A. Henderson, K. Hirasawa, and J. R. James, *Small Antennas*. Letchworth, U.K., New York: Research Studies Press, Wiley, 1987.
- [21] H. A. Wheeler, "Antenna Topics in My Experience," *IEEE Trans. Antennas Propagat.*, Vol. 33, No. 2, pp. 144-151, Feb 1985.
- [22] A. R. Lopez, "Fundamental Limitations of Small Antennas: Validation of Wheeler's Formulas," *IEEE Antennas Propagat. Mag.*, Vol. 48, No. 4, pp. 28-36, Aug 2006.
- [23] L. J. Chu, "Physical Limitations on Omni-Directional Antennas," *J. Appl. Phys.*, Vol. 9, pp. 1163-1175, 1948.
- [24] A. D. Yaghjian and S. R. Best, "Impedance, Bandwidth and Q of Antennas," *IEEE Trans. Antennas and Propagat.*, Vol. 53, No. 4, pp. 1298-1324, Apr 2005.
- [25] J. S. McLean, "A Re-Examination of the Fundamental Limits on the Radiation Q of Electrically Small Antennas," *IEEE Trans. Antennas Propagat.*, Vol. 44, pp. 672-676, May 1996.
- [26] EZNEC/4 Pro v5, www.ez nec.com, Roy Lewallen
- [27] Microwave Studio, www.cst.com
- [28] H. L. Thal, "New Radiation Q Limits for Spherical Wire Antennas," *IEEE Trans. Antennas Propagat.*, Vol. 54, No. 10, pp. 2757-2763, Oct 2006.
- [29] A. D. Yaghjian, "Internal Energy, Q-Energy, Poynting's Theorem, and the Stress Dyadic in Dispersive Material," *IEEE Trans. Antennas Propagat.*, Vol. 55, No. 6, pp. 1495-1505, Jun 2007.



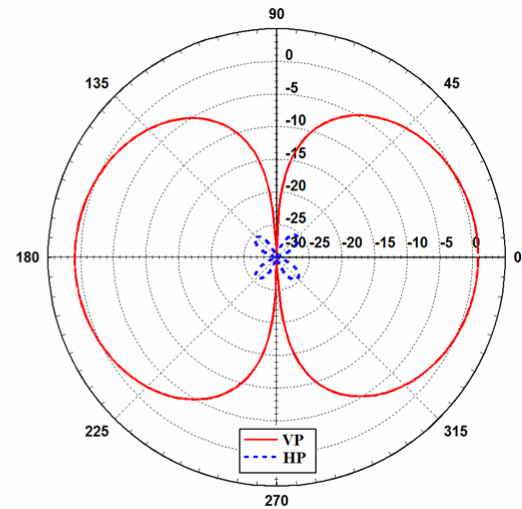
(a) The folded spherical helix.



(b) Impedance.

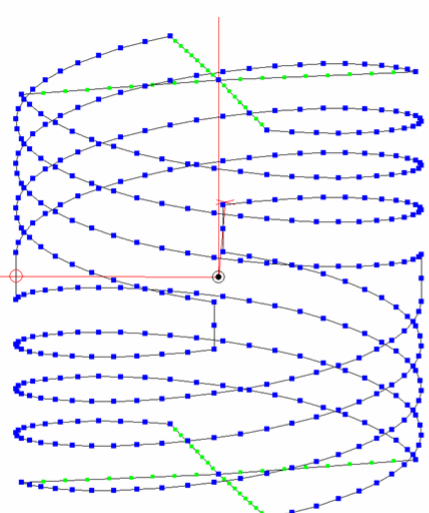


(c) Matched VSWR.

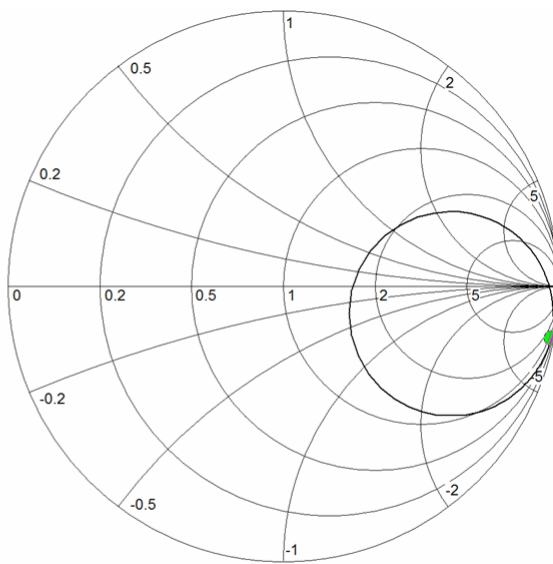


(d) Radiation pattern.

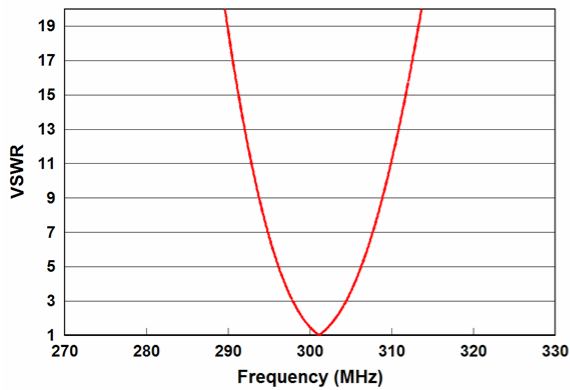
Fig. 1. (a) The 4-arm folded spherical helix, (b) its impedance over a frequency range of 270 – 330 MHz, (c) its matched VSWR and (d) its radiation pattern.



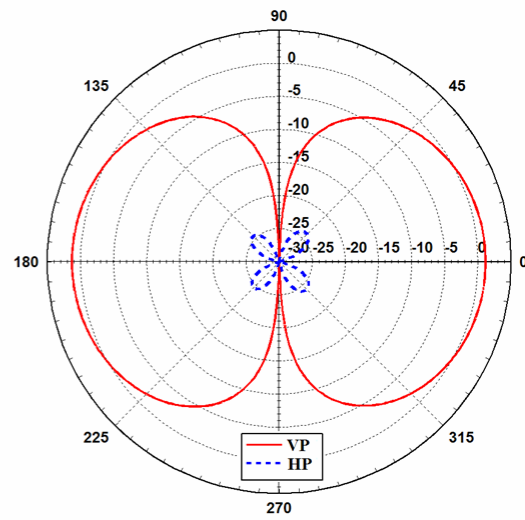
(a) The folded cylindrical helix.



(b) Impedance.

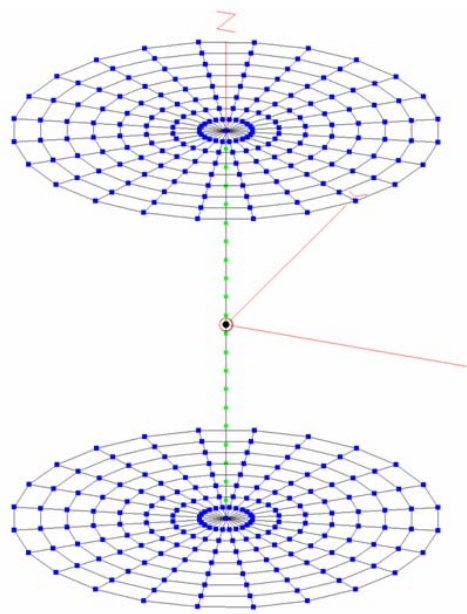


(c) Matched VSWR

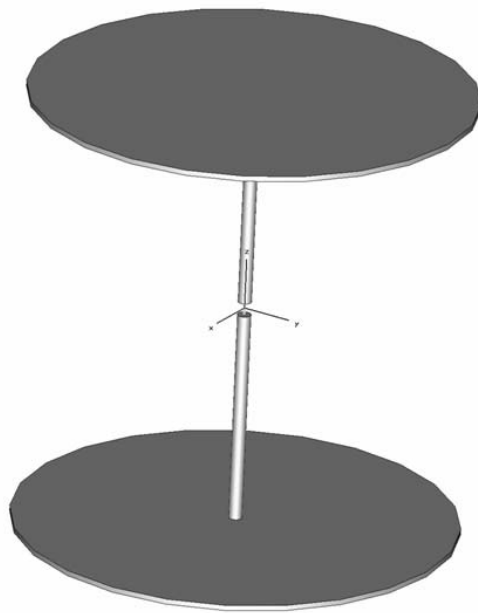


(d) Radiation pattern.

Fig. 2. (a) The 4-arm folded cylindrical helix, (b) its impedance over a frequency range of 270 – 330 MHz, (c) its matched VSWR and (d) its radiation pattern.

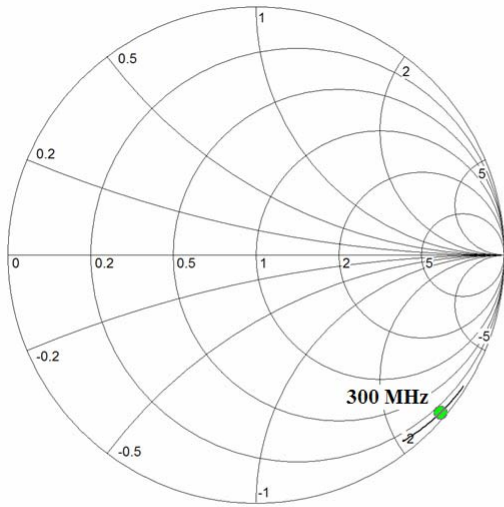


(a) The wire-grid disk-loaded dipole.

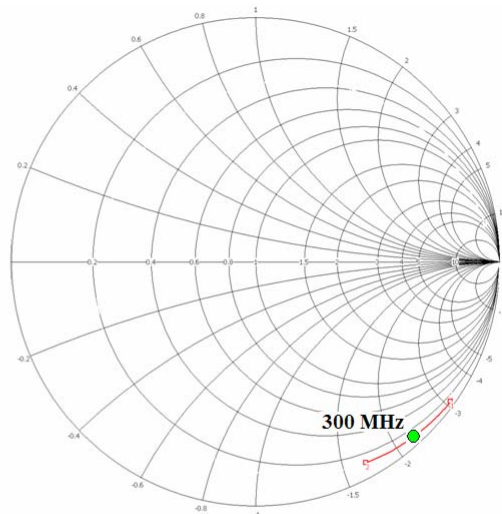


(b) The solid disk-load dipole.

Fig. 3. The wire-grid and solid disk-loaded loaded dipole antennas.

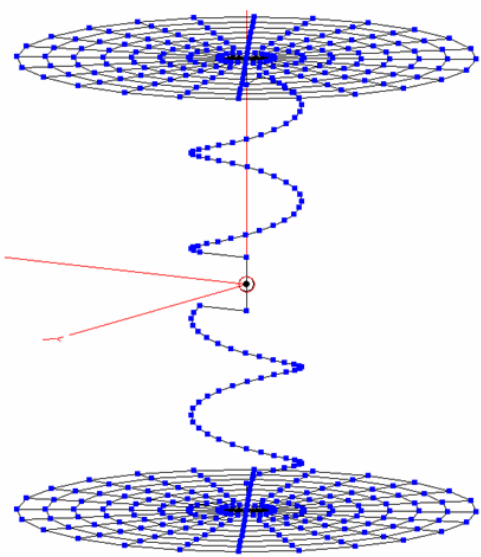


(a) Impedance of the wire-grid disk loaded dipole.

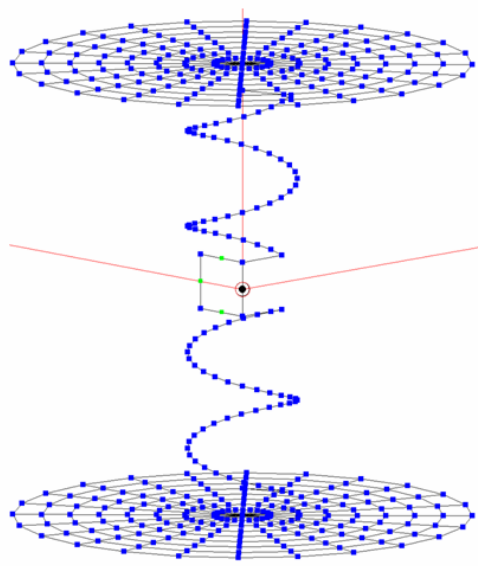


(b) Impedance of the solid disk-loaded dipole

Fig. 4. Impedances of the wire-grid and solid disk-loaded loaded dipole antennas.



(a) Tuned disk-loaded dipole.



(b) Matched disk-loaded dipole.

Fig. 5. (a) The helical-coil tuned disk-loaded dipole. (b) The shunt stub matched disk-loaded dipole.

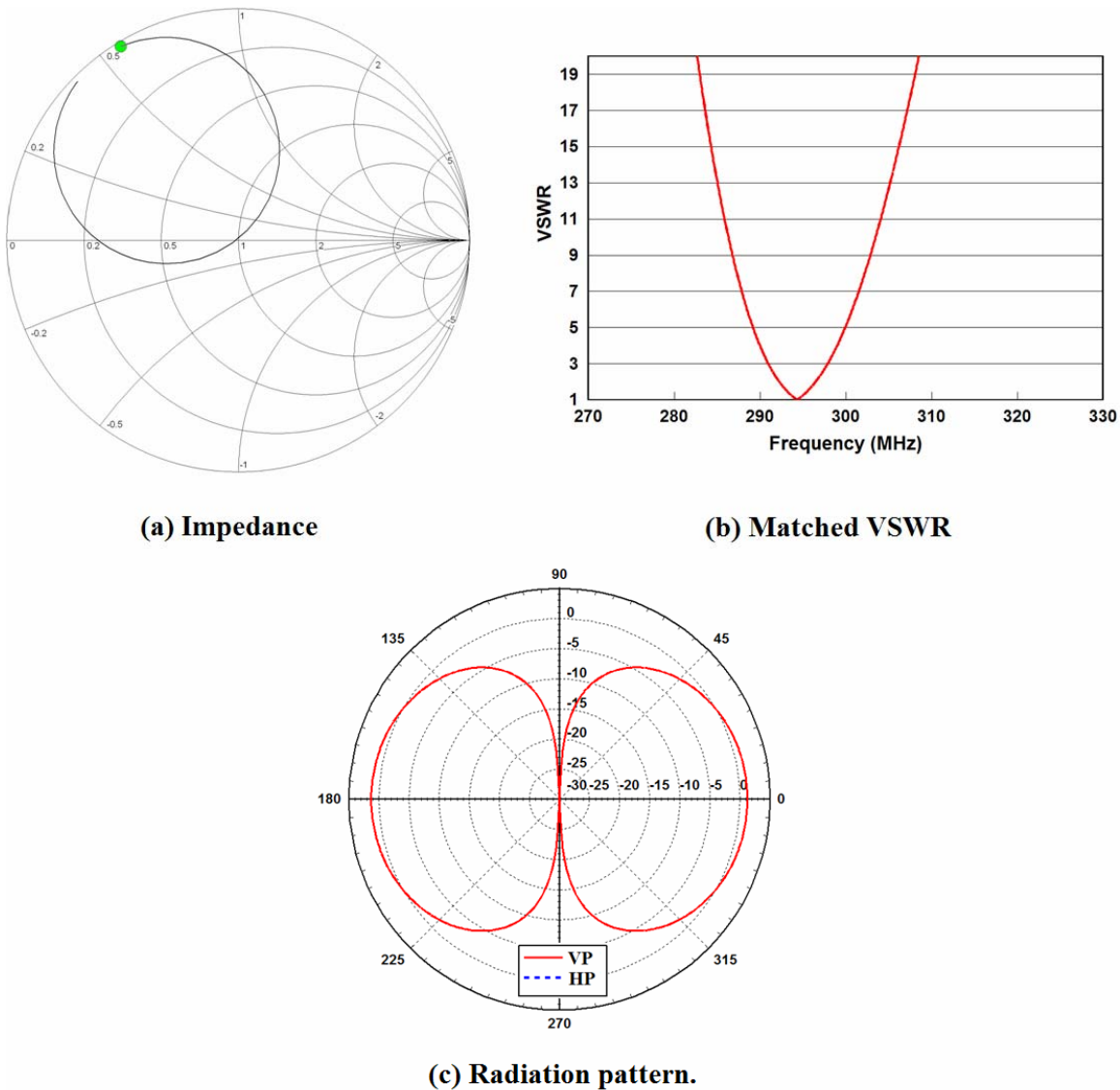
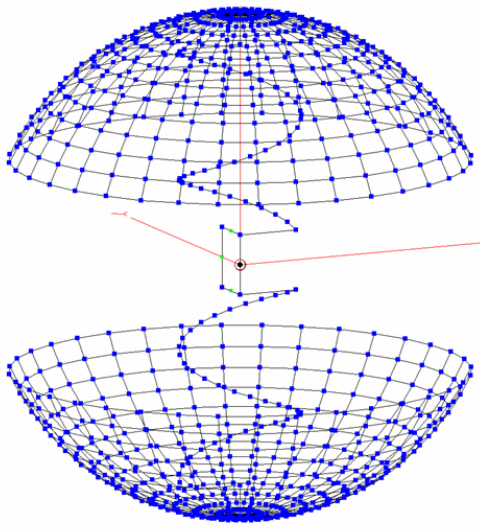
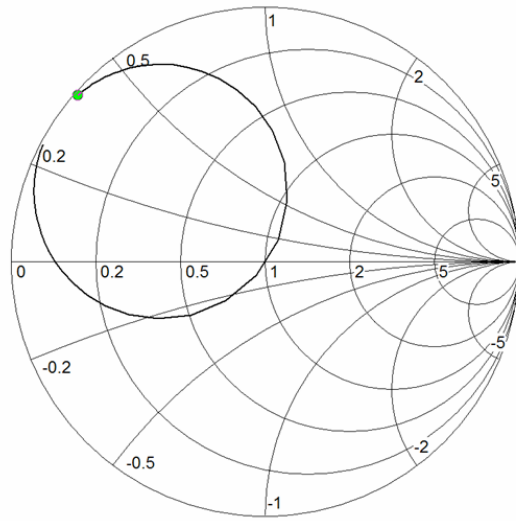


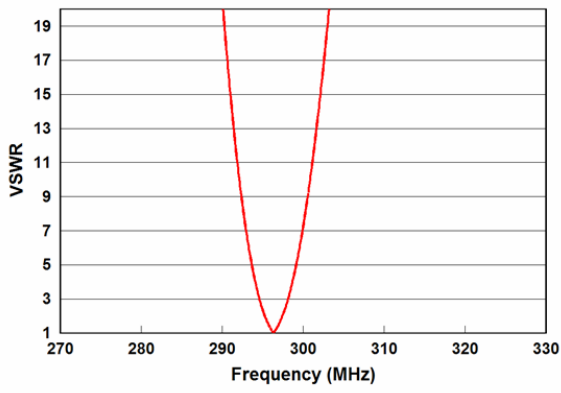
Fig. 6. Radiation properties of the matched disk-loaded dipole: (a) Impedance over a frequency range of 270 – 330 MHz, (b) Matched VSWR and (c) Radiation pattern.



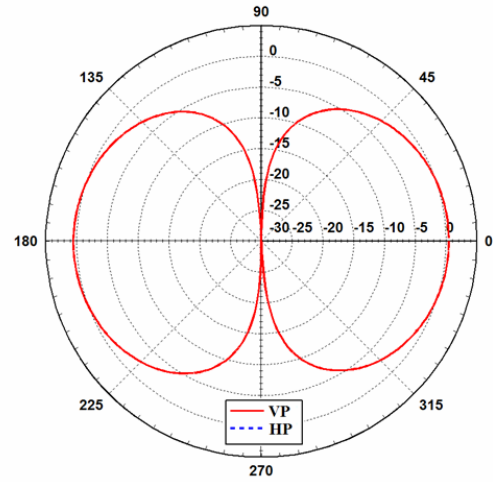
(a) The spherical-cap dipole.



(b) Impedance.



(c) Matched VSWR.



(d) Radiation Pattern.

Fig. 7. (a) The spherical-cap dipole, (b) its impedance over a frequency range of 270 – 330 MHz, (c) its matched VSWR and (d) its radiation pattern.

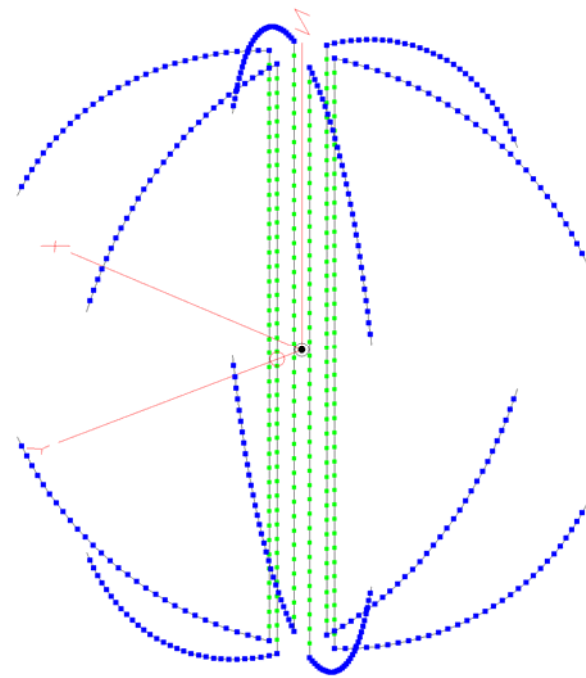


Fig. 8. The 6-arm spherical resonator antenna.

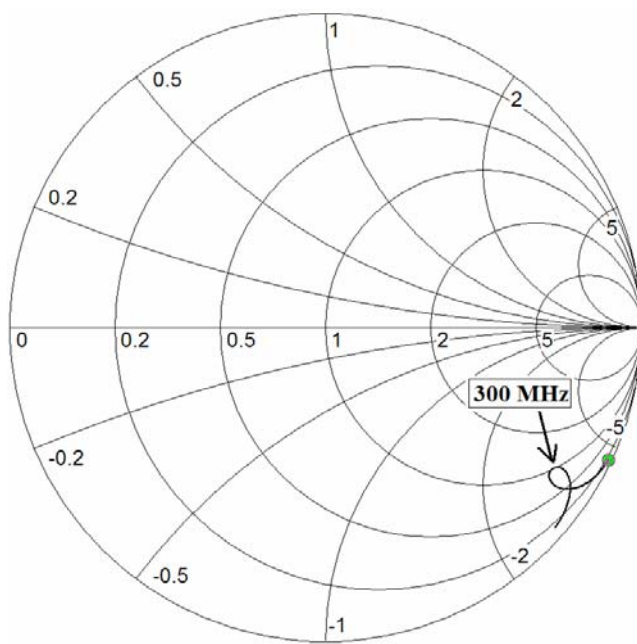
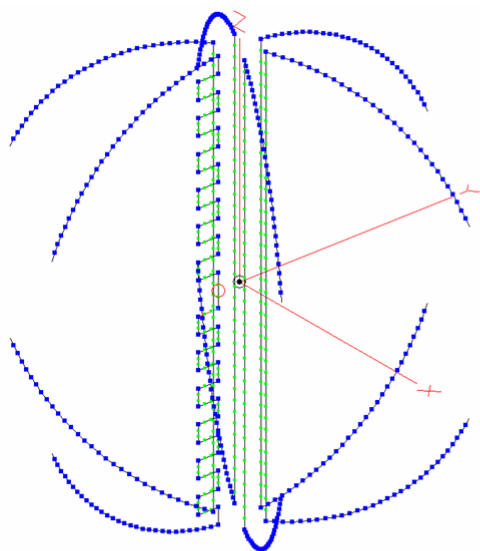
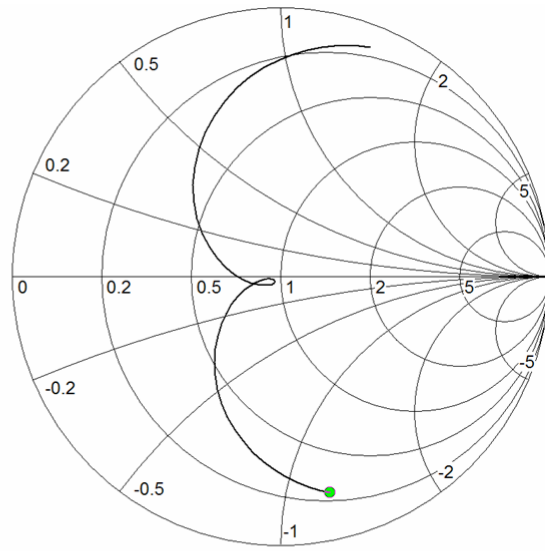


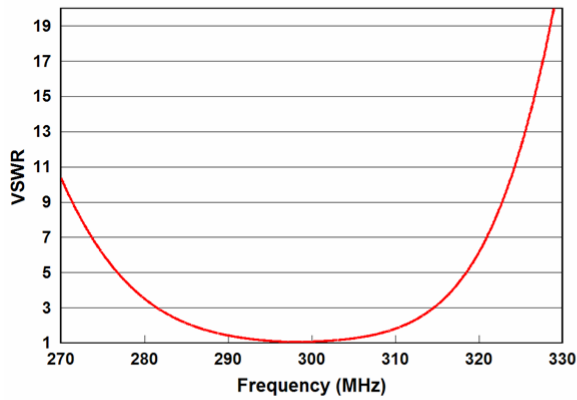
Fig. 9. Impedance of the 6-arm spherical resonator antenna.



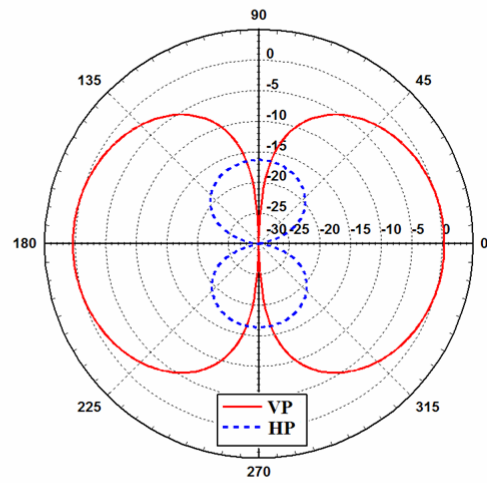
(a) The matched spherical resonator.



(b) Impedance.

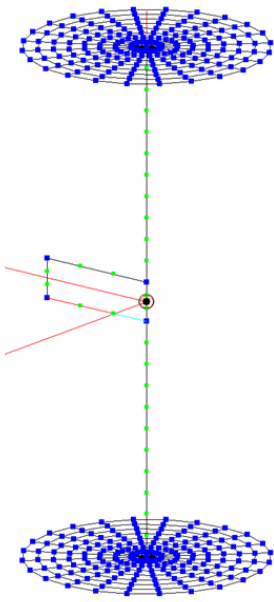


(c) Matched VSWR.

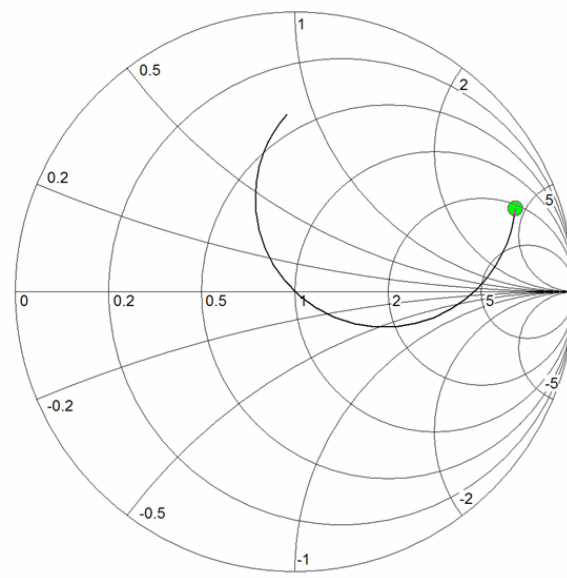


(d) Radiation pattern.

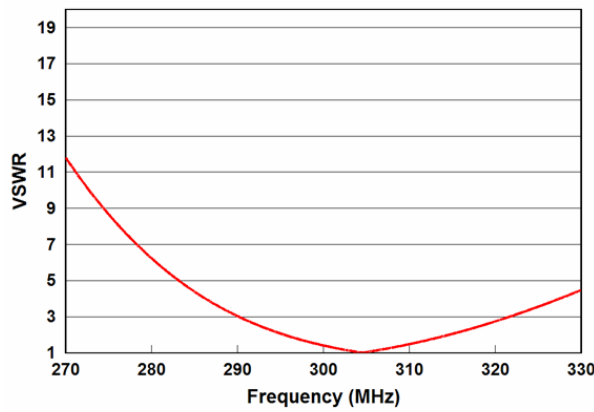
Fig. 10. (a) The matched spherical resonator antenna, (b) its impedance over a frequency range of 270 – 330 MHz, (c) its matched VSWR and (d) its radiation pattern.



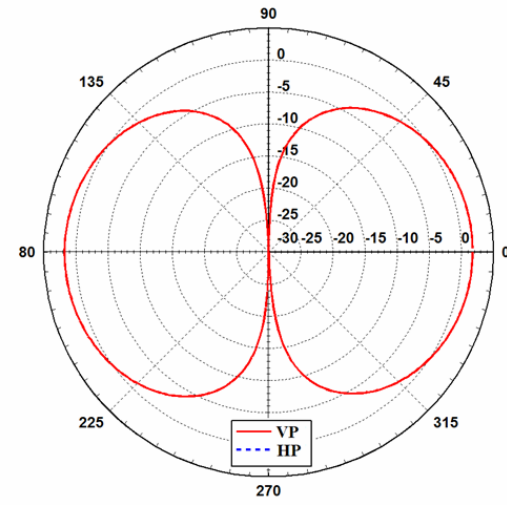
(a) Matched disk-loaded dipole.



(b) Impedance.

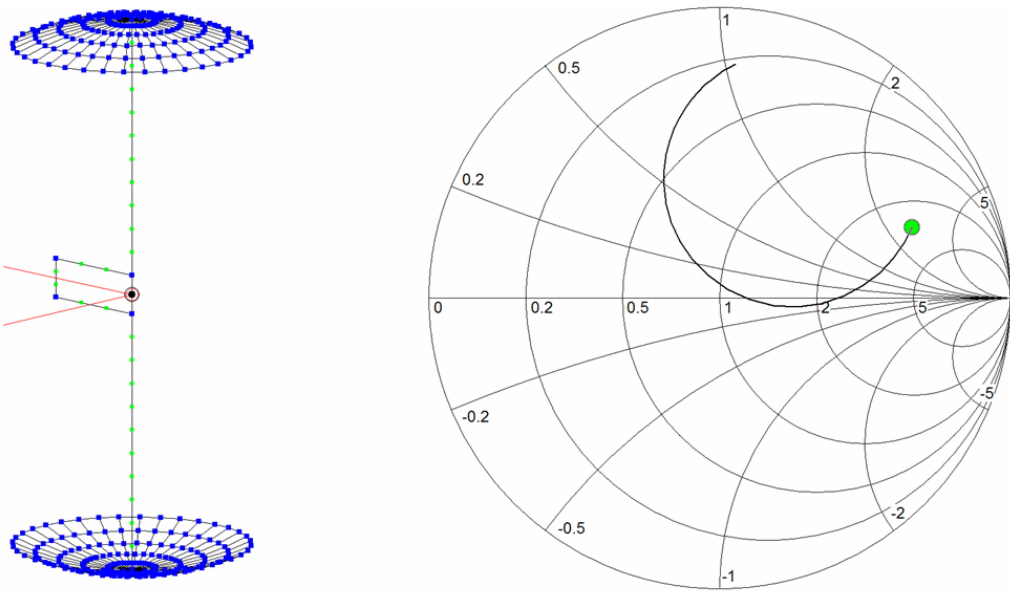


(c) Matched VSWR



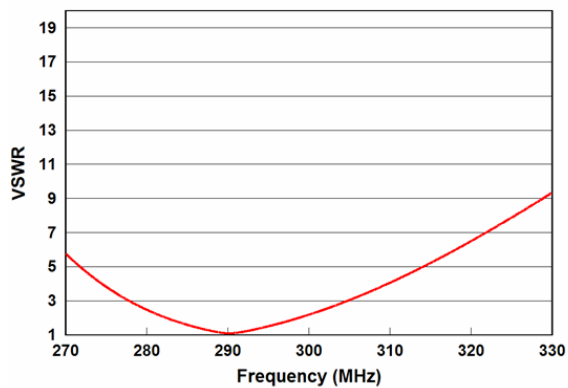
(d) Radiation pattern.

Fig. 11. (a) The matched disk-load dipole having a $ka = 0.634$, (b) its impedance over a frequency range of 270 – 330 MHz, (c) its matched VSWR and (d) its radiation pattern.

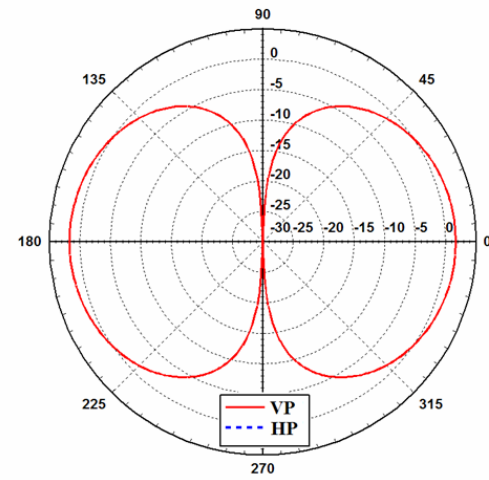


(a) Matched spherical-cap dipole.

(b) Impedance.

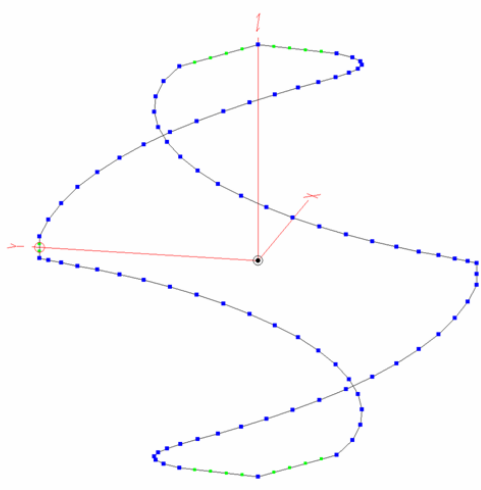


(c) Matched VSWR.

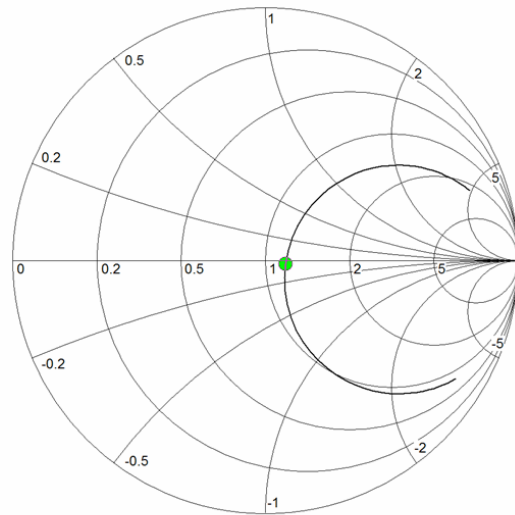


(d) Radiation pattern.

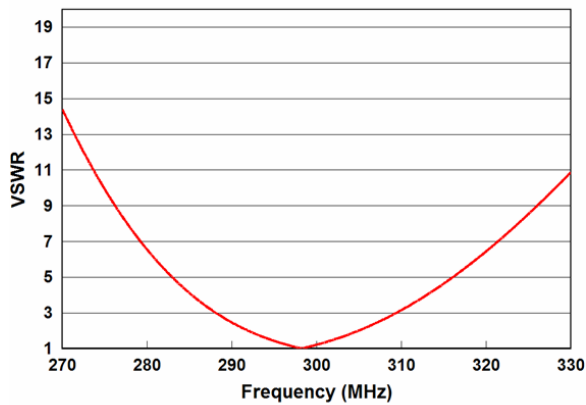
Fig. 12. (a) The matched spherical-cap dipole having a $ka = 0.605$, (b) its impedance over a frequency range of 270 – 330 MHz, (c) its matched VSWR and (d) its radiation pattern.



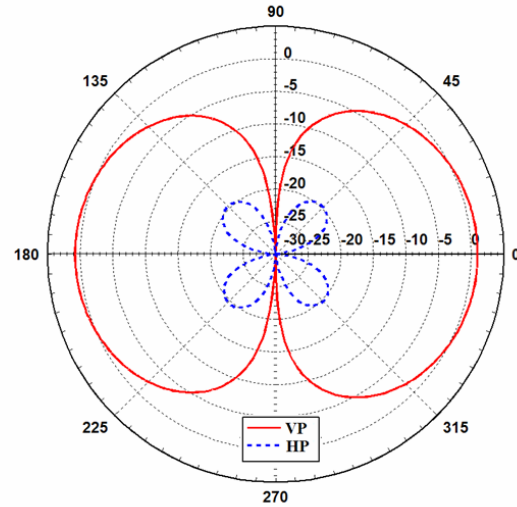
(a) 2-arm folded spherical helix.



(b) Impedance.

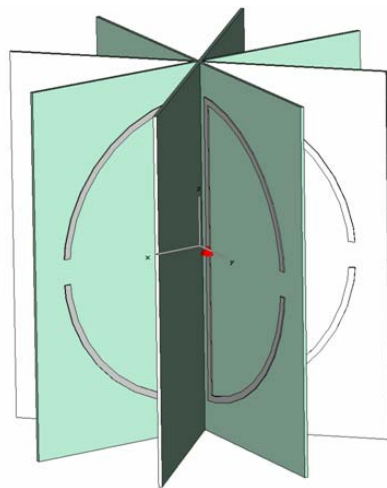


(c) Matched VSWR.

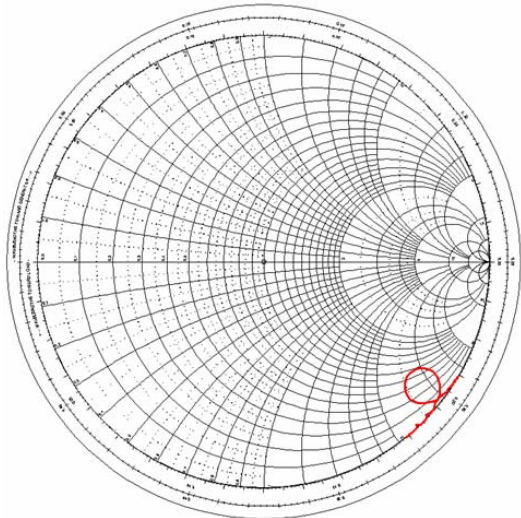


(d) Radiation Pattern

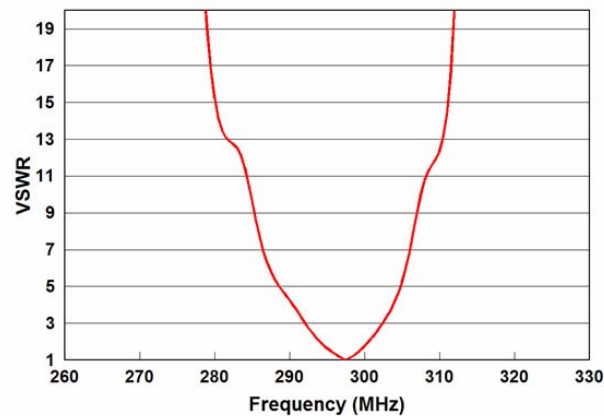
Fig. 13. (a) The 2-arm folded spherical helix antenna having a $ka = 0.621$, (b) its impedance over a frequency range of 270 – 330 MHz, (c) its matched VSWR and (d) its radiation pattern.



(a) The 8-arm spherical resonator.



(b) Impedance.



(c) Matched VSWR.

Fig. 14. (a) The 8-arm, dielectric loaded spherical resonator antenna having a $ka = 0.428$, (b) its impedance over a frequency range of 270 – 330 MHz, and (c) its matched VSWR.

NON-FOSTER MATCHING OF A LOSSY, ELECTRICALLY-SMALL ANTENNA OVER AN EXTENDED FREQUENCY RANGE

STEPHEN E. SUSSMAN-FORT

EDO Corporation, Bohemia, Long Island, NY 11716 USA stephen.sussman-fort@edocorp.com
and

Department of Electrical And Computer Engineering, State University of New York,
Stony Brook, NY 11794 USA

RON M. RUDISH

EDO Corporation, Bohemia, Long Island, NY 11716 USA ronald.rudish@edocorp.com

ABSTRACT

Electrically-small antennas cannot be efficiently impedance-matched over any significant frequency band because of the gain-bandwidth restrictions which arise from the difficult impedances that such antennas present. Non-Foster matching bypasses this fundamental restriction by employing negative reactive elements, realized by means of negative impedance converters (NICs).

We have previously demonstrated, in antenna-range experiments, how non-Foster matching improved the signal-to-noise ratio of a 6-inch monopole and 12-inch dipole connected to an 8 dB noise-figure receiver. The comparison was between no matching whatsoever and the corresponding non-Foster-matched antenna. Because of the high-Q of the antennas, no matching is actually a viable choice among the best possible passive wideband matching networks that can be designed. For the dipole, up to 20 dB improvement in S/N was measured over 20 – 120 MHz.

In our present work, we have extended the frequency range over which non-Foster matching may be applied. In particular, we use non-Foster techniques to impedance match a lossy electrically-small dipole antenna. On the antenna range, we measured up to 30 dB gain improvement over 60 – 200 MHz, with several dB of improvement as high as 400 MHz. Again, the comparison was to the same antenna with no matching at all.

Although no S/N measurements were made, the circuits we used were based upon the same low-noise designs developed earlier for our lower-frequency circuits. Because of the lossiness of the antenna, passive matching can do a little better than no matching at all, and these results are illustrated in simulation.

1. Introduction

Non-Foster networks employ negative elements, realized using negative impedance converters (NICs), to achieve impedance matching far better than can be obtained using passive networks. The benefits of non-Foster matching are particularly striking for electrically-small antennas, where the gain-bandwidth limitations of the classical passive approach permit only a very narrow-band or lossy match. On the other hand, negative elements can yield multi-octave matching. We have built 6" monopole and 12" dipole NIC-based receive antennas that greatly outperform conventional, commercially-available antennas of twice the size over 20 – 100 MHz. These results have been reported in [1] and [2]. After a review of the basics of NICs and non-Foster matching, we present our results for the NIC-based matching of an electrically-small antenna over 60 – 400 MHz. Of particular note are some previously classified references that have recently become available in the public domain ([12] and [13]).

1.1 The Linvill Circuits

Perhaps the earliest reference to negative impedance converters is due to Crisson [3], who developed negative-resistance repeaters to cancel the loss in telephone transmission lines. The first practical NICs were designed, built and tested by Linvill [4] in 1954. Linvill discovered these two-ports as a consequence of his research into active filters. In particular, he found that any two-port LC filter function could be synthesized as a cascade of an RC network, a negative impedance converter, and another RC network as shown in Fig. 1.

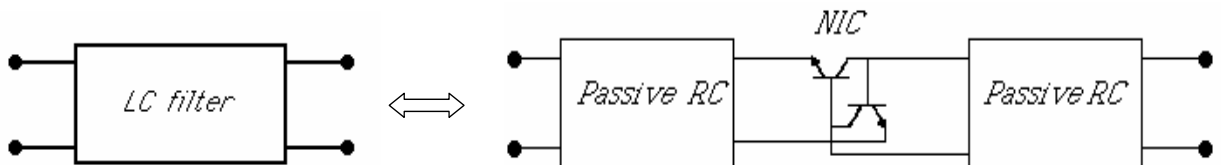


Fig. 1: The transfer function of any LC filter is realizable via an RC-NIC-RC structure

Linvill built negative resistance circuits using both grounded (common-terminal) and floating NICs terminated as shown in Fig. 2. With ideal transistors, a pure negative resistance is obtained. In Linvill's actual realizations, a substantial reactive component of the input impedance Z accompanies the negative resistance, resulting in a low Q , where the “resistive” Q is defined in this case as:

$$Q = |\operatorname{Re}(Z) / \operatorname{Im}(Z)| \quad (1)$$

The circuits shown are “open-circuit stable” (OCS), meaning, practically, that if a very large resistance terminates the negative-resistance one-ports on the left, then the overall network will be stable. Note that the loop impedance through such a termination and R_{in} would be positive. The networks of Fig. 2 can be turned around as shown in Fig. 3, where negative resistances of the “short-circuit stable” (SCS) variety are obtained. Again, practically speaking, this means these networks will be stable if a very large *conductance* is placed across the input.

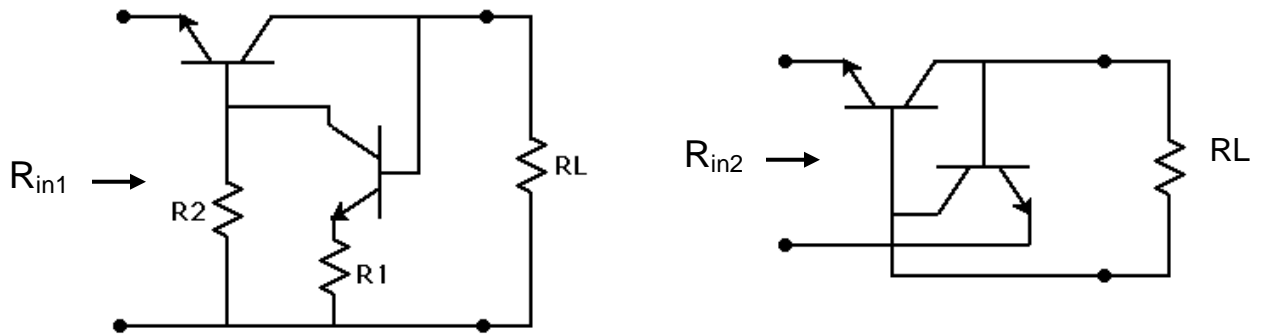


Fig. 2: Linvill’s ideal OCS NICs terminated in a resistance: common-terminal circuit $R_{in1} = -(R_2/R_1)RL$; floating circuit $R_{in2} = -RL$. With non-ideal transistors, the input impedance is $Z = Re(Z) + j[Im(Z)]$, where $Re(Z) < 0$ over a finite frequency band.

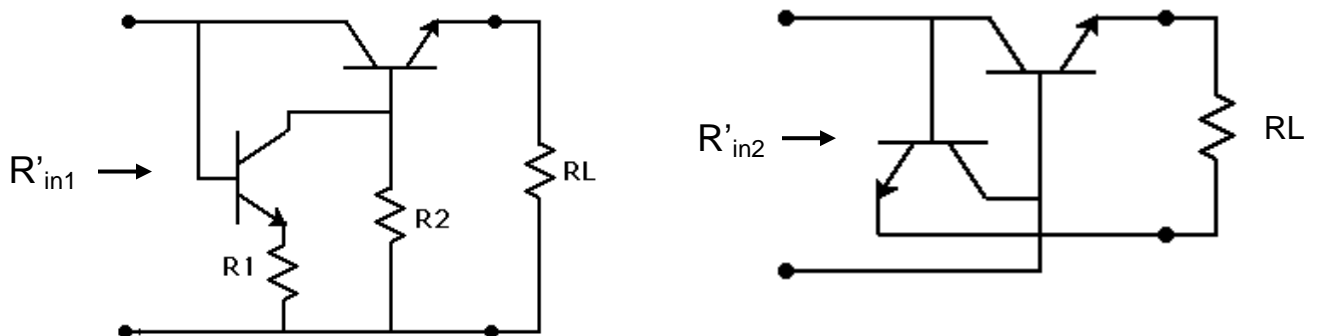


Fig. 3: Linvill’s ideal SCS NICs terminated in a resistance: common-terminal circuit $R'_{in1} = -(R_1/R_2)RL$; floating circuit $R'_{in2} = -RL$. With non-ideal transistors, the input impedance is $Z = Re(Z) + j[Im(Z)]$, where $Re(Z) < 0$ over a finite frequency band.

Open- and short-circuit stability are intrinsic properties of NICs. Brownlie [5] and Hoskins [6] show that one port of *any* NIC must always be SCS with the other port being OCS. Furthermore, in the design of ladder networks employing negative elements realized as terminated NICs, Linvill says that OCS versions should be used only as series elements, while SCS versions should be configured only in shunt. The problem of designing NICs for stability with arbitrary terminations is a daunting one, as is the problem of stabilizing NICs to realize high-Q negative reactances; some solutions are discussed in [1]. In [7], Aberle presents some interesting and modern non-Foster realizations where NIC stability is predicted using the stability-factor approach commonly used in microwave amplifier design.

1.2 Other NIC circuits

The author has identified ten different transistorized common-terminal NICs, including Linvill's, and they are catalogued in [8]. Of all of these, only Linvill's circuits and a triode vacuum-tube version of Yanagisawa's NIC [9] have been built and tested, the others only having been theoretically analyzed. Kuo [10-11] gives a family of at least 12 floating NICs which includes Linvill's circuit as a special case. Experimental results verify that these circuits can realize a negative resistance. In none of the cases is any effort made to minimize the parasitic reactive component of the impedance that comes along with the negative resistance. The operating bandwidth of these early NICs is very much a function of the devices used and was limited to the audio-frequency range.

We may also realize NICs using amplifiers, and the basic idea is illustrated in Fig. 4. Op amp versions of this circuit are well-known and are used to obtain low-Q negative resistance. Note that the gain A must be positive and greater than 1 to achieve the negation of Z ; when A is negative, this circuit is often used as the basis for modeling the "Miller-effect" in common-emitter transistor amplifiers.

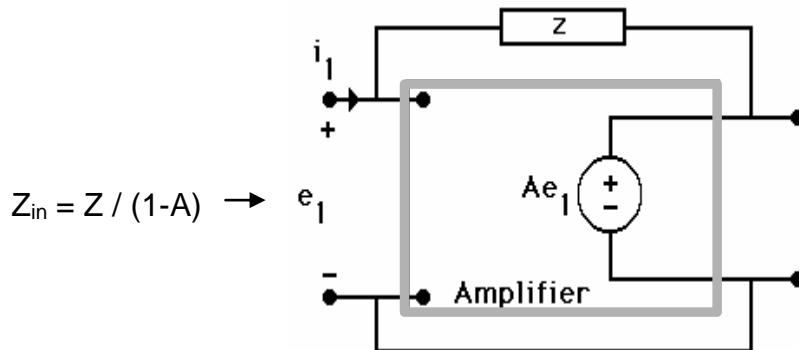


Fig. 4: Amplifier-based NIC. When the gain $A = +2$, $Z_{in} = -Z$.

2. Non-Foster Matching of Electrically-Small Antennas for Receive

An electrically-small antenna, with a physical length of less than a tenth of a wavelength, simply cannot be efficiently matched by passive techniques except, perhaps, over exceedingly small bandwidths. The problem with passive matching is so pronounced that using no matching at all is actually a viable alternative. On the other hand, the use of a single, *negative*, reactive element (i.e. a “non-Foster” element) will achieve an enormous improvement in received signal gain.

However, gain improvement is clearly not enough; if it were, a low-noise amplifier at the antenna terminals would solve the small-antenna problem. It is the improvement in *signal-to-noise ratio* that we seek, and this can be achieved with non-Foster matching under the right conditions. Consider the conceptualization below (Fig. 5) of the signal and noise power at a receiver as a function of antenna gain.

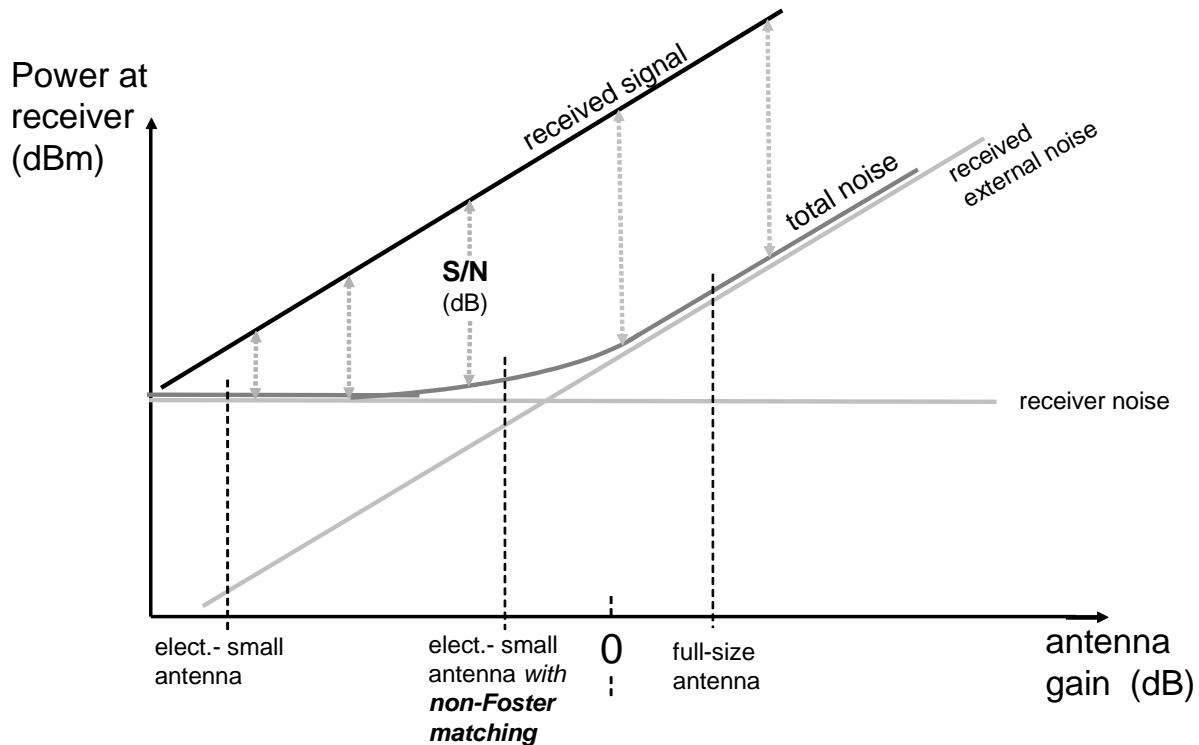


Fig. 5: Non-Foster matching increases S/N at VHF – a conceptualization

We consider a situation at VHF frequencies where the power at the receiver comprises the signal along with a combination of received *external noise* plus intrinsic, constant *receiver noise*. An electrically-small VHF antenna may have, typically, a gain of 20 – 30 dB below isotropic. A military receiver designed for the best compromise between sensitivity and dynamic range will possess a noise figure of 6 – 8 dB. For such a system, it is receiver noise – not external noise – that limits sensitivity. Fig. 5 reflects this scenario. Because of the low gain of the unmatched electrically-small antenna, the receiver noise dominates over external noise. We may increase the gain of the antenna and improve the system S/N by improving the match. When the gain reaches the point where the external noise begins to dominate over the receiver noise, no further improvement in S/N can result. We note that with a full-size antenna, the external noise dominates, so non-Foster matching cannot provide any further S/N improvement.

2.1 Early Work on Non-Foster Matching for Receive

The earliest application of non-Foster matching to electrically-small antennas was by Harris and Myers [10] in 1968. Their work is summarized with reference to Fig. 6 below. They began with an electrically small antenna (a), and considered its simplified equivalent circuit (b) as a series combination of the radiation resistance R and a parasitic capacitance C with reactance $X = -1/(\omega C)$. The parallel equivalent circuit (c) of the monopole is valid because the Q very high.

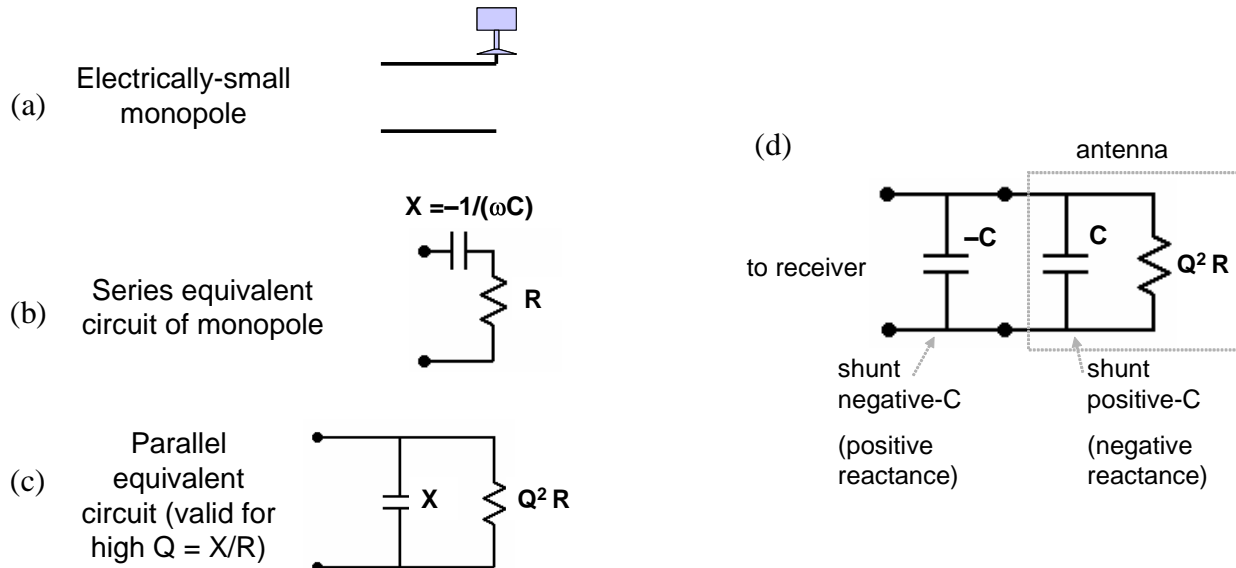


Fig. 6: Schematic description of the work of Harris and Myers

Working from this parallel equivalent circuit, Harris and Myers cancelled the parasitic capacitance C by adding a negative capacitance $-C$ in shunt, as in (d). The negative capacitance circuit used was a multistage transistorized version of the circuit shown in Fig. 4. They performed measurements on signals “of opportunity” (e.g. commercial broadcasts) using a communications receiver, comparing the performance of 2½ inch and 10 inch monopoles to that of a 16 foot untuned whip over 0.5 – 10 MHz. The results, from the original reference, are shown below in Fig. 7. The gain of the miniature antennas is better than the whip over a good portion of the band.

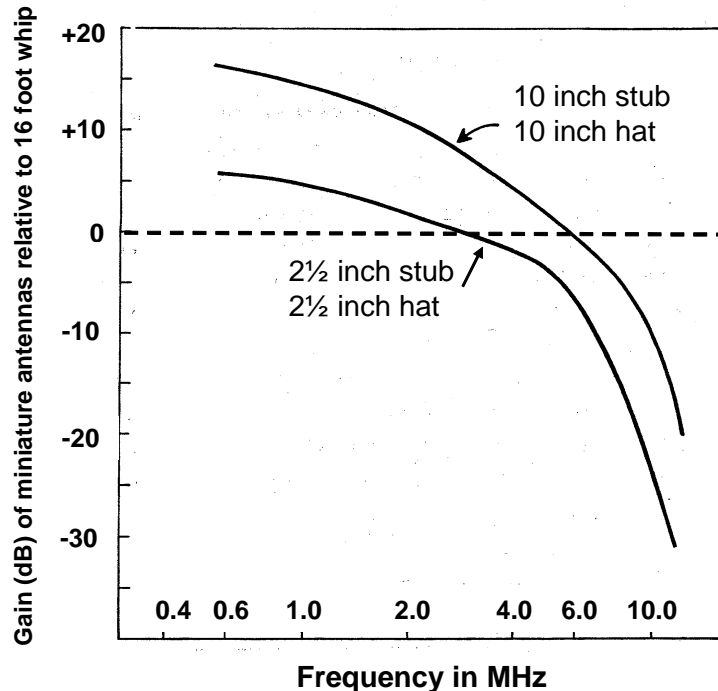


Fig. 6: Gain of Harris and Myers’ non-Foster-matched electrically-small monopoles relative to that of a 16 foot untuned whip

Harris and Myers performed no noise measurements in their experiments, but they expressed an understanding that negative-impedance matching would be advantageous in improving received signal-to-noise ratio only in those frequency ranges where receivers are “device-noise limited” rather than “natural-noise” limited. Harris and Myers performed pioneering work in non-Foster matching and were certainly the first researchers to create the stable high-Q negative capacitance necessary for this technique.

2.2 Continued Early Efforts on Non-Foster Matching

A. K. Perry [11] performed landmark research and experimentation on non-Foster matching for receive applications. Like Harris and Myers, he developed shunt negative-capacitors to cancel the parasitic capacitance of electrically-small monopoles. His realizations of negative-capacitors included op amp versions of the NIC of Fig. 4 as well as Linvill's floating SCS circuit of Fig. 2, with a positive-valued capacitor replacing R_L in that figure. Perry's work is a comprehensive treatise on negative impedance converters and their application to broadband matching. Representative of his excellent results are those given in Fig. 7, where the gain of an NIC-matched 3 inch monopole is compared to that of a 12 foot untuned whip.

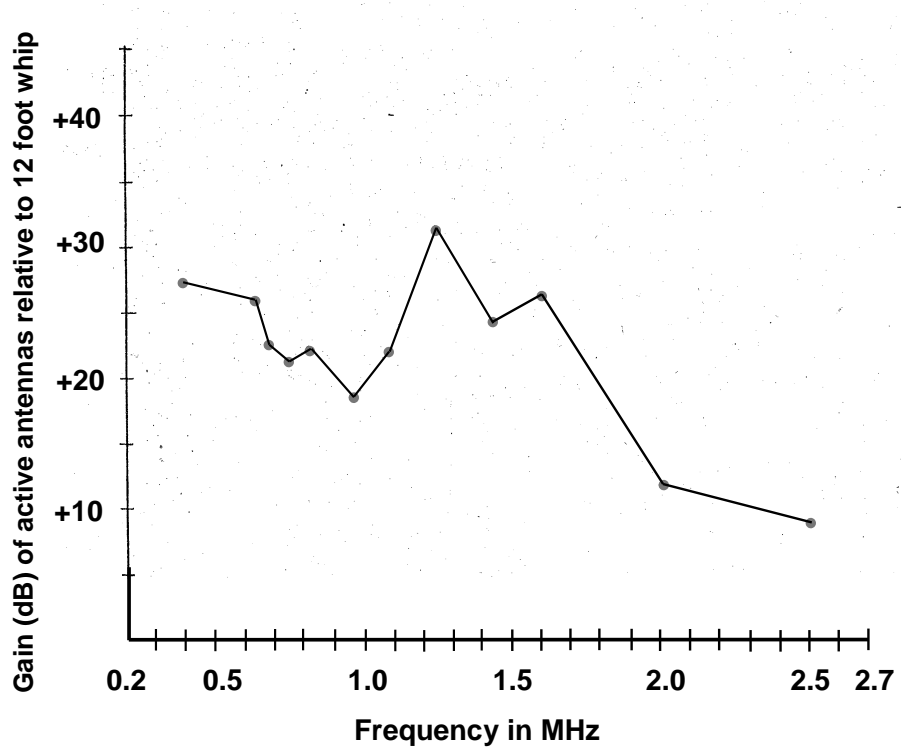


Fig. 7: Gain of Perry's 3 inch monopole with a shunt negative-capacitance as compared to that of a 12 foot untuned whip (from the original reference)

Again, no noise measurements were performed by Perry. However the formidable problems of high-Q realization and stability were analyzed and solved for Perry's circuits, and the state-of-the art of NIC design and construction was advanced sufficiently to the point that

“A ‘proof of concept model’ of a potential broadband antenna, based on the op-amp NIC design ... was completed in 1973 and provided to a very large East Coast Submarine subcontractor for developmental testing. A similar version was provided to a large Government Agency. In each case, the actual testing/implementations and follow-through were classified.” [12]

2.3 Reduction of Noise Figure with Negative Resistance

In [13], Bahr analyzes the noise performance of a receive system consisting of an electrically-small antenna, an active coupling network, and a receiver whose first stage is a high-gain preamplifier.

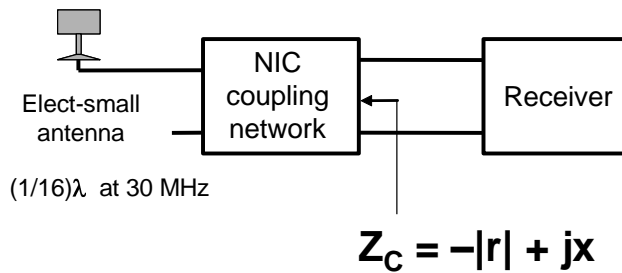
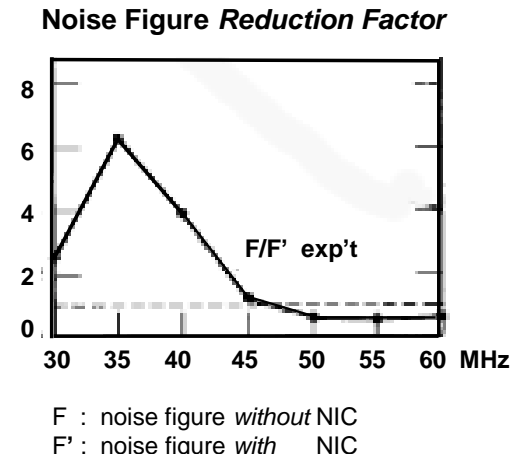


Fig. 8: Bahr’s negative-resistance method for improving noise figure

He shows that noise figure circles in the output impedance plane of the coupling network lie partially in the left-half plane, and lower noise figures can result when the impedance Z_C has a negative real-part. Note that non-Foster matching generally implies the use of negative reactance to cancel antenna parasitics so as to improve S/N, while Bahr’s method uses negative resistance to improve the noise matching of the receiver preamp to the antenna. His experimental results are summarized in Fig. 9, where he plots the factor by which noise figure is reduced when the NIC coupling network is introduced.

Fig. 9: Noise figure reduction factor for Bahr’s negative-resistance matching (from the original reference)



3. Non-Foster Matching of a Six Inch Monopole – Comparison to Families of Passive Match Solutions

Our previous work [1] demonstrated how the received signal-to-noise ratio of an electrically-small monopole could be dramatically improved, relative to no matching at all, by using a series-negative capacitor to improve the match. In fact, we have updated results, improved from those of [1], reflecting our use of a SiGe BJT (NESG2101M05) device rather than the NE85630 originally employed. The experimental procedure on the antenna range, along with the ultimate S/N enhancement, are summarized in Fig. 10.

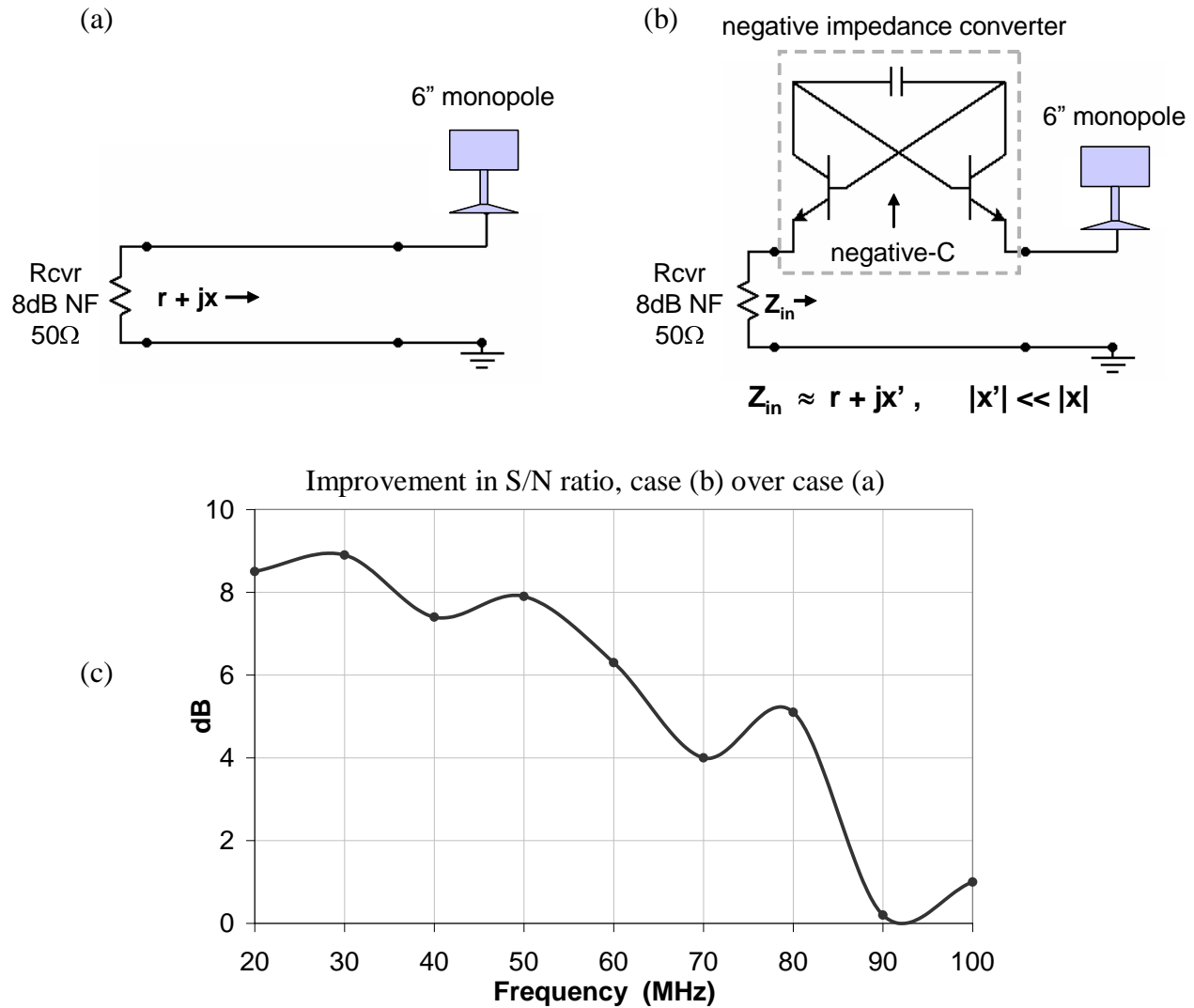


Fig. 10: (a) 6-inch monopole connected via 50Ω line to a receiver with 8 dB noise figure (b) Same 6-inch monopole with a negative capacitor in series at the antenna terminals, connected via 50Ω line to the same receiver (c) Improvement in signal-to noise ratio for case (b) over case (a)

In this experiment, we have compared non-Foster matching to no matching at all, and we now verify the assertion that no matching is indeed a viable option. In a computer simulation, we designed a number of “best-effort” passive matching networks and calculated the transducer gain (S_{21}) between a 50 ohm source and the complex impedance of our 6-inch monopole. We calculated, as well, S_{21} for no matching and S_{21} for a single, ideal negative capacitance whose value (-5.54pF) exactly cancels the antenna reactance at 30 MHz. Plots of the real and imaginary parts of the antenna impedance are shown in Fig. 11. The various matching networks are illustrated in Fig. 12; each of these would appear in place of the NIC in Fig. 10b.

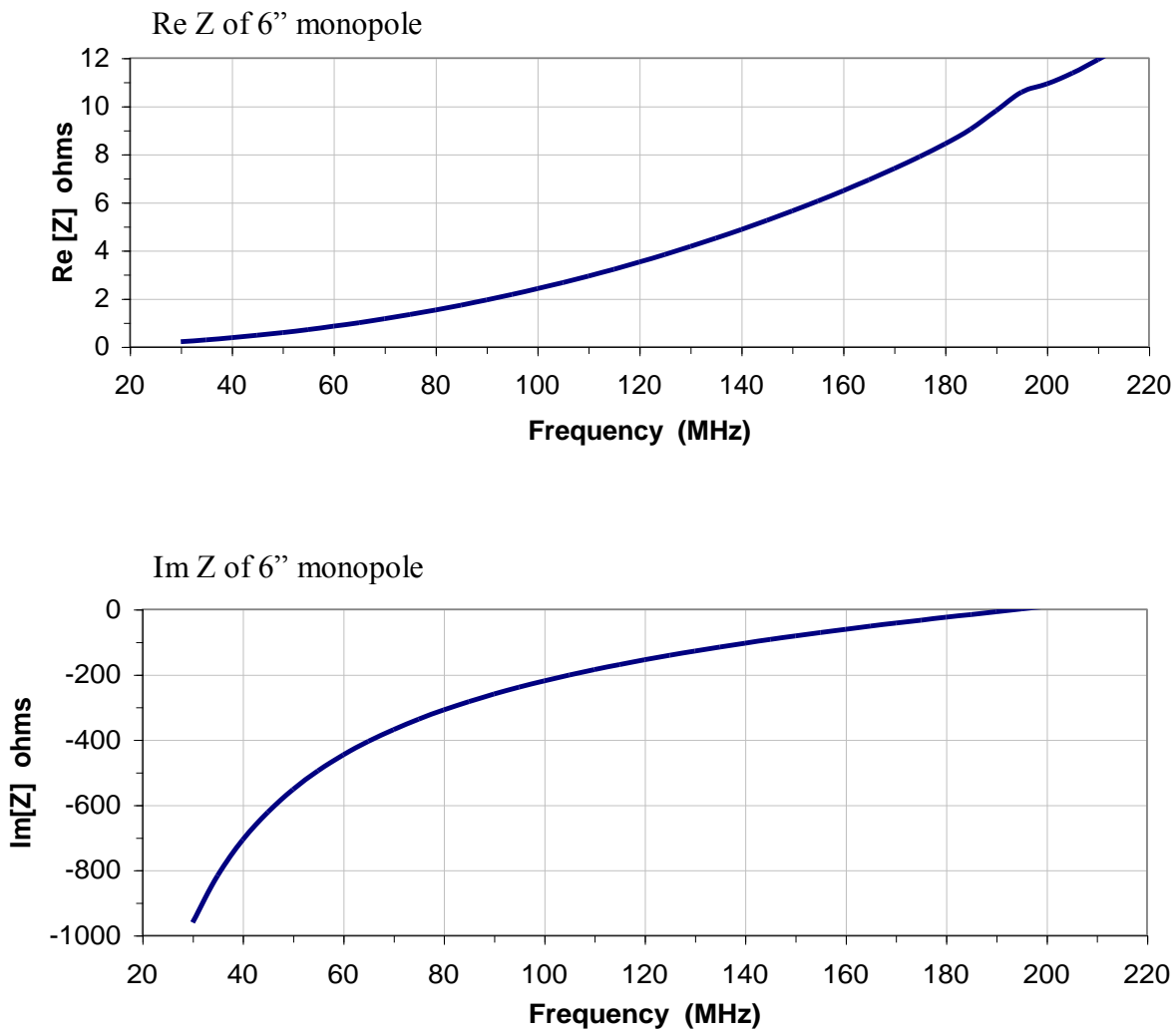


Fig. 11: The real and imaginary parts of the impedance of a six-inch monopole (simulated)

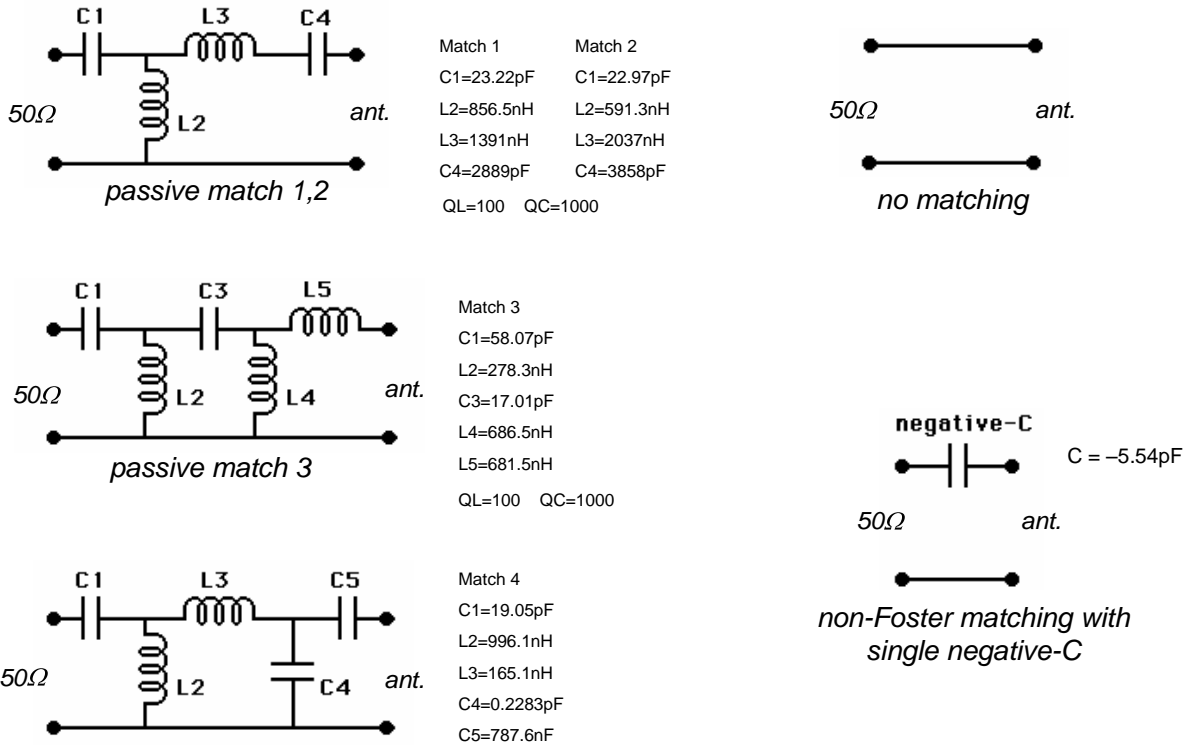


Fig. 12: Family of matching networks for electrically-small monopole

Fig. 13 shows plots of the computed transducer gain between the 50Ω source and the monopole. With conventional matching the passive networks can enhance S_{21} somewhat, but no matching is clearly an excellent alternative. Considering the entire frequency band, non-Foster matching is much better matching than any other approach; this is a consequence of gain-bandwidth limitations. At the high end of the band, our monopole is no longer electrically-small, and no matching performs better than non-Foster, as would be expected. The average value of S_{21} over the band, in gain-order, for each matching network is given in the table below:

Average gain 30-220 MHz

Non-Foster neg-C: -13.2 dB

Passive match 4:	-21.9 dB
Passive match 3:	-23.1 dB
No matching:	-23.9 dB
Passive match 1:	-26.7 dB
Passive match 2:	-28.4 dB

Table 1: Average value of S_{21} for matching networks of Fig. 12.

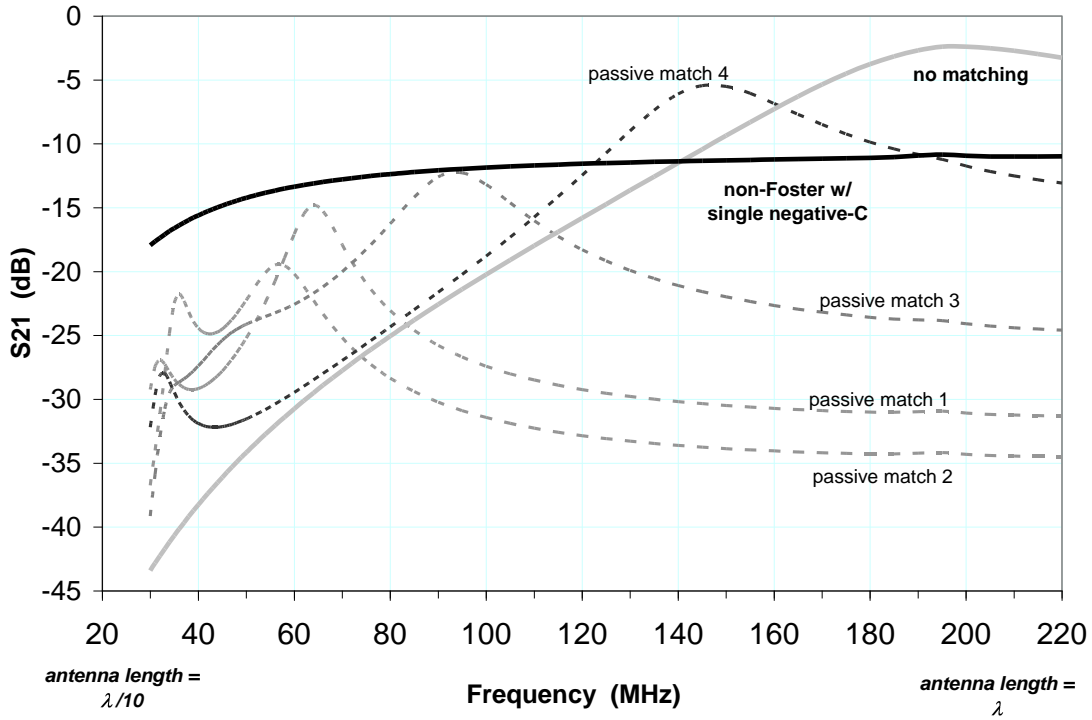


Fig. 13: Transducer gain between $50\ \Omega$ and antenna for matching networks of Fig. 12.

Upon examination of Figs. 10c and 13, the question naturally arises as to why we get 9 dB of S/N improvement at 30 MHz in an actual experiment, while the simulation predicts an increase in S_{21} of 26 dB when comparing non-Foster matching to no matching.

The first part of the answer lies in the interpretation of Fig. 5, where increased antenna gain (i.e. S_{21}) results in an improved S/N only when receiver noise dominates over external noise. Once the external noise becomes comparable to or exceeds the receiver noise, any further increase in gain augments both the signal and the dominating external noise, and the S/N remains relatively constant. Second, the simulation assumes that all the parasitic capacitance of the antenna is cancelled by an ideal negative capacitor. In practice, some residual positive capacitance must remain, otherwise the circuit would become unstable; this reduces the actual gain achieved. Finally, the active circuitry of the NIC generates noise, clearly to the detriment of the S/N improvement. We comment that our circuits are quite low-noise themselves, although improvement still may be possible. We have experimented with NICs made using low-noise op amps, and have found that those circuits generate at least 10 dB more noise at 30 MHz than our 2-transistor NICs (for an 8 dB noise-figure receiver).

4. Non-Foster Matching of a Lossy Electrically-Small Dipole: 60 – 400 MHz

We now consider the non-Foster matching of a lossy, electrically-small dipole antenna provided to us by a customer. The antenna's lossiness is intentional and is a consequence of special construction and application details. Trusting that increased antenna gain will improve their system S/N, the customer wanted us to compare measured E-plane antenna patterns for the cases of (1) no matching whatsoever and (2) non-Foster matching.

We performed a further comparison to an available, somewhat shorter, *lossless* antenna without any matching at all. Fig. 14 shows a schematic representation of the antennas, which are constructed from thin sheets of a proprietary material for the lossy element, and of copper for the lossless element.

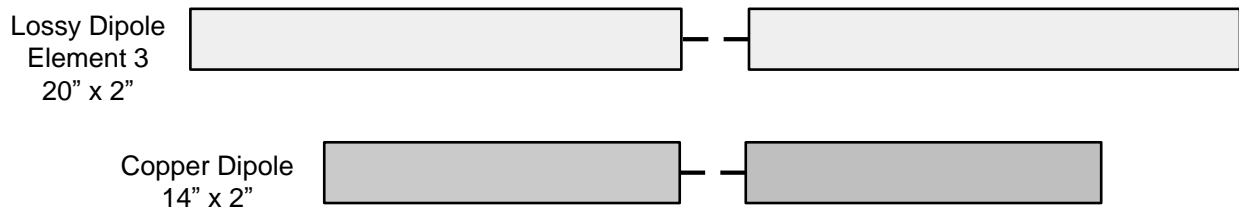


Fig. 14: Schematic representation of electrically-small lossy and lossless antennas

The experimental procedure on the antenna range is summarized in Figs. 15a and b. In the no-matching case of Fig. 15a, a transformer balun is connected at the antenna and a $50\ \Omega$ coaxial line then runs to an 8 dB noise-figure receiver. With non-Foster matching as in Fig. 15b, separate and identical negative capacitance circuits are connected in series with each arm of the lossy dipole. Unity-gain buffers connect to the balun, and then a $50\ \Omega$ coaxial line runs to the receiver. The buffers use only a few transistors and contribute very little noise to the system. Our latest designs employ a special low-noise active balun which combines the functions of the buffers and the transformer balun into a single package. The buffers and active balun possess $50\ \Omega$ input and output impedances, allowing them to be placed either at the antenna or at the receiver. They also possess bias-Ts for easy application of power to the negative capacitors. We note that op amp implementations of the buffers or active baluns are far noisier than the transistor designs we use.

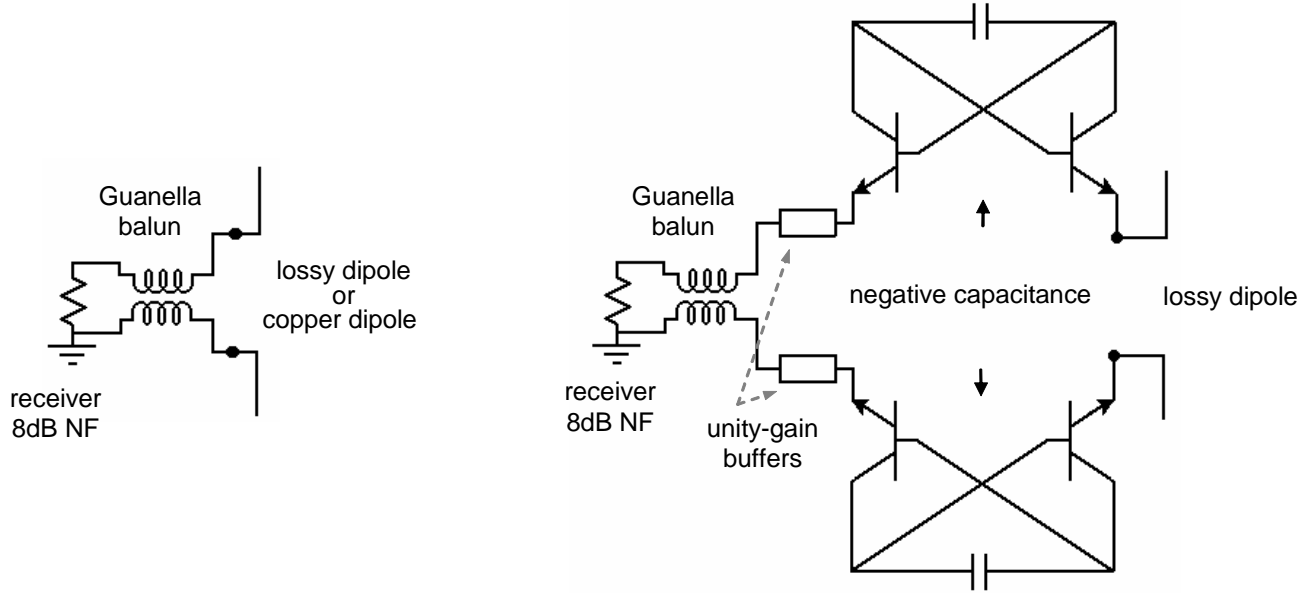


Fig. 15: (a) No-matching case for the lossy and copper (lossless) dipoles. (b) Non-Foster matching of the lossy dipole

Figs. 16 shows selected E-plane pattern measurements of relative gain of the lossy and copper dipoles with no matching, and the lossy dipole with non-Foster matching. Shown are the data for 60, 100, 180, and 400 MHz. In each case, “Element #3 Active” (the lossy dipole with non-Foster matching) gives better gain than the same antenna with no matching. Not surprisingly, the copper dipole, although smaller, does better than the lossy dipole. We note that the dipole patterns possess a somewhat peculiar shape. This is a consequence of the partial ground plane that was used with all the antennas as well as the reflections on and limitations of the measurement range. The active dipoles also may have been unbalanced somewhat, by virtue of slightly different tunings for the NICs in series with each antenna arm.

Consider now the improvement in gain of the lossy antenna with non-Foster matching over the gain of the same antenna with no matching. This gain improvement has been averaged over 360° at each frequency and is plotted in Fig. 17. Non-Foster matching is most effective where the antenna is electrically-small; hence we see the most gain advantage at the low end of the band. The decrease in gain improvement below 90 MHz is deliberate and due to the values chosen for the coupling and bypass capacitors and for the RF chokes used in biasing. At higher frequencies the gain advantage decreases because the antenna becomes less electrically-small and non-Foster matching gradually loses its benefit. Nevertheless, non-Foster matching was still able to achieve 2.5 – 5.0 dB of gain improvement over 300 – 400 MHz. In the present design, we employed NE68019 BJTs in the NICs because these devices provided better overall performance over the

frequency range than the NE2101M05 SiGe transistors mentioned in Sec. 3.0. This struck us as curious, inasmuch as $f_T = 17$ GHz for the NE2101M05 and as $f_T = 10$ GHz for the NE68019. However this result is consonant with our experience that computer models for devices, while accurately predicting responses for conventional circuits such as amplifiers, often do *not* do the same for NICs.

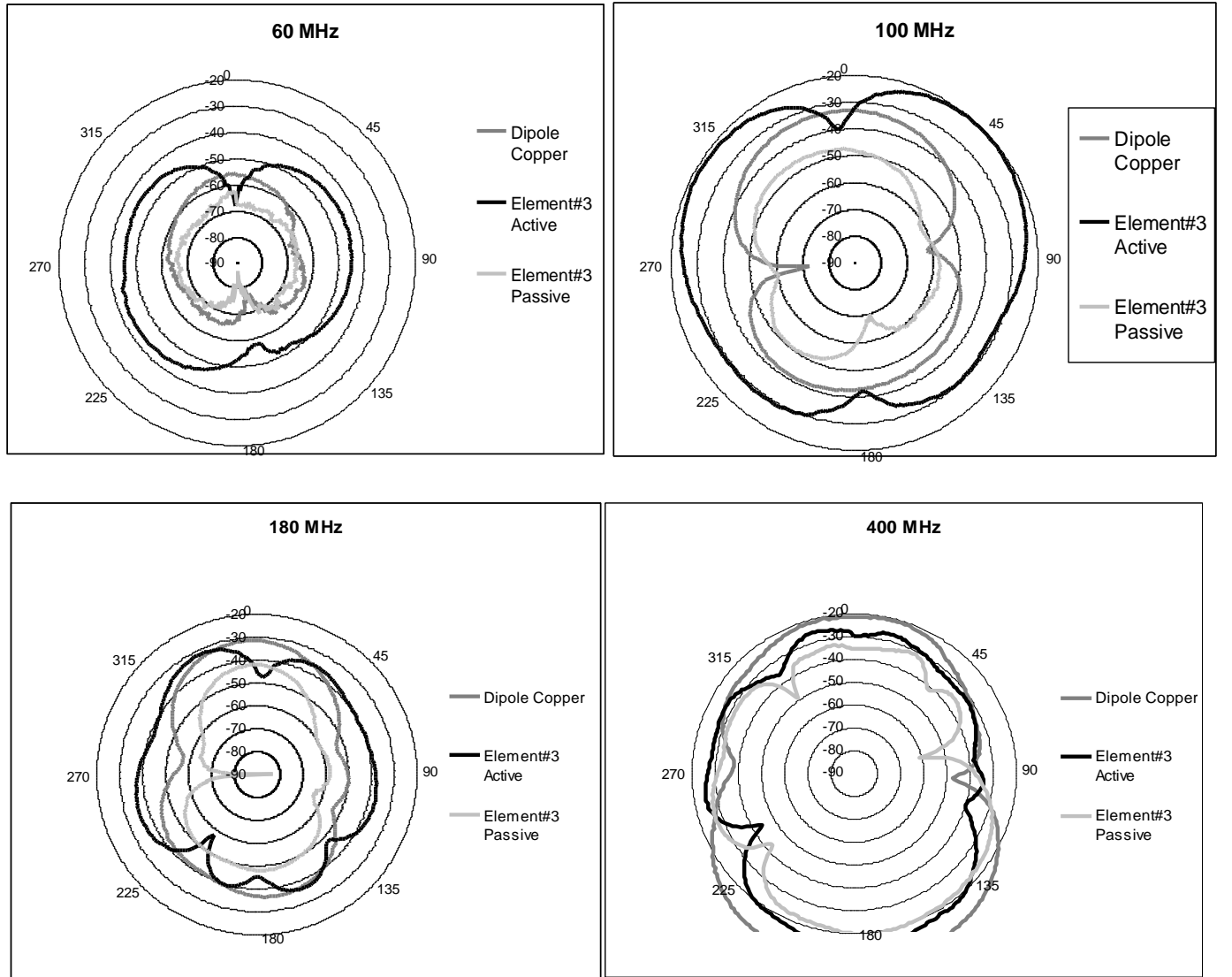


Fig. 16: E-plane measurement plots of the relative gain of the lossy antenna with no matching (element #3 passive); the lossy antenna with non-Foster matching (element #3 active); and the lossless antenna (dipole copper) at 60, 100, 180, and 400 MHz.

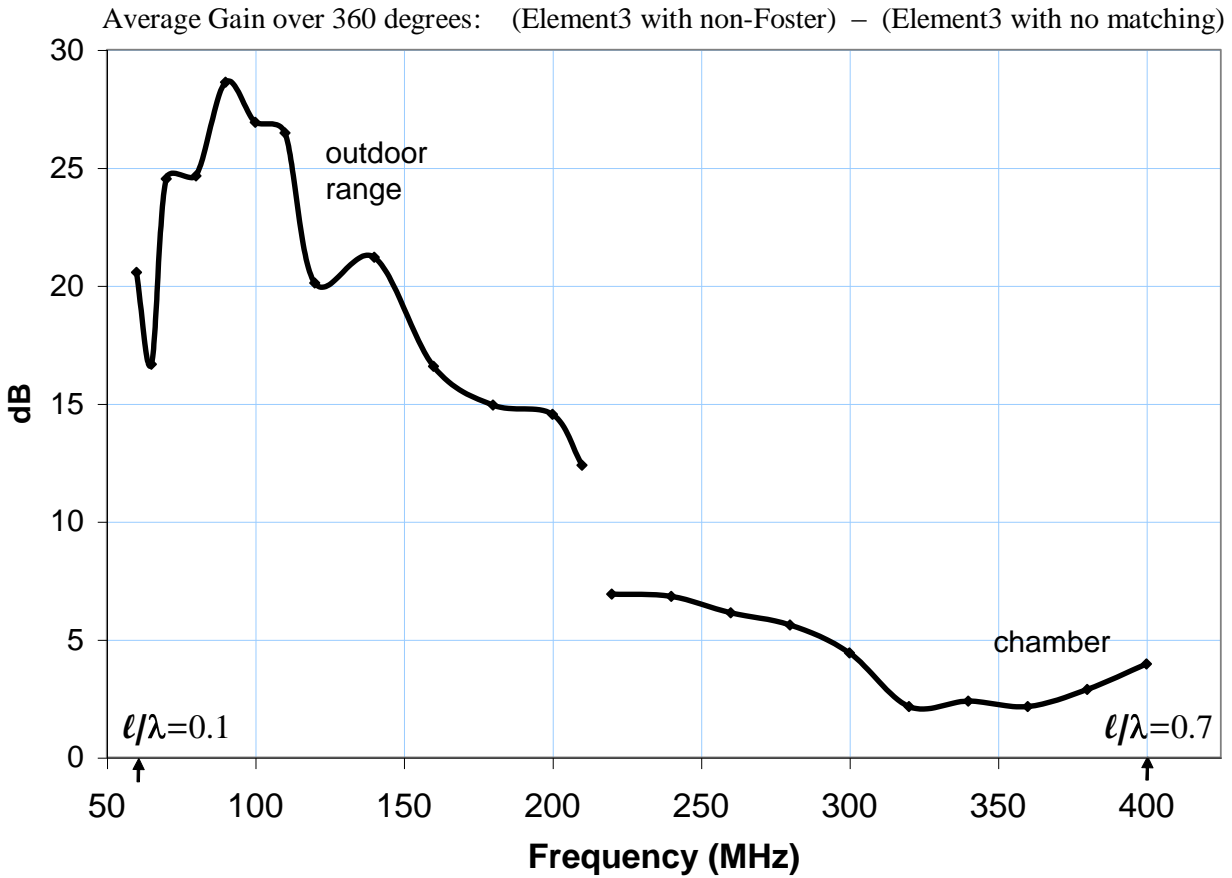


Fig. 17: Gain improvement of the lossy dipole with non-Foster matching over the same antenna with no matching, averaged over 360° , at each frequency. Measurements were taken on an outdoor range as well as in a chamber as indicated. The ratio of antenna length to wavelength, ℓ/λ , is also indicated.

4.1 Non-Foster Matching of a Lossy Electrically-Small Dipole – Comparison to Families of Passive Match Solutions

We now examine the assertion that no matching is a viable option for the lossy dipole of Sec. 4. In a computer simulation, we designed a number of passive matching networks and calculated the transducer gain (S_{21}) between a 50 ohm source and the radiation resistance of the dipole. We also calculated S_{21} for no matching and for a single, ideal negative capacitance whose value exactly cancels the antenna reactance. For simplicity in the simulation, we considered one-half of the dipole as shown in Fig. 18. We assume the use of the active balun mentioned in Sec. 4 which provides a 50 ohm termination to each dipole-half. In the present instance we used a network model for the dipole-half that assumes constant resistive loss and that ignores radiation-resistance variation with

frequency. The indicated equivalent circuit nevertheless provides a reasonable approximation to the (proprietary) antenna impedance and allows a meaningful evaluation of the matching networks examined.

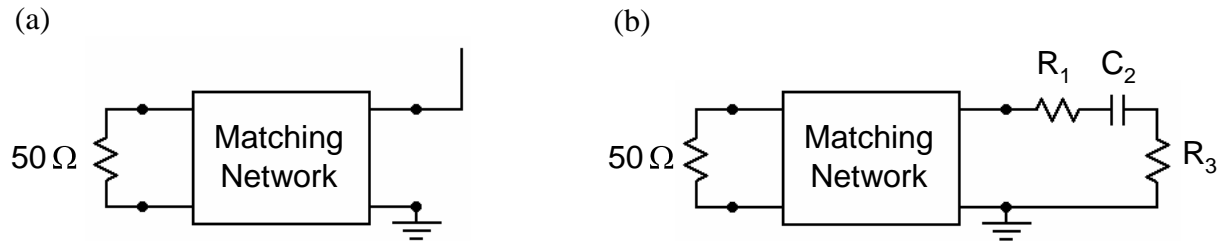


Fig. 18: (a) Matching network connected between a 50Ω source one-half of the lossy dipole of Fig. 14. (b) The network model replaces the dipole-half. $R_1 = 14 \Omega$ (loss); $C_2 = 3.56 \text{ pF}$ (parasitic capacitance); and $R_3 = 1 \Omega$ (radiation resistance).

Fig 19 shows the various networks considered for matching the lossy dipole-half to 50Ω . These passive LC networks represent a sampling of the best networks that could be designed for this matching problem.

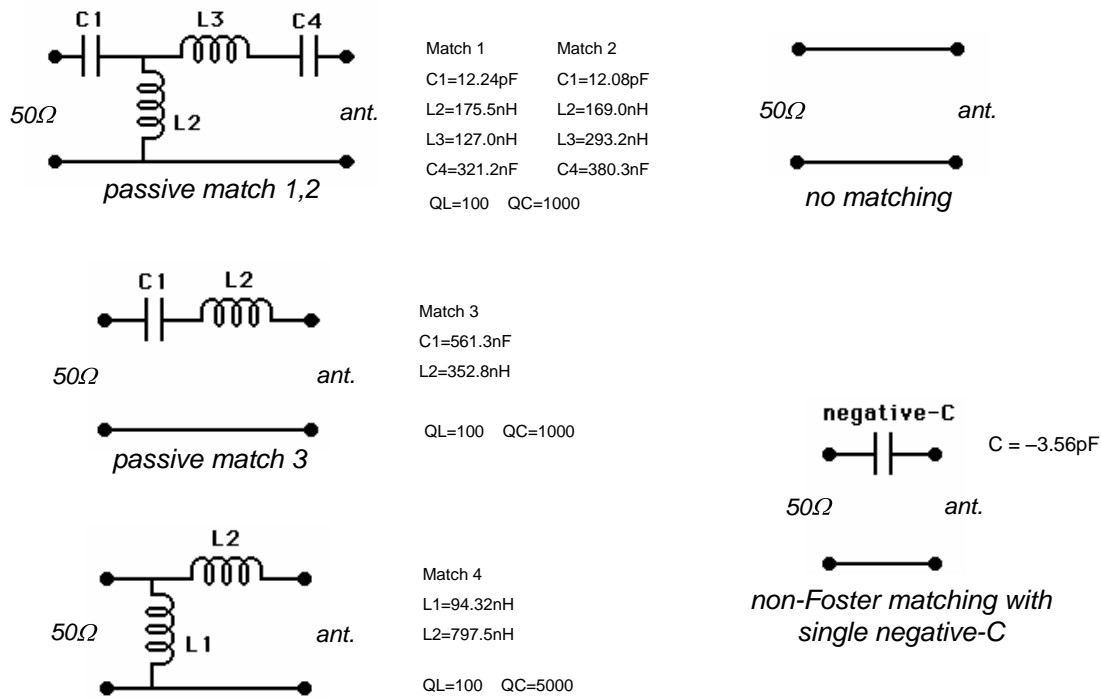


Fig. 19: Family of matching networks for one-half of the lossy dipole of Fig. 14.

Fig. 20 shows plots of the computed transducer gain between the 50Ω source and the lossy dipole-half. Clearly, non-Foster matching with an idealized single negative capacitor is superior to any other approach; again, this is a consequence of gain-bandwidth limitations. Among the passive networks, no matching is still a viable alternative, but “passive 1” does provide a better response. With lossy antennas, it appears that some form of passive matching will perform noticeably better than no matching at all. At the high end of the band, even though the lossy dipole is no longer electrically-small, non-Foster still performs better than no matching. This behavior is to be contrasted with that of the lossless antenna of Sec. 3.

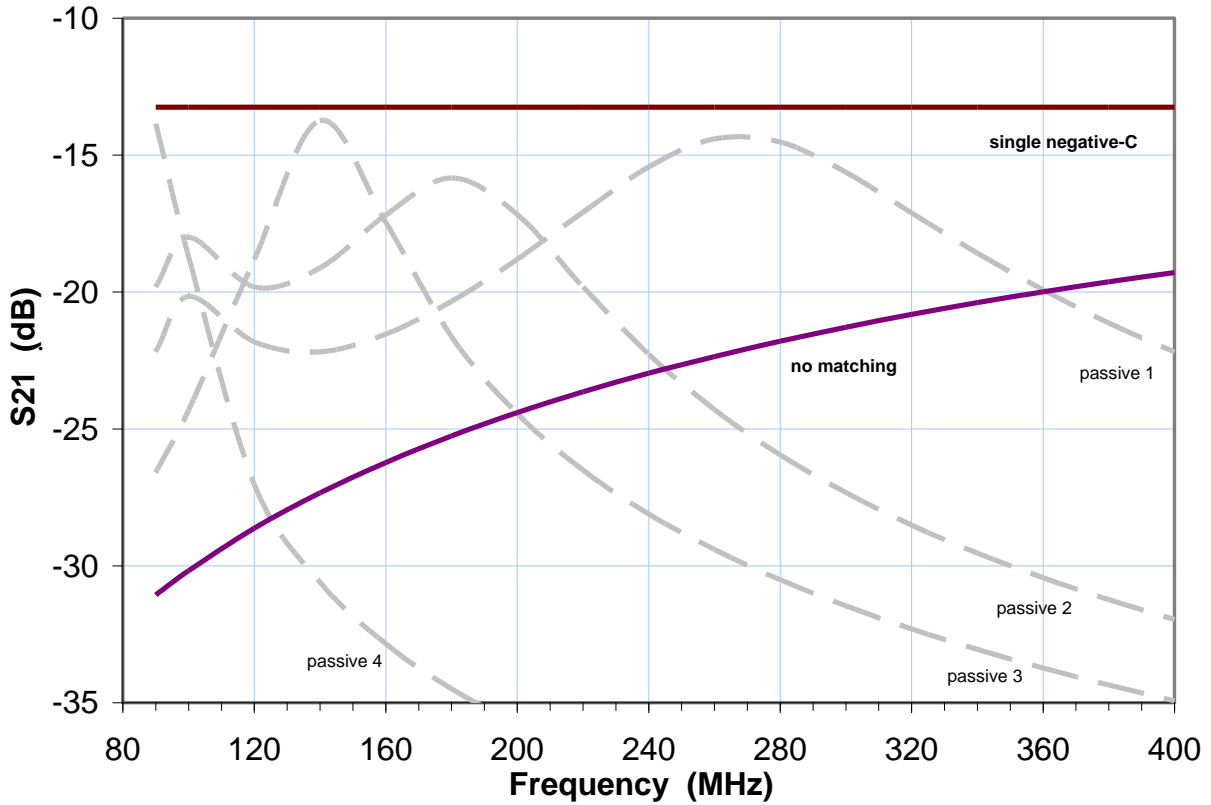


Fig. 20: Transducer gain between 50Ω and lossy dipole-half for matching networks of Fig. 19.

The average value of S_{21} over the band, in gain-order, for each matching network is given in the table below:

Average gain 60-400 MHz

Non-Foster neg-C: -13.3 dB

Passive match 1: -19.0 dB

Passive match 2: -23.4 dB

No matching: -23.8 dB

Passive match 3: -27.1 dB

Passive match 4: -35.0 dB

Table 2: Average value of S_{21} for matching networks of Fig. 19.

5. Conclusion

Non-Foster matching of electrically-small antennas improves the S/N over a broad frequency band in receivers where the dominant noise contribution is from the receiver itself. This situation arises in many practical applications. Passive matching cannot compete because of the gain-bandwidth limitations. In this paper, we have presented our results in extending the application of non-Foster matching to higher frequencies. We have also given a historical perspective of the approach, including some references that only recently have become available in the public domain. We expect to continue our research in developing new topologies for both shunt and series negative capacitors and inductors to matching electrically-small monopoles, dipoles, and loops.

6. Acknowledgments

We gratefully acknowledge the support of the EDO Corp. IR&D who has sponsored the work reported here.

7. References:

- [1] Stephen E. Sussman-Fort, "Matching Network Design Using Non-Foster Impedances," *International Journal of RF and Microwave Computer-Aided Engineering*, vol. 16, issue 2, pp. 135-142, March 2006.
- [2] Stephen E. Sussman-Fort and Ronald M. Rudish, "Progress In Use Of Non-Foster Impedances To Match Electrically-Small Antennas And Arrays", *Twenty-Ninth Antenna Applications Symposium*, Allerton Park, IL, Sept. 21-23, 2005.
- [3] G. Crisson, "Negative impedances and the twin 21-type repeater," Bell Sys. Tech. Jour., vol. 10, pp. 485-513; July, 1931.

- [4] J. G. Linvill, "Transistor Negative Impedance Converters," *Proc. IRE*, vol. 41, June 1953, 725-729.
- [5] J. D. Brownlie, "On the Stability Properties of a Negative Impedance Converter," *IEEE Trans. Circuit Theory*, CT-13(1), March 1966, 98-99.
- [6] R. F. Hoskins, "Stability of Negative Impedance Converters", *Electronics Letters*, 2 (9) Sept.1966, 341
- [7] James T. Aberle and Robert Loepsinger-Romak, *Active Antennas with Non-Foster Matching Networks*, San Francisco, Morgan and Claypool Publishers, 2007.
- [8] Stephen E. Sussman-Fort, "Gyrator-Based Biquad Filters and Negative Impedance Converters for Microwaves," *International Journal of RF and Microwave Computer-Aided Engineering*, (Special Issue on Network Synthesis Methods in Microwave Design), vol. 8, no. 3, pp. 86-101, Mar. 1998.
- [9] T. Yanagisawa, "RC Active Networks Using Current Inversion Type Negative Impedance Converters," *IRE Transactions on Circuit Theory*, pp. 140-144, Sept. 1957.
- [10] C. K. Kuo and K. L. Su, "Some New Four Terminal NIC Circuits," IEEE Proc. Circuit Theory, pp. 379-381, August 1969.
- [11] C. K. Kuo, "Realization of Negative-Immittance Converters and Negative Resistances with Controlled Sources, School of Elec. Engrg., Georgia Institute of Technology, Atlanta, Research Rept. 67-9, December 1967.
- [12] Andrew D. Harris, and Glen A. Myers, "An Investigation of Broadband Miniature Antennas," Technical Report, Naval Postgraduate School, Monterey CA, Sept. 1968. (Document AD677320, *National Technical Information Service*)
- [13] Albert K. Perry, "Broadband Antennas Systems Realized by Active Circuit Conjugate Impedance Matching" Electrical Engineer's Degree Thesis, Naval Postgraduate School, Monterey CA, Sept. 1973. (Document AD769800, *National Technical Information Service*)
- [14] Albert K. Perry, private communication, Feb. 23, 2007.
- [15] A. J. Bahr, "On the use of active coupling networks with electrically-small receiving antennas," *IEEE Trans. Antennas and Propagation*, vol. AP-25, no. 6, pp. 334-338, Nov. 1977.

MICROFLUIDIC RECONFIGURATION OF ANTENNAS

Gregory H. Huff⁽¹⁾, Pradipkumar Bahukudumbi⁽²⁾, W. Neil Everett⁽²⁾, Ali Beskok⁽²⁾, Michael A. Bevan⁽³⁾, Dimitris Lagoudas⁽⁴⁾, Zoubeida Ounaies⁽⁴⁾

⁽¹⁾Department of Electrical and Computer Engineering

⁽²⁾Department of Mechanical Engineering

⁽³⁾Department of Chemical Engineering

⁽⁴⁾Aerospace Engineering Department

Texas A&M University

College Station, TX 77843-3128

Abstract: This work examines the integration and application of novel microfluidic devices which are under development to dynamically reconfigure the impedance bandwidth and radiation behavior of antennas. As the mechanism that facilitates change in the electromagnetic fields (both directly and parasitically), the choice of reconfiguration mechanism represents a key element in the design and implementation of a reconfigurable antenna (or reconfigurable antenna system). By including the behavior of this mechanism into the design of reconfigurable antenna – or alternatively, considering what electromagnetic properties or boundary conditions it can provide within the context of the reconfigurable antenna system – the overall performance can be significantly enhanced. The microfluidic reconfiguration mechanisms under consideration in this work base their operation on the transport, mixing, and kinetic behavior of colloidal dispersions composed of dielectric and magnetic particles (e.g., electromagnetically tunable fluids). This provides a unique degree of freedom to the design, and results in a diverse class of material-based mechanisms and devices that can provide a very large degree of impedance control. This can be used to facilitate the dynamic reconfiguration of an antenna across a wide range of states using pressure driven microfluidic systems (also reducing the amount of complexity in the overall design by eliminating many biasing and control structures from the antenna). Examples of antennas and devices enabled by this microfluidic technology are provided, as well as the methods used to determine the properties of the material systems.

I. Introduction

This work addresses several of the initial development and integration challenges associated with the use of magnetodielectric colloidal materials dispersed in a

liquid, pressure driven system for use in reconfigurable antennas and other tunable devices. These material systems are based on pressure driven microfluidic flows that both transport and mix dispersions of dielectric, magnetic, and conductive colloidal particles (1 nm – 1000 nm) to *in situ* alter the local homogeneous material properties and/or alter the electromagnetic boundary conditions. These systems can encompass a vast number of embodiments, and can be used purely as a pressure driven system or locally biased to alter the microstructure and electromagnetic properties. In many cases, these systems can reduce overall footprint of biasing networks by remotely controlling the flow of materials and routing them through areas where they are electrically transparent or will have minimal undesired effects.

Several of the underlying concepts associated with the use of colloidal and microfluidic elements are discussed first, including the materials for electromagnetically tunable fluids, mixing rules, and other system parameters that have a direct impact on the overall performance. The direct integration – or distributed impedance control – of microfluidically transported magnetodielectric colloids into an antenna follows this, and includes a design example of a microstrip patch antenna with measured results for a colloidal magnetic material. The next section discusses the current development of N-port antenna reconfiguration mechanisms and covers two device-level embodiments – the pressure-driven flow of colloidal materials and reversibly microstructured colloids. The work concludes with a brief summary and discussion of future work.

II. Elements of Microfluidic Impedance Control

A. Electromagnetically Tunable Fluids (*ETFs*)

Electromagnetically Tunable Fluids (*ETFs*) – the term used herein to describe the dynamic electromagnetic properties associated with dielectric, magnetic, and conductive colloidal particles suspended in a fluid media – are key elements in this work. Although examples of antenna-fluid systems exist [1-5], the overall ability to *in situ* alter the material properties through fine-tuned magnetodielectric colloid materials in microfluidic and kinetic systems has remained primarily unexamined for antenna applications. In addition, liquids have traditionally been considered in and around devices *only* in the capacity as a cooling mechanism (much like the radiator in a combustion engine) – such that their sole purpose lies in the mitigation of heat that accumulates from resistive power dissipation in these devices and their local packaging. In most cases this heat is a result of conductor and material losses, and the fluidic components are electromagnetically shielded –

or isolated – from the operation of the device. Under this framework the microfluidic elements transport particle laden suspensions of *ETFs* that interact directly with the electromagnetic fields and perform an operational role in the functionality of the device.

In the case employing only pressure driven flow, the local concentration of particles will be tuned by pumping particles from local reservoirs to different positions. Implementation of such an approach require proper placement of various colloidal fluids with specific electrical and magnetic properties within a vascular network. In addition, geometric constraints may be imposed on the static vascular network and its associated reservoir system to optimize transient (e.g., speed of reconfiguration) responses achieved by altering local particle concentrations within such a structure. By adding the ability to alter the microstructure of the colloids with local AC electric fields to direct the assembly of particle configurations, many interesting electrical properties have been examined that can be useful mechanisms within a reconfigurable antenna system [6-7].

B. Microfluidic Elements

In addition to the electromagnetic properties of the *ETFs*, the design of microfluidic systems to transport them requires careful consideration of several fluid mechanical issues associated with changing local particle concentrations within the network. The dynamic response in such systems will be related to the range of flow rates that can be achieved with pressure driven flow as well as convective and diffusive mixing of concentrated colloidal streams with dilute or pure solvent streams. For example, flow rates and operating pressures scale with the radius of microfluidic channels to the fourth power, which becomes increasingly significant at small length scales. In another example, diffusive mixing of particles depends on the particle radius to the first power in bulk media, but depends on the particle radius squared in confined geometries due to lubrication interactions. Other important fluid mechanical variables include the continuous fluid viscosity, dielectric and magnetic properties, and density (in terms of how it affects the buoyancy of entrained colloidal particles). Although this work will not address these issues, they are considered in the overall development of these systems.

C. Mixing Rules and Formulas

Several basic mixing rules using the volume fraction ϑ of colloidal materials dispersed in the solvent (fluid) are examined in this work to approximate the

homogeneous material parameters of the mixed sol (e.g., the two phase mixture). Figure 1 shows a generic capillary mixing device mixing spherical colloidal particles (ϵ_{r2} , μ_{r2} , σ_{r2}) into a fluid (ϵ_{rl} , μ_{rl} , σ_{rl}) and the resulting homogeneous (mixed) material (ϵ_{eff} , μ_{eff} , σ_{eff}) that illustrate the process. The maximum diameter of the colloidal particles are assumed electrically small with respect to the effective wavelength in the material with the highest electrical density ($a_{max} \ll \lambda_{eff}$) to satisfy quasi-static approximations in the mixing formulas.

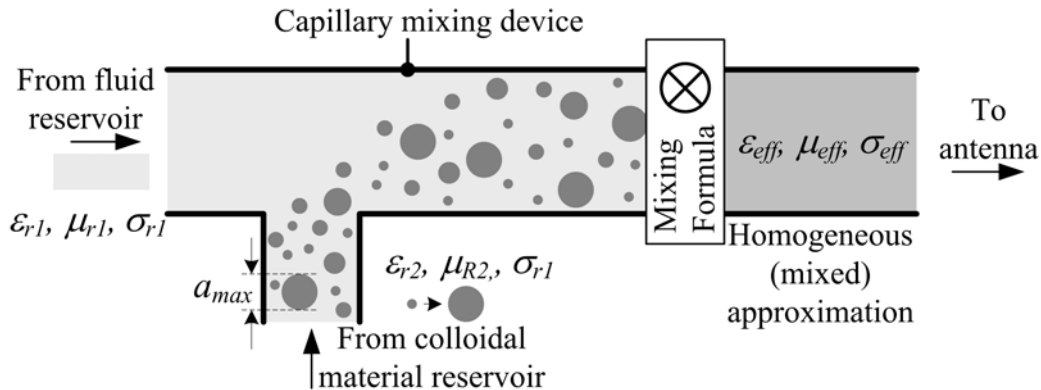


Figure 1. A generic microfluidic mixer showing the transport of colloid materials from a reservoir into the vascular network, illustrating the use of mixing rules at this scale.

Given the diverse nature of the mixing problem – made apparent by the vast amount of available literature on the subject and available materials – there exists a variety of potential means to determine the effective material parameters [8-11]. This work examines two generalized families of mixing rules, structure-Dependent formulas and non-structure dependent (exponential) formulas. Together, these mixing rules provide a bounded envelope of effective homogeneous (mixed) material properties that best encompasses experimental data found in literature. These rules are shown for a non-specific parameter s that can represent relative permittivity ϵ_r , permeability μ_r , or conductivity σ – where s_1 refers to the fluid properties, s_2 refers to the colloidal material properties, and s_{eff} refers to the effective (mixed) properties.

The first case comes from the family of mixing formulas which has the structure-dependent parameter ξ related to the geometry of the particles (e.g., the formula pays specific attention to the microscopic structure of the mixture). For the fundamental case of spherical particles, $\xi = 0$ and Equation 1 reduces to the Maxwell-Garnett (or Raleigh) mixing formula (Equation 2). When the polarizability of the particles is included this formula is known as the Lorentz-

Lorenz formula or the Clausius-Mossotti formula.

$$\frac{s_{eff} - s_1}{s_{eff} + 2s_1 + \xi(s_{eff} - s_1)} = \vartheta \frac{s_2 - s_1}{s_2 + 2s_1 + \xi(s_2 - s_1)} \quad (1)$$

$$\frac{s_{eff} - s_1}{s_{eff} + 2s_1} = \vartheta \frac{s_2 - s_1}{s_2 + 2s_1} \quad (2)$$

The second set of experimentally-based exponential mixing rules relies primarily on the volume fraction ϑ and the parameter χ ($\chi = 1$ for parallel mixing and $\chi = 1$ for series mixing). Equation 3 shows the general form of this mixing rule, and Equations 4 demonstrates the formula for a two-phase ($N = 2, \chi = 1$).

$$s_{eff}^\chi = \sum_{i=1}^N f_i s_i^\chi \quad (3)$$

$$s_{eff} = [(1 - \vartheta) s_1^\chi + \vartheta s_2^\chi]^{1/\chi} \quad (4)$$

D. Material Spectroscopy

Given the diverse number of materials (and material combinations) available, the spectroscopy of the magnetodielectric mixtures will also have an important role in the functionality of the microfluidic system and its performance as an antenna reconfiguration mechanism. Ergo, a material with considerably high frequency dependant material parameters can create significant dispersive effects within a device. These effects are not discussed in this manuscript; however, they are under consideration as a key component in the entire system due to its role in broadband and/or frequency independent antenna designs.

III. Distributed Impedance Control of a Microstrip Patch Antenna

A linearly polarized microstrip patch antenna provides an excellent vehicle to explore some of the concepts associated with microfluidic reconfiguration of antennas. It's resonant behavior and analytical models provide (1) the ability to effectively model the structure while placing an emphasis on the investigation and implementation of the microfluidic elements, (2) a means to link the electromagnetic contribution of the nanoparticles to the overall behavior of an antenna, and (3) a narrowband frequency range that largely avoids the dispersive and frequency-dependent behavior of the materials (the microscopic interaction between the nanoscale materials in an electromagnetic field will not be directly

addressed in this section of work). The patch antenna considered in this example has dimensions length L and width W , and resides atop a substrate of height h with material properties ϵ_{rp} , μ_{rp} , and σ_p . Colloidal magnetodielectric materials with properties ϵ_{rf} , μ_{rf} , and σ_f are then used in a substrate-embedded (vascular) microfluidic system to transport, mix, and ultimately reconfigure the antenna parameters.

A. Integration of Microfluidic Capillaries

The proper placement of material-transporting capillary represents one of the key steps towards integrating them into the substrate of a microstrip patch antenna. Perturbational techniques, variational methods, and transmission line theory are valuable analytical tools in this effort as they provide valuable physical insight in this process and conceptual guidance towards the placement of these microfluidic channels. The microstrip patch example utilizes these techniques by examining the electromagnetic field structure provided by its associated cavity model [12] and the effects of a generic material perturbation within a cavity – general form shown in Equation 6. Without calculation it can be seen that a decrease in the patch's resonant frequency can be expected (the net result for any materials perturbation in a cavity) – which results in a frequency reconfigurable antenna. To this end, it can also be inferred that different magnetodielectric material perturbations within the cavity will have a greater effect when (1) placing a vertically orientated, primarily dielectric colloidal material at the radiating edges – where the electric field is greatest and (2) placing a horizontally orientated, primarily magnetic material (coincident to the width) located at the center – where the magnetic field is the strongest.

In conjunction with the cavity model, the transmission line model provides the next stage of design-level insight into the placement of these capillaries and alludes to several location and material constraints for the microfluidic elements. The first of these constraints comes about through the desire to avoid (for now) interfering with the radiation mechanism, such that placing a higher dielectric material at the edges of the patch (where it will be most visible to the electric fields) will reactively load the radiating slots. This infers that a magnetic material should be used at the center of the patch (where the magnetic fields are highest).

These next of these constraints comes by examining the phase-length symmetry about the feed location in the transmission line model that must be maintained throughout reconfiguration (e.g., increasing the effective permeability of the *ETF* by increasing the volume fraction of colloidal materials) to maintain an appreciable impedance bandwidth and resonance. This constraint leads to the

placement of a second embedded capillary structure carrying magnetic material, such that two capillaries must be present to maintain symmetry – one on either side of the feed location (in the length direction). Figure 2 shows the transmission line model used to examine the effects of two embedded capillaries filled with magnetic materials. To obtain an intuitive understanding the structure's resonant behavior, this work considers the effect of the colloidal magnetodielectric material that flows through the substrate as (1) a scaled impedance Z_m proportional to the particle-free microstrip patch impedance Z_p ($Z_m \sim Z_p \sqrt{\mu_r/\epsilon_r}$)

and (2) similarly the TEM propagation velocity $\gamma_m \sim \gamma_p (\epsilon_r \mu_r)^{1/2}$ – effectively raising the impedance and increasing the propagation constant (both of which are considered complex to account for the finite conductivity of the material systems). The geometry of the capillary for this conceptual component has not been considered in this model and it has been assumed that the mixing rules can be assumed to provide an accurate approximation to the associated sections of substrate (analogous to some of the structures in [13]).

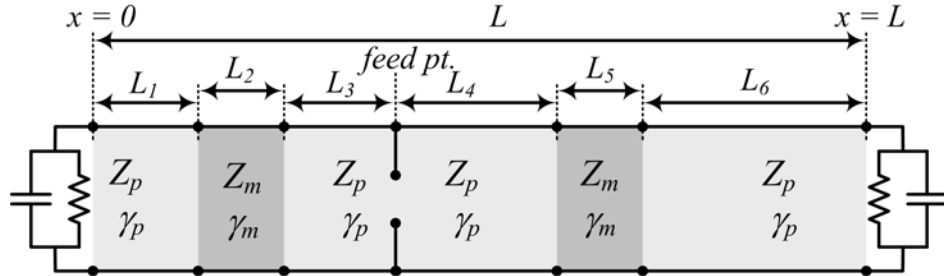


Figure 2. Transmission line model of the linearly polarized patch antenna with magnetodielectric materials altering the homogeneous electrical properties.

Several statements can also be made about the radiation behavior of the antenna throughout the range of reconfiguration by examining both the cavity and transmission line models of the patch. These are a result of the earlier constraint that avoids altering the (radiating) slot parameters (radiation conductance and capacitive reactance from fringing fields), the fixed physical length between the slots, and the effective increase in the phase length between the slots. Given the expected downward shift in impedance bandwidth and resonant frequency, this implies that the overall directivity and gain of the structure will decrease slightly due to the reduced electrical distance between the slots as the antenna experiences a decrease in its resonant frequency. This decrease in directivity will be accompanied by a broadening of the beamwidth.

B. Example: A Frequency Reconfigurable Patch Antenna

The transmission line model can then be translated into the detailed physical layout for the patch antenna on a substrate (material properties denoted by the subscript “ rp ”) and embedded microfluidic capillaries carrying magnetodielectric colloids dispersed in a fluid (material properties denoted by the subscript “ rf ”). Figure 3 shows the CAD model of this structure. If these structures are electrically small, the effective of these sections can be approximated to resemble the transmission line model by utilizing the mixing rules applied to approximate the length-wise cross-section section of substrate with an embedded capillary as a homogeneous material (properties denoted by the subscript “ rm ”). This represents a two-fold use of a mixing rule – once for the colloidal dispersion and one for the substrate – and illustrates the importance of including these into the overall analysis and design process.

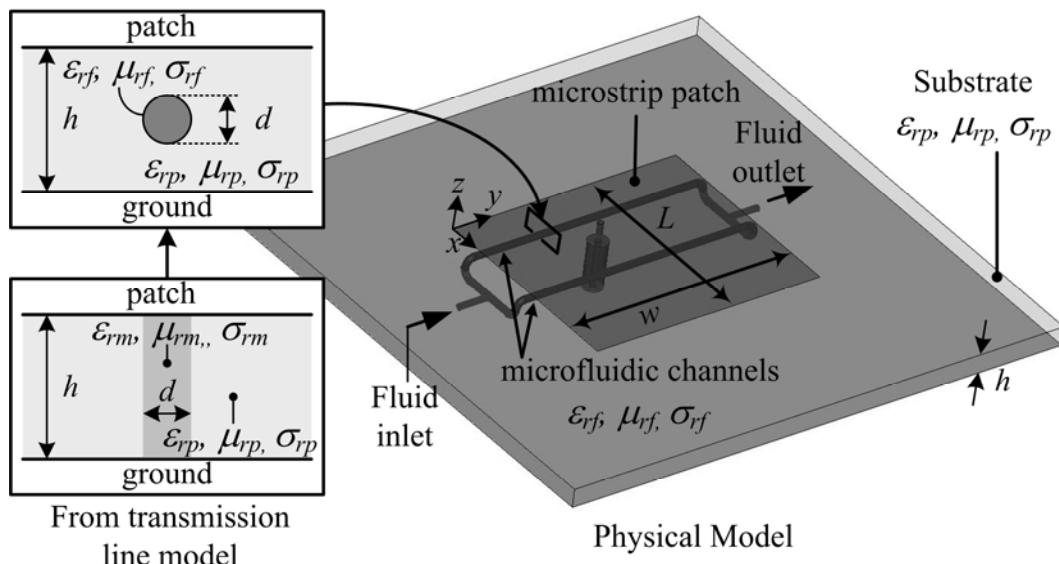


Figure 3. CAD Model of the microstrip patch antenna with capillaries embedded in the substrate material, including the transformation between the physical structure and the transmission line model

1. Simulated Antenna

An HFSS model has been constructed from the CAD model shown in Figure 3 for a 3 GHz patch antenna with length $L = 43.5$ mm and width $W = 50$ mm residing on a Rochelle foam (air) substrate ($\epsilon_{rp} = 1$, $\mu_{rp} = 1$, $\sigma_{rp} = 0$ S/m) of height $h = 4$

mm. The capillaries are used to carry a colloidal ferrite material [13] ($\epsilon_{rp} = 12$, $\mu_{rp} = 1000$, $\sigma_{rp} = 0.01$ S/m) suspended in low-loss silicon oil ($\epsilon_{rp} = 2.4$, $\mu_{rp} = 1$, $\sigma_{rp} = 10^{-13}$ S/m) with a diameter $d = 1.5$ mm. The effective material properties of the colloidal suspension and the resulting substrate sections have been calculated and are shown in the Table 1 for a volume fraction up to $\vartheta = 0.1$, or 10% of the total volume in the capillary occupied by colloidal material.

Table 1. Effective material properties of the capillary and substrate section.

ϑ	Mixture			Substrate Section		
	ϵ_{rf}	μ_{rf}	σ_{rf}	ϵ_{rm}	μ_{rm}	σ_{rm}
0.00	2.42	1	1×10^{-13}	1.53	1	1×10^{-13}
0.025	2.66	25.98	2.5×10^{-4}	1.62	10.37	9.38×10^{-5}
0.05	2.90	50.95	5×10^{-4}	1.71	19.35	1.88×10^{-4}
0.075	3.14	75.93	7.5×10^{-4}	1.80	29.10	2.81×10^{-4}
0.10	3.38	100.9	1×10^{-3}	1.89	38.46	3.75×10^{-4}

Figures 4 and 5 show the simulated VSWR and radiation patterns for the structure in Figure 3 using the calculated (mixed) capillary material properties. The effect on VSWR agrees with earlier statements by demonstrating a decreasing impedance bandwidth, down from 3.0 GHz to 1.92 GHz – hence, increasing the concentration of colloidal magnetic particles in the capillary results in a decrease in the impedance bandwidth and percent bandwidth equivalently. The effects on radiation behavior demonstrated thought these exercises are also in agreement with earlier statements. Figure 5 shows the co-polar and cross-polar radiation patterns in the two primary elevation planes, with the length direction of the patch (and in the direction slot beamforming). At 3 GHz (when $\vartheta = 0.00$) the radiating slots are physically separated by just less than half wavelength due to the air dielectric – a null from the array factor in this direction – which accounts for the decreased Co-Polar gain (E_θ) in the endfire direction when there are no magnetic particles present. The overall presence of asymmetry in the structure to maintain the impedance bandwidth (e.g., using two capillaries) slightly steers this null from the direction of the slot closest to the edge. As the concentration of magnetic particles increases the impedance bandwidth decreases and the physical separation between the two radiating slots decreases and the null becomes less prevalent and the directivity decreases – shown for a 30 dB dynamic range, and normalized to the maximum gain when $\vartheta = 0.00$ (3 GHz) in Figure 5.

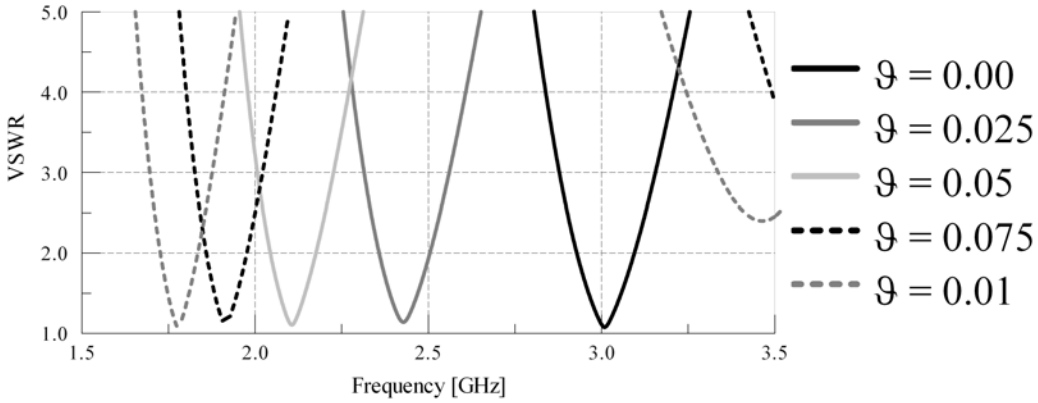


Figure 4. Simulated VSWR for the physical structure shown in Figure 3, demonstrating the downward shift in impedance bandwidth as the permeability (or concentration of magnetic material) is increased.

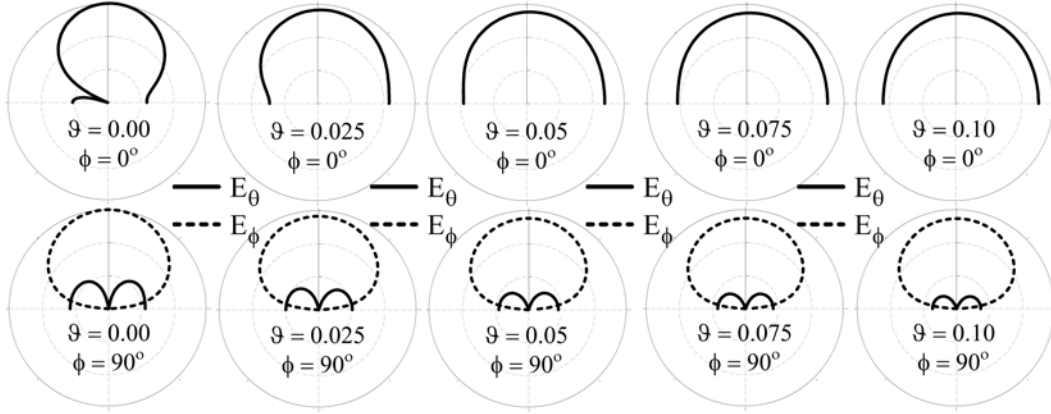


Figure 5. Simulated radiation patterns (both polarizations in the two principle elevation planes) for the physical structure shown in Figure 3.

2. Measured Antenna

An experimental model of a patch antenna with substrate-embedded capillaries holding varying concentrations of magnetodielectric materials was fabricated according to the dimensions of the transmission line model (e.g., same as the CAD model) in Figure 3. Solder-tacked strips of electrical tape were used to form the SMA probe-fed patch structure, and two very thin walled plastic tubes (diameter $d = 2\text{mm}$) were representative of the microfluidic capillaries. The patch structure Figure 6 shows the antenna and measured VSWR. Strontium Hexaferrite ($\text{Sr}_4\text{Fe}_4\text{O}_{11}$) powder with a particle diameter d ranging from $\sim 2\ \mu\text{m}$ to $2000\ \mu\text{m}$, – which are not purely geometrically colloidal (spherical) – was used as

the magnetodielectric material (the exact material properties over the frequency range of interest were not available at the time of this experiment). Silicon oil was used as the dispersant. The results of the experiment show that the expected trends in VSWR were obtained. The radiation patterns were not measured at the time of this manuscript but are currently being examined, and are expected to follow the trends from calculated and HFSS simulations.

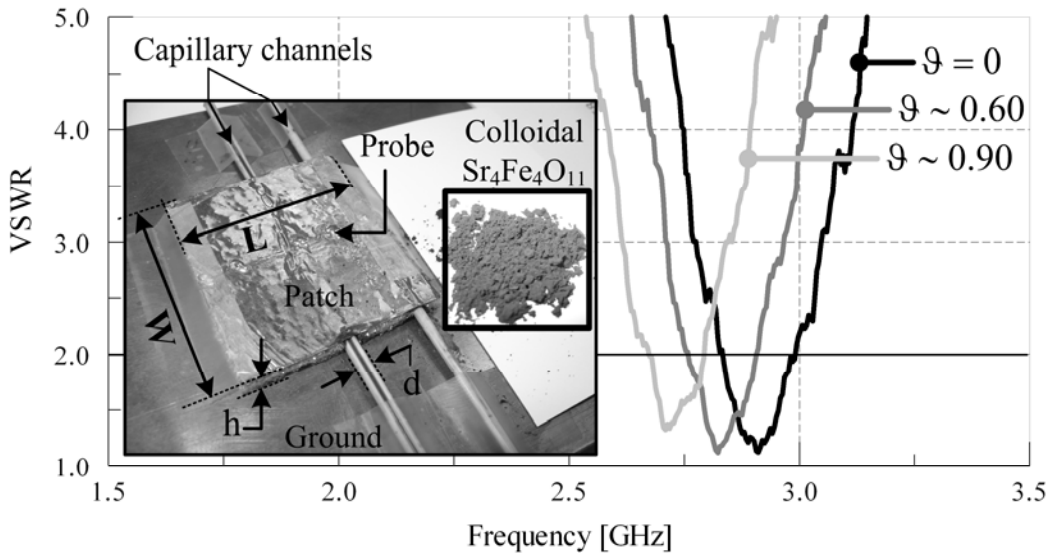


Figure 6. Measured VSWR for the experimental microstrip patch with substrate-embedded capillary structures demonstrating the downward shift in impedance bandwidth as the permeability (or concentration of magnetic material) is increased.

IV. N-port Microfluidic Reconfiguration Mechanisms for Impedance Control

A. COaxial Stub Microfluidic Impedance X-former (COSMIX)

In addition to providing the ability to characterize the fluid-based material systems (one of the methods currently being used in this work), the coaxial structure can be used very effectively as a 1-port reactive impedance control device. Figure 7 shows a particularly useful embodiment of said microfluidic technologies – the COaxial Stub Microfluidic Impedance X-former (transformer) (*COSMIX*), its transmission line model, and the simulated results (HFSS) for a nominal design. The device works on the principle that the dynamic material properties (homogeneous permittivity and permeability) can be used within the geometry – a reflect-line configuration shown here – to reconfigure the electrical length (phase velocity) and characteristic impedance (wave impedance). In

conjunction with the capacitive reactance formed by the open circuit stub (reactance approximated by Equation 6 from [15]), this dictates the reactive input impedance and facilitates control of the structure.

$$\frac{B}{Y_0} \sim \frac{4b\sqrt{\epsilon_r\mu_r}}{\lambda} \ln \frac{a}{b} \left(\frac{\pi b}{4d} + \ln \frac{a-b}{d} \right) \quad (5)$$

The simulated results shown are for a design operating at a frequency $f = 1$ GHz, with a length $L = 5$ mm (only 1% of a free-space wavelength), gap $d = 0.1$ mm, outer/inner diameter $2a/2b = 0.25$ mm/0.05 mm. The heterogeneous material properties represent a modest range of material properties ($\epsilon_r = 1$, $1 \leq \mu_r \leq 80$ and $\epsilon_r = 10$, $1 \leq \mu_r \leq 80$) and demonstrate potential for mixing and varying the concentration of different materials. The key result from this example resides in the ability to (1) calibrate the effects of microfluidic networks, and (2) alter the reactive impedance from capacitive to inductive – thus, the ability to make a full trip around the Smith chart and provide a reactive impedance at any point along the way.

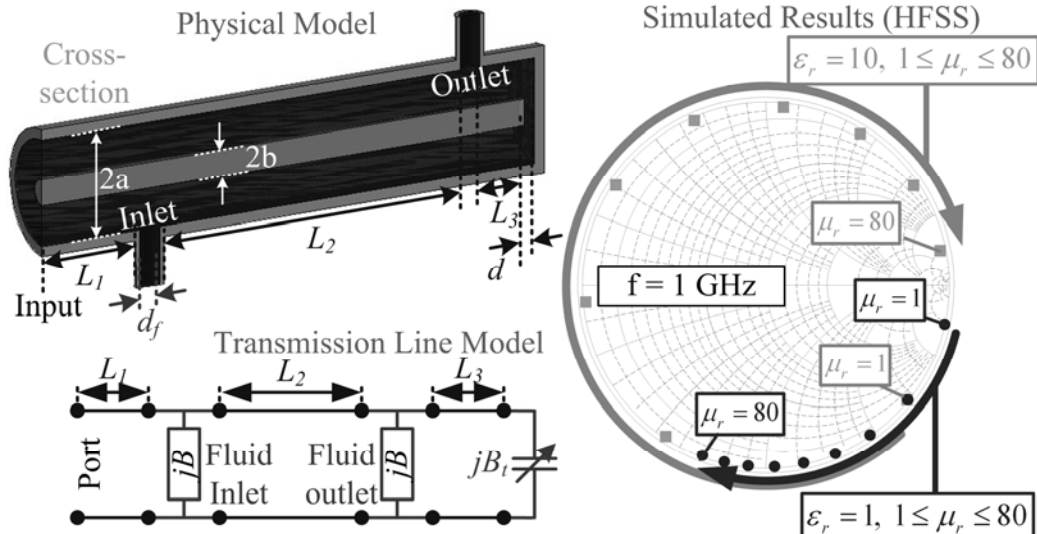


Figure 7. Simulated COSMIX device using material properties $\epsilon_r = 1$, $1 \leq \mu_r \leq 80$ and $\epsilon_r = 10$, $1 \leq \mu_r \leq 80$ to demonstrate the potential of mixing and varying the concentration of different materials

An experimental, preliminary version of the *COSMIX* has been developed to examine a candidate material system and verify the trends in simulated data. The measured results shown are for a design operating at a frequency $f = 1$ GHz, with

a length $L = 15$ mm, gap $s = 2.5$ mm, inner/outer diameter $2a/2b = 2.1$ mm/0.615 mm. These dimensions are a scaled version of the simulated structure (to accommodate available SMA probe dimensions available at the time of this experiment). This example uses air (e.g., the absence of materials), Teflon ($\epsilon_r = 2.1$), Ethyl Alcohol (ETOH) ($\epsilon_r \sim 30$), and ETOH with super-paramagnetic Nickel-Iron (NiFe) colloidal particles (the exact permeability was not fully known before these measurements). The impedance difference between the latter two appears small, but verifies dielectric mixing rules – as NiFe is introduced into the mixture, the losses are reduced (e.g. closer to the perimeter of the Smith Chart), and the addition of magnetic material increases the phase and impedance. The result (in total) shows the ability of the device to transform a very capacitive reactance (air) into a nominally inductive reactance (ETOH w/ NiFe).

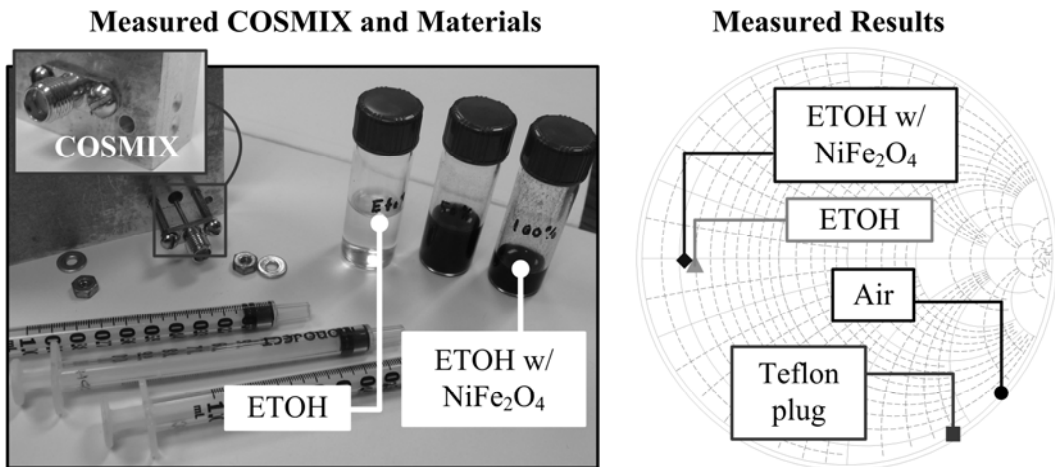


Figure 8. Measured COSMIX device using, Teflon ($\epsilon_r = 2.1$), Ethyl Alcohol (ETOH) ($\epsilon_r \sim 30$), and ETOH with super-paramagnetic Nickel-Iron (NiFe) colloidal particles

B. Dipolar Chain Rheostat

The final example of microfluidic impedance control focuses on the microstructure and AC electrical properties of metal colloids in a coplanar, gold film electrode. This has been used to demonstrate the ability to control the impedance characteristics within a microfluidic/electronic device via electric field mediated assembly of various colloidal microstructures. The reversible, fluid nature of such colloidal based devices exhibits unique impedance responses and tunability not easily achieved with solid-state materials or microelectromechanical devices in terms of the applied voltages used to achieve these properties and the potential for other material-based systems. A detailed discussion of the physical

mechanisms responsible for this behavior has been provided in [6], and has been omitted for brevity.

The experimental arrangement and results shown in Figures 9 and 10 (respectively) consists of nominal 800 nm diameter gold colloids that are electrostatically levitated above lithographically patterned gold film electrodes on glass microscope slides. The gold electrodes are 50 nm thick in an interdigitated configuration with 30 μm lateral spacing between the interdigitated fingers. The gold colloids were dispersed in aqueous 0.1 mM NaHCO₃ with a conductivity of 9 $\mu\text{S}/\text{cm}$. The gold colloids are confined within a thin, quasi-twodimensional quasi-2D layer near the surface due to gravity and particle-surface electrostatic repulsion. A function generator and impedance analyzer are connected in series to the patterned electrodes to tune colloidal assembly and acquire an impedance spectra up to 1 MHz, and the steady-state colloidal configurations for the different field conditions shown in Figure 10.

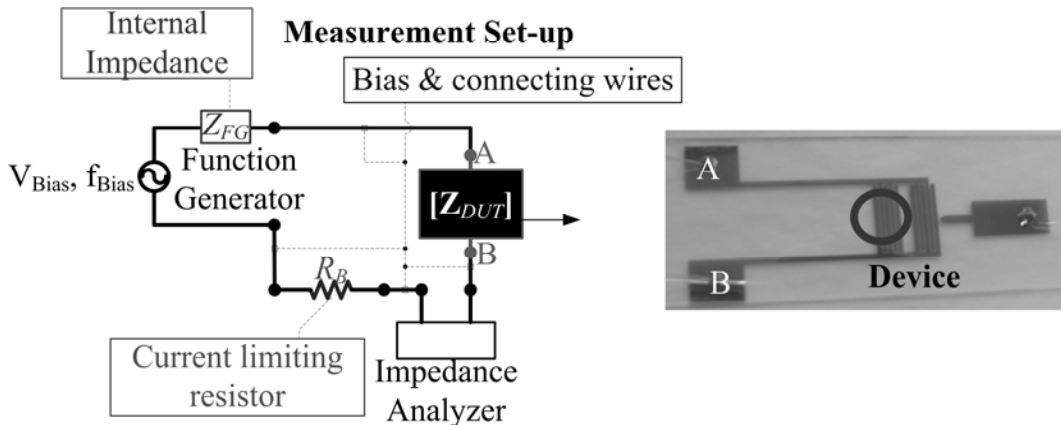


Figure 9. Measurement set-up and device used to examine the microstructure properties and electromagnetic impedance of colloidal gold microstructures.

In the absence of any applied fields, the gold colloids are randomly distributed parallel to the glass and electrode surfaces. In the presence of ac electric fields, Figure 10 shows a matrix of steady-state microstructures assembled in between and above a single electrode pair gap as a function of ac voltage from 0.5–2.5 V and frequency $\omega = 10 \text{ Hz} - 1 \text{ MHz}$. All colloidal microstructures in Figure 10 are reversibly assembled. The observed structures in Figure 10 and their transient assembly can be explained in terms of a competition between sedimentation, self-diffusion, and several ac electric field mediated transport mechanisms including electrophoresis EP , ac electro-osmosis EO , and dielectrophoresis DP .In all cases, sedimentation concentrates particles onto the interdigitated electrode

surface, and Brownian motion tends to produce laterally homogeneous, random configurations.

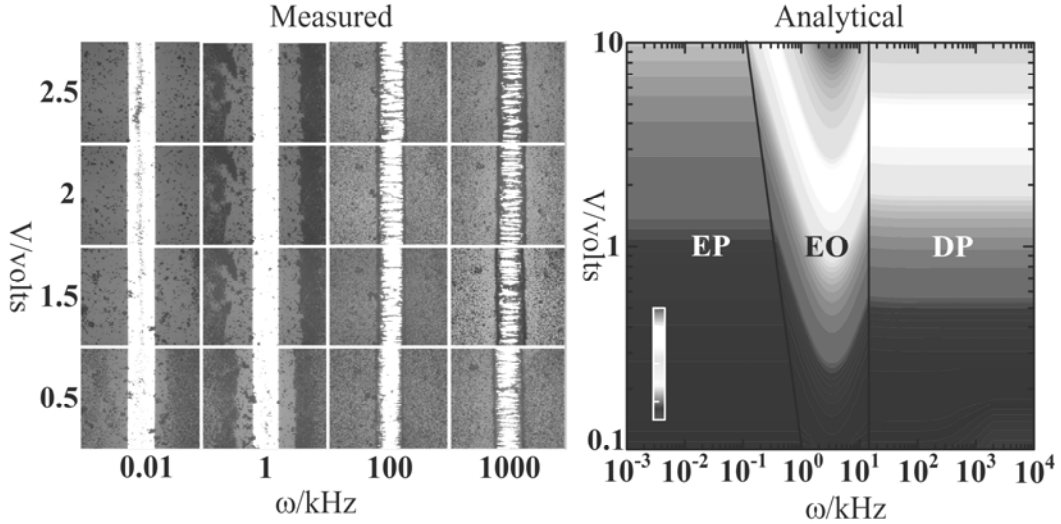


Figure 10. Measured and modeled results for the device shown in Figure 9.

The results in Figure 10 can be organized based on three distinct steady-state microstructures that emerge based primarily on ac field frequency regimes and to a lesser extent on ac field amplitude. For $\omega = 1\text{--}100 \text{ Hz}$, colloids track the ac field and centrally oscillate within a band in the electrode gap, whereas colloids above the electrodes experience lateral aggregation. For $\omega = 1\text{--}100 \text{ kHz}$, colloids are expelled from the electrode gap and concentrate on top of the electrodes with a depleted zone near the electrode edges. For $\omega > 100 \text{ kHz}$, colloids assemble into chains bridging the electrodes and align with the expected field lines in the gap. For all cases in Figure 10, greater ac field amplitudes in each frequency regime do not appreciably alter the microstructure type but primarily enhance the assembly rate and the structural fidelity.

By understanding ac field mediated microstructure types and dominant transport mechanisms in Figure 10, it is possible to interpret the measured impedance spectra in Figure 11 for colloids in the presence 2.5 V , $\omega = 1 \text{ MHz}$ and absence (0 V , $\omega = 0 \text{ Hz}$) of an applied ac electric fields. As shown in the insets of Figure 11, equivalent circuits were used to model the measured impedance spectra. Systematic control measurements were used to independently determine the contributions of the substrate, electrodes, electrolyte solution, measurement system, function generator, and different colloidal configurations so that no adjustable parameters were required to specify equivalent circuit components. In

both cases in Figure 11, impedance spectra were reproduced at least five times and accurately modeled by equivalent circuits.

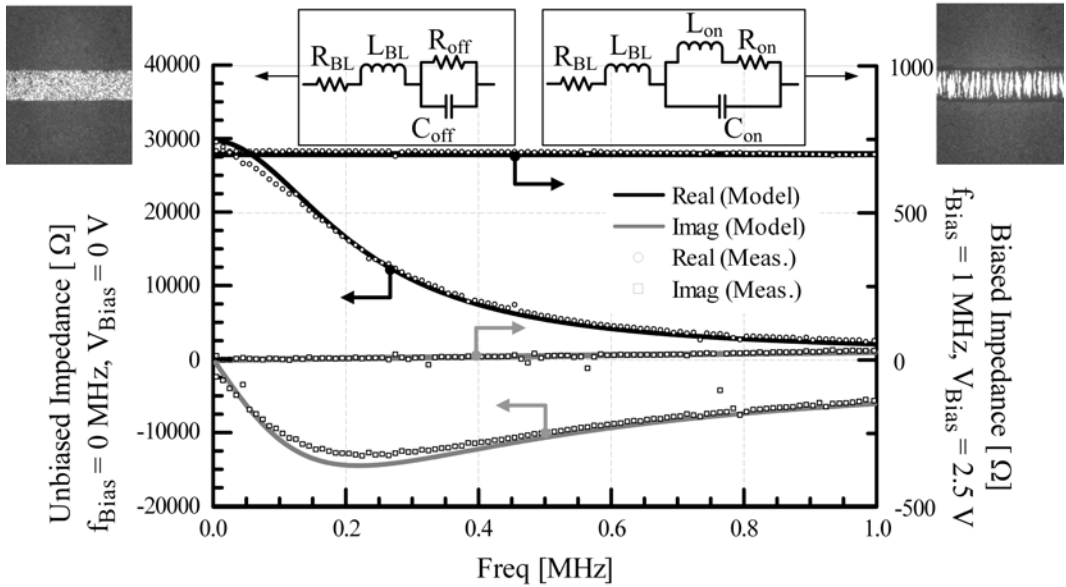


Figure 11. Measured impedance spectra for the device shown in Figure 9 in two states (biased and unbiased).

In control measurements, the micropatterned gold film electrodes in air and a current limiting resistor had a combined resistance of $R_{BL} = 700 \Omega$, the connecting wires had an inductance of $L_{BL} = 4.69 \mu\text{H}$, and the electrolyte media/ unassembled colloids had a resistance of $R_{off} = 29 \text{ k}\Omega$. The collective capacitance of the electrodes, aqueous media, and gold colloids with and without ac fields was $C_{on} = C_{off} = 25 \text{ pF}$. Without the application of an ac electric field, the corresponding impedance spectrum in Figure 11 is dominated by the properties of the static gold microelectrode arrangement, glass substrate, and aqueous electrolyte media. In the presence of an applied ac electric field of 2.5 V and $\omega = 1 \text{ MHz}$, the equivalent circuit components representing the device and aqueous media remain unchanged, but the assembled dipolar chains and electrolyte now produce a gap resistance of $R_{on} = 1.7 \Omega$ and an inductance of $L_{on} = 17 \text{ fH}$. With 20 parallel wires/100 μm from the image in Figure 10 and a 5 mm electrode interface, the resistance per wire is estimated to be 1.7 $\text{k}\Omega$. The cross sectional area per chain is not obvious given the bundling of many single chains via lateral dipolar chain attraction. In any case, the electrostatic repulsion due to overlapping electrical double layers plays a vital role in preventing adhesive contacts while providing a path of low resistance that allows such chains to function as “dipolar chain rheostats.”

When colloids were flushed from the electrode gap via EO transport, the impedance response and equivalent circuit were essentially the same as in the unbiased device. For the dominant EP transport at low frequencies, concentrated bands of colloids within the electrode gap produced impedance spectra suggestive of an enhanced capacitive response that is consistent with the parallel electrode/colloid-band arrangement. However, instabilities in the impedance spectra probably require a different measurement configuration to handle large transients in these low frequency measurements. Although the microstructure formed via EP at low applied ac field frequencies needs to be better characterized, its apparent increased capacitance might be exploited as a sort of “electrophoretic varactor.”

V. Conclusions

This work has illustrated several of the ongoing efforts that utilize magnetodielectric colloidal materials in a microfluidic system to reconfigure antennas and tune other devices. The microstrip patch example demonstrates the ability to use these mechanisms for distributed, reactive impedance control. At the device level, the COSMIX devices and dipolar Chain Rheostat/Electrophoretic Varactor demonstrate the ability to create N-port mechanisms that can both reactively load a structure and provide switching capabilities. Future work will involve multi-scale modeling of these and other devices to create highly versatile reconfiguration mechanisms and uniquely integrated distributed impedance control in reconfigurable antennas and other tunable devices.

VI. Acknowledgements

The authors would like to thank Michael L. VanBlaricum and Thomas L. Larry from Toyon Research Corporation for their insightful discussions on this topic. The authors acknowledge financial support from DARPA (W911NF-06-1-0050 and FA9550-07-C-0002) for this work. In addition, the authors would like to thank Fermag Technologies, Inc. for supplying the Ferrite Powder #UHE (colloidal $\text{Sr}_4\text{Fe}_4\text{O}_{17}$) used in the microstrip patch experiments.

VII. References

- [1] Pozar D M 1993 A magnetically switchable ferrite radome for printed antennas IEEE Microwave Guided Wave Lett. 3 67–9.

- [2] S. Mikuteit, H. T. Buscher, R. M. McIntyre, "An Artificial Dielectric Liquid Phase Shifter," 2nd European Microwave Conference, vol. 2, October 1971, pp. 1 – 4.
- [3] H. T. Buscher, R. M. McIntyre, and S. Mikuteit, "Variable-Permittivity Artificial Dielectrics," GMTT International Microwave Symposium Digest, vol. 71, May 1971, pp. 192 – 194.
- [4] Y. Kosta, and S. Kosta, "Liquid antenna systems," in proc. IEEE Antennas and Propagation Society International Symposium, vol. 3, June 2004, pp. 2392 – 2395.
- [5] H. T. Buscher, "Electrically Controllable Liquid Artificial Dielectric Media," IEEE Transactions on Microwave Theory and Techniques, vol. 27, pp. 540 – 545, May 1979.
- [6] P. Bahukudumbi, W. N. Everett, A. Beskok, M. A. Bevan, G. H. Huff, D. Lagoudas, and Z. Ounaies, "Colloidal microstructures, transport, and impedance properties within interfacial microelectrodes," *Applied Physics Letters*, vol. 90, 224102, May 2007.
- [7] G. H. Huff, P. Bahukudumbi, W. N. Everett, A. Beskok, M. A. Bevan, D. Lagoudas, and Z. Ounaies, "Electromagnetically Tunable Fluids for Microfluidic Reconfiguration of Antennas," in proc. 2007 URSI North American Radio Science Meeting, Ottawa, ON, Canada, July 2007.
- [8] A. H. Sihvola, "Self-consistency aspects of dielectric mixing theories," *Geoscience and Remote Sensing, IEEE Transactions on*, vol. 27, pp. 403-415, 1989.
- [9] A. H. Sihvola and E. Alanen, "Studies of mixing formulae in the complex plane," *Geoscience and Remote Sensing, IEEE Transactions on*, vol. 29, pp. 679-687, 1991.
- [10] A. H. Sihvola and E. Alanen, "Studies of mixing formulae in the complex plane," *Geoscience and Remote Sensing, IEEE Transactions on*, vol. 29, pp. 679-687, 1991.
- [11] A. H. Sihvola, "How strict are theoretical bounds for dielectric properties of mixtures?," *Geoscience and Remote Sensing, IEEE Transactions on*, vol. 40, pp. 880-886, 2002.
- [12] Y. T. Lo, D. Solomon, and W. Richards, "Theory and experiment on microstrip antennas," *IEEE Transactions on Antennas and Propagation*, vol. 27, pp. 137 – 145, July 1979.
- [13] J. Fladie and J. T. Bernhard, "Analysis of sectioned substrate patch antennas utilizing a deterministic approach," in Proc. 2005 IEEE/URSI International Symposium on Antennas and Propagation, July 2005.
- [14] Ansoft, HFSS[®] v9.1, Pittsburgh, PA 15219.
- [15] N. Marcuvitz, *Waveguide Handbook*. New York, NY: McGraw-Hill Book Company, 1951.

NOVEL RECONFIGURABLE MULTI-BAND ANTENNAS FOR WIRELESS RECEIVERS

Songnan Yang¹, Helen K. Pan²,
Aly E. Fathy¹, Samir M. El-Ghazaly¹ and Vijay K. Nair²

¹EECS Department, University of Tennessee, Knoxville, TN 37996

²Intel Corporation, Hillsboro, OR 97124

Abstract — Combined reconfigurable and multi-band design concepts have been utilized to design antennas for mobile multi-radio platforms. Two concepts are introduced here; one is based on meandering branch-line monopoles for mobile handsets, and the other on planar inverted-F antennas (PIFA) for laptops applications. Both have unique structures to comply with space and service requirements, and are utilizing switches to provide two operating reconfigurable multi-band states. Each state is capable of covering specific service group to simplify service switching, and minimize out-of-band input noise.

1. INTRODUCTION

Multi-band antennas are widely used for many multi-radio platforms, where either one service could have multiple standards utilized at different countries, or many services need to be simultaneously supported at the same country, but should be received through the same antenna. Reconfigurable antennas, on the other hand, are designed to switch to a desired service and to be solely dedicated to one service to achieve maximum out-of-band noise rejection performance. As the number of services increases, the development of either of these antennas becomes more and more challenging due to the fundamental limitations of the achievable bandwidth for a certain given volume for the former, while for the latter, its design becomes more complicated and suffer from high loss and unacceptable DC power consumption when using multiple switching devices.

We propose here two novel hybrid reconfigurable multi-band antenna structures that are based on these two concepts. In other words, reconfiguring the multi-band antenna, where multitudes of switching devices are used to hop between several multi-band configurations. Through judicious grouping of frequency bands for each configuration, advantages of both the multi-band and the reconfigurable antenna structures can be simultaneously achieved while supporting more services.

Our developed design for handsets is comprised of a compact reconfigurable meandered monopole antenna, and covers almost all WWAN and WLAN standards with only two configurations, one serving all the cellular bands and the other covering all wireless frequencies. Similarly for laptops, alike concept is realized by a novel

reconfigurable multi-band PIFA structure, which supports all US cellular and indoor WLAN frequencies. Both these designs have been optimized to minimize the number of switches, where only two are required. The multi-band construction strategy, switch integration schemes, and simulated and measured results of these novel designs will be presented here in detail.

2. RECONFIGURABLE MULTI-BAND ANTENNA DESIGN

2.1. Frequency Band Grouping

In order to support the required wireless services for different mobile multi-radio platforms listed in Table 1, the frequency bands need to be strategically grouped to minimize the number of switchable configurations while still covering the required services. The guidelines for this selective grouping include:

- 1). Different standards of the same services can be grouped together, since only one frequency band will only be used at a certain time in a certain country. For instance, the GSM850 and GSM900 bands can be grouped into one configuration.
- 2). Different services with close frequency bands need to be allocated at different configurations to improve out-of-band noise rejection. For example, 2.4GHz WLAN services need to be separated from the cellular ones that are around 2GHz (PCS/DCS/IMT2000) to avoid their interference and simplify out-of-band noise filtering.

According to our grouping criterions, the required services are separated into two distinct application groups as shown in Table 1. For instance, in the handset case, all cellular services including GSM850, GSM900, DCS, PCS, and IMT2000 (WCDMA/HSDPA) frequency bands are grouped together and classified as WWAN configuration. On the other hand, all internet services including 802.11.a, b, g, and n are consolidated in the other configuration, which is utilized for WLAN services. For each configuration, a multi-band antenna is required. It is given here that any two services from these grouped configurations will not be required to operate at the same time. Similar grouping is applied for laptop antennas with fewer services supported.

2.2. Concept I: Meandered Monopoles for Mobile Handset

Basic antenna structures need to be selected according to the form factor of the designated mobile platform. For mobile handsets, antennas are always placed at either end of the handset and its size is limited by the width of PCB. Therefore meandered monopole antennas are suitable for mobile handset applications for its compact size and ease of reconfiguring the resonance frequency by altering its length. For each configuration, a multi-band response can be achieved by having two meandered branches

TABLE I
FREQUENCY GROUPING OF HANDSET AND LAPTOP ANTENNA CONFIGURATIONS

Unit: GHz		WWAN Configuration				WLAN Configuration		
Grouped Bands	Handset	0.824-0.96 (15%)		1.71-2.17 (23.7%)		(3.5%)	4.9-5.85 (16.8%)	
	Laptop	(8.3%)	N/A	(7.3%)	N/A	(3.5%)	4.9-5.35 (8.8%)	N/A
Service	GSM850	GSM900	DCS	PCS	IMT2000	802.11 b/g/n	802.11 a	
Frequency	0.82-0.89	0.88-0.96	1.71-1.88	1.85-1.99	1.92-2.17	2.4-2.48	4.9-5.25	5.15-5.35
Country	U.S.	Europe/Asia		U.S.	Universal	Japan/ U.S. Indoor	Outdoor	

resonating at the lower and upper bands respectively. As shown in Fig.1 (highlighted parts are metal). The developed antenna consists of two bent monopoles branches with different length. Two switches are utilized, one in each branch to control the physical length of the monopole. According to the previous grouping, when both switches are turned on (the gaps in the monopoles are hard-wired), the antenna works at the WWAN configuration, receiving the lower frequency cellular services. When switches are off (as shown in Fig. 1), the antenna operates in the WLAN configuration. Since a shorter length is utilized, it would result in higher resonant frequencies.

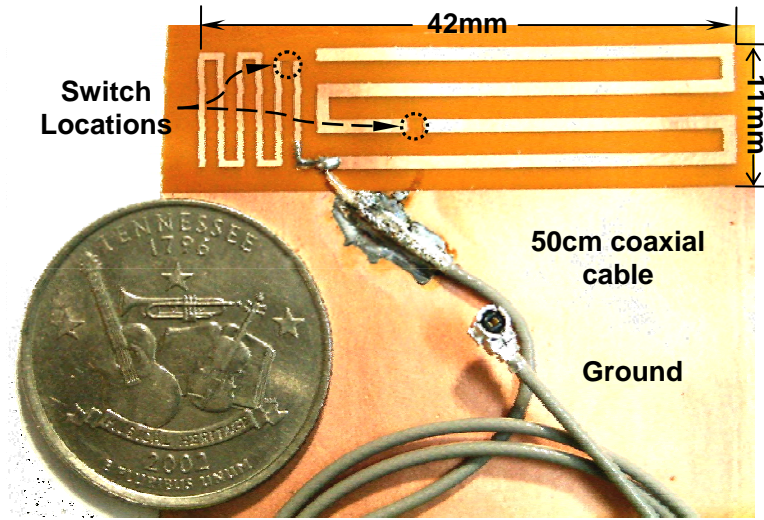
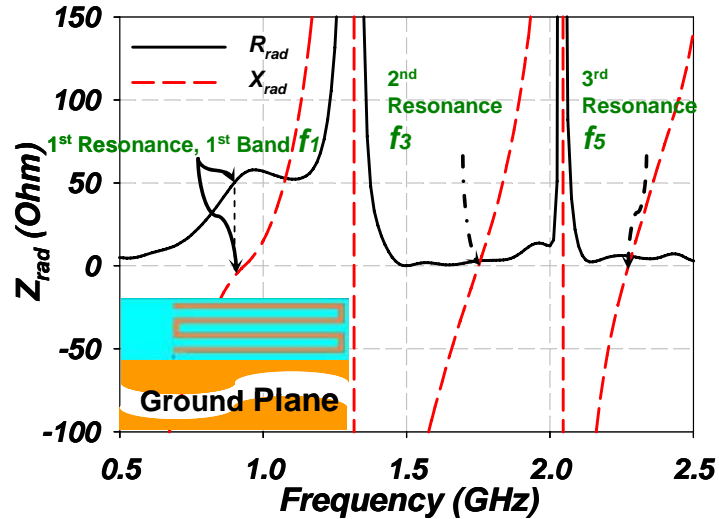


Fig. 1. Fabricated reconfigurable meandered monopole antenna

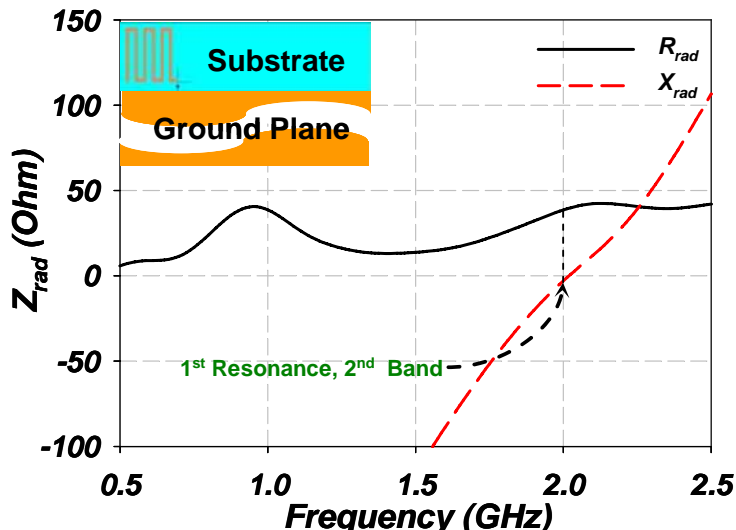
The major challenge of this proposed frequency grouping is its relatively wide bandwidth requirements, especially for the higher band (DCS/PCS/IMT2000) in the WWAN configuration, where a 23.7% bandwidth is required. In our design, we have extended the branch line monopole antennas described by [1] to cover all five cellular bands by utilizing the monopoles higher order resonances.

We started with a straight monopole main branch covering the GSM850 and GSM900 bands with a length of $0.25 \lambda_1$ at $f_1 = 892$ MHz. It also has a third order resonance at $f_3 = 3f_1$ and fifth order resonance at $f_5 = 5f_1$. The structure is meandered to be compact. Because of the coupling between the meandered lines, the total length needs to be extended to maintain the same f_0 . However, due to weaker coupling effects at higher frequencies, the third and fifth order resonances are significantly shifted lower when the total length is increased. As shown in Fig. 2 (a), we can control the number of turns and the spacing of the meander line to alter the coupling factor such that with the same fundamental resonance ($f_1 = 892$ MHz) the higher WWAN band lies between the third and fifth resonances, that is $f_3 < 1.71\text{GHz} < 2.17\text{GHz} < f_5$. Then a second meandered monopole with a fundamental resonance within the higher WWAN band is constructed.

The meandering orientations of those two monopoles are orthogonal to each other to reduce their coupling, such that each branch can be designed separately. In the final step, these two branches are placed together in shunt, where the fast varying radiation impedance of the main branch is compensated by the slow varying counterpart of the second branch as shown in Fig. 2 (b). The overall radiation impedance is depicted in Fig.2 (c), where a much wider impedance bandwidth is achieved by combining these two branches in shunt. More importantly, the third and fifth order resonances of the main branch provides strong cut offs of the return loss response at the higher WWAN bands. This filter-like response will help reducing the requirements of subsequent front-end filtering stages. Similarly, two switches can be strategically placed along the two branches to shorten their lengths and reconfigure them to operate at higher frequencies, i.e. providing a multi-band configuration to serve the WLAN bands.



(a)



(b)

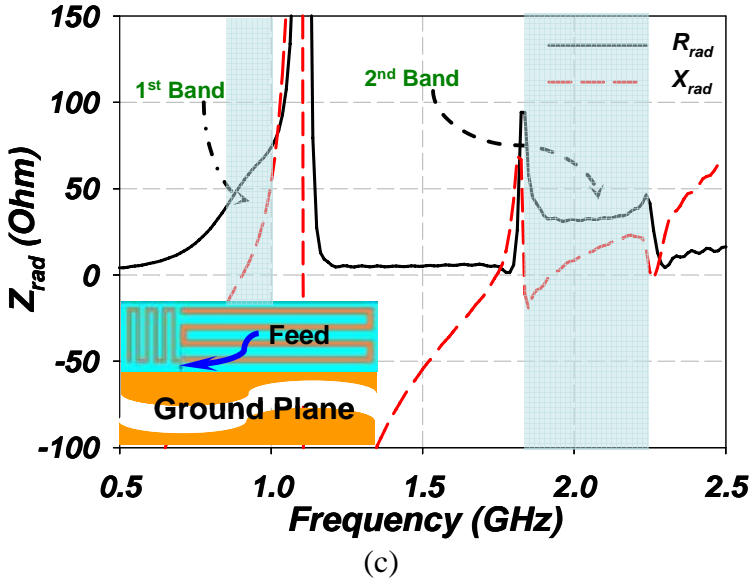


Fig.2. Simulated radiation resistance of independent branches, (a) main longer branch, (b) shorter branch, (c) two branches in shunt.

2.3. Concept II: Twin PIFA Antennas for Laptops

Monopole antennas are generally not suitable for laptop applications since when placed close to a large ground plane (e.g. laptop lids) they exhibit very low radiation resistances. Meanwhile, PIFA antennas could achieve a good match to 50Ohm feeds even if they are placed only few millimeters from the ground plane. However, due to the fundamental limitations of the achievable bandwidth, a tradeoff is required between the height of the antennas (i.e. width of LCD rims) and the number of services supported. As a result, service coverage is usually compromised to support only local standards, where in our laptop antenna design, four essential services for laptop application including GSM850, PCS WWAN services and 2.4GHz and 5GHz indoor WLAN services are selected as listed in Table.1. Using the same frequency grouping, two WWAN frequencies are supported by one configuration while the WLAN standards by another.

In our design, two PIFA structures are placed back to back sharing the same feed point (Fig. 3(a)). Two switches are used to switch the shorting pin location in order to toggle between the WWAN and WLAN configurations. As shown in Fig. 3(b), when switch1 is “ON” and switch2 is “OFF”, it forms a dual band PIFA structure [2] operating at the WWAN mode. The length of the top inverted-F structure is about $0.25\lambda_0$ of $f_0 = 859\text{GHz}$ and it covers the GSM850 band. Beneath the “F” structure, a grounded “L” shaped structure is also placed close to the feed. This parasitic element can be tuned to resonate at a higher frequency, in our case, PCS band. Similarly, when switch1 is “OFF” and switch2 is “ON”, the “F” and “L” shaped structures of the WWAN configuration is shorted to form a shorting pin for another pair of “F” and “L” antennas designed to cover

the WLAN frequencies (as shown in Fig. 3(c)). A wedge shape is used instead of the “L” in the fabricated design (as shown in Fig.4.) to extend the bandwidth of parasitic element.

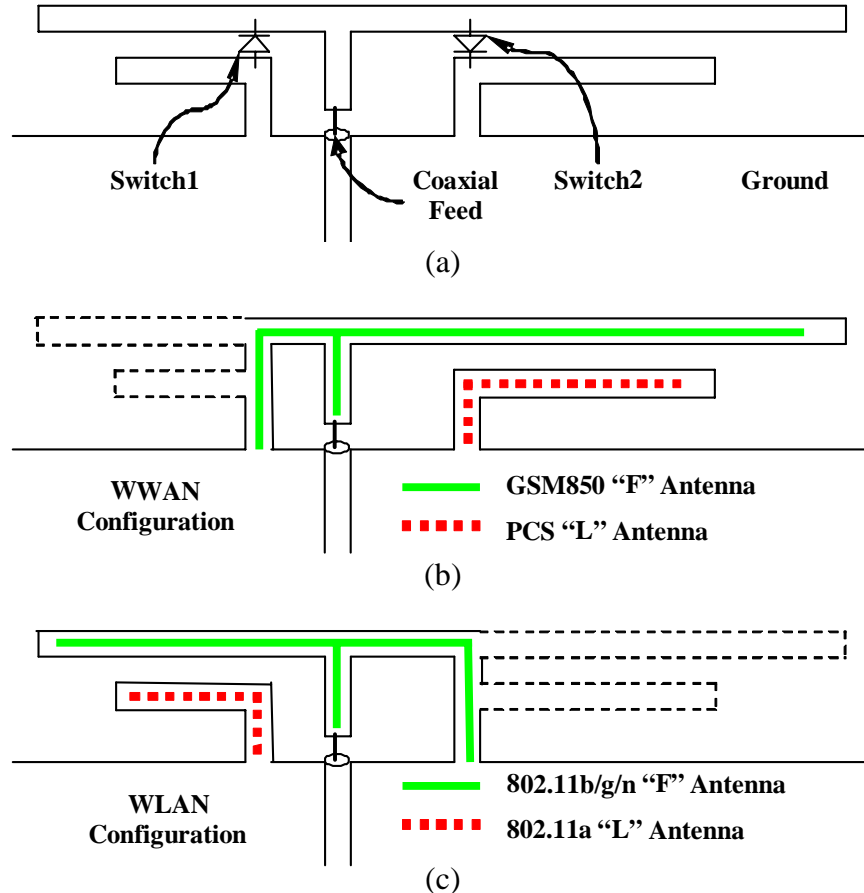


Fig.3. (a) Twin PIFA reconfigurable antenna with P-I-N diode switches, (b) WWAN Configurations, (b) WLAN Configuration

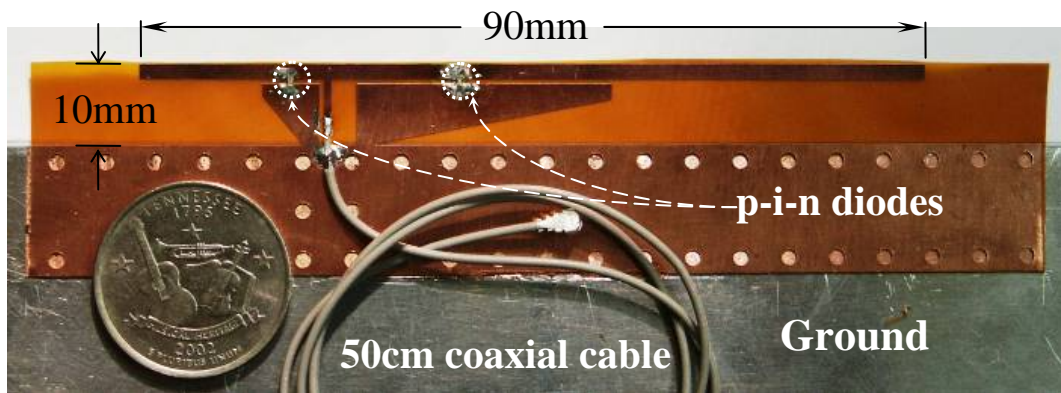


Fig. 4. Fabricated reconfigurable twin-PIFA antenna for laptops

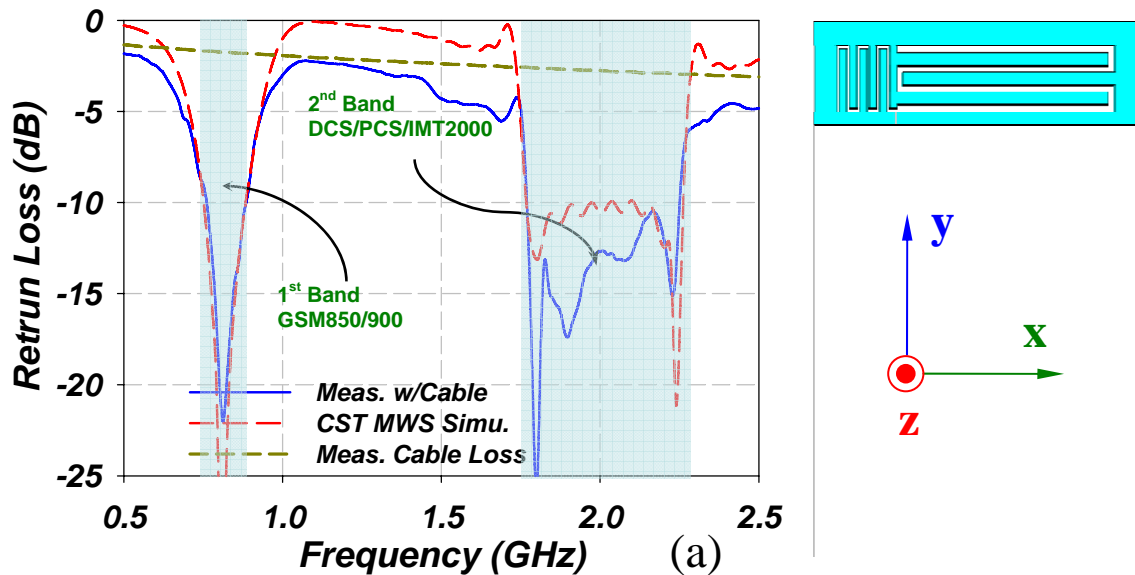
A novel switch integration and DC feed scheme is implemented to the twin-PIFA antenna, where only two PIN diode switches are required. As shown in Fig.4, the two switches are strategically placed across the gap between the two “F” and “L” shape pairs with opposite orientations. The control voltage signal is carried by the feeding coaxial cable and applied between the feed and ground. Since the two “L” shapes provides a return path for DC current, no additional control lines are required. Each switch can be addressed individually by reversing the polarity of the DC signal, which toggles the operating configuration. This approach completely eliminates the DC feed lines and their parasitic effects to the antenna structures.

3. MEASURED RESULTS

For validating our concepts, both antennas are fabricated on DuPont Kapton flexible circuit material, as indicated in Fig.1 and Fig.4. The hard-wired version of the meandered monopole is used for measurements while the twin-PIFA structure is fully integrated with p-i-n diode switches.

3.1. Meandered Monopoles for Mobile Handset

The simulated and measured return losses of the reconfigurable meandered monopole antenna in WWAN and WLAN configurations are shown in Fig.5 and Fig.6 respectively, where excellent agreements are achieved. Their radiation patterns are measured at the center of each frequency-band, and the summary of the measured results of the primary cuts is given in Table 2.



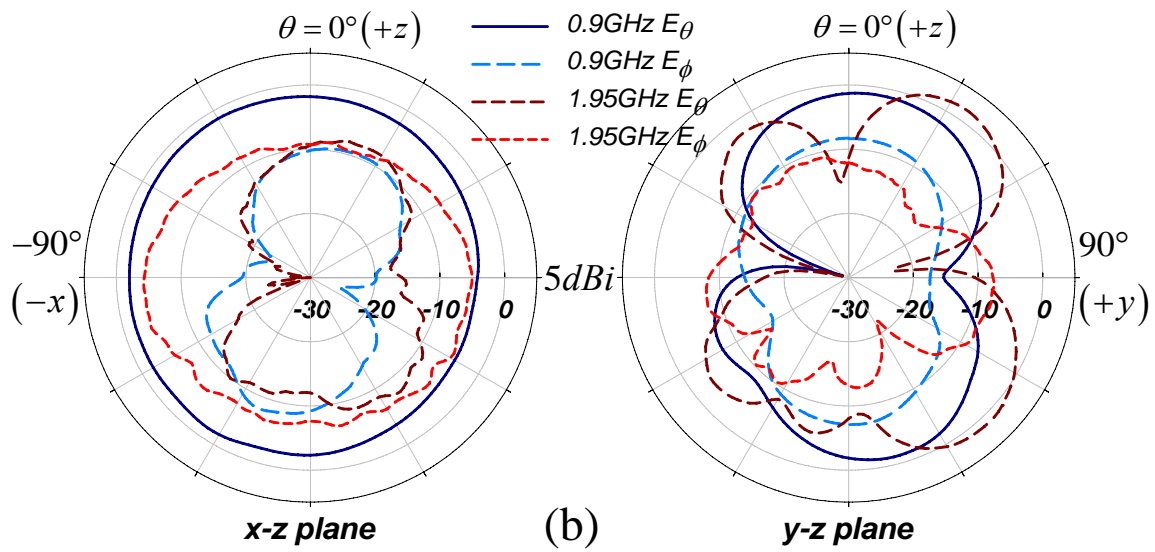
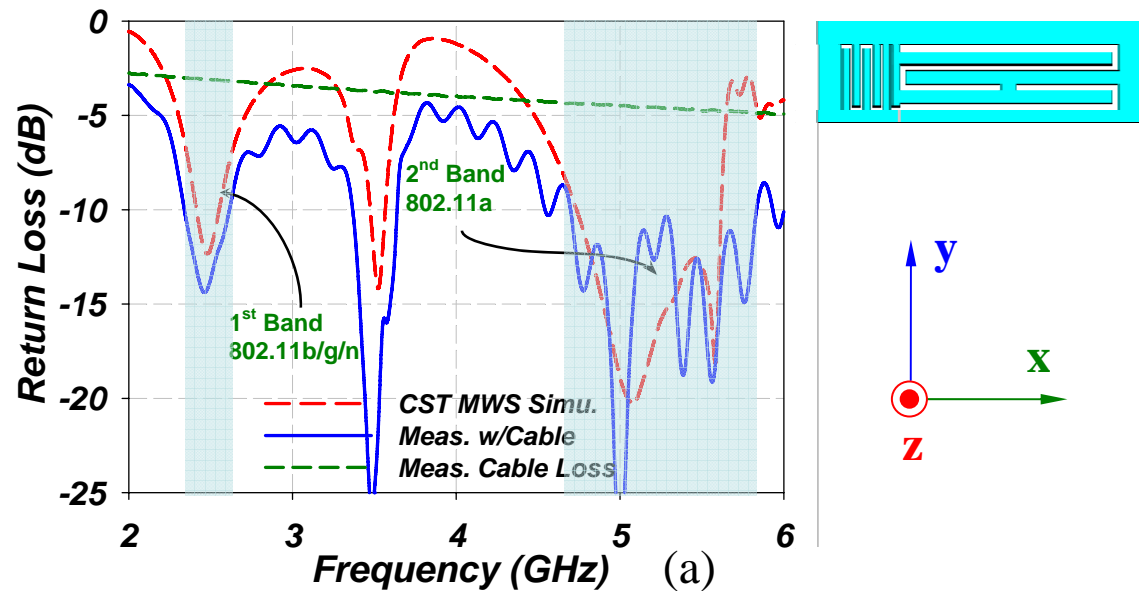


Fig. 5. (a)Simulated and measured return loss of the WWAN configuration and (b) measured radiation patterns



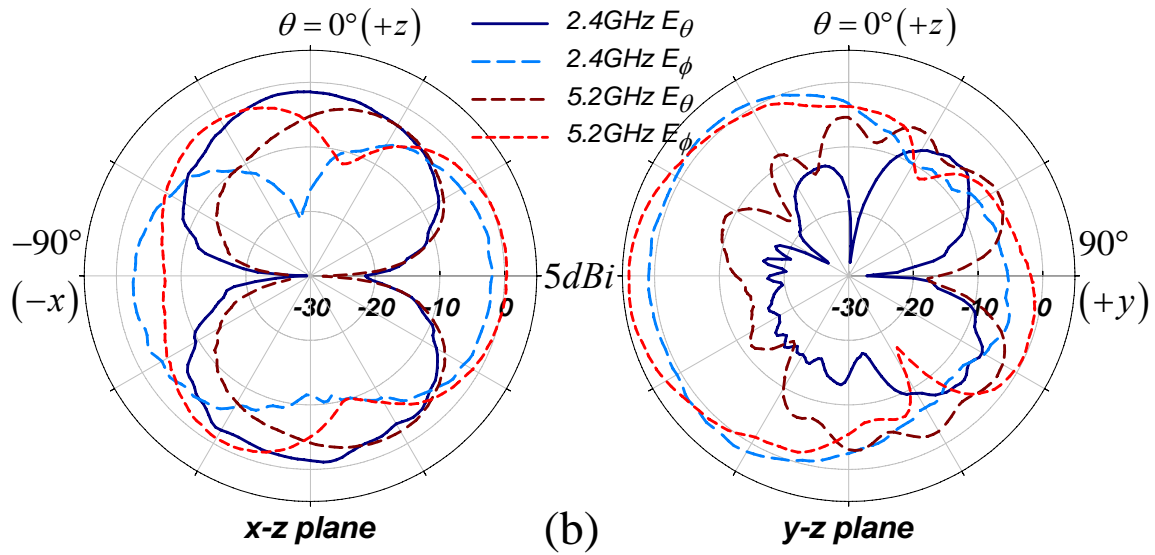


Fig. 6. (a)Simulated and measured return loss of the WLAN configuration and (b) measured radiation patterns

TABLE II
MEASURED GAIN OF MEANDERED MONOPOLE ANTENNA

Frequency (GHz)		0.9	1.95	2.4	5.2
Gain (dBi)	x-z	-1.0/-2.1	-3.7/-5.4	-0.6/-1.8	4.1/0.3
Max/Average	y-z	-0.3/-3.7	1.9/-2.7	0.6/-1.5	0.6/-1.4

3.2. Twin PIFA Antennas for Laptops with p-i-n Diode Switch

As shown in Fig.4, two Microsemi MPP4203 p-i-n diode switches are mounted with opposite orientation across the gaps between the main and parasitic radiators. These switches are controlled by applying +1V or -1V on the coaxial cable to toggle between WWAN and WLAN modes. The simulated and measured return losses of the WWAN and WLAN configurations are shown in Fig.7 and Fig.8 respectively, and excellent agreement is observed. Large rectangular metal plates (32cm x 20cm) are used to emulate the lid and body of a laptop. The antenna is placed on the top and side of the metal plate during the measurement and the radiation patterns at the center of each frequency band are shown together with the measured gain of the horizontal cuts given in Table 3.

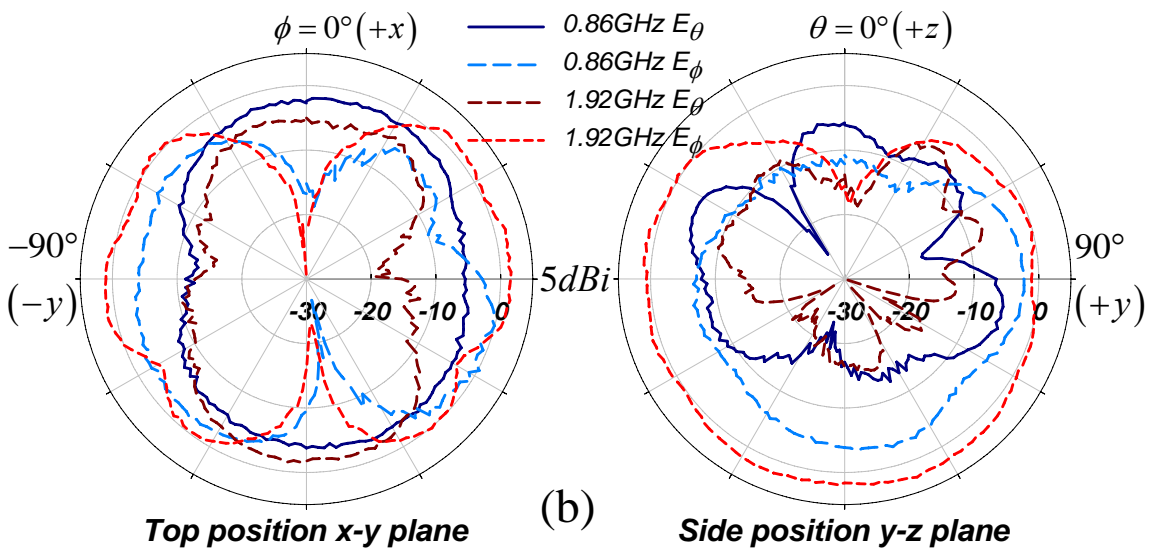
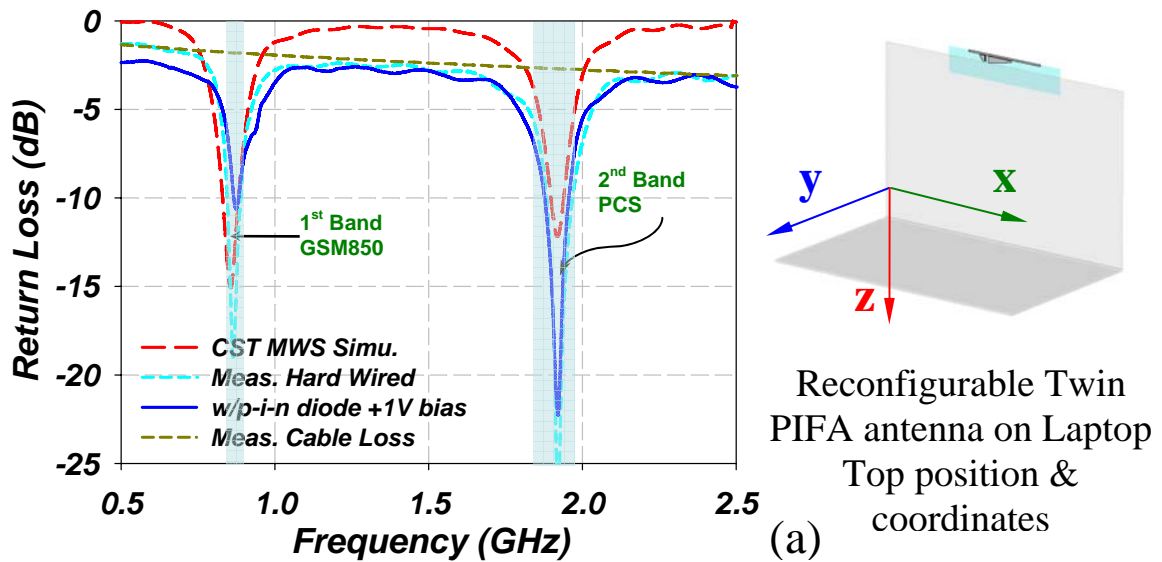


Fig. 7. (a)Simulated and measured return loss of the WWAN configuration and (b) measured radiation patterns

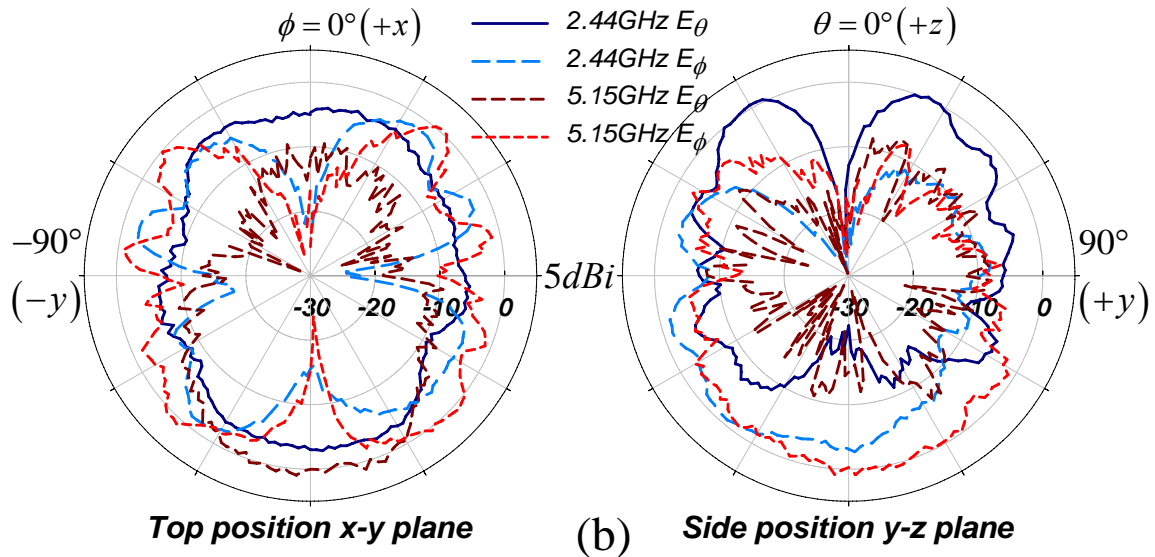
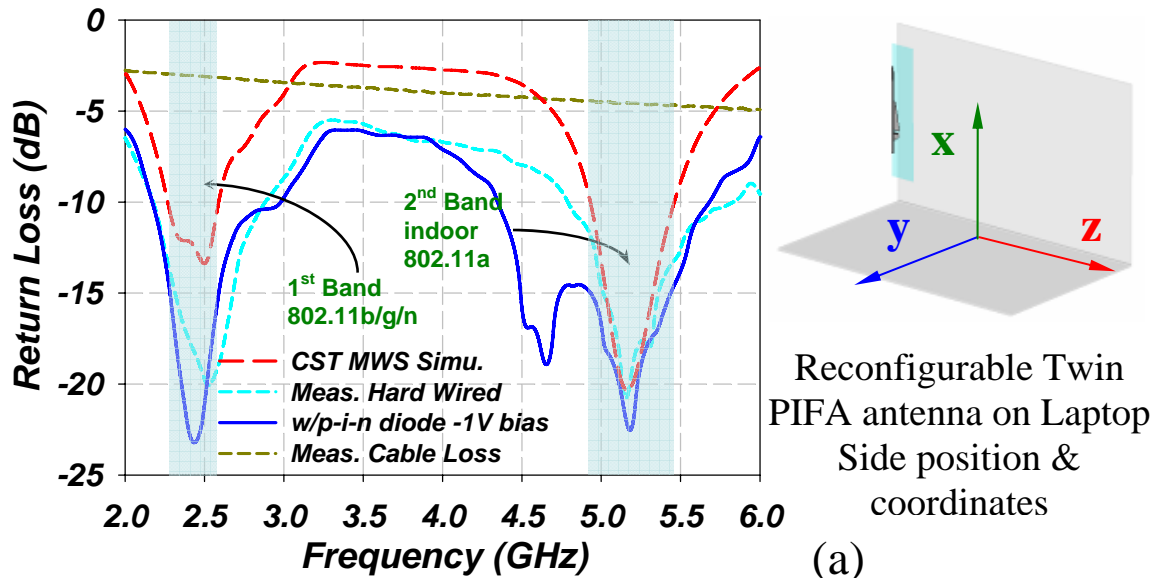


Fig. 8. (a) Simulated and measured return loss of the WLAN configuration and (b) measured radiation patterns

TABLE III
MEASURED GAIN OF TWIN PIFA ANTENNA WITH SWITCHES

Frequency (GHz)	0.96	1.92	2.4	5.15
Gain (dBi)	Top	2.8/-0.1	1.7/-2.8	0.1/-2.8
Max/Average	Side	-0.2/-3.0	2.3/-0.8	0.6/-3.1

In order to evaluate the efficiency of the reconfigurable antenna with switches, the average gain is measured with different biasing current conditions and compared to its hard-wired counterpart. As shown in Fig. 9, as the biasing current increases, the series resistance of p-i-n diode reduces and gain increases. However, after 100mA, the gain starts to saturate, and the DC consumption becomes prohibitively high for mobile platform. A bias current around 50mA is desirable for both antenna gain and battery life.

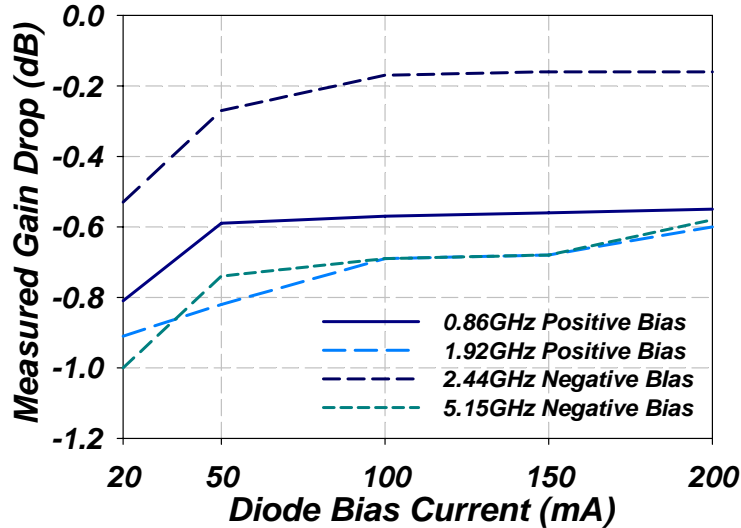


Fig. 9. Measured average gain drop comparing with hard-wired version at various p-i-n diode biasing conditions

4. CONCLUSION

Reconfigurable multi-band antennas have great potential and two novel concepts are introduced here. The first is a meandered monopole structure suitable for all WWAN and WLAN services after bandwidth enhancement. This structure, with its demonstrated excellent gain and omni-directional performance, can be utilized for mobile handsets. Meanwhile the second is a reconfigurable multi-band PIFA antenna which can support the GSM850 and PCS services in one configuration and the WLAN frequencies in the other. With its low profile, it can be embedded into laptop lids. P-i-n diodes have been utilized and integrated with these antennas, and the overall performance of this antenna, as expected, is a function of the driving current.

REFERENCES

- [1] Teng, P.L. "Planar monopole folded into a compact structure for very-low-profile multi-band mobile phone antenna", *Microwave Opt. Tech. Lett.*, vol. 33, Apr. 2002, pp. 22-25.
- [2] Liu, D., Gaucher, B. and Hildner, T., "A dual-band antenna for cellular Applications," in Proc. IEEE AP-S International Symp., Jul.2006, pp 4689-4693